Update to Proposal for an Experiment to Measure Mixing, CP Violation and Rare Decays in Charm and Beauty Particle Decays at the Fermilab Collider - BTeV[*]

March 2002

G.Y. Drobychev, A.S. Lobko, A.R. Lopatik and R.F. Zouevsky
> Belarussian State University, National Science and Education Center, 240040, Minsk

J. Link and P. Yager
> University of California at Davis, Exp. High Energy Group, One Shields Ave.,
> Davis CA 95616-8677 USA

J. Cumalat
> University of Colorado, High Energy Physics, Campus Box 390,
> Boulder, CO 80309, USA

J. A. Appel, E. Barsotti, C. N. Brown, J. Butler, H. Cheung, G. Chiodini, D. Christian,
S. Cihangir, R. Coluccia, I. Gaines, P. Garbincius, L. Garren, E. E. Gottschalk,
A. Hahn, G. Jackson, P. Kasper, P. H. Kasper, R. Kutschke, S. W. Kwan, P. Lebrun,
P. McBride, M. Votava, M. Wang, and J. Yarba
> Fermilab, PO Box 500, Batavia, IL 60510, USA

P. Avery
> University of Florida, Gainesville, FL 32611, USA

M. Bukhari, K. Lau, B.W. Mayes, V. Rodriguez, and S. Subramania
> University of Houston, Houston, TX 77204-5506, USA

R.A. Burnstein, D.M. Kaplan, L.M. Lederman, H.A. Rubin, and C. White
> Illinois Institute of Technology, Chicago, IL 60616, USA

M. Haney, D. Kim, M. Selen, and J. Wiss
> University of Illinois at Urbana-Champaign, High Energy Physics,
> 441 Loomis Lab. of Physics, 1110 W. Green St., Urbana, IL 61801-3080, USA

R. W. Gardner and D. R. Rust
> Physics Department, Indiana University, Bloomington, Indiana, 47405, USA

M. Bertani, L. Benussi, S. Bianco, M.A. Caponero, F. Fabbri, A. Felli, M. Giardoni,
A. LaMonaca, E. Pace, M. Pallotta and A. Paolozzi
> INFN - Laboratori Nazionali di Frascati, CP 13, via E. Fermi 40,
> 1-00044, Frascati, Roma, Italy

G. Alimonti, P. D'Angelo, L. Edera, S. Erba, S. Magni, D. Menasce, L. Moroni,
D. Pedrini, S. Sala and L. Uplegger
> INFN and University of Milano, Italy

G. Boca, G. Liguori, and P. Torre

---

[*]Spokespersons: Joel Butler and Sheldon Stone

INFN - Pavia, Dipartimento di Fisica Nucleare e Teorica, Universita' di Pavia,
Sez. di Pavia, Italy

R. Arcidiacono, S. Argiro, S. Bagnasco, N. Cartiglia, R. Cester, F. Marchetto
E. Menichetti, R. Mussa, and N. Pastrone

INFN - Uni. degli Studi di Torino; Dipt. di Fisica Teorica,
via Pietro Giuria 1; 1-10125, Torino, Italy

A. A. Derevschikov, Y. M. Goncharenko, V. Yu. Khodyrev, V. Kravtsov, A. P. Meschanin,
V. Mochalov, D. Morozov, L. V. Nogach, P. Semenov, K. E. Shestermanov, L. F. Soloviev,
A. Uzunian and A. N. Vasiliev

Institute of High Energy Physics (IHEP), Protvino, Moscow Region, Russia

P. Ratcliffe and M. Rovere

University of Insubria in Como

C. Newsom and R. Braunger

The University of Iowa, Department of Physics & Astronomy,
Iowa City, IA 52242-1479

V. V. Frolov, Y. Kubota, R. Poling, and A. Smith

University of Minnesota, High Energy Physics, Tate Laboratory of Physics,
116 Church St. S.E., Minneapolis, MN 55455, USA

T. Y. Chen, D. Gao, S. Du, Ming Qi, B.P. Zhang, Z. Xi Zhang, and J.W. Zhao

Nanjing University, Dept. of Physics, Nanjing 210008, China

V. Papavassiliou

New Mexico State University

K. Honscheid, and H. Kagan

Ohio State University, HEP Group, Dept. of Experimental or Theoretical Physics,
Smith Lab, 174 W. 18th Ave., Columbus, OH 43210, USA

W. Selove

University of Pennsylvania, Philadelphia, PA 19104, USA

A. Lopez and W. Xiong

University of Puerto Rico, Mayaguez, Puerto Rico

G. Datao, L. Hao, Ge Jin, T. Yang and X.Q. Yu

University of Science and Technology of China, Department of Modern Physics,
Joint Institute for High Energy Physics, Hefei, Anhui 230027, China

C.F. Feng, Yu Fu, Mao He, J.Y. Li, L. Xue, N. Zhang, and X. Y. Zhang

Shandong University, High Energy Physics Group; Jinan, Shandong 250100, China

T. Coan

Southern Methodist University, Dallas, TX 75275, USA

M. Alam

State University of New York at Albany,
Dept. of Physics, Albany, NY 12222, USA

M. Artuso, S. Blusk, C. Boulahouache, O. Dorjkhaidav, K. Khroustalev,
R. Mountain, R. Nandakumar, T. Skwarnicki, S. Stone, J. C. Wang, and H.W. Zhao

Syracuse University, 201 Physics Bldg., Syracuse, NY 13244-1130, USA

K. Cho, T. Handler and R. Mitchell
>University of Tennessee, Knoxville, TN 37996-1200, USA

A. Napier
>Tufts University, High Energy Physics, Science & Technology Center,
>4 Colby St., Medford, MA 02155, USA

W. Johns, P. Sheldon, K. Stenson, Vaandering, and M. Webster
>Vanderbilt University, Department of Physics and Astronomy,
>Nashville, TN 37235, USA

M. Arenton, S. Conetti, B. Cox, and A. Ledovskoy
>University of Virginia, High Energy Physics Group, Charlottesville, VA 22901, USA

G. Bonvicini, D. Cinabro, and A. Schreiner
>Wayne State University, Department of Physics and Astronomy,
>666 W. Hancock, Detroit, MI 48202, USA

M. Sheaff
>University of Wisconsin, Phenomenology Inst., Dept. of Physics,
>1150 University Ave., Madison, WI 53706, USA

J. Slaughter
>Yale University, High Energy Physics, 219 Prospect St.,
>554 JWG, Box 6666, New Haven, CT 06511, USA

S. Menary
>York University, Dept. of Physics
>4700 Keele St., Toronto, ON M3J 1P3, Canada

Contents

i

Summary of Submitted Documents

We have been requested to submit an update of the BTeV plan to the Fermilab Physics Advisory Committee, where to save money the detector has only one arm and there is no new interaction region magnet construction planned. These are to come from a currently running collider experiment at the appropriate time.

The "Physics Case" section is complete and updated with the section on the "New Physics" capabilites of BTeV greatly expanded. We show that precise measurments of rare flavor-changing neutral current processes and CP violation are and will be complementary to the Tevatron and LHC to unraveling the electroweak breaking puzzle.

We include a revised summary of the physics sensitivities for the one-arm detector, which are not simply taking our proposal numbers and dividing by two, because of additional improvements. One important change resulted from an improved understanding of just how important the RICH detector is to muon and electron identification, that we can indeed separate electrons from pions and muons from pions, especially at relatively large angles beyond the physical appature of the EM calorimeter or the Muon Detector. This is documented in the "Physics Sensitivities" section.

The section on the detector includes the motivation for doing b and c physics at a hadron collider, and shows the changes in the detector since the proposal based on our ongoing R&D program. We do not here include a detailed description of the entire detector. That is available in the May, 2000 proposal.[2] We include a summary of our R&D activities for the entire experiment.

Finally, we also include a fully updated cost estimate for the one-arm system.

---

[2]http://www-btev.fnal.gov/public_documents/btev_proposal/index.html

Chapter 1

The Physics Case for BTeV

1.1 Introduction

Experimental particle physics seeks answers to many questions about nature. Some central issues include:

- How are fermion masses generated?

- Why is there a family structure?

- Why are there three families rather than one?

The Standard Model [1] describes current experimental data quite well, but does not directly address these questions. Thus far all predictions are consistent with experiment. Symmetries and symmetry violations are crucially important physics phenomena. Weak decays are known to violate parity, P, and the product of charge-conjugation and parity, CP in the K^o and B^o systems. [2]. That the three family structure allows CP violation to occur naturally via quark mixing is an important clue that we are on the right track. However, the Standard Model is more of a description than an explanation.

The magnitude of CP violation is intimately tied to the question of "baryogenesis," or how did the Universe get rid of the anti-baryons? A possible solution was first proposed by Sakharov [3]. It requires three ingredients: CP violation, lack of thermal equilibrium at some time and baryon non-conservation. The Standard Model provides the third component via quantum corrections to anomaly diagrams. Inflation can provide the lack of thermal equilibrium. Although the Standard Model incorporates CP violation, it is believed that the amount is far too small. Of course we may find that the Standard Model explanation is incorrect.

We describe here a program of measurements that need to be performed in order to test whether the Standard Model indeed describes quark mixing and CP violation. There are many important experimental measurements to be made. We will describe the reasons why these measurements are crucial. We will also point out the important tests that probe physics beyond the Standard Model.

There are many other interesting and important physics topics concerning issues of heavy quark production, the phenomenology of weak decays, CPT violation, etc., that we do not discuss here. It should be kept in mind that other areas of interesting physics can be addressed by BTeV.

1.2 The CKM Matrix

1.2.1 Introduction

The physical point-like states of nature that have both strong and electroweak interactions, the quarks, are mixtures of base states described by the Cabibbo-Kobayashi-Maskawa (CKM) matrix [4],

$$
\begin{pmatrix} d' \\ s' \\ b' \end{pmatrix} = \begin{pmatrix} V_{ud} & V_{us} & V_{ub} \\ V_{cd} & V_{cs} & V_{cb} \\ V_{td} & V_{ts} & V_{tb} \end{pmatrix} \begin{pmatrix} d \\ s \\ b \end{pmatrix} .
\tag{1.1}
$$

The unprimed states are the mass eigenstates, while the primed states denote the weak eigenstates. The V_{ij}'s are complex numbers that can be represented by four independent real quantities. These numbers are fundamental constants of nature that need to be determined from experiment, like any other fundamental constant such as α or G. In the Wolfenstein approximation the matrix is written as [5]

$$
V_{CKM} = \begin{pmatrix} 1 - \lambda^2/2 & \lambda & A\lambda^3(\rho - i\eta(1 - \lambda^2/2)) \\ -\lambda & 1 - \lambda^2/2 - i\eta A^2\lambda^4 & A\lambda^2(1 + i\eta\lambda^2) \\ A\lambda^3(1 - \rho - i\eta) & -A\lambda^2 & 1 \end{pmatrix} .
\tag{1.2}
$$

This expression is accurate to order λ^3 in the real part and λ^5 in the imaginary part. It is necessary to express the matrix to this order to have a complete formulation of the physics we wish to pursue. The constants λ and A have been measured using semileptonic s and b decays [6]; $\lambda \approx 0.22$ and $A \approx 0.8$. The phase η allows for CP violation. There are experimental constraints on ρ and η that will be discussed below.

1.2.2 Unitarity Triangles

The unitarity of the CKM matrix[1] allows us to construct six relationships. These equations may be thought of as triangles in the complex plane. They are shown in Fig. 1.1

In the **bd** triangle, the one usually considered, the angles are all thought to be relatively large. It is described by:

$$
V_{ub}V_{ud}^* + V_{cb}V_{cd}^* + V_{tb}V_{td}^* = 0 \quad .
\tag{1.3}
$$

To a good approximation

$$
|V_{ud}^*| \approx |V_{tb}| \approx 1,
\tag{1.4}
$$

---

[1]Unitarity implies that any pair of rows or columns are orthogonal.
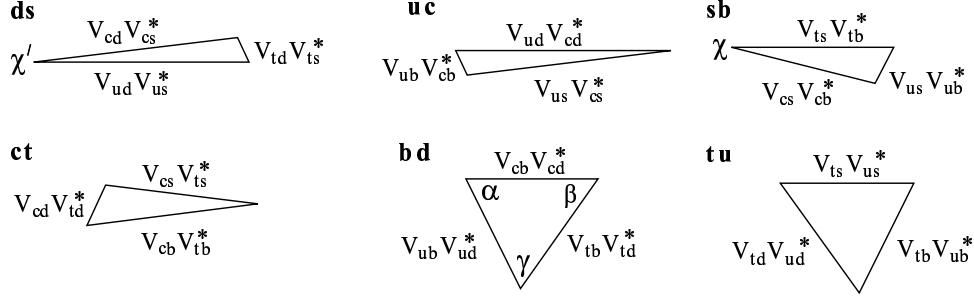
Figure 1.1: The six CKM triangles. The bold labels, i.e **ds** refer to the rows or columns used in the unitarity relationship. (Angles are also shown for later reference.)

which implies

$$\frac{V_{ub}}{V_{cb}} + \frac{V_{td}^*}{V_{cb}} + V_{cd}^* = 0 \quad . \tag{1.5}$$

Since $V_{cd}^* = \lambda$, we can define a triangle with sides

$$1 \tag{1.6}$$

$$\left| \frac{V_{td}}{A\lambda^3} \right| = \sqrt{(\rho - 1)^2 + \eta^2} = \frac{1}{\lambda} \left| \frac{V_{td}}{V_{ts}} \right| \tag{1.7}$$

$$\left| \frac{V_{ub}}{A\lambda^3} \right| = \sqrt{\rho^2 + \eta^2} = \frac{1}{\lambda} \left| \frac{V_{ub}}{V_{cb}} \right| . \tag{1.8}$$

This CKM triangle is depicted in Fig. 1.2.
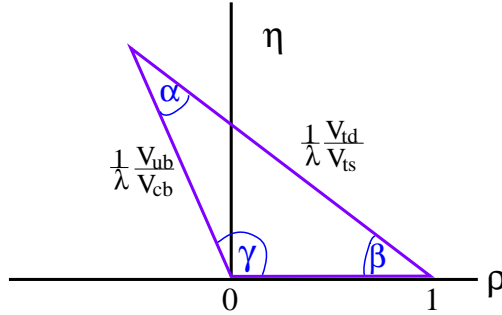
Figure 1.2: The CKM triangle shown in the $\rho - \eta$ plane. The left side is determined by $|V_{ub}/V_{cb}|$ and the right side can be determined using mixing in the neutral B system. The angles can be directly determined by making measurements of CP violation in B decays.

We know two sides already: the base is defined as unity and the left side is determined within a relatively large error by the measurements of $|V_{ub}/V_{cb}|$ [7]. The right side can, in principle, be determined using mixing measurements in the neutral B system. However, even though B_d mixing is well measured, there are theoretical parameters needed that have

4

large uncertainties (see the next section). Later we will discuss other measurements that can determine this side, especially that of B_s mixing. The figure also shows the angles α, β, and γ. These angles can be determined by measuring CP violation in the B system.

Aleksan, Kayser and London [8] created an alternative parameterization expressing the CKM matrix in terms of four independent phases. These are taken as:

$$\beta = arg\left(-\frac{V_{tb}V_{td}^*}{V_{cb}V_{cd}^*}\right), \qquad \gamma = arg\left(-\frac{V_{ub}^*V_{ud}}{V_{cb}^*V_{cd}}\right),$$
$$\chi = arg\left(-\frac{V_{cs}^*V_{cb}}{V_{ts}^*V_{tb}}\right), \qquad \chi' = arg\left(-\frac{V_{ud}^*V_{us}}{V_{cd}^*V_{cs}}\right) . \qquad (1.9)$$

These angles are shown in Fig. 1.1; we have changed the confusing notation of Aleksan *et al.* from ϵ, ϵ' to χ and χ'. We will address the usefulness of this parameterization in section 1.12.2.

1.2.3   Neutral B Mixing

Neutral B mesons can transform to their anti-particles before they decay. The Standard Model diagrams for B_d mixing are shown in Fig. 1.3. (The diagrams for B_s mixing are similar with s quarks replacing d quarks.) Although u, c and t quark exchanges are all shown, the t quark plays a dominant role, mainly due to its mass, since the amplitude of this process grows with the mass of the exchanged fermion.
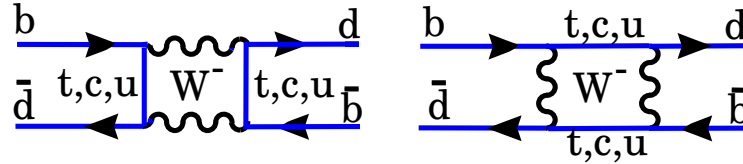
Figure 1.3: The two diagrams for B_d mixing.

The probability of B^o mixing is given by [9]

$$r = \frac{N\left(\overline{B}^o\right)}{N\left(B^o\right)} = \frac{x^2}{2+x^2} , \text{ where} \qquad (1.10)$$

$$x \equiv \frac{\Delta m}{\Gamma} = \frac{G_F^2}{6\pi^2}B_B f_B^2 m_B \tau_B |V_{tb}^*V_{td}|^2 m_t^2 F\left(\frac{m_t^2}{M_W^2}\right)\eta_{QCD}, \qquad (1.11)$$

where $B_B f_B^2$ is related to the probability of the d and $\bar{b}$ quarks forming a hadron and must be estimated theoretically; F is a known function given by Inami and Lin [10] that increases approximately as m_t^2, and η_{QCD} is a QCD correction, with a value ≈ 0.8 [11]. By far the largest uncertainty arises from the unknown decay constant, f_B. This number is associated with the coupling between the B and the W^-. The product $f_B|V_{ub}|$ could in principle be

determined by finding the decay rate of $B^+ \to \mu^+\nu$ or $B^+ \to \tau^+\nu$, both of which are very difficult to measure. Since

$$|V_{tb}^* V_{td}|^2 \propto |(1 - \rho - i\eta)|^2 = (\rho - 1)^2 + \eta^2, \quad (1.12)$$

measuring mixing gives a circle centered at (1,0) in the $\rho - \eta$ plane. The best recent mixing measurements have come from a variety of sources [12], yielding a value (for B_d) of $\Delta m = (0.472 \pm 0.017) \times 10^{12} \, \hbar s^{-1}$.

The right-hand side of the triangle can be determined by measuring B_s mixing using the ratio

$$\frac{\Delta m_s}{\Delta m_d} = \left(\frac{B_s}{B}\right) \left(\frac{f_{B_s}}{f_B}\right)^2 \left(\frac{m_{B_s}}{m_B}\right) \left|\frac{V_{ts}}{V_{td}}\right|^2, \quad (1.13)$$

where

$$\left|\frac{V_{td}}{V_{ts}}\right|^2 = \lambda^2 \left[(\rho - 1)^2 + \eta^2\right]. \quad (1.14)$$

The uncertainty in using the B_d mixing measurement to constrain ρ and η is largely removed since many sources of theoretical uncertainty cancel in the ratio of the first two factors in equation (1.13), which is believed to be known to $\pm 20\%$ [13].

1.2.4   Current Status of the CKM Matrix

Since λ and A have been measured, λ precisely, and A to about $\pm 7\%$ [14], we can view other measurements as giving constraints in the $\rho - \eta$ plane. We will leave the inclusion of CP violation measurements in B^o decay to a later section. One constraint on ρ and η is given by the K_L^o CP violation measurement (ϵ) [15] :

$$\eta \left[(1 - \rho)A^2(1.4 \pm 0.2) + 0.35\right] A^2 \frac{B_K}{0.75} = (0.30 \pm 0.06), \quad (1.15)$$

where B_K is parameter that cannot be measured and thus must be calculated. A reasonable range is $0.9 > B_k > 0.6$, given by an assortment of theoretical calculations [15]; this number is one of the largest sources of uncertainty. Other constraints come from current measurements on V_{ub}/V_{cb}, B_d mixing and a lower limit on B_s mixing. Measurements of $|V_{ub}/V_{cb}|^2$ are proportional to $\rho^2 + \eta^2$ and thus form a circular constraint in the $\rho - \eta$ plane centered at (0,0). Similarly, mixing measurements form a circular constraint centered on (1,0). The current status of constraints on ρ and η is shown in Figure 1.4 from Hocker *et al.* [16]. The confidence level contours are generated using a method where theoretical parameters, such as f_B and B_K, are given equal probability to exist within arbitary selected limits. We caution the reader that this plot is only a guide, since the measured quantities all have large or even dominant errors due to theoretical models. This analysis is in good agreement with that of Rosner [17] and Plaszczynski and Schune [18], but not in agreement with Ciuchini *et al.* [19], who extract what we view as unreasonably small errors from the data [20].

Recent measurements of ϵ'/ϵ in $K_L \to \pi\pi$ decay determine η directly [2]. However, the theoretical errors are so large that all that can be said is that the measurement is consistent with the allowed region.
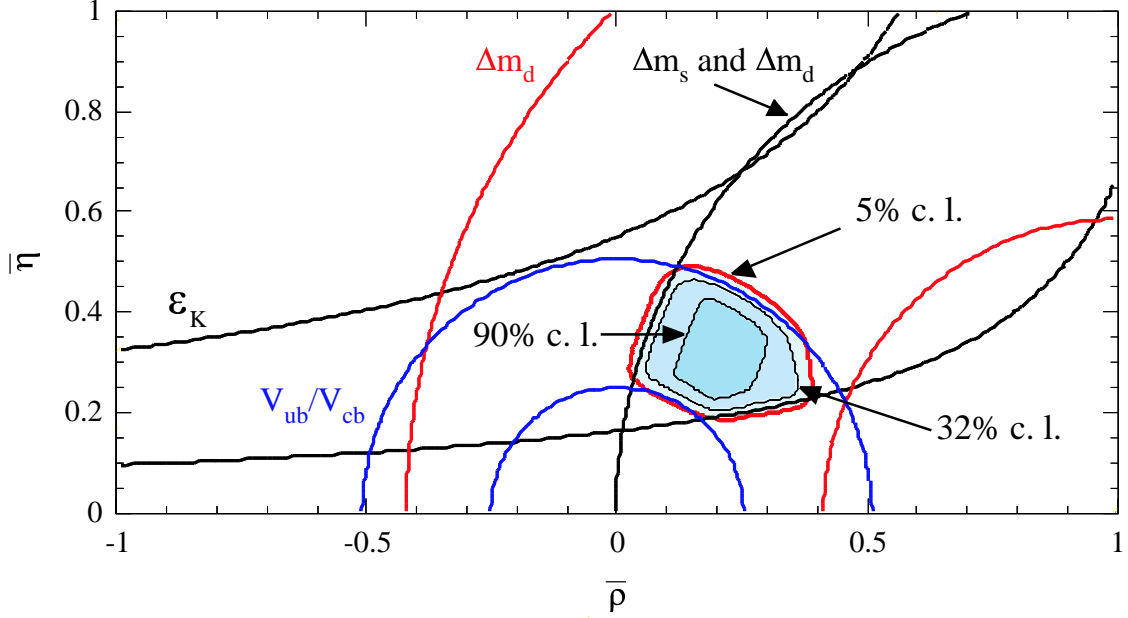
Figure 1.4: The regions in $\overline{\rho} - \overline{\eta}$ space (shaded), where $\overline{\rho} = \rho(1 - \lambda^2/2)$ and $\overline{\eta} = \eta(1 - \lambda^2/2)$, consistent with measurements of CP violation in K_L^o decay (ϵ), V_{ub}/V_{cb} in semileptonic B decay, B_d^o mixing, and the excluded region from limits on B_s^o mixing. The allowed region is defined by a fit from Hocker *et al.* [16]. The large width of the B_d mixing band is dominated by the uncertainty in $B_B f_B^2$. The lines that are not specified are at 5% confidence level.

1.3 CP Violation in Charged B Decays

The fact that the CKM matrix is complex allows CP violation. The theoretical basis of the study of CP violation in B decays was given in a series of papers by Carter and Sanda, and Bigi and Sanda [21]. We start with charged B decays. Consider the final states $f^{\pm}$ which can be reached by two distinct weak processes with amplitudes $\mathcal{A}$ and $\mathcal{B}$, respectively.

$$\mathcal{A} = a_s e^{i\theta_s} a_w e^{i\theta_w}, \quad \mathcal{B} = b_s e^{i\delta_s} b_w e^{i\delta_w} \quad . \tag{1.16}$$

The strong phases are denoted by the subscript s and weak phases are denoted by the subscript w. Under the CP operation the strong phases are invariant but the weak phases change sign, so

$$\overline{\mathcal{A}} = a_s e^{i\theta_s} a_w e^{-i\theta_w}, \quad \overline{\mathcal{B}} = b_s e^{i\delta_s} b_w e^{-i\delta_w} \quad . \tag{1.17}$$

The rate difference is

$$\Gamma - \overline{\Gamma} = |\mathcal{A} + \mathcal{B}|^2 - |\overline{\mathcal{A}} + \overline{\mathcal{B}}|^2 \tag{1.18}$$

$$= 2a_s a_w b_s b_w \sin(\delta_s - \theta_s) \sin(\delta_w - \theta_w) \quad . \tag{1.19}$$

A weak phase difference is guaranteed in the appropriate decay mode (different CKM phases), but the strong phase difference is not; it is very difficult to predict the magnitude of strong phase differences.

As an example consider the possibility of observing CP violation by measuring a rate difference between $B^- \to K^- \pi^o$ and $B^+ \to K^+ \pi^o$. The $K^- \pi^o$ final state can be reached either by tree or penguin diagrams as shown in Fig. 1.5. The tree diagram has an imaginary
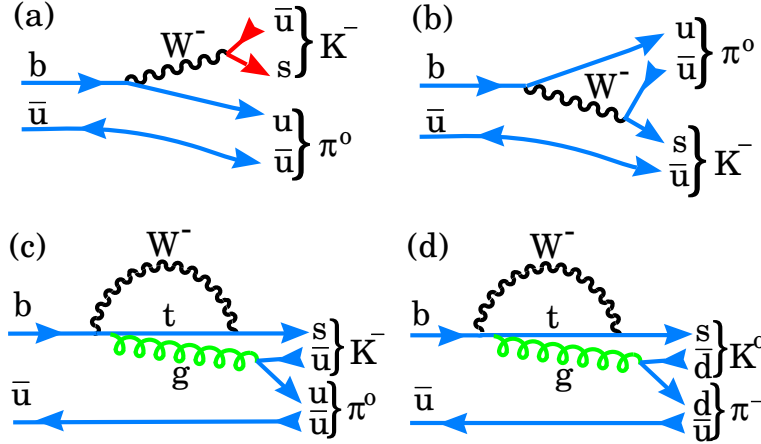
Figure 1.5: Diagrams for $B^- \to K^- \pi^o$, (a) and (b) are tree level diagrams where (b) is color suppressed; (c) is a penguin diagram. (d) Shows a penguin diagram for $B^- \to K^o \pi^-$, which cannot be produced via a tree diagram.

part coming from the V_{ub} coupling, while the penguin term does not, thus insuring a weak phase difference. This type of CP violation is called "direct." Note also that the process $B^- \to K^o \pi^-$ can only be produced by the penguin diagram in Fig. 1.5(d). Therefore, in this simple example, we do not expect a rate difference between $B^- \to K^o \pi^-$ and $B^+ \to K^o \pi^+$. (There have been suggestions that rescattering effects may contribute here and produce a rate asymmetry, see section 1.8.)

1.4 CP Violation Formalism in Neutral B decays

For neutral mesons we can construct the CP eigenstates

$$|B_1^o\rangle = \frac{1}{\sqrt{2}} \left(|B^o\rangle + |\overline{B}^o\rangle \right) \ , \tag{1.20}$$

$$|B_2^o\rangle = \frac{1}{\sqrt{2}} \left(|B^o\rangle - |\overline{B}^o\rangle \right) \ , \tag{1.21}$$

where

$$CP|B_1^o\rangle = |B_1^o\rangle \ , \tag{1.22}$$
$$CP|B_2^o\rangle = -|B_2^o\rangle \ . \tag{1.23}$$

Since B^o and $\overline{B}^o$ can mix, the mass eigenstates are superpositions of $a|B^o\rangle + b|\overline{B}^o\rangle$ which obey the Schrödinger equation

$$i\frac{d}{dt}\begin{pmatrix} a \\ b \end{pmatrix} = H\begin{pmatrix} a \\ b \end{pmatrix} = \left(M - \frac{i}{2}\Gamma\right)\begin{pmatrix} a \\ b \end{pmatrix}. \tag{1.24}$$

If CP is not conserved then the eigenvectors, the mass eigenstates $|B_L\rangle$ and $|B_H\rangle$, are not the CP eigenstates but are

$$|B_L\rangle = p|B^o\rangle + q|\overline{B}^o\rangle, \quad |B_H\rangle = p|B^o\rangle - q|\overline{B}^o\rangle, \tag{1.25}$$

where

$$p = \frac{1}{\sqrt{2}}\frac{1+\epsilon_B}{\sqrt{1+|\epsilon_B|^2}}, \quad q = \frac{1}{\sqrt{2}}\frac{1-\epsilon_B}{\sqrt{1+|\epsilon_B|^2}}. \tag{1.26}$$

CP is violated if $\epsilon_B \neq 0$, which occurs if $|q/p| \neq 1$.

The time dependence of the mass eigenstates is

$$|B_L(t)\rangle = e^{-\Gamma_L t/2}e^{-im_L t/2}|B_L(0)\rangle \tag{1.27}$$

$$|B_H(t)\rangle = e^{-\Gamma_H t/2}e^{-im_H t/2}|B_H(0)\rangle, \tag{1.28}$$

leading to the time evolution of the flavor eigenstates as

$$|B^o(t)\rangle = e^{-\left(im+\frac{\Gamma}{2}\right)t}\left(\cos\frac{\Delta mt}{2}|B^o(0)\rangle + i\frac{q}{p}\sin\frac{\Delta mt}{2}|\overline{B}^o(0)\rangle\right) \tag{1.29}$$

$$|\overline{B}^o(t)\rangle = e^{-\left(im+\frac{\Gamma}{2}\right)t}\left(i\frac{p}{q}\sin\frac{\Delta mt}{2}|B^o(0)\rangle + \cos\frac{\Delta mt}{2}|\overline{B}^o(0)\rangle\right), \tag{1.30}$$

where $m = (m_L + m_H)/2$, $\Delta m = m_H - m_L$ and $\Gamma = \Gamma_L \approx \Gamma_H$. Note that the fraction of B^o remaining at time t is given by $\langle B^o(t)|B^o(t)\rangle^*$, and is a pure exponential, $e^{-\Gamma t}$, in the absence of CP violation.

Indirect CP violation in the neutral B system

As in the case of K_L decay, we can look for the rate asymmetry

$$a_{sl} = \frac{\Gamma\left(\overline{B}^o(t) \to X\ell^+\nu\right) - \Gamma\left(B^o(t) \to X\ell^-\overline{\nu}\right)}{\Gamma\left(\overline{B}^o(t) \to X\ell^+\nu\right) + \Gamma\left(B^o(t) \to X\ell^-\overline{\nu}\right)} \tag{1.31}$$

$$= \frac{1 - \left|\frac{q}{p}\right|^4}{1 + \left|\frac{q}{p}\right|^4} \approx O\left(10^{-3}\right). \tag{1.32}$$

These final states occur only through mixing as the direct decay occurs only as $B^o \to X\ell^+\nu$. To generate CP violation we need an interference between two diagrams. In this case the

9

two diagrams are the mixing diagram with the t-quark and the mixing diagram with the c-quark. This is identical to what happens in the K_L^o case. This type of CP violation is called "indirect." The small size of the expected asymmetry is caused by the off-diagonal elements of the Γ matrix in equation (1.24) being very small compared to the off-diagonal elements of the mass matrix, i.e. $|\Gamma_{12}/M_{12}| \ll 1$ and $\text{Im}(\Gamma_{12}/M_{12}) \neq 0$. This results from the nearly equal widths of the B_L^o and B_H^o [22].

In the case of the B_s^o a relatively large, $\approx 15\%$ component of B_s decays is predicted to end up as a $c\bar{c}s\bar{s}$ final state. Since $\overline{B}_s$ decays with the same rate into the same final state, it has been predicted [23, 24, 25] that there will be a substantial width difference $\Delta\Gamma = \Gamma_H - \Gamma_L \approx 15\%\Gamma$, between CP+ and CP- eigenstates. BTeV can easily measure this lifetime difference by measuring the lifetime of a mixed CP state such as $D_s^+\pi^-$ and comparing with the CP+ state $J/\psi\eta'$. The CP+ state K^+K^- can also be used [26]. For finite $\Delta\Gamma$, equations 1.29 and 1.30 are modified [27]. See section 1.8.5 for more details.

CP violation for B via interference of mixing and decays

Here we choose a final state f which is accessible to both B^o and $\overline{B}^o$ decays. The second amplitude necessary for interference is provided by mixing. Fig. 1.6 shows the decay into f either directly or indirectly via mixing. It is necessary only that f be accessible from either
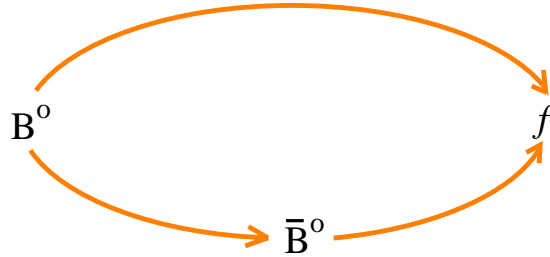
Figure 1.6: Two interfering ways for a B^o to decay into a final state f.

state. However if f is a CP eigenstate the situation is far simpler. For CP eigenstates

$$CP|f_{CP}\rangle = \pm|f_{CP}\rangle. \tag{1.33}$$

It is useful to define the amplitudes

$$A = \langle f_{CP}|\mathcal{H}|B^o\rangle, \quad \bar{A} = \langle f_{CP}|\mathcal{H}|\overline{B}^o\rangle. \tag{1.34}$$

If $\left|\frac{\bar{A}}{A}\right| \neq 1$, then we have "direct" CP violation in the decay amplitude, which was discussed above. Here CP can be violated by having

$$\lambda = \frac{q}{p} \cdot \frac{\bar{A}}{A} \neq 1, \tag{1.35}$$

10

which requires only that λ^2 acquire a non-zero phase, i.e. $|\lambda|$ could be unity and CP violation can occur.

The asymmetry, in this case, is defined as

$$a_{f_{CP}} = \frac{\Gamma\left(B^o(t) \to f_{CP}\right) - \Gamma\left(\overline{B}^o(t) \to f_{CP}\right)}{\Gamma\left(B^o(t) \to f_{CP}\right) + \Gamma\left(\overline{B}^o(t) \to f_{CP}\right)}, \tag{1.36}$$

which for $|q/p| = 1$ gives

$$a_{f_{CP}} = \frac{(1 - |\lambda|^2)\cos(\Delta mt) - 2\mathrm{Im}\lambda\sin(\Delta mt)}{1 + |\lambda|^2}. \tag{1.37}$$

For the cases where there is only one decay amplitude A, $|\lambda|$ equals 1, and we have

$$a_{f_{CP}} = -\mathrm{Im}\lambda\sin(\Delta mt). \tag{1.38}$$

Only the amplitude, $-\mathrm{Im}\lambda$ contains information about the level of CP violation, the sine term is determined only by B^o mixing. In fact, the time integrated asymmetry is given by

$$a_{f_{CP}} = -\frac{x}{1 + x^2}\mathrm{Im}\lambda \quad, \tag{1.39}$$

where $x = \frac{\Delta m}{\Gamma}$. For the case of the B_d^o, $x/(1+x^2) = 0.48$, which is quite lucky as the maximum size of the coefficient is -0.5.

Imλ is related to the CKM parameters. Recall $\lambda = \frac{q}{p} \cdot \frac{\bar{A}}{A}$. The first term is the part that comes from mixing:

$$\frac{q}{p} = \frac{(V_{tb}^*V_{td})^2}{|V_{tb}V_{td}|^2} = \frac{(1 - \rho - i\eta)^2}{(1 - \rho + i\eta)(1 - \rho - i\eta)} = e^{-2i\beta} \quad \text{and} \tag{1.40}$$

$$\mathrm{Im}\frac{q}{p} = -\frac{2(1 - \rho)\eta}{(1 - \rho)^2 + \eta^2} = \sin(2\beta). \tag{1.41}$$

To evaluate the decay part we need to consider specific final states. For example, consider $f \equiv \pi^+\pi^-$. The simple spectator decay diagram is shown in Fig. 1.7. For the moment we will assume that this is the only diagram which contributes. Later we will show why this is not true. For this $b \to u\bar{u}d$ process we have

$$\frac{\bar{A}}{A} = \frac{(V_{ud}^*V_{ub})^2}{|V_{ud}V_{ub}|^2} = \frac{(\rho - i\eta)^2}{(\rho - i\eta)(\rho + i\eta)} = e^{-2i\gamma}, \tag{1.42}$$

and

$$\mathrm{Im}(\lambda) = \mathrm{Im}(e^{-2i\beta}e^{-2i\gamma}) = \mathrm{Im}(e^{2i\alpha}) = \sin(2\alpha) \quad . \tag{1.43}$$

---

[2]λ here is not the same variable that occurs in the Wolfenstein representation of the CKM matrix.
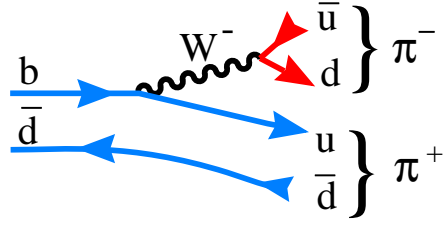
Figure 1.7: Decay diagram at the tree level for $B^o \to \pi^+\pi^-$.

The final state $J/\psi K_S$ plays an especially important role in the study of CP violation. It is a CP eigenstate and its decay is dominated by only one diagram, shown in Fig. 1.8. In this case we do not get a phase from the decay part because

$$\frac{\bar{A}}{A} = \frac{(V_{cb}V_{cs}^*)^2}{|V_{cb}V_{cs}|^2} \tag{1.44}$$

is real. In this case the final state is a state of negative CP, i.e. $CP|J/\psi K_S\rangle = -|J/\psi K_S\rangle$.
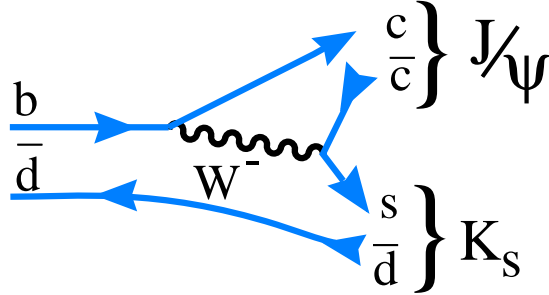
Figure 1.8: Decay diagram at the tree level for $B^o \to J/\psi K_S$.

This introduces an additional minus sign in the result for Imλ. Before finishing discussion of this final state we need to consider in more detail the presence of the K_S in the final state. Since neutral kaons can mix, we pick up another mixing phase. This term creates a phase given by

$$\left(\frac{q}{p}\right)_K = \frac{(V_{cd}^*V_{cs})^2}{|V_{cd}V_{cs}|^2}, \tag{1.45}$$

which is zero. It is necessary to include this term, however, since there are other formulations of the CKM matrix than Wolfenstein, which have the phase in a different location. It is important that the physics predictions not depend on the CKM convention.[3]

In summary, for the case of $f = J/\psi K_S$, Im$\lambda = -\sin(2\beta)$.

---

[3]Here we don't include CP violation in the neutral kaon since it is much smaller than what is expected in the B decay.

1.5 Techniques for Determining β

The decay $B^o \rightarrow J/\psi K_S$ is the primary source for measurements of $\sin(2\beta)$. In the common phase convention, CP violation is expected to arise mostly from the mixing, driven by $\mathrm{Im}(q/p)$, while the decay amplitude, $\mathrm{Im}(\bar{A}/A)$, is expected to contribute only a small part (see Fig. 1.8).[4]

1.5.1 Results on $\sin 2\beta$

For years observation of large CP violation in the B system was considered to be one of the corner stone predictions of the Standard Model. Yet it took a very long time to come up with definitive evidence. The first statistically significant measurements of CP violation in the B system were made recently by BABAR and BELLE [2]. This enormous achievement was accomplished using an asymmetric e^+e^- collider on the $\Upsilon(4S)$ which was first suggested by Pier Oddone. The measurements are listed in Table 1.1, along with other previous indications [12].

Table 1.1: Measurements of $\sin 2\beta$.

Experiment	$\sin 2\beta$
BABAR	$0.59 \pm 0.14 \pm 0.05$
BELLE	$0.99 \pm 0.14 \pm 0.06$
Average	0.79 ± 0.11
CDF	$0.79^{+.41}_{-0.44}$
ALEPH	$0.84^{+0.82}_{-1.04} \pm 0.16$
OPAL	$3.2^{+1.8}_{-2.0} \pm 0.5$

The average value of 0.79 ± 0.11 is taken from BABAR and BELLE only. These two measurements do differ by a sizeable amount, but the confidence level that they correctly represent the same value is 6%. This value is consistent with what is expected from the other known constraints on ρ and η. We have

$$\overline{\eta} = (1 - \overline{\rho})\frac{1 \pm \sqrt{1 - \sin^2 2\beta}}{\sin 2\beta} \quad . \tag{1.46}$$

There is a four fold ambiguity in the translation between $\sin 2\beta$ and the linear constraints in the $\rho - \eta$ plane. These occur at β, $\pi/2 - \beta$, $\pi + \beta$ and $3\pi/2 - \beta$. Two of these constraints are shown in Figure 1.9. The other two can be viewed by extending these to negative $\overline{\eta}$. We think $\eta > 0$ based only on measurement of ϵ' in the neutral kaon system. This analysis clearly shows that current data are consistent with the Standard Model.

---

[4]Actually the only phase that has physical meaning is the product of $q/p \cdot \bar{A}/A$.
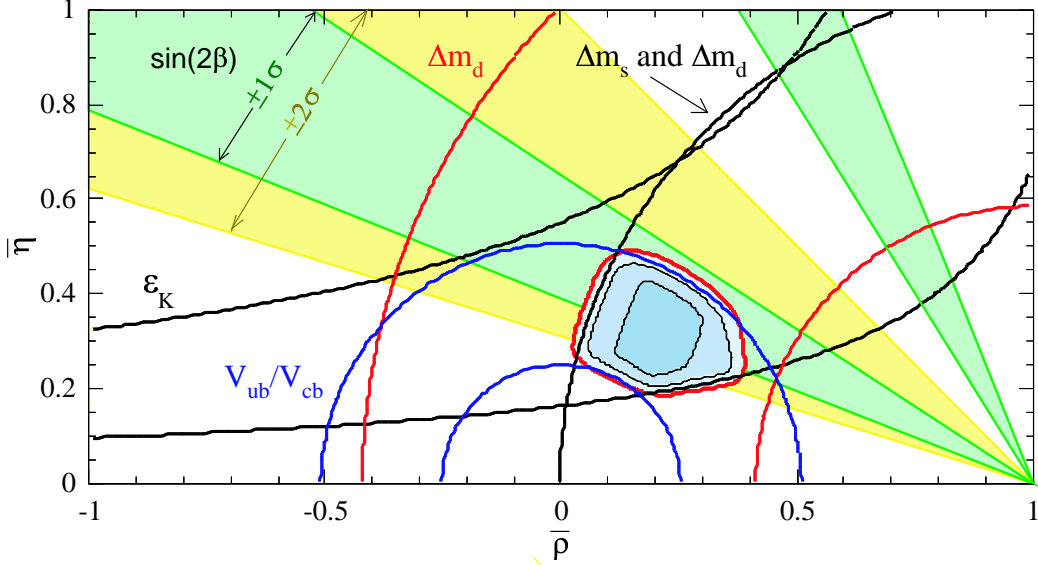
Figure 1.9: Constraints from $\sin 2\beta$ measurement overlaid with other constraints from Hocker *et al.* [16]. The inner band is at 1σ while the outer band, shown on one band only, is at 2σ.

In BTeV, we aim to improve significantly on the precision of the $\sin(2\beta)$ measurement. Furthermore, we intend to be able to remove "ambiguities." When we measure $\sin(2\phi)$, where ϕ is any angle, we have a four-fold ambiguity in ϕ, namely ϕ, $\pi/2 - \phi$, $\phi + \pi$ and $3\pi/2 - \phi$. These ambiguities can mask the effects of new physics. Our task is to remove as many of the ambiguities as possible.

1.5.2 Removal of Two of the β Ambiguities

The decay $B \to J/\psi\, K^*(890)$, where $K^* \to K_S\pi^o$ can be used to get information about the sign of $\cos(2\beta)$, which would remove two of the ambiguities [28]. This decay is described by three complex decay amplitudes. Following a suggestion of Dighe, Dunietz, and Fleischer [29, 30], we write the decay amplitudes $A_0 = -\sqrt{1/3}\,S + \sqrt{2/3}\,D$, $A_\| = \sqrt{2/3}\,S + \sqrt{1/3}\,D$, and $A_\perp = P$, where S, P, and D denote S, P, and D wave amplitudes, respectively. Normalizing the decay amplitudes to $|A_0|^2 + |A_\||^2 + |A_\perp|^2 = 1$ and eliminating one overall phase leaves four independent parameters.

The full angular distribution of a B meson decaying into two vector particles is specified by three angles. The helicity angle basis [31] has been used for angular analyses of $B \to J/\psi\, K^*$ decays. An alternative basis, called the transversity basis is more suitable for extracting parity information [30].

In the transversity basis, the direction of the K^* in the J/ψ rest frame defines the x-axis of a right-handed coordinate system. The $K\pi$ plane fixes the y-axis with $p_y(K) > 0$ and the normal to this plane defines the z-axis. The transversity angles θ_{tr} and ϕ_{tr} are then defined as polar and azimuth angles of the l^+ in the J/ψ rest frame. The third angle, the

K^* decay angle θ_{K^*}, is defined as that of the K in the K^* rest frame relative to the negative of the J/ψ direction in that frame. Using these definitions the full angular distribution of the $B \to J/\psi\, K^*$ decay is [30]:

$$\frac{1}{\Gamma}\frac{d^3\Gamma}{d\cos\theta_{\mathrm{tr}}\, d\cos\theta_{K^*}\, d\phi_{\mathrm{tr}}}$$
$$= \tfrac{9}{32\pi}\{2\,|A_0|^2\,\cos^2\theta_{K^*}(1-\sin^2\theta_{\mathrm{tr}}\cos^2\phi_{\mathrm{tr}})$$
$$+\,|A_\parallel|^2\,\sin^2\theta_{K^*}(1-\sin^2\theta_{\mathrm{tr}}\sin^2\phi_{\mathrm{tr}})$$
$$+\,|A_\perp|^2\,\sin^2\theta_{K^*}\sin^2\theta_{\mathrm{tr}}\sin^2\phi_{\mathrm{tr}}$$
$$-\,\mathrm{Im}\,(A_\parallel^*A_\perp)\,\sin^2\theta_{K^*}\sin 2\theta_{\mathrm{tr}}\sin\phi_{\mathrm{tr}}$$
$$+\,\tfrac{1}{\sqrt{2}}\,\mathrm{Re}\,(A_0^*A_\parallel)\,\sin 2\theta_{K^*}\sin^2\theta_{\mathrm{tr}}\sin 2\phi_{\mathrm{tr}}$$
$$+\,\tfrac{1}{\sqrt{2}}\,\mathrm{Im}\,(A_0^*A_\perp)\,\sin 2\theta_{K^*}\sin 2\theta_{\mathrm{tr}}\cos\phi_{\mathrm{tr}}\ \}. \qquad (1.47)$$

For $\bar{B}$ decays the interference terms containing $A_\perp$ switch sign while all other terms remain unchanged.

Results shown in Table 1.2 have been obtained from CLEO, CDF and BABAR using the decay $\bar{K}^{*o} \to K^-\pi^+$.

Parameter	CLEO [32]	CDF [33]	BABAR [34]
$|A_0|^2\ =\ \Gamma_{\mathrm{L}}\,/\,\Gamma$	$0.52 \pm 0.07 \pm 0.04$	$0.59 \pm 0.06 \pm 0.02$	$0.60 \pm 0.03 \pm 0.02$
$|A_\perp|^2\ =\ |P|^2$	$0.16 \pm 0.08 \pm 0.04$	$0.13\,^{+0.12}_{-0.06} \pm 0.03$	$0.16 \pm 0.03 \pm 0.01$

Table 1.2: Resulting decay amplitudes from the fit to the transversity angles. The first error is statistical and the second is the estimated systematic uncertainty.

The parity odd component, $|A_\perp|^2$, has been definitely established by BABAR as being significantly non-zero, and is $\approx 25\%$ of the rate of the parity even component. This is likely large enough to allow the determination of the sign of the interference terms using the tagged $K^{*o} \to K_S\pi^o$ decays; that, in turn, allows a determination of the sign of the product of $\cos(2\beta)$ with a strong phase-shift. The sign of this phase-shift can either be obtained from factorization, which is a dangerous procedure, or using the much weaker assumption of SU(3) symmetry, and analyzing the time-dependent oscillations in the decay $B_s \to J/\psi\phi$ [28], where the mixing phase is expected to be small.

Another independent method of removing two of the ambiguities is to measure the sign of the $\cos(2\beta)$ term in the decay $B^o \to J/\psi K^o$, $K^o \to \pi^\pm\ell^\mp\nu$. This idea developed by Kayser [35], works because of the interference between K_L and K_S in the decay, where the decay amplitudes are equal. The time evolution of the decay width can be expressed in terms of the B^o decay time (t_B) and the K^o decay time (t_K) as

$$\Gamma(t_B, t_K) \propto$$
$$e^{-\Gamma_B t_B} \Big\{ e^{-\gamma_s t_K} \left[1 \mp sin(2\beta) sin(\Delta m_B t_B)\right]$$
$$+ e^{-\gamma_L t_K} \left[1 \pm sin(2\beta) sin(\Delta m_B t_B)\right]$$
$$\pm (\mp) 2 e^{-\frac{1}{2}(\gamma_s + \gamma_L) t_K} \big[\cos(\Delta m_B t_B) \cos(\Delta m_K t_K)$$
$$+ \cos(2\beta) sin(\Delta m_B t_B) sin(\Delta m_K t_K) \big] \Big\},$$

$$(1.48)$$

where the top sign of each pair is for B^o, and the bottom for $\overline{B}^o$. The first pair of signs in the third line refers to the kaon decay mode $\pi^- \ell^+ \nu$ (K), while the second pair is for $\pi^+ \ell^- \bar{\nu}$ $(\overline{K})$.

To get an idea of the predicted asymmetries, we integrate this equation over t_B. There are four different rates that can be denoted as combinations of B and $\overline{B}$ with K and $\overline{K}$. In Fig. 1.10 we show the four rates as solid lines if $cos(2\beta)$ were positive and the four rates as dashed lines if $cos(2\beta)$ were negative. These were done for $sin(2\beta) = 0.7$. If $sin(2\beta)$ were smaller the rate differences would be larger and vice-versa.
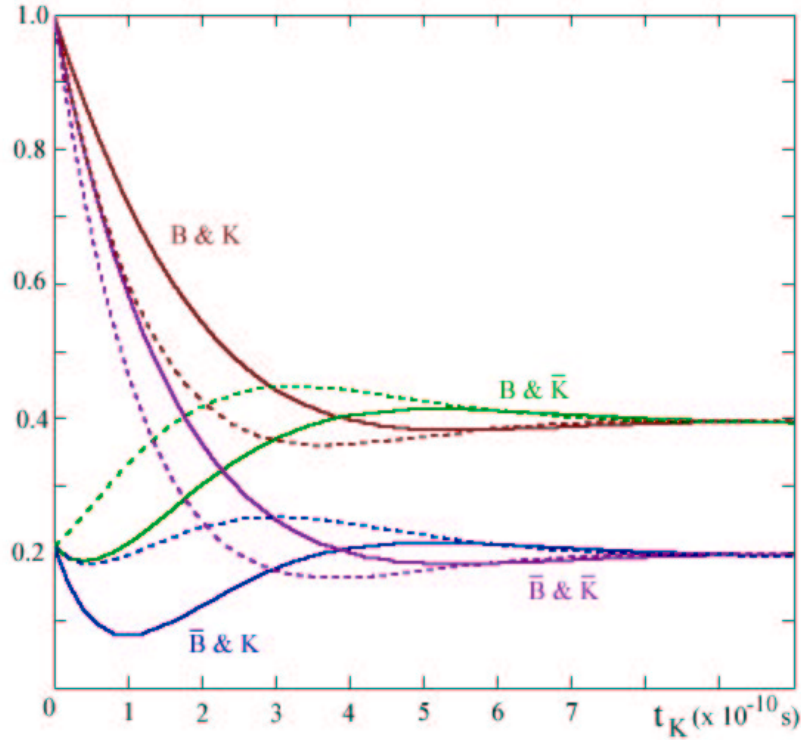
Figure 1.10: The decay rates for $B^o \to J/\psi K^o$, $K^o \to \pi \ell \nu$, as a function of K^o decay time, integrated over the B^o decay time. The solid lines have the sign of the $cos(2\beta)$ term as positive, while the corresponding dashed lines have negative values. The absolute normalization is arbitrary, and $sin(2\beta)$ was fixed at 0.7.

The differences are large over about five K_S lifetimes. Since only the sign of the $cos(2\beta)$

term needs to be found, all other parameters, including $\sin(2\beta)$ are specified. Unfortunately, the event rate is rather small, since $\mathcal{B}(K_S \to \pi\ell\nu) = 1.4 \times 10^{-3}$ and although $\mathcal{B}(K_L \to \pi\ell\nu) = 0.66$, only 1% of the K_L decay soon enough to be of use. Roughly, we have about 100 times fewer events than in $J/\psi K_S$. However, if the backgrounds are not too large, it will only take on the order of a hundred events to successfully determine the sign of $\cos(2\beta)$ using this technique.

It is interesting to note that measuring this combination of B^o and K^o decay modes can lead to measurements of CPT violation [36].

1.5.3 Other Modes for Measuring $\sin(2\beta)$

New physics can add differently to the phases in different decay modes if it contributes differently to the relative decay amplitudes $A/\overline{A}$. Therefore it is interesting to measure CP violation in redundant modes. For example, the decay $B^o \to \phi K_S$ should also measure $\sin(2\beta)$. If it is different than that obtained by $B^o \to J/\psi K_S$, that would be a strong indication of new physics [37]. We list in Table 1.3 other interesting modes to check $\sin(2\beta)$. The branching ratios listed with errors have been measured [38, 39, 40], while those without are theoretical estimates.

Table 1.3: Other modes useful for cross-checking $\sin(2\beta)$

Decay Mode	Branching Ratio
$B^o \to \phi K_S$	$(4.0 \pm 2.1)) \times 10^{-6}$
$B^o \to D^+ D^-$	$\approx 10^{-3}$
$B^o \to D^{*+} D^-$	$\approx 10^{-3}$
$B^o \to \eta\prime K^o$,	$(5.9 \pm 1.9) \times 10^{-5}$
$B^o \to J/\psi(\pi^o,\ \eta\ \text{or}\ \eta\prime)$	$(3.4 \pm 1.6) \times 10^{-5}$

1.6 Comment on Penguin Amplitudes

Many processes can have penguin components. The diagram for $B^o \to \pi^+\pi^-$ is shown in Fig. 1.11. The $\pi^+\pi^-$ final state is expected to have a rather large penguin amplitude $\sim 20\%$ of the tree amplitude. Then $|\lambda| \neq 1$ and $a_{f_{CP}}$, equation 1.37, develops a $\cos(\Delta mt)$ term. In the $J/\psi K_S$ case, the penguin amplitude is expected to be small since a $c\bar{c}$ pair must be "popped" from the vacuum; even if the penguin decay amplitude were of significant size here, the decay phase, $\text{Im}(\overline{A}/A)$ is the same as the tree level process, and quite small.

17
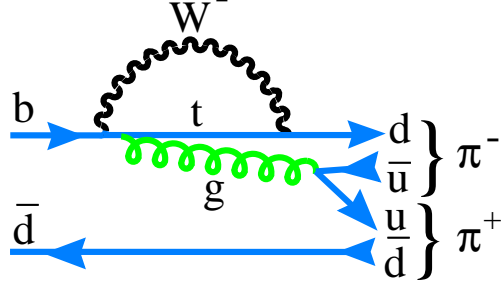
Figure 1.11: Penguin diagram for $B^o \to \pi^+\pi^-$.

1.7 Techniques for Determining α

1.7.1 Introduction

Measuring α is more difficult than measuring β in several respects. First of all, the decay amplitudes are modulated by V_{ub} rather than V_{cb}, making the overall rates small. Secondly, the gluonic penguin rates are of the same order causing well known difficulties in extracting the weak phase angle (see section 1.6 above). The penguin diagrams add a third amplitude to the tree level and mixing amplitudes. It turns out, however, that this complication can be a blessing in disguise. The interference generates $\cos(2\alpha)$ terms in the decay rate, that can be used to remove discrete ambiguities.

The decay $B^o \to \pi^+\pi^-$ has oft been cited as a way to measure $\sin(2\alpha)$. However, the penguin pollution mentioned above, makes it difficult to extract the angle. Table 1.4 lists the currently measured branching ratios for B decays into $\pi\pi$ or $K\pi$.

Table 1.4: Branching Ratios for $B \to K\pi$ and $B \to \pi\pi$ in units of 10^{-6}.

Mode	CLEO [41]	BABAR [42]	BELLE [43]	Average
$\pi^+\pi^-$	$4.7^{+1.8}_{-1.5} \pm 0.6$	$4.1 \pm 1.0 \pm 0.7$	$5.6^{+2.3}_{-2.0} \pm 0.4$	$4.5^{+0.9}_{-0.8}$
$\pi^+\pi^o$	<12	<9.6	<13.4	
$K^\pm\pi^\mp$	$18.8^{+2.8}_{-2.6} \pm 1.3$	$16.7 \pm 1.6 \pm 1.3$	$19.3^{+3.4+1.5}_{-3.2-.06}$	$17.7^{+1.6}_{-1.5}$
$K^+\pi^o$	$12.1^{+3.0+2.1}_{-2.8-1.4}$	$10.8^{+2.1}_{-1.9} \pm 1.6$	$16.3^{+3.5+1.6}_{-3.3-1.8}$	$12.1^{+1.7}_{-1.6}$
$K^o\pi^-$	$18.2^{+4.6}_{-4.0} \pm 1.6$	$18.2^{+3.3}_{-3.0} \pm 2.0$	$13.7^{+5.7+1.9}_{-4.8-1.8}$	$17.3^{+2.7}_{-2.4}$
$K^o\pi^o$	$14.8^{+5.9+2.4}_{-5.1-3.3}$	$8.2^{+3.1}_{-2.7} \pm 1.2$	$16.0^{+7.2+2.5}_{-5.9-2.7}$	$10.4^{+2.7}_{-2.5}$

These results indicate that the penguin amplitude is quite large and cannot be ignored. Gronau and London [44] have shown that an isospin analysis using the additional decays $B^- \to \pi^-\pi^o$ and $B^o \to \pi^o\pi^o$ can be used to extract α [45], but the $\pi^o\pi^o$ final state is extremely difficult to detect in any existing or proposed experiment. Other authors have suggested different methods [46], but they all have theoretical assumptions. Thus, measurement of the

CP asymmetry in $B^o \to \pi^+\pi^-$ cannot, in our view, provide an accurate determination of $\sin(2\alpha)$ unless some new breakthrough in theory occurs.

1.7.2 Using $B^o \to \rho\pi \to \pi^+\pi^-\pi^o$ To Determine α

There is however, a theoretically clean method to determine α. The interference between tree and penguin diagrams can be exploited by measuring the time dependent CP violating effects in the decays $B^o \to \rho\pi$ as shown by Snyder and Quinn [47]. There are three such neutral decay modes, listed in Table 1.5 with their respective penguin and tree amplitudes, denoted by T^{ij}, where i lists charge of the ρ and j the charge of the π. For the $\rho^o\pi^o$ mode, isospin constraints are used to eliminate T^{oo}. The amplitudes for the charged decays are also given.

Table 1.5: $B^o \to \rho\pi$ Decay Modes

Decay Mode	Decay Amplitudes		
$\sqrt{2}A(B^+ \to \rho^+\pi^o)$	$=S_1$	$=T^{+o} + 2P_1$	
$\sqrt{2}A(B^+ \to \rho^o\pi^+)$	$=S_2$	$=T^{o+} - 2P_1$	
$A(B^o \to \rho^+\pi^-)$	$=S_3$	$=T^{+-} + P_1 + P_o$	
$A(B^o \to \rho^-\pi^+)$	$=S_4$	$=T^{-+} - P_1 + P_o$	
$2A(B^o \to \rho^o\pi^o)$	$=S_5$	$=T^{+-} + T^{+-} - T^{+o} - T^{o+} - 2P_o$	

For the $\rho\pi$ final state, the ρ decay amplitude can be parameterized as

$$f(m,\theta) = \frac{\cos(\theta)\Gamma_\rho}{2(m_\rho - m - i0.5\Gamma_\rho)} \quad , \tag{1.49}$$

where m_ρ is the ρ mass of 0.77 GeV and Γ_ρ, the width of 0.15 GeV. θ is the helicity decay angle and the $\cos(\theta)$ dependence arises because the ρ must be fully polarized in this decay which starts with a spin-0 B and ends with a spin-1 ρ and spin-0 π.

The full decay amplitudes for $B^o \to \rho\pi \to \pi^+\pi^-\pi^o$ and the corresponding $\overline{B}^o$ decay are given by

$$
\begin{aligned}
A(B^o) &= f^+ S_3 + f^- S_4 + f^o S_5/2 \\
A(\overline{B}^o) &= f^+ \overline{S}_3 + f^- \overline{S}_4 + f^o \overline{S}_5/2 \quad ,
\end{aligned}
\tag{1.50}
$$

where the superscript on the f indicates the charge of the ρ. The sum over the three neutral B decay amplitudes involves only tree amplitudes; the penguins vanish. The angle between this sum for B^o decays ($\equiv T$) and the sum for $\overline{B}^o$ ($\equiv \overline{T}$) is precisely α. Computing the amplitudes gives a series of terms which have both $\sin(\Delta mt)$ and $\cos(\Delta mt)$ time dependences and coefficients which depend on both $\sin(2\alpha)$ and $\cos(2\alpha)$.

To extract α only the neutral modes need be measured. Further constraints and information about penguin phases can be extracted if the charged B's are also measured. But this is difficult because there are two π^o's in the $\rho^+\pi^o$ decay mode.

The $\rho\pi$ final state has many advantages. First of all, it has a relatively large branching ratio. The CLEO measurement for the $\rho^o\pi^+$ final state is $(1.0\pm0.3\pm0.2)\times10^{-5}$ [48]. The rate for the neutral B final state $\rho^\pm\pi^\mp$ is $(2.8^{+0.8}_{-0.7}\pm0.4)\times10^{-5}$, while the $\rho^o\pi^o$ final state is limited at 90% confidence level to $< 5.1 \times 10^{-6}$ [49]. BABAR finds a quite similar rate for $\rho^\pm\pi^\mp$ of $(2.9\pm0.5\pm0.4)\times10^{-5}$, and limits $\rho^o\pi^o$ at 90% confidence level to $< 10.6\times10^{-6}$ [42]. These measurements are consistent with theoretical expectations [50]. Secondly, since the ρ is fully polarized, the periphery of the Dalitz plot to be heavily populated, especially the corners. A sample Dalitz plot is shown in Fig. 1.12. This kind of distribution is good for maximizing the interferences, which helps minimize the error. Furthermore, little information is lost by excluding the Dalitz plot interior, a good way to reduce backgrounds.
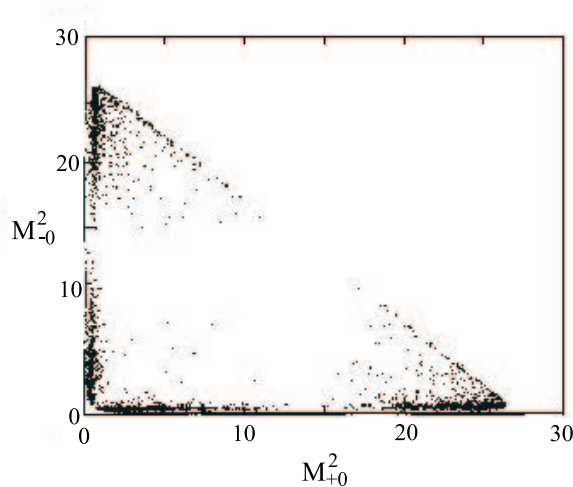
Figure 1.12: The Dalitz plot for $B^o \rightarrow \rho\pi \rightarrow \pi^+\pi^-\pi^o$ from Snyder and Quinn.

Snyder and Quinn have performed an idealized analysis that uses 1000 or 2000 flavor tagged background free events. The 1000 event sample usually yields good results for α, but sometimes does not resolve the ambiguity. With the 2000 event sample, however, they always succeed.

Recently Quinn and Silva have pointed out ways of using time integrated untagged data to specify some of the parameters with larger data samples [51]. Some concern for the effect of the B^* pole on the data has been expressed by Deandrea *et al.* [52].

1.7.3   Use of $B^o \rightarrow \pi^+\pi^-$ for Ambiguity Resolution

The decay $B^o \rightarrow \pi^+\pi^-$ can be used with some theoretical input to resolve the remaining ambiguity in $\sin(2\alpha)$. The difference in CP asymmetries between $\pi\pi$ and $\rho\pi$ is given by

$$a(\pi\pi) - a(\rho\pi) = -2(A_P/A_T)cos(\delta_P - \delta_T)\left[cos(2\alpha)\sin(\alpha)\right] \quad, \qquad (1.51)$$

where A_P and A_T denote the penguin and tree amplitudes, respectively, and the δ's represent their strong phase shifts. Factorization can be used to get the sign of A_P/A_T and the strong phase shifts are believed to be small enough that $\cos(\delta_P - \delta_T)$ is positive [53].

1.8 Techniques for Determining γ

The angle γ could in principle be measured using a CP eigenstate of B_s decay that was dominated by the $b \to u$ transition. One such decay that has been suggested is $B_s \to \rho^o K_S$. However, there are the same "penguin pollution" problems as in $B^o \to \pi^+\pi^-$, but they are more difficult to resolve in the vector-pseudoscalar final state. (Note, the pseudoscalar-pseudoscalar final state here is $\pi^o K_S$, which does not have a measurable decay vertex.)

Fortunately, there are other ways of measuring γ. CP eigenstates are not used, which introduces discrete ambiguities. However, combining several methods should remove these. We have studied three methods of measuring γ.

1.8.1 Measurement of γ Using Time-Dependent CP violation in B_s Decays

The first method uses the decays $B_s \to D_s^\pm K^\mp$ where a time-dependent CP violation can result from the interference between the direct decays and the mixing-induced decays [54]. Fig. 1.13 shows the two direct decay processes for $\overline{B}_s^o$.
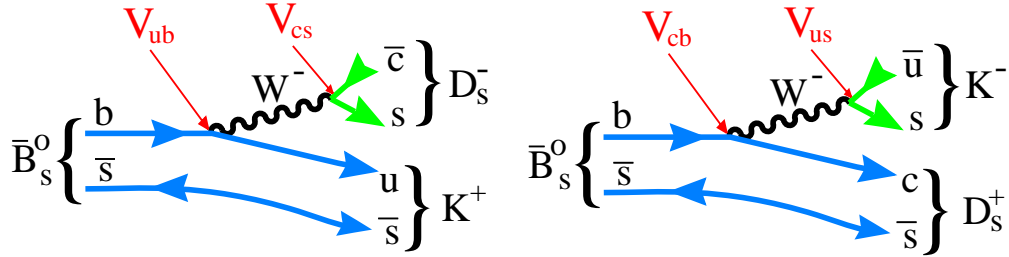
Figure 1.13: Two diagrams for $\overline{B}_s^o \to D_s^\pm K^\mp$.

Consider the following time-dependent rates that can be separately measured using flavor tagging of the other b:

$$\Gamma(B_s \to f) = |M|^2 e^{-t}\{\cos^2(xt/2) + \rho^2 \sin^2(xt/2) - \rho\sin(\phi + \delta)\sin(xt)\}$$

$$\Gamma(\bar{B}_s \to \bar{f}) = |M|^2 e^{-t}\{\cos^2(xt/2) + \rho^2 \sin^2(xt/2) + \rho\sin(\phi - \delta)\sin(xt)\}$$

$$\Gamma(B_s \to \bar{f}) = |M|^2 e^{-t}\{\rho^2 \cos^2(xt/2) + \sin^2(xt/2) - \rho\sin(\phi - \delta)\sin(xt)\}$$

$$\Gamma(\bar{B}_s \to f) = |M|^2 e^{-t}\{\rho^2 \cos^2(xt/2) + \sin^2(xt/2) + \rho\sin(\phi + \delta)\sin(xt)\}, \qquad (1.52)$$

where $M = \langle f|B \rangle$, $\rho = \frac{\langle f|\bar{B} \rangle}{\langle f|B \rangle}$, ϕ is the weak phase between the 2 amplitudes and δ is the strong phase between the 2 amplitudes. The three parameters ρ, $\sin(\phi + \delta), \sin(\phi - \delta)$ can be extracted from a time-dependent study. If $\rho = O(1)$ the fewest number of events are required.

In the case of B_s decays where $f = D_s^+ K^-$ and $\bar{f} = D_s^- K^+$, the weak phase is γ.[5] Using this technique $\sin(\gamma)$ is determined with a four-fold ambiguity. If $\Delta\Gamma(B_s)$ is of the order of 10%, then the ambiguities can be directly resolved.

1.8.2 Measurement of γ Using Charged B Decay Rates

Another method for extracting γ has been proposed by Atwood, Dunietz and Soni [55], who refined a suggestion by Gronau and Wyler [56]. A large CP asymmetry can result from the interference of the decays $B^- \rightarrow K^- D^o, D^o \rightarrow f$ and $B^- \rightarrow K^- \overline{D}^o, \overline{D}^o \rightarrow f$, where f is a doubly-Cabibbo suppressed decay of the D^o (for example $f = K^+\pi^-, K\pi\pi$, etc.). The overall amplitudes for the two decays are expected to be approximately equal in magnitude. (Note that $B^- \rightarrow K^- \overline{D}^o$ is color-suppressed and $B^- \rightarrow K^- D^0$ is color-allowed.) The weak phase difference between them is γ. To observe a CP asymmetry there must also be a non-zero strong phase between the two amplitudes. It is necessary to measure the branching ratio $\mathcal{B}(B^- \rightarrow K^- f)$ for at least 2 different states f in order to determine γ up to discrete ambiguities. Three-body D^o decays are not suggested since the strong D decay phase shifts can vary over the Dalitz plot. Even in quasi-two body decays, such as $K^*\pi$ there may be residual interference effects which could lead to false results. Therefore, the modes that can best be used are $D^o \rightarrow K^-\pi^+$ and K^+K^- ($\pi^+\pi^-$) final states.

We now discuss this method in more detail. Consider a two-body B^- decay into a neutral charmed meson, either a D^o or a $\overline{D}^o$ and a K^-. Let us further take the final state of the charmed meson to be a $K^+\pi^-$. There are two sequential decay processes that can lead to this situation, shown in Fig. 1.14. One is where the B^o decays into a D^o, that decays in a doubly-Cabibbo suppressed process. The other is where the B^o decays via a $b \rightarrow u$ transition to a D^o, that decays via a Cabibbo allowed process.

Remarkably, the decay rate for these two processes is quite similar leading to the possibility of large interference effects. Even if the interference effects are not large it is possible to use this method to determine γ, with some ambiguities. To see how this works, let us define the decay amplitudes and phases in Table 1.6 for two processes, one as described above and the other where the D^o or $\overline{D}^o$ decays into a CP eigenstate. (To be specific, we will take the K^+K^- final state.)

All quantities remain the same for the B^+ decays, except that the phase γ changes sign. The observed decay rates for the four processes can now be calculated by adding and squaring the amplitudes for the same final state. For example, the decay rate for $B^- \rightarrow [K^+\pi^-] K^-$ (where $[K^+\pi^-]$ denotes a $K^+\pi^-$ pair at the D^o mass), is given by

$$\Gamma(B^- \rightarrow [K^+\pi^-] K^-) = ac_d + bc + 2\sqrt{ac_d bc}\cos(\xi_1 + \gamma) \ , \tag{1.53}$$

---

[5]This is an approximation. The phase is precisely $\gamma - 2\chi + \chi'$, see section 1.12.2.

22
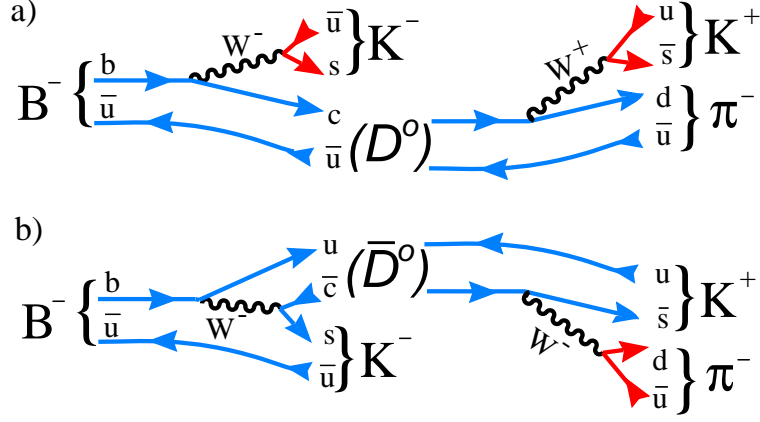
Figure 1.14: Diagrams for the two interfering processes, (a) $B^- \to D^o K^-$ (color allowed) followed by $D^o \to K^+ \pi^-$ (doubly-Cabibbo suppressed), and (b) $B^- \to \overline{D}^o K^-$ (color suppressed) followed by $D^o \to K^- \pi^+$ (Cabibbo allowed).

Table 1.6: Amplitudes and Phases for $B^- \to D^o/\overline{D}^o K^-$

Decay Mode	B Amplitude	D Amplitude	Strong Phase	Weak Phase
$B^- \to D^o K^-$, $D^o \to K^+\pi^-$	$\sqrt{a}$	$\sqrt{c_d}$	$\delta_{B1} + \delta_{Cd}$	0
$B^- \to \overline{D}^o K^-$, $\overline{D}^o \to K^+\pi^-$	$\sqrt{b}$	$\sqrt{c}$	$\delta_{B2} + \delta_C$	γ
$B^- \to D^o K^-$, $D^o \to K^+ K^-$	$\sqrt{a}$	$\sqrt{c_{CP}}$	$\delta_{B1} + \delta_{CP}$	0
$B^- \to \overline{D}^o K^-$, $\overline{D}^o \to K^- K^+$	$\sqrt{b}$	$\sqrt{c_{CP}}$	$\delta_{B2} + \delta_{CP}$	γ

where ξ_1 is a combination of B and D phase shifts, $\delta_{B2} - \delta_{B1} + \delta_C - \delta_{Cd}$ and is unknown. Similarly, the decay rates for the other processes are

$$
\begin{aligned}
\Gamma(B^+ \to \left[K^-\pi^+\right]K^+) &= ac_d + bc + 2\sqrt{ac_d bc}\cos(\xi_1 - \gamma) \\
\Gamma(B^- \to \left[K^+ K^-\right]K^-) &= ac_{CP} + bc_{CP} + 2\sqrt{abc_{CP}^2}\cos(\delta_B - \gamma) \\
\Gamma(B^+ \to \left[K^+ K^-\right]K^+) &= ac_{CP} + bc_{CP} + 2\sqrt{abc_{CP}^2}\cos(\delta_B + \gamma)
\end{aligned}
$$
(1.54)

where $\delta_B = \delta_{B1} - \delta_{B2}$.

In these four equations, the quantities which are known, or will be precisely known before this measurement is attempted are the decay widths a, c_d, c and c_{CP}. The unknowns are the decay width b, two strong phase shifts ξ_1 and δ_B and the weak phase shift γ. Thus the four equations may be solved for the four unknowns. We can find $\sin\gamma$ with a two-fold ambiguity. If more decay modes are added the ambiguity can be removed. The B^- decay mode can

be changed from a K^- to a K^{*-}, which could change the strong B decay phase shift, or a different D^o decay mode can be used, such as $K^-\pi^+\pi^+\pi^-$, which would change the strong D decay phase shift. In the latter case, we have to worry about differences in strong phase shifts between D^o and $\overline{D}^o$ due to resonant structure, but use of this mode can shed some information on ambiguity removal.

Comparison of the solutions found here and using $B_s \to D_s^\pm K^\mp$ as described in the previous section are likely to remove the ambiguities.

1.8.3 Measurement of γ Using $B \to K\pi$ and $B \to \pi\pi$ Decay Rates and Asymmetries

The branching ratios into $\pi^+\pi^-$ and $K^\pm\pi^\mp$ shown in Table 1.4 can be used to get a very rough estimate of the ratio of penguin to tree contribution in the $\pi^+\pi^-$ final state. The $K\pi$ rate is about 4 times the $\pi\pi$ rate and is mostly penguin. Taking a Cabibbo suppression factor of ~ 16, we predict a penguin rate that is 25% of the tree rate in $\pi^+\pi^-$ and thus an amplitude that is about 50%. Therefore, the penguin and tree contributions for $B \to K\pi$ probably do not differ by more than a factor of four, so they can produce observable CP violating effects.

Several model dependent methods using the light two-body pseudoscalar decay rates have been suggested for measuring γ The basic idea in all these methods can be summarized as follows: $B^o \to \pi^+\pi^-$ has the weak decay phase γ. In order to reproduce the observed suppression of the decay rate for $\pi^+\pi^-$ relative to $K^\pm\pi^\mp$ we require a large negative interference between the tree and penguin amplitudes. This puts γ in the range of $90°$. There is a great deal of theoretical work required to understand rescattering, form-factors etc...

Proposals for extracting information on γ have been made using the following experimental ratios:

$$
\begin{aligned}
R &= \frac{\tau(B^+)}{\tau(B^0)} \frac{\mathcal{B}(B^0 \to \pi^- K^+) + \mathcal{B}(\bar{B}^0 \to \pi^+ K^-)}{\mathcal{B}(B^+ \to \pi^+ K^0) + \mathcal{B}(B^- \to \pi^- \bar{K}^0)}, \\
R_* &= \frac{\mathcal{B}(B^+ \to \pi^+ K^0) + \mathcal{B}(B^- \to \pi^- \bar{K}^0)}{2[\mathcal{B}(B^+ \to \pi^0 K^+) + \mathcal{B}(B^- \to \pi^0 K^-)]},
\end{aligned}
\tag{1.55}
$$

The first, R, is by Fleischer and Mannel [57], and the second R_*, is by Neubert and Rosner [58], who updated an older suggestion of Gronau and Rosner [59]. The latter paper prompted much theoretical discussion about the effects of isospin conservation and rescattering [60, 61, 62, 63]. Neubert [64] takes into account these criticisms and provides a framework to limit γ.

More information is obtainable if the CP averaged $\pi^\pm\pi^o$ branching ratios are also measured, and a CP violating observable defined as

$$
\widetilde{A} \equiv \frac{A_{\text{CP}}(\pi^0 K^+)}{R_*} - A_{\text{CP}}(\pi^+ K^0) \quad,
\tag{1.56}
$$

where for example

24

$$A_{\text{CP}}(\pi^0 K^+) = \frac{\Gamma(B^+ \to \pi^o K^+) - \Gamma(B^- \to \pi^o K^-)}{\Gamma(B^+ \to \pi^o K^+) + \Gamma(B^- \to \pi^o K^-)} \quad . \tag{1.57}$$

To summarize Neubert's strategy for determining γ: From measurements of the CP-averaged branching ratio for the decays $B^\pm \to \pi^\pm \pi^0$, $B^\pm \to \pi^\pm K^0$ and $B^\pm \to \pi^0 K^\pm$, the ratio R_* and a parameter $\bar\varepsilon_{3/2}$ are determined. Next, from measurements of the rate asymmetries in the decays $B^\pm \to \pi^\pm K^0$ and $B^\pm \to \pi^0 K^\pm$ the quantity $\widetilde{A}$ is determined.

In Fig. 1.15, we show the contour bands as given by Neubert in the ϕ-γ plane. Here ϕ is a strong interaction phase-shift. Assuming that $\sin\gamma > 0$ as suggested by the global analysis of the unitarity triangle, the sign of $\widetilde{A}$ determines the sign of $\sin\phi$. In the plot, we assume here that $0° \leq \phi \leq 180°$. For instance, if $R_* = 0.7$ and $\widetilde{A} = 0.2$, then the two solutions are $(\gamma, \phi) \approx (98°, 25°)$ and $(\gamma, \phi) \approx (153°, 67°)$, only the first of which is allowed by the upper bound $\gamma < 105°$ following from the global analysis of the unitarity triangle shown here (section 1.2 or in [16]). It is evident that the contours are rather insensitive to the rescattering effects. According to Neubert, the combined theoretical uncertainty is of order $\pm 10°$ on the extracted value of γ.
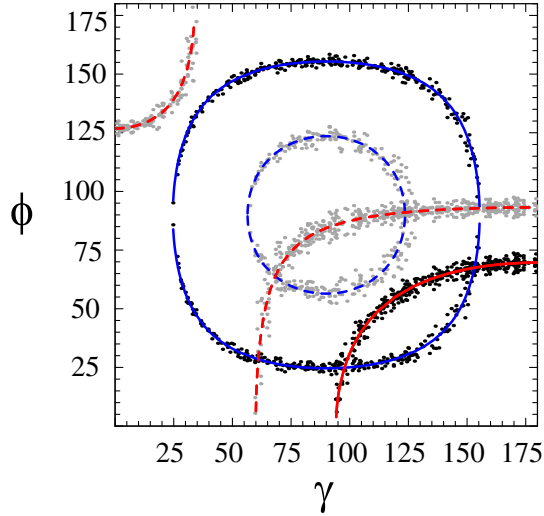
Figure 1.15: Contour plots from Neubert [64] for the quantities R_* ("hyperbolas") and $\widetilde{A}$ ("circles") plotted in the $\phi - \gamma$ plane. The units are degrees. The scatter plots show the results including rescattering effects, while the lines refer to $\varepsilon_a = 0$. The solid curves correspond to the contours for $R_* = 0.7$ and $\widetilde{A} = 0.2$, the dashed ones to $R_* = 0.9$ and $\widetilde{A} = 0.4$.

From the contour plots for the quantities R_* and $\widetilde{A}$ the phases γ and ϕ can then be extracted up to discrete ambiguities. There are also errors in theoretical parameters that must be accounted for.

Beneke *et al.* [65] have recently developed a sophisiticated model of QCD factorization with corrections. Fig. 1.16 shows how values of γ that can be found in their framework, once

better data are obtainable. Of course the value of γ found using this method has an unknown level of theoretical uncertainty. However, it may be very useful in resolving ambiguities.
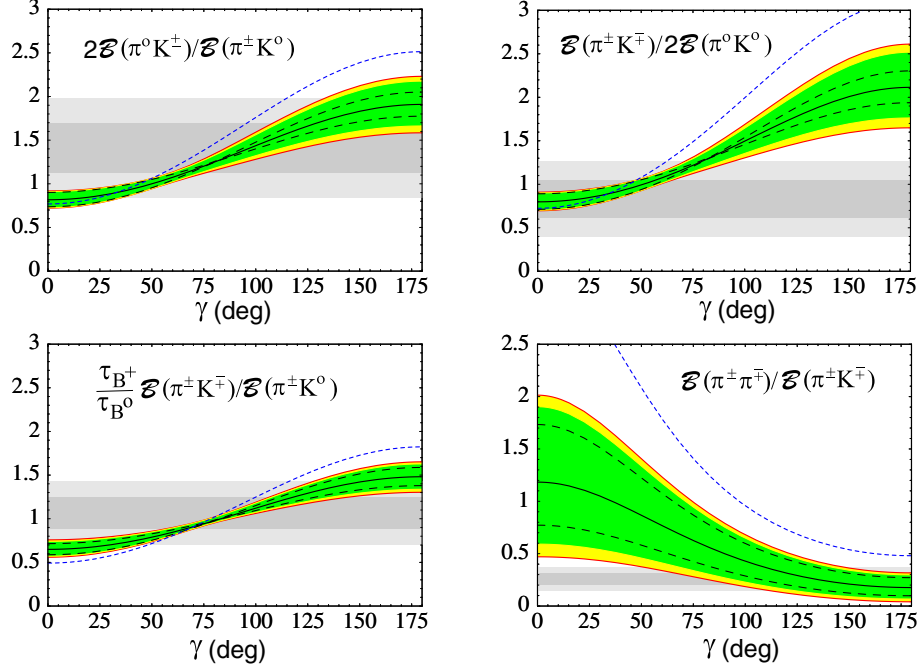
Figure 1.16: Model predictions from Beneke *et al.* as a function of the indicated rate ratios. The dotted curve shows the predictions from naive factorization. The curved bands show the total model uncertainties where the inner band comes from theoretical input uncertainties, while the outer band allows for errors to corrections on the theory. The specific sensitivity to $|V_{ub}|$ is showed as the dashed curves. The gray bands show the current data with a 1σ error while the lighter bands are at 2σ.

1.8.4 Measurement of γ Using CP Asymmetries in $B^o \rightarrow \pi^+\pi^-$ and $B_s^o \rightarrow K^+K^-$

Yet another interesting method for determining γ has been suggested by Fleischer [66]. The decays $B^o \rightarrow \pi^+\pi^-$ and $B_s^o \rightarrow K^+K^-$ are related to each other by interchanging all down and strange quarks, which is called U-spin flavor symmetry [67]. Both channels can occur via penguin or singly-Cabibbo suppressed tree levels diagrams, shown in Fig. 1.17.

For $B^o \rightarrow \pi^+\pi^-$ the transition amplitude is given by

$$A(B_d^0 \rightarrow \pi^+\pi^-) = \lambda_u^{(d)}\left(A_{cc}^u + A_{pen}^u\right) + \lambda_c^{(d)}A_{pen}^c + \lambda_t^{(d)}A_{pen}^t, \tag{1.58}$$

where A_{cc}^u is due to the tree contributions, and the amplitudes A_{pen}^j describe penguin topologies with internal j quarks ($j \in \{u,c,t\}$). These penguin amplitudes take into account both
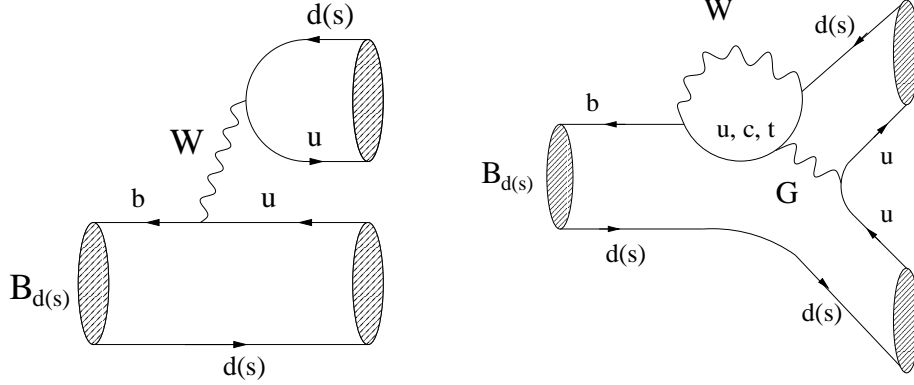
Figure 1.17: Feynman diagrams contributing to $B_d \to \pi^+\pi^-$ and $B_s \to K^+K^-$ (from Fleischer).

QCD and electroweak penguin contributions. The quantities

$$\lambda_j^{(d)} \equiv V_{jd}V_{jb}^* \tag{1.59}$$

are the usual CKM factors. If we make use of the unitarity of the CKM matrix and use the Wolfenstein parameterization, we have

$$A(B_d^0 \to \pi^+\pi^-) = e^{i\gamma}\left(1 - \frac{\lambda^2}{2}\right)\mathcal{C}\left[1 - d\,e^{i\theta}e^{-i\gamma}\right], \tag{1.60}$$

where

$$\mathcal{C} \equiv \lambda^3 A\, R_b\left(A_{cc}^u + A_{pen}^{ut}\right) \tag{1.61}$$

with $A_{pen}^{ut} \equiv A_{pen}^u - A_{pen}^t$, and

$$d\,e^{i\theta} \equiv \frac{1}{(1 - \lambda^2/2)R_b}\left(\frac{A_{pen}^{ct}}{A_{cc}^u + A_{pen}^{ut}}\right). \tag{1.62}$$

The quantity A_{pen}^{ct} is defined in analogy to A_{pen}^{ut}, and the CKM factors are given by

$$\lambda \equiv |V_{us}| = 0.22\,, \quad A \equiv \frac{1}{\lambda^2}|V_{cb}| \sim 0.8\,, \quad R_b \equiv \frac{1}{\lambda}\left|\frac{V_{ub}}{V_{cb}}\right| \sim 0.4. \tag{1.63}$$

For the following considerations, time-dependent CP asymmetries play a key role. In the case of a general B_d decay into a final CP eigenstate $|f\rangle$, satisfying

$$(\mathcal{CP})|f\rangle = \eta\,|f\rangle, \tag{1.64}$$

where η here is not the Wolfenstein parameter, we have (see equation 1.37)

$$\begin{aligned}
a_{CP}(B_d(t) \to f) &\equiv \frac{\Gamma(B_d^0(t) \to f) - \Gamma(\overline{B_d^0}(t) \to f)}{\Gamma(B_d^0(t) \to f) + \Gamma(\overline{B_d^0}(t) \to f)} \\
&= \mathcal{A}_{CP}^{dir}(B_d \to f)\cos(\Delta m_d t) + \mathcal{A}_{CP}^{mix}(B_d \to f)\sin(\Delta m_d t)\,.
\end{aligned} \tag{1.65}$$

For the case of $B^o \to \pi^+\pi^-$, the decay amplitude takes the same form as (1.60), and we obtain the following expressions for the "direct" and "mixing-induced" CP-violating observables:

$$\mathcal{A}_{\text{CP}}^{\text{dir}}(B_d \to f) = -\left[\frac{2\,d\sin\theta\sin\gamma}{1 - 2\,d\cos\theta\cos\gamma + d^2}\right] \tag{1.66}$$

$$\mathcal{A}_{\text{CP}}^{\text{mix}}(B_d \to f) = \eta\left[\frac{\sin(2\beta + 2\gamma) - 2\,d\,\cos\theta\,\sin(2\beta + \gamma) + d^2\sin 2\beta}{1 - 2\,d\cos\theta\cos\gamma + d^2}\right], \tag{1.67}$$

where η is equal to $+1$; for negligible values of the "penguin parameter" d, we have $\mathcal{A}_{\text{CP}}^{\text{mix}}(B_d \to \pi^+\pi^-) = \sin(2\beta + 2\gamma) = -\sin(2\alpha)$. However, the penguin contributions are expected to play an important role.

Consider now the decay $B_s^0 \to K^+K^-$. It originates from $\bar{b} \to \bar{u}u\bar{s}$ quark-level processes, as can be seen in Fig. 1.17. Using a notation similar to that in (1.60), we obtain

$$A(B_s^0 \to K^+K^-) = e^{i\gamma}\lambda\mathcal{C}'\left[1 + \left(\frac{1 - \lambda^2}{\lambda^2}\right)d'e^{i\theta'}e^{-i\gamma}\right], \tag{1.68}$$

where

$$\mathcal{C}' \equiv \lambda^3 A\,R_b\left(A_{\text{cc}}^{u'} + A_{\text{pen}}^{ut'}\right) \tag{1.69}$$

and

$$d'e^{i\theta'} \equiv \frac{1}{(1 - \lambda^2/2)R_b}\left(\frac{A_{\text{pen}}^{ct'}}{A_{\text{cc}}^{u'} + A_{\text{pen}}^{ut'}}\right) \tag{1.70}$$

correspond to (1.61) and (1.62), respectively. The primes remind us that we are dealing with a $\bar{b} \to \bar{s}$ transition. It should be emphasized that (1.60) and (1.68) are completely general parameterizations of the $B_d^0 \to \pi^+\pi^-$ and $B_s^0 \to K^+K^-$ decay amplitudes within the Standard Model, relying only on the unitarity of the CKM matrix. In particular, these expressions take into account also final-state interaction effects, which can be considered as long-distance penguin topologies with internal up- and charm-quark exchanges.

There may be a sizeable width difference $\Delta\Gamma_s \equiv \Gamma_{\text{H}}^{(s)} - \Gamma_{\text{L}}^{(s)}$ between the B_s mass eigenstates [68], which may allow studies of CP violation with "untagged" B_s data samples [25]. Such untagged rates take the following form:

$$\Gamma(B_s^0(t) \to f) + \Gamma(\overline{B_s^0}(t) \to f) \propto R_{\text{H}}\,e^{-\Gamma_{\text{H}}^{(s)}t} + R_{\text{L}}\,e^{-\Gamma_{\text{L}}^{(s)}t}, \tag{1.71}$$

whereas the time-dependent CP asymmetry is given by

$$a_{\text{CP}}(B_s(t) \to f) \equiv \frac{\Gamma(B_s^0(t) \to f) - \Gamma(\overline{B_s^0}(t) \to f)}{\Gamma(B_s^0(t) \to f) + \Gamma(\overline{B_s^0}(t) \to f)}$$

$$= 2\,e^{-\Gamma_s t}\left[\frac{\mathcal{A}_{\text{CP}}^{\text{dir}}(B_s \to f)\cos(\Delta m_s t) + \mathcal{A}_{\text{CP}}^{\text{mix}}(B_s \to f)\sin(\Delta m_s t)}{e^{-\Gamma_{\text{H}}^{(s)}t} + e^{-\Gamma_{\text{L}}^{(s)}t} + \mathcal{A}_{\Delta\Gamma}(B_s \to f)\left(e^{-\Gamma_{\text{H}}^{(s)}t} - e^{-\Gamma_{\text{L}}^{(s)}t}\right)}\right] \tag{1.72}$$

with $\mathcal{A}_{\Delta\Gamma}(B_s \rightarrow f) = (R_H - R_L)/(R_H + R_L)$. If the $B_s^0 \rightarrow f$ decay amplitude takes the same form as (1.68), we have

$$\mathcal{A}_{CP}^{dir}(B_s \rightarrow f) = + \left[\frac{2\,\tilde{d}' \sin\theta' \sin\gamma}{1 + 2\,\tilde{d}' \cos\theta' \cos\gamma + \tilde{d}'^2} \right] \tag{1.73}$$

$$\mathcal{A}_{CP}^{mix}(B_s \rightarrow f) = + \eta \left[\frac{\sin(2\chi + 2\gamma) + 2\,\tilde{d}'\,\cos\theta'\,\sin(2\chi + \gamma) + \tilde{d}'^2 \sin 2\chi}{1 + 2\,\tilde{d}' \cos\theta' \cos\gamma + \tilde{d}'^2} \right] \tag{1.74}$$

$$\mathcal{A}_{\Delta\Gamma}(B_s \rightarrow f) = - \eta \left[\frac{\cos(2\chi + 2\gamma) + 2\,\tilde{d}'\cos\theta'\cos(2\chi + \gamma) + \tilde{d}'^2 \cos 2\chi}{1 + 2\,\tilde{d}' \cos\theta' \cos\gamma + \tilde{d}'^2} \right]. \tag{1.75}$$

These observables are not independent quantities, and satisfy the relation

$$\left[\mathcal{A}_{CP}^{dir}(B_s \rightarrow f) \right]^2 + \left[\mathcal{A}_{CP}^{mix}(B_s \rightarrow f) \right]^2 + \left[\mathcal{A}_{\Delta\Gamma}(B_s \rightarrow f) \right]^2 = 1. \tag{1.76}$$

In the general expressions (1.73)–(1.75), we have introduced the abbreviation

$$\tilde{d}' \equiv \left(\frac{1 - \lambda^2}{\lambda^2} \right) d', \tag{1.77}$$

and $2\chi = 2\arg(V_{ts}^* V_{tb})$ denotes the B_s^o–$\overline{B_s^o}$ mixing phase. Within the Standard Model, we have $2\chi \approx 0.03$ due to a Cabibbo suppression of $\mathcal{O}(\lambda^2)$, implying that 2χ is very small. This phase can be determined using $B_s \rightarrow J/\psi\,\eta\prime$ decays (see section 1.12.2).

Since the decays $B_d \rightarrow \pi^+\pi^-$ and $B_s \rightarrow K^+K^-$ are related to each other by interchanging all strange and down quarks, the U-spin flavor symmetry of strong interactions implies

$$d' = d \tag{1.78}$$
$$\theta' = \theta. \tag{1.79}$$

In contrast to certain isospin relations, electroweak penguins do not lead to any problems in the U-spin relations (1.78) and (1.79), according to Fleischer.

In general we have five physics quantities of interest, 2χ, d, θ, 2β and γ. Let us now assume that $\sin(2\beta)$ will be measured and $\sin(2\chi)$ either measured or tightly limited. Only d, θ and γ then need to be determined.

We have four possible measured quantities provided by the time-dependent CP asymmetries of the modes $B_d \rightarrow \pi^+\pi^-$ and $B_s \rightarrow K^+K^-$. These four quantities are $\mathcal{A}_{CP}^{mix}(B_s \rightarrow K^+K^-)$, $\mathcal{A}_{CP}^{mix}(B_d \rightarrow \pi^+\pi^-)$, $\mathcal{A}_{CP}^{dir}(B_s \rightarrow K^+K^-)$ and $\mathcal{A}_{CP}^{dir}(B_d \rightarrow \pi^+\pi^-)$. To implement this plan we need measure only 3 of these four quantities, or combinations of them. For example, it may be difficult to independently determine $\mathcal{A}_{CP}^{mix}(B_d \rightarrow \pi^+\pi^-)$ and $\mathcal{A}_{CP}^{dir}(B_d \rightarrow \pi^+\pi^-)$, because of the small number of observable B^o oscillations before the exponential decay reduces the number of events too much. However, the sum

$$\begin{aligned} a_{CP}^{\pi^+\pi^-} &= \int_0^\infty \mathcal{A}_{CP}^{dir} \cos(\Delta m_d t) + \mathcal{A}_{CP}^{mix} \sin(\Delta m_d t) \\ &= \frac{1}{1 + x^2}\mathcal{A}_{CP}^{dir} + \frac{x}{1 + x^2}\mathcal{A}_{CP}^{mix} \end{aligned} \tag{1.80}$$

29

can be determined and used with the other two measurements from $B_s^o \to K^+K^-$. Clearly other scenarios are possible.

1.8.5   Opportunities with B_s Mesons if $\Delta\Gamma$ is $\sim 10\%$

Measurement of $\Delta\Gamma$ can be used to estimate in an interesting but model dependent manner the value of Δm_s and thus provides a redundant check on B_s mixing measurements [25].

Should a large enough $\Delta\Gamma$ be determined there exist other possible ways to determine some of the interesting physics quantities discussed above. Some of these studies can be done without flavor tagging. In fact, the time evolution of untagged observables for a B_s decay into a vector-vector final state is proportional to

$$\left(e^{-\Gamma_H t} - e^{-\Gamma_L t}\right)\sin\phi_{CKM}, \tag{1.81}$$

where ϕ_{CKM} is a CP violating angle from the CKM matrix and depends on the specific decay mode.

In general the angular distribution for $B_s \to VV$ is expressed in terms of transversity in a manner similar to equation 1.47, with the major difference being that the angular variables are time dependent. The time evolution of the decay $B_s \to J/\psi\phi$ is given in Table 1.7 [69].

Observable	Time evolution
$|A_0(t)|^2$	$|A_0(0)|^2 \left[e^{-\Gamma_L t} - e^{-\overline{\Gamma} t}\sin(\Delta mt)\sin(2\chi)\right]$
$|A_\parallel(t)|^2$	$|A_\parallel(0)|^2 \left[e^{-\Gamma_L t} - e^{-\overline{\Gamma} t}\sin(\Delta mt)\sin(2\chi)\right]$
$|A_\perp(t)|^2$	$|A_\perp(0)|^2 \left[e^{-\Gamma_H t} + e^{-\overline{\Gamma} t}\sin(\Delta mt)\sin(2\chi)\right]$
$\mathrm{Re}(A_0^*(t)A_\parallel(t))$	$|A_0(0)||A_\parallel(0)|\cos(\delta_2 - \delta_1)\left[e^{-\Gamma_L t} - e^{-\overline{\Gamma} t}\sin(\Delta mt)\sin(2\chi)\right]$
$\mathrm{Im}(A_\parallel^*(t)A_\perp(t))$	$|A_\parallel(0)||A_\perp(0)|\left[e^{-\overline{\Gamma} t}\sin(\delta_1 - \Delta mt)\right.$ $\left. + \frac{1}{2}\left(e^{-\Gamma_H t} - e^{-\Gamma_L t}\right)\cos(\delta_1)\sin(2\chi)\right]$
$\mathrm{Im}(A_0^*(t)A_\perp(t))$	$|A_0(0)||A_\perp(0)|\left[e^{-\overline{\Gamma} t}\sin(\delta_2 - \Delta mt)\right.$ $\left. + \frac{1}{2}\left(e^{-\Gamma_H t} - e^{-\Gamma_L t}\right)\cos(\delta_2)\sin(2\chi)\right]$

Table 1.7: Time evolution of the decay $B_s \to J/\psi(\to l^+l^-)\phi(\to K^+K^-)$ of an initially (i.e. at $t = 0$) pure B_s meson. $\delta_{1,2}$ are strong phase shifts.

Combining with the decay of the $\overline{B}_s$ the time evolution of the untagged sample is given by

$$\frac{d^3\Gamma(J/\psi(\to l^+l^-)\phi(\to K^+K^-))}{d\cos\theta \; d\varphi \; d\cos\psi} \propto \frac{9}{16\pi}\left[2|A_0(0)|^2 e^{-\Gamma_L t}\cos^2\psi(1 - \sin^2\theta\cos^2\varphi)\right.$$

$$\left. + \sin^2\psi\{|A_\parallel(0)|^2 e^{-\Gamma_L t}(1 - \sin^2\theta\sin^2\varphi) + |A_\perp(0)|^2 e^{-\Gamma_H t}\sin^2\theta\} \right.$$

$$+\frac{1}{\sqrt{2}}\sin 2\psi\left\{|A_0(0)||A_\parallel(0)|\cos(\delta_2-\delta_1)e^{-\Gamma_L t}\sin^2\theta\sin 2\varphi\right\}$$

$$+\left\{\frac{1}{\sqrt{2}}|A_0(0)||A_\perp(0)|\cos\delta_2\sin 2\psi\sin 2\theta\cos\varphi\right.$$

$$\left.-|A_\parallel(0)||A_\perp(0)|\cos\delta_1\sin^2\psi\sin 2\theta\sin\varphi\right\}\frac{1}{2}\left(e^{-\Gamma_H t}-e^{-\Gamma_L t}\right)\delta\phi\right] \quad . \tag{1.82}$$

Thus a study of the time dependent angular distributions can lead to a measurement of $\sin(2\chi)$, especially if $\Delta\Gamma$ is determined before hand. It is also possible to integrate over two of the angles if statistics is limited. The distribution in J/ψ decay angle can be written as

$$\frac{d\Gamma(t)}{d\cos\theta}\propto(|A_0(t)|^2+|A_\parallel(t)|^2)\frac{3}{8}(1+\cos^2\theta)+|A_\perp(t)|^2\frac{3}{4}\sin^2\theta \tag{1.83}$$

where the CP violating angle originates from the imaginary parts of the interference terms in the A's.

Other final states have been suggested that provide a measurement of γ using the above ideas. One particularly interesting set of decays is $B_s\to K^{*+}K^{*-}$ and $B_s\to K^{*o}\bar{K}^{*o}$ [70].

Finally, it is important to realize that determination of a non-zero $\Delta\Gamma$ allows the measurement of $Re\left(\frac{q}{p}\cdot\frac{\bar{A}}{A}\right)$, that in turn allows the removal of the ambiguities in the CKM angle of interest [25]. For the B_s decays mentioned here this could be γ or χ.

1.9 Summary of Crucial Measurements for CKM Physics

Table 1.8 lists the most important physics quantities and the decay modes that can be used to measure them.

Other modes which also may turn out to be useful include $B^o\to D^{*+}\pi^-$ and its charge-conjugate [71], which measures $\sin(-2\beta-\gamma)$ albeit with a small $\approx 1\%$ predicted asymmetry,[6] and $B\to K\pi$ modes which can be used to find γ albeit with theoretical uncertainties. There are three alternative ways to measure γ, discussed in section 1.8, which serve both to remove ambiguities and perform checks. It will be much more difficult to find other modes to check α, however. One approach is to measure the CP asymmetry in $B^o\to\pi^+\pi^-$ and use theoretical models to estimate the effects of penguin pollution. Minimally, a great deal would be learned about the models. It also turns out that the third ambiguity in α can be removed by comparing the CP violating asymmetry in $\pi^+\pi^-$ with that found in $\rho\pi$ and using some mild theoretical assumptions [53]. After the three angles α, β and γ have been measured, we need to check if they add up to 180°. A discrepancy here would be unexpected. To be sure, this check is not complete if ambiguities have not been removed. (Even if the angles sum to 180°, new physics could hide.)

---

[6]To measure a CP asymmetry this way requires using equations 1.52, and extracting the strong phase, amplitude ratio, and a small asymmetry: a very difficult task.

Table 1.8: Required CKM Measurements for b's

Physics Quantity	Decay Mode
$\sin(2\alpha)$	$B^o \to \rho\pi \to \pi^+\pi^-\pi^o$
$\cos(2\alpha)$	$B^o \to \rho\pi \to \pi^+\pi^-\pi^o$
$\mathrm{sign}(\sin(2\alpha))$	$B^o \to \rho\pi$ & $B^o \to \pi^+\pi^-$
$\sin(\gamma)$	$B_s \to D_s^{\pm}K^{\mp}$
$\sin(\gamma)$	$B^- \to \overline{D}^0 K^-$
$\sin(\gamma)$	$B^o \to \pi^+\pi^-$ & $B_s \to K^+K^-$
$\sin(2\chi)$	$B_s \to J/\psi\eta\prime,\ J/\psi\eta$
$\sin(2\beta)$	$B^o \to J/\psi K_s$
$\cos(2\beta)$	$B^o \to J/\psi K^o,\ K^o \to \pi\ell\nu$
$\cos(2\beta)$	$B^o \to J/\psi K^{*o}$ & $B_s \to J/\psi\phi$
x_s	$B_s \to D_s^+\pi^-$
$\Delta\Gamma$ for B_s	$B_s \to J/\psi\eta\prime,\ D_s^+\pi^-,\ K^+K^-$

We also want to measure as precisely as possible the side of the **bd** triangle (see Fig. 1.2) that requires a precise measurement of B_s mixing [72]. The other side is proportional to the magnitude of V_{ub}. This will no doubt be measured by e^+e^- b-factories and the precision will be limited by theoretical concerns if form-factors in the exclusive decays and q^2 distributions in the inclusive decays have been decisively measured. It is possible that measuring the rate $\Lambda_b \to p\ell\nu$ or the ratio of this rate to $\Lambda_b \to \Lambda_c\ell\nu$, could help determine the theoretical uncertainties since the form-factors are different.

1.10 Rare Decays as Probes beyond the Standard Model

Rare decays have loops in the decay diagrams which makes them sensitive to high mass gauge bosons and fermions. Thus, they are sensitive to new physics. However, it must be kept in mind that any new effect must be consistent with already measured phenomena such as B_d^o mixing and $b \to s\gamma$.

These processes are often called "penguin" processes, for unscientific reasons [73]. A Feynman loop diagram is shown in Fig. 1.18 that describes the transition of a b quark into a charged -1/3 s or d quark, which is effectively a neutral current transition. The dominant charged current decays change the b quark into a charged +2/3 quark, either c or u.

The intermediate quark inside the loop can be any charge +2/3 quark. The relative size of the different contributions arises from different quark masses and CKM elements. For $b \to s$, in terms of the Cabibbo angle (λ=0.22), we have for t:c:u - λ^2:λ^2:λ^4. The mass dependence favors the t loop, but the amplitude for c processes can be quite large $\approx$30%. Moreover, as pointed out by Bander, Silverman and Soni [74], interference can occur between
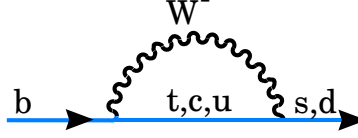
Figure 1.18: Loop or "Penguin" diagram for a $b \rightarrow s$ or $b \rightarrow d$ transition.

t, c and u diagrams and lead to CP violation. In the Standard Model it is not expected to occur when $b \rightarrow s$, due to the lack of a CKM phase difference, but could occur when $b \rightarrow d$. In any case, it is always worth looking for this effect; all that needs to be done, for example, is to compare the number of $K^{*-}\gamma$ events with the number of $K^{*+}\gamma$ events.

There are other possibilities for physics beyond the Standard Model to appear. For example, the W^- in the loop can be replaced by some other charged object such as a Higgs; it is also possible for a new object to replace the t.

1.10.1 $b \rightarrow s\gamma$

This process occurs when any of the charged particles in Fig. 1.18 emits a photon. CLEO first measured the inclusive rate [75] as well as the exclusive rate into $K^*(890)\gamma$ [76]. There is an updated CLEO measurement [77] using 1.5 times the original data sample and measurements from ALEPH [78] and BELLE [79].

To remove background CLEO used two techniques originally, one based on "event shapes" and the other on summing exclusively reconstructed B samples. CLEO uses eight different shape variables [75], and defines a variable r using a neural network to distinguish signal from background. The idea of the B reconstruction analysis is to find the inclusive branching ratio by summing over exclusive modes. The allowed hadronic system is composed of either a $K_S \rightarrow \pi^+\pi^-$ candidate or a $K^{\mp}$ combined with 1-4 pions, only one of which can be neutral. The restriction on the number and kind of pions maximizes efficiency while minimizing background. It does however lead to a model dependent error. Then both analysis techniques are combined. Currently, most of the statistical power of the analysis ($\sim$80%) comes from summing over the exclusive modes.

Fig. 1.19 shows the photon energy spectrum of the inclusive signal, compared with the model of Ali and Greub [80]. A fit to the model over the photon energy range from 2.1 to 2.7 GeV/c gives the branching ratio result shown in Table 1.9, where the first error is statistical and the second systematic.

ALEPH reduces the backgrounds by weighting candidate decay tracks in a $b \rightarrow s\gamma$ event by a combination of their momentum, impact parameter with respect to the main vertex and rapidity with respect to the b-hadron direction [78]. Their result is also listed in Table 1.9. The world average experimental value is also given, as well as the theoretical prediction.

The Standard Model prediction is in good agreement with the data. The consistency with Standard Model expectation has ruled out many models. Hewett has given a good review of the many minimal supergravity models which are excluded by the data [82]. Improved
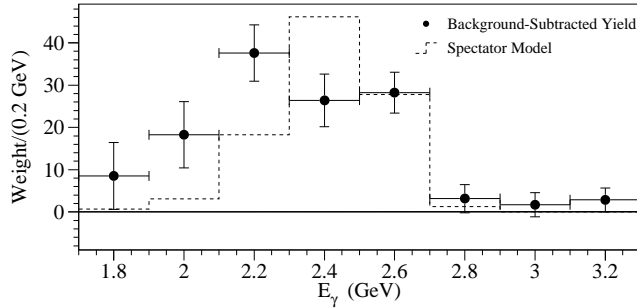
Figure 1.19: The background subtracted photon energy spectrum from CLEO. The dashed curve is a spectator model prediction from Ali and Greub.

Table 1.9: $\mathcal{B}(b \rightarrow s\gamma)$.

Experiment	$\mathcal{B} \times 10^{-4}$
CLEO	$3.21 \pm 0.43 \pm 0.27^{+0.18}_{-0.10}$
ALEPH	$3.11 \pm 0.80 \pm 0.72$
BELLE	$3.36 \pm 0.53 \pm 0.44^{+0.50}_{-0.54}$
Average	3.23 ± 0.42
Theory [81]	$(3.73 \pm 0.30) \times 10^{-4}$

experimental and theoretical accuracy are required to move beyond the Standard Model here. A measurement of $b \rightarrow d\gamma$ would be most interesting.

Triple gauge boson couplings are of great interest in checking the standard model. If there were an anomalous $WW\gamma$ coupling it would serve to change the Standard Model rate. $p\bar{p}$ collider experiments have also published results limiting such couplings [83]. In a two-dimensional space defined by $\Delta\kappa$ and λ, the D0 constraint appears as a tilted ellipse and the $b \rightarrow s\gamma$ as nearly vertical bands. In the standard model both parameters are zero.

1.10.2 The Exclusive Decays $K^*\gamma$ and $\rho\gamma$

The exclusive branching ratio is far more difficult to predict than the inclusive. CLEO measures $\mathcal{B}(B \rightarrow K^*(890)\gamma) = (4.2 \pm 0.8 \pm 0.6) \times 10^{-5}$, with this exclusive final state comprising $(18 \pm 7)\%$ of the total $b \rightarrow s\gamma$ rate [84]. BABAR [85] has made a more precise measurement separately for $K^{*o}\gamma$ of $(4.23 \pm 0.40 \pm 0.12) \times 10^{-5}$ and $K^{*+}\gamma$ of $(3.83 \pm 0.62 \pm 0.22) \times 10^{-5}$.

CLEO also limits $\mathcal{B}(B \rightarrow \rho\gamma) < 1.2 \times 10^{-5}$ at 90% confidence level [84]. This leads to a model dependent limit on $|V_{td}/V_{ts}|^2 < 0.45 - 0.56$, which is not very significant. It may be possible that improved measurements can find a meaningful limit, although that has been disputed [86].

1.10.3 $b \to s\ell^+\ell^-$

The diagrams that contribute to $b \to s\ell^+\ell^-$, where ℓ refers to either an electron or muon are shown in Fig. 1.20.
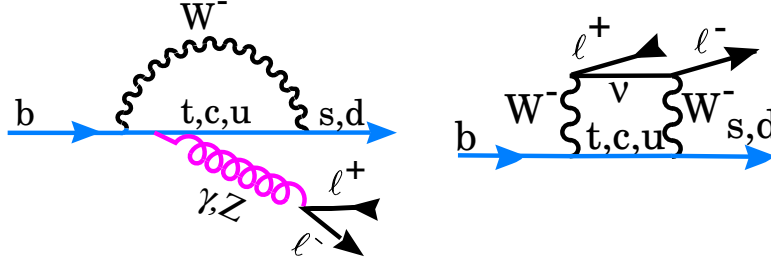
Figure 1.20: Loop or "Penguin" diagram for a $b \to s\ell^+\ell^-$ transition.

Since more diagrams contribute here than in $b \to s\gamma$, different physics can be probed. CP violation can be looked at in both the branching ratios and the polarization of the lepton pair [87]. When searching for such decays, care must be taken to eliminate the mass region in the vicinity of the J/ψ or ψ' resonances, lest these more prolific processes, that are not rare decays, contaminate the sample. Most searches have turned out negative. The results are listed in Table 1.10.

Table 1.10: Searches for $b \to s\ell^+\ell^-$ decays

b decay mode	90% c.l. upper limit	Group	Ali *et al.* Prediction [88]
$s\mu^+\mu^-$	50×10^{-6}	UA1 [89]	$(8 \pm 2) \times 10^{-6}$
	5.7×10^{-6}	CLEO [90]	
$K^{*o}\mu^+\mu^-$	4.0×10^{-6}	CDF [92]	2.9×10^{-6}
	23×10^{-6}	UA1 [89]	
	9.5×10^{-6}	CLEO [90]	
	3.2×10^{-6}	BABAR [91]	
$K^{*o}e^+e^-$	13×10^{-6}	CLEO [90]	5.6×10^{-6}
	6.6×10^{-6}	BABAR [91]	
$K^-\mu^+\mu^-$	9.7×10^{-6}	CLEO [90]	0.6×10^{-6}
	5.2×10^{-6}	CDF [92]	
	1.2×10^{-6}	BABAR [91]	
$K^-e^+e^-$	2.5×10^{-6}	CLEO [90]	0.6×10^{-6}
	0.8×10^{-6}	BABAR [91]	

The BELLE Collaboration [93] has claimed a positive signal for $\mathcal{B}(\overline{B}^o \to K^-\mu^+\mu^-) = (0.99^{+0.40+0.13}_{-0.32-0.14}) \times 10^{-6}$. Thus far this signal is has not been established in the analogous $K^-e^+e^-$ channel or by BABAR.

BTeV has the ability to search for both exclusive and inclusive dilepton final states. The inclusive measurement can be done following the techniques used by CLEO to discover inclu-

sive $b \to s\gamma$ and set upper limits on $b \to s\ell^+\ell^-$. CLEO doesn't have vertex information, so they choose track combinations assigning a kaon hypothesis to one track and pion hypotheses to the other charged tracks. They allow up to four pions, only one of which can be neutral and proceed to reconstruct each combination as if it were an exclusive decay mode. If any combination succeeds, they keep it. BTeV can improve on this procedure in two ways. First of all BTeV will have RICH $K\pi$ separation. Secondly we can insist that the charged particles are consistent with coming from a b decay vertex. Of course, we lose the power of the beam energy constraint that is so efficient at rejecting background at the $\Upsilon(4S)$. However, it is a detailed question as to whether or not we more than make up the rejection power by using our advantages.

B's can also decay into dilepton final states. The Standard Model diagrams are shown in Fig. 1.21. In (a) the decay rate is proportional to $|V_{ub}|^2 f_B^2$. The diagram in (b) is much larger for B_s than B_d, again the factor of $|V_{ts}/V_{td}|^2$. Results of searches are given in Table 1.11.
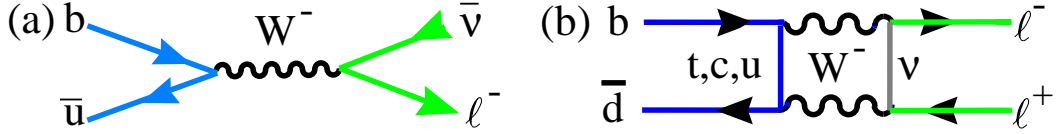
Figure 1.21: Decay diagrams resulting in dilepton final states. (a) is an annihilation diagram, and (b) is a box diagram.

Table 1.11: Upper limits on $b \to$ dilepton decays (@90% c.l.)

| | $\mathcal{B}(B^o \to \ell^+\ell^-)$ | | $\mathcal{B}(B_s \to \ell^+\ell^-)$ | $\mathcal{B}(B^- \to \ell^-\bar{\nu})$ | | |
	e^+e^-	$\mu^+\mu^-$	$\mu^+\mu^-$	$e^-\bar{\nu}$	$\mu^-\bar{\nu}$	$\tau^-\bar{\nu}$
SM[†]	2×10^{-15}	8×10^{-11}	2×10^{-9}	10^{-15}	10^{-8}	10^{-5}
UA1 [89]		8.3×10^{-6}				
CLEO [94]	5.9×10^{-6}	5.9×10^{-6}		1.5×10^{-5}	2.1×10^{-5}	2.2×10^{-3}
CDF [95]		2.0×10^{-6}	6.8×10^{-6}			
ALEPH [96]						1.8×10^{-3}
L3 [97]						5.7×10^{-4}

[†]SM is the Standard Model prediction [98].

Searches for rare decays modes make up an important part of the BTeV physics program.

1.11 The Search for Mixing and CP Violation in Charm Decays

Predictions of the Standard Model contribution to mixing and CP violation in charm decay are small. Thus, this provides a good place to search for new physics.

The current experimental limit on charm mixing [99] is

$$r_D = \frac{1}{2}\left[\left(\frac{\Delta m_D}{\Gamma}\right)^2 + \left(\frac{\Delta\Gamma}{2\Gamma}\right)^2\right] < 5 \times 10^{-3} \quad , \qquad (1.84)$$

while the Standard Model expectation is $\sim 10^{-6}$ [100] [101].

For CP violation the current limit is $\sim$10% [12], while the Standard Model expectation is $\sim 10^{-3}$ [100] [102]. BTeV can probably reach the Standard Model level of CP violation in charm decays. (The D^{*+} provides a wonderful flavor tag.)

1.12 New Physics

1.12.1 Introduction

There are many reasons why we believe that the Standard Model is incomplete and there must be physics beyond. One is the plethora of "fundamental parameters," for example quark masses, mixing angles, etc... The Standard Model cannot explain the smallness of the weak scale compared to the GUT or Planck scales; this is often called "the hierarchy problem." It is believed that the CKM source of CP violation in the Standard Model is not large enough to explain the baryon asymmetry of the Universe [103]; we can also take the view that we will discover additional large unexpected effects in b and/or c decays. Finally, gravity is not incorporated. John Ellis said "My personal interest in CP violation is driven by the search for physics beyond the Standard Model" [104].

We must realize that *all* our current measurements are a combination of Standard Model and New Physics; any proposed models must satisfy current constraints. Since the Standard Model tree level diagrams are probably large, let's consider them a background to New Physics. Therefore loop diagrams and CP violation are the best places to see New Physics. The most important current constraints on New Physics models are

- The neutron electric dipole moment, $d_N~ < 6.3 \times 10^{-26}$e-cm.

- $\mathcal{B}(b \to s\gamma) = (3.23 \pm 0.42) \times 10^{-4}$ and $\mathcal{B}(b \to s\ell^+\ell^-) < 4.2 \times 10^{-5}$.

- CP violation in K_L decay, $\epsilon_K = (2.271 \pm 0.017) \times 10^{-3}$.

- B^o mixing parameter $\Delta m_d = (0.487 \pm 0.014)$ ps^{-1}.

1.12.2 Generic Tests for New Physics

We can look for New Physics either in the context of specific models or more generically, for deviations from the Standard Model expectation.

One example is to examine the rare decays $B \to K\ell^+\ell^-$ and $B \to K^*\ell^+\ell^-$ for branching ratios and polarizations. According to Greub et al. [105], "Especially the decay into K^*

yields a wealth of new information on the form of the new interactions since the Dalitz plot is sensitive to subtle interference effects."

Another important tactic is to test for inconsistencies in Standard Model predictions independent of specific non-standard models. Recall that the unitarity of the CKM matrix allows us to construct six relationships shown as triangles in the complex plane in Fig. 1.1.

All six of these triangles can be constructed knowing four and only four independent angles such as β, γ, χ or χ' (see equation 1.9) [106][8][107]. (We could substitute α for γ.) We know that β is large and γ is also likely to be large, while χ is estimated to be small ≈ 0.02, but measurable, while χ' is likely to be much smaller.

It has been pointed out by Silva and Wolfenstein [106] that measuring only angles may not be sufficient to detect new physics. For example, suppose there is new physics that arises in $B^o - \overline{B}^o$ mixing. Let us assign a phase θ to this new physics. If we then measure CP violation in $B^o \to J/\psi K_s$ and eliminate any penguin pollution problems in using $B^o \to \pi^+\pi^-$, then we actually measure $2\beta' = 2\beta + \theta$ and $2\alpha' = 2\alpha - \theta$. So while there is new physics, we miss it, because $2\beta' + 2\alpha' = 2\alpha + 2\beta$ and $\alpha' + \beta' + \gamma = 180°$.

1.12.2.1 A Critical Check Using χ

The angle χ (see equation 1.9) can be extracted by measuring the time dependent CP violating asymmetry in the reaction $B_s \to J/\psi \eta^{(\prime)}$, or if one's detector is incapable of quality photon detection, the $J/\psi \phi$ final state can be used. However, in this case there are two vector particles in the final state, making this a state of mixed CP, requiring a time-dependent angular analysis to extract χ, that requires large statistics.

Measurements of the magnitudes of CKM matrix elements all come with theoretical errors. Some of these are hard to estimate. The best measured magnitude is that of $\lambda = |V_{us}/V_{ud}| = 0.2205 \pm 0.0018$. Silva and Wolfenstein [106] [8] show that the Standard Model can be checked in a profound manner by seeing if:

$$\sin \chi = \left| \frac{V_{us}}{V_{ud}} \right|^2 \frac{\sin \beta \ \sin \gamma}{\sin(\beta + \gamma)} \quad . \tag{1.85}$$

Here the precision of the check will be limited initially by the measurement of $\sin \chi$, not of λ. This check can reveal new physics, even if other measurements have not shown any anomalies. Other relationships to check include:

$$\sin \chi = \left| \frac{V_{ub}}{V_{cb}} \right|^2 \frac{\sin \gamma \ \sin(\beta + \gamma)}{\sin \beta} \quad , \qquad \sin \chi = \left| \frac{V_{td}}{V_{ts}} \right|^2 \frac{\sin \beta \ \sin(\beta + \gamma)}{\sin \gamma} \quad . \tag{1.86}$$

These two equations lead to the non-trivial relationship:

$$\sin^2 \beta \left| \frac{V_{td}}{V_{ts}} \right|^2 = \sin^2 \gamma \left| \frac{V_{ub}}{V_{cb}} \right|^2 \quad . \tag{1.87}$$

This constrains these two magnitudes in terms of two of the angles. Note, that it is in principle possible to determine the magnitudes of $|V_{ub}/V_{cb}|$ and $|V_{td}/V_{ts}|$ without model

dependent errors by measuring β, γ and χ accurately. Alternatively, β, γ and λ can be used to give a much more precise value than is possible at present with direct methods. For example, once β and γ are known $|V_{ub}/V_{cb}|^2 = \lambda^2 \sin^2 \beta / \sin^2(\beta + \gamma)$.

1.12.2.2 Finding Inconsistencies

Another interesting way of viewing the physics was given by Peskin [108]. Non-Standard Model physics would show up as discrepancies among the values of (ρ, η) derived from independent determinations using CKM magnitudes ($|V_{ub}/V_{cb}|$ and $|V_{td}/V_{ts}|$), or B_d^o mixing (β and α), or B_s mixing (χ and γ). Peskin destinguishes among four classes of CP violation measurements, corresponding to four different physical systems, such that each class would determine the unitarity triangle completely if the CKM model were a complete description of CP violation. This test of the CKM model comes from the comparison of the triangles shown in Figure 1.22, with error boxes for the sides or angles that might, he believes, be realized within the next decade.
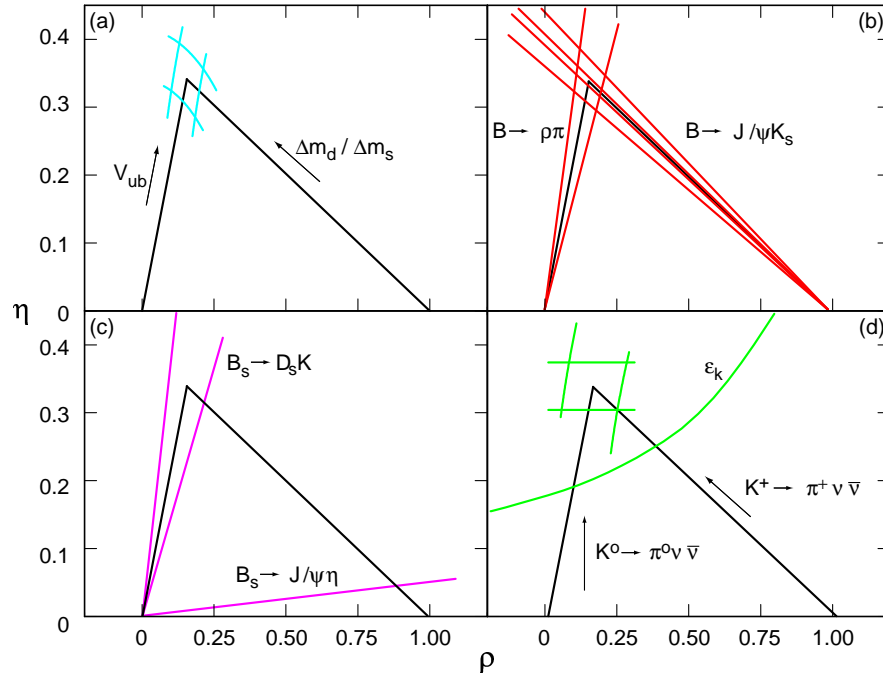
Figure 1.22: Illustration of four determinations of the unitarity triangle, by (a) non-CP observables, (b) B asymmetries, (c) B_s asymmetries, (d) K rare decays from Peskin [108].

Figure 1.22(a) shows the 'non-CP triangle'. This triangle takes advantage of the fact that one can determine the unitarity triangle by measuring the absolute values of CKM matrix elements and thus show the existence of the phase through non-CP-violating observables.

Figure 1.22(b) shows the 'B triangle'. This triangle is constructed from the CP asymmetries in $B^o/\overline{B}^o$ decays. To draw the figure, Peskin used the asymmetry in $B \to J/\psi K_S^o$

and the asymmetry in $B \to \rho\pi$. (Ignoring the discrete ambiguities in determining the CKM angles from the measured asymmetries.) Both of these asymmetries involve the phase in the B^o–$\overline{B}^o$ mixing amplitude and are sensitive to new physics through this source.

Figure 1.22(c) shows the 'B_s triangle'. The time-dependent CP asymmetry in $B_s \to D_s^{\pm}K^{\mp}$ is connected to $\sin\gamma$. The B_s system also allows an interesting null experiment. The time-dependent CP violation in $B_s \to c\bar{c}s\bar{s}$ decays is expected to be very small in the Standard Model. Thus the phase in $B_s \to J/\psi\eta$ will be a very sensitive indicator for new CP violating physics in the B_s–$\bar{B}_s$ mixing amplitude. This constraint is shown, just for the purpose of illustration, as a constraint on the base of the unitarity triangle.

Figure 1.22(d) shows the 'K triangle'. This is the triangle determined by two rare K decays $K^+ \to \pi^+\nu\bar{\nu}$, with a Standard Model amplitude approximately proportional to V_{td}, and $K_L^o \to \pi^o\nu\bar{\nu}$, a CP-violating process with a Standard Model amplitude proportional to $\text{Im}[V_{td}]$. These decays proceed through box diagrams which could well have exotic contributions from new particles with masses of a few hundred GeV. Though Peskin says that: "The rare K decays are frighteningly difficult to detect."

1.12.3   New Physics Tests in Specific Models

1.12.3.1   Supersymmetry

Supersymmetry is a kind of super-model. The basic idea is that for every fundamental fermion there is a companion boson and for every boson there is a companion fermion. There are many different implementations of couplings in this framework [109]. In the most general case we pick up 80 new constants and 43 new phases. This is clearly too many to handle so we can try to see things in terms of simpler implementations. In the minimal model (MSSM) we have only two new fundamental phases. One, θ_D, would arise in B^o mixing and the other, θ_A, would appear in B^o decay. A combination would generate CP violation in D^o mixing, call it $\phi_{K\pi}$ when the $D^o \to K^-\pi^+$ [110]. Table 1.12 shows the CP asymmetry in three different processes in the Standard Model and the MSSM.

Table 1.12: CP Violating Asymmetries in the Standard Model and the MSSM.

Process	Standard Model	New Physics
$B^o \to J/\psi K_s$	$\sin 2\beta$	$\sin 2(\beta + \theta_D)$
$B^o \to \phi K_s$	$\sin 2\beta$	$\sin 2(\beta + \theta_D + \theta_A)$
$D^o \to K^-\pi^+$	0	$\sim \sin \phi_{K\pi}$

Two direct effects of New Physics are clear here. First of all, the difference in CP asymmetries between $B^o \to J/\psi K_s$ and $B^o \to \phi K_s$ would show the phase ϕ_A. Secondly, there would be finite CP violation in $D^o \to K^-\pi^+$ where none is expected in the Standard Model.

Manifestations of specific SUSY models lead to different patterns. Table 1.13 shows the expectations for some of these models in terms of these variables and the neutron electric

dipole moment d_N; see [110] for details. Note, that "Approximate CP" has already been

Table 1.13: Some SUSY Predictions.

Model	$d_N \times 10^{-25}$	θ_D	θ_A	$\sin \phi_{K\pi}$
Standard Model	$\leq 10^{-6}$	0	0	0
Approx. Universality	$\geq 10^{-2}$	$\mathcal{O}(0.2)$	$\mathcal{O}(1)$	0
Alignment	$\geq 10^{-3}$	$\mathcal{O}(0.2)$	$\mathcal{O}(1)$	$\mathcal{O}(1)$
Heavy squarks	$\sim 10^{-1}$	$\mathcal{O}(1)$	$\mathcal{O}(1)$	$\mathcal{O}(10^{-2})$
Approx. CP	$\sim 10^{-1}$	$-\beta$	0	$\mathcal{O}(10^{-3})$

ruled out by the measurements of $\sin 2\beta$.

In the context of the MSSM there will be significant contributions to B_s mixing, and the CP asymmetry in the charged decay $B^{\mp} \to \phi K^{\mp}$. The contribution to B_s mixing significantly enhances the CP violating asymmetry in modes such as $B_s \to J/\psi\eta$. (Recall the CP asymmetry in this mode is proportional to $\sin 2\chi$ in the Standard Model.) The Standard Model and MSSM diagrams are shown in Fig. 1.23. The expected CP asymmetry in the MSSM is $\approx \sin \phi_\mu \cos \phi_A \sin(\Delta m_s t)$, which is approximately 10 times the expected value in the Standard Model [111].
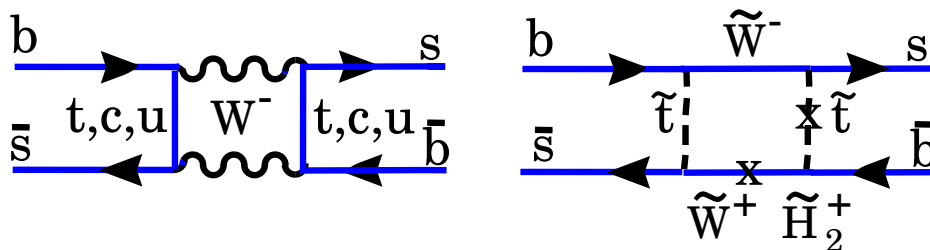
Figure 1.23: The Standard Model (left) and MSSM (right) contributions to B_s^o mixing.

We observed that a difference between CP asymmetries in $B^o \to J/\psi K_s$ and ϕK_s arises in the MSSM due to a CP asymmetry in the decay phase. It is possible to observe this directly by looking for a CP asymmetry in $B^{\mp} \to \phi K^{\mp}$. The Standard Model and MSSM diagrams are shown in Fig. 1.24. Here the interference of the two diagrams provides the CP asymmetry. The predicted asymmetry is equal to $(M_W/m_{squark})^2 \sin \phi_\mu$ in the MSSM, where m_{squark} is the relevant squark mass [111].

The ϕK and ϕK^* final states have been observed, first by CLEO [112] and subsequently by BABAR [113]. The average branching ratio is $\mathcal{B}(B^- \to \phi K^-) = (6.8 \pm 1.3) \times 10^{-6}$ showing that in principle large samples can be acquired especially at hadronic machines.
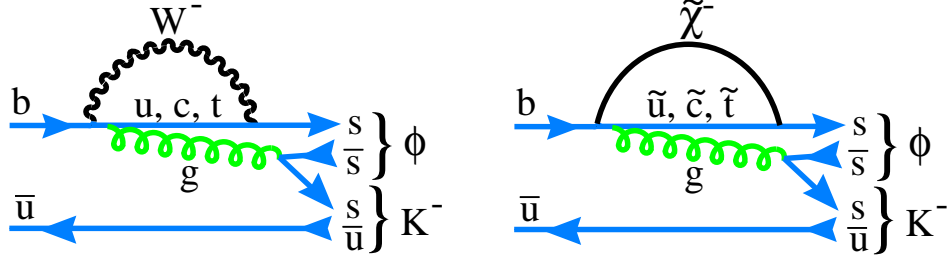
Figure 1.24: The Standard Model (left) and MSSM (right) contributions to $B^- \to \phi K^-$.

1.12.3.2 Other New Physics Models

There are many other specific models that predict New Physics in b decays. We list here a few of these with a woefully incomplete list of references, to give a flavor of what these models predict.

- *Two Higgs and Multi-Higgs Doublet Models-* They predict large effects in ϵ_K and CP violation in $D^o \to K^-\pi^+$ with only a few percent effect in B^o [110]. Expect to see 1-10% CP violating effects in $b \to s\gamma$ [114].

- *Left-Right Symmetric Model-* Contributions compete with or even dominate over Standard Model contributions to B_d and B_s mxing. This means that CP asymmetries into CP eigenstates could be substantially different from the Standard Model prediction [110].

- *Extra Down Singlet Quarks-* Dramatic deviations from Standard Model predictions for CP asymmetries in b decays are not unlikely [110].

- *FCNC Couplings of the Z boson-* Both the sign and magnitude of the decay leptons in $B \to K^*\ell^+\ell^-$ carry sensitive information on new physics. Potential effects are on the of 10% compared to an entirely negligable Standard Model asymmetry of $\sim 10^{-3}$ [115]. These models also predict a factor of 20 enhancement of $b \to d\ell^+\ell^-$ and could explain a low value of $\sin 2\beta$ [116].

- *Noncommutative Geometry-* If the geometry of space time is noncommutative, i.e. $[x_\mu, x_\nu] = i\theta_{\mu\nu}$, then CP violating effects may be manifest a low energy. For a scale <2 TeV there are comparable effects to the Standard Model [117].

- *MSSM without new flavor structure-* Can lead to CP violation in $b \to s\gamma$ of up to 5% [118]. Ali and London propose [119] that the Standard Model formulas are modified by Supersymmetry as

$$\Delta m_d = \Delta m_d(\text{SM}) \left[1 + f\left(m_{\chi_2^\pm}, m_{\tilde{t}_R}, m_{H^\pm}, tan\beta\right)\right] \tag{1.88}$$

$$\Delta m_s = \Delta m_s(\text{SM}) \left[1 + f\left(m_{\chi_2^\pm}, m_{\tilde{t}_R}, m_{H^\pm}, tan\beta\right)\right] \tag{1.89}$$

$$|\epsilon_K| \;=\; \frac{G_F^2 f_K^2 M_K M_W^2}{6\sqrt{2}\pi^2 \Delta M_K} B_K (A^2 \lambda^6 \overline{\eta}) \left[y_c \left(\eta_{ct} f_3(y_c, y_t) - \eta_{cc} \right) \right.$$
$$\left. + \eta_{tt} y_t f_s(y_t) \left[1 + f\left(m_{\chi_2^\pm}, m_{\tilde{t}_R}, m_{H^\pm}, tan\beta \right) \right] A^2 \lambda^4 (1 - \overline{\rho}) \right] \quad, \quad (1.90)$$

where $\Delta m(SM)$ refers to the Standard Model formula and the expression for $|\epsilon_K|$ would be the Standard Model expression if f were set equal to zero. Ali and London show that it is reasonable to expect that $0.8 > f > 0.2$, so since the CP violating angles will not change from the Standard Model, determining the value of (ρ, η) using the magnitudes $\Delta m_s / \Delta m_d$ and $|\epsilon_K|$ will show an inconsistency with values obtained using other magnitudes and angles.

- *Extra Dimensions*- We are beginning to see papers predicting b decay phenomena when the world has extra dimensions. See [120].

We close this section with a quote from Masiero and Vives [121]: "The relevance of SUSY searches in rare processes is not confined to the usually quoted possibility that indirect searches can arrive 'first' in signaling the presence of SUSY. Even after the possible direct observation of SUSY particles, the importance of FCNC and CP violation in testing SUSY remains of utmost relevance. They are and will be complementary to the Tevatron and LHC establishing low energy supersymmetry as the response to the electroweak breaking puzzle."

We agree, except that we would replace "SUSY" with "New Physics." It is clear that precision studies of b decays can bring a wealth of information to bear on new physics, that probably will be crucial in sorting out anything seen at the LHC.

Bibliography

[1] P. Langacker, "CP Violation and Cosmology," in *CP Violation*, ed. C. Jarlskog, World Scientific, Singapore p 552 (1989).

[2] For CP violation in the kaon system see J. H. Christenson *et al.*, *Phys. Rev. Lett.* **13**, 138 (1964); A. Alavi-Harati *et al.*, *Phys. Rev. Lett.* **83**, 22 (1999); V. Fanti *et al.*, *Phys. Lett.* B **465**, 335 (1999); G. D. Barr *et al.*, *Phys. Lett.* B **317**, 233 (1993). For CP violation in the B^o system see B. Aubert *et al.*, *Phys. Rev. Lett.* **87**, 091801 (2001), *ibid.* **86**, 2525 (2001), and B. Aubert *et al.*, "A Study of Time-Dependent CP-Violating Asymmetries and Flavor Oscillations in Neutral B Decays at the Upsilon(4S)," (hep-ex/0201020) (2002); K. Abe etal, *Phys. Rev. Lett.* **87**, 091802 (2001).

[3] A. D. Sakharov, *JETP Lett.* **6**, 24 (1967).

[4] N. Cabibbo, *Phys. Rev. Lett.* **10**, 531 (1963); M. Kobayashi and K. Maskawa, *Prog. Theor. Phys.* **49**, 652 (1973).

[5] L. Wolfenstein, *Phys. Rev. Lett.* **51**, 1945 (1983).

[6] S. Stone, "Prospects For B-Physics In The Next Decade," in *Techniques and Concepts of High-Energy Physics IX*, ed. by T. Ferbel, NATO ASI Series, Plenum, NY (1996).

[7] M. Artuso, "Flavour Physics: The Questions, The Clues and the Challenges," in proceedings of the Int. Europhysics Conf. on High Energy Physics, Tampere, Finland, July, 1999, ed. K. Huitu, H. Kurki-Suonio and J. Maalampi, Inst. of Physics Publishing (Bristol) p91 (hep-ph/9911347).

[8] R. Aleksan, B. Kayser and D. London, *Phys. Rev. Lett.* **73**, 18 (1994) (hep-ph/9403341).

[9] M. Gaillard and B. Lee, *Phys. Rev.* D 10, 897, (1974); J. Hagelin, *Phys. Rev.* D **20**, 2893, (1979); A. Ali and A. Aydin, *Nucl. Phys.* B **148**, 165 (1979); T. Brown and S. Pakvasa, *Phys. Rev.* D **31**, 1661 (1985); S. Pakvasa, *Phys. Rev.* D **28**, 2915 (1985); I. Bigi and A. Sanda, *Phys. Rev.* D **29**, 1393 (1984).

[10] T. Inami and C. S. Lim, *Prog. Theor. Phys.* **65**, 297 (1981); Erratum ibid., **65**, 1772 (1981).

[11] J. Rosner, "The Cabibbo-Kobayashi-Maskawa Matrix," in *B* **Decays,** *Revised 2nd Edition*, ed. S. Stone, World Scientific, Singapore (1994), p470.

[12] Particle Data Group, D. E. Groom *et al.*, *The European Physical Journal* **C15**, (2000) 1.

[13] L. Lellouch and C.-J. D. Lin, CERN-TH/99-344 (hep-ph/9912322); D. Becirevic *et al.*, ROMA 1285/00 (hep-lat/0002025)

[14] S. Stone, "*B* Phenomenology," Presented at 55th Scottish Universities Summer School in Physics on "Heavy Flavour Physics" A NATO Advanced Study Insititute, St. Andrews, Scotland, August, 2001(hep-ph/0112008).

[15] A. J. Buras, "Theoretical Review of B-physics," in *BEAUTY '95* ed. N. Harnew and P. E. Schlein, *Nucl. Instrum. Methods* **A368**, 1 (1995).

[16] A. Hocker, H. Lacker, S. Laplace, F. Le Diberder, "A New Approach to a Global Fit of the CKM Matrix," *Eur. Phys. J.* **C21**, 225 (2001).

[17] J.L. Rosner, *Nucl. Phys. Proc. Suppl.* **73** 29, (1999) (hep-ph/9809545).

[18] S. Plaszczynski and M. H. Schune, "Overall Determination of the CKM Matrix," presented at "Heavy Flavours 8," Southampton, UK, July, 1999, to appear in proceedings, hep-ph/9911280.

[19] M. Ciuchini, *et al.*, "2000 CKM-Triangle Analysis A Critical Review with Updated Experimental Inputs and Theoretical Parameters," hep-ph/0012308.

[20] Objections to the Bayesian statistical procedure used in Ciuchini *et al.*[19] have been documented by Hocker *et al.* [16] and commented on by Stone [14].

[21] The first papers explaining the physics of mixing and CP violation in *B* decays were A. Carter and A. I. Sanda, *Phys. Rev. Lett.* 45, 952 (1980); *Phys. Rev. D* **23**, 1567 (1981); I. I. Bigi and A. I. Sanda, *Nucl. Phys.* B **193**, 85 (1981); ibid **281**, 41 (1987).

[22] I. Bigi, V. Khoze, N. Uraltsev, in **CP Violation**, ed. C. Jarlskog, World Scientific, Singapore 175 (1989).

[23] A. S. Dighe, I. Dunietz, H. J. Lipkin, J. L. Rosner, *Phys. Lett.* B **369**, 144 (1996); R. Fleischer and I. Dunietz, *Phys. Lett.* B **387** 361 (1996); Y. Azimov and I. Dunietz,*Phys. Lett.* B **395**, 334 (1997).

[24] M. Beneke, G. Buchalla, I. Dunietz, *Phys. Rev. D* **54**, 4419 (1996).

[25] I. Dunietz, *Phys. Rev. D* **D2**, 3048 (1995).

[26] If $\Delta\Gamma$ is non-zero and there is large penguin amplitude contributing, the lifetime distribution is not a simple exponential. However, using a $\Delta\Gamma$ of 15% and a ratio of penguin to tree rates of 4 to 1, we find only a 1% effect on the lifetime.

[27] For the exact formulae see I. Bigi and A. Sanda, "CP Violation," Cambridge (1999), p183.

[28] A. Dighe, I. Dunietz, and R. Fleischer, *Phys. Lett.* B **433**, 147 (1998) (hep-ph/9804254).

[29] I. Dunietz, H. Quinn, A. Snyder, W. Toki, and H.J. Lipkin, *Phys. Rev. D* **43** (1991) 2193.

[30] A.S. Dighe, I. Dunietz, H.J. Lipkin and J.L. Rosner, *Phys. Lett.* B **369** (1996) 144.

[31] See, for example, M. Jacob and G. C. Wick, *Ann. Phys.* (N.Y.) **7** (1959) 404.

[32] C. P. Jessop, *et al.*, *Phys. Rev. Lett.* **79**, 4533 (1997).

[33] A. Ribon, "B-Physics at the Tevatron Collider," presented at Les Rencontres de Physique de la Vallee d'Aoste, La Thuile, Italy, Feb. 28-March 6, 1999.

[34] B. Aubert, *et al.*, *Phys. Rev. Lett.* **87**, 241801 (2001).

[35] B. Kayser, "Cascade Mixing and the CP-Violating Angle Beta," in Les Arcs 1997, Electroweak Interactions and Unified Theories, p389 (hep-ph/9709382). Previous work in this area was done by Y. Aimov, Phys. Rev. **D42**, 3705 (1990).

[36] D-S. Du and Z-T. Wei, "Test of CPT Symmetry in Cascade Decays," *Eur. Phys. J.* C**14**, 479 (2000) (hep-ph/9904403).

[37] Y. Grossman, G. Isidori, M. Worah, *Phys. Rev.* D **58**, 057504 (1998).

[38] S. J. Richichi *et al.* (CLEO) "Two-Body B Meson Decays to η and η' - Observation of $B \to \eta K^*$" Conf 99-12 (hep-ex/9908019) (1999).

[39] S. Kopp, "Studies of B^o Decays for Measuring $\sin(2\beta)$" presented at DPF'99, to appear in proceedings (hep-ex/9904009).

[40] B. Aubert *et al.*, Phys. Rev. Lett. **87**, 151801 (2001).

[41] Y. Gao, "Recent results from CLEO collaboration," to appear in proceeding of the International Conference on Flavor Physics (ICFP2001) (hep-ex/0108005) (2001).

[42] M. Bona, BABAR preprint BABAR-CONF-01/71, SLAC-PUB-9045 (hep-ex/0111017).

[43] K. Abe *et al.*, Phys. Rev. Lett. **87**, 101801 (2001) (hep-ex/0104030).

[44] M. Gronau, Phys. Rev. Lett. **63**, 1451 (1989); M. Gronau and D. London, Phys. Rev. Lett. **65**, 3381 (1990).

[45] The theoretical accuracy of this approach is limited by electroweak penguins, that are expected to be rather small in this case. In principle, they can be taken into account, as pointed out by A. J. Buras and R. Fleischer, *Eur. Phys. J.* C**11**, 93 (1999) (hep-ph/9810260), and also by M. Gronau, D. Pirjol and T-M. Yan, *Phys. Rev.* D **60**, 034021 (1999) (hep-ph/9810482).

[46] N. G. Deshpande, X. G. He, and S. Oh, *Phys. Lett. B* **384**, 283 (1996) (hep-ph/9604336), and references therein.

[47] A. E. Snyder and H. R. Quinn, *Phys. Rev. D.* **48**, 2139 (1993).

[48] A. Gritsan "Charmless Hadronic B Meson Decays with CLEO," presented at Lake Louise Winter Institute 2000, to appear in proceedings; Y. Gao and F. Würthwein, CLEO preprint (hep-ex/9904008).

[49] Y. Gao and F. Wurthwein, "Charmless Hadronic B Decays at CLEO," in DPF99 proceedings, (hep-ex/9904008).

[50] A. Ali, G. Kramer, and C.D. Lu, *Phys. Rev.* D **59**, 014005 (1999) (hep-ph/9805403).

[51] H. R. Quinn and J. P. Silva, "The Use of Early Data on $B \to \rho\pi$ Decays," *Phys. Rev.* D **62**, 054002 (2000) (hep-ph/0001290).

[52] A. Deandrea *et al.*, "Measuring $B \to \rho\pi$ Decays and the Unitarity Angle Alpha," *Phys. Rev.* D **62**, 036001 (2000) (hep-ph/0002038).

[53] Y. Grossman and H. R. Quinn, "Removing Discrete Ambiguities in CP Asymmetry Measurments," *Phys. Rev.* D **56**, 7259 (1997) (hep-ph/9705356).

[54] D. Du, I. Dunietz and Dan-di Wu, *Phys. Rev.* D **34**, 3414 (1986). R. Aleksan, I Dunietz, and B. Kayser, *Z. Phys.* C **54**, 653 (1992). R. Aleksan, A. Le Yaouanc, L. Oliver, O. Pène and J.-C. Raynal, *Z. Phys.* C **67**, 251 (1995) (hep-ph/9407406).

[55] D. Atwood, I. Dunietz and A. Soni, *Phys. Rev. Lett.* **78**, 3257 (1997).

[56] M. Gronau and D. Wyler, *Phys. Lett.* B **265**, 172 (1991).

[57] R. Fleischer, and T. Mannel, *Phys. Rev.* D **57**, 2752 (1998) (hep-ph/9704423).

[58] M. Neubert and J. L. Rosner, *Phys. Rev. Lett.* **81**, 5076 (1998) (hep-ph/9809311).

[59] M. Gronau and J. L. Rosner, *Phys. Rev.* D **57,** 6843 (1998) (hep-ph/9711246); M. Gronau, and D. Pirjol, "A Critical Look at Rescattering Effects on γ from $B^+ \to K\pi$, hep-ph/9902482 (1999); M. Gronau and J. L. Rosner, "Combining CP Asymmetries in $B \to K\pi$ Decays, (hep-ph/9809384) (1998).

[60] J.-M. Gerard and J. Weyers, *Eur. Phys. J.* C**7**, 1 (1999) (hep-ph/9711469).

[61] A. Falk, A. Kagan, Y. Nir and A. Petrov, *Phys. Rev.* D **57**, 4290 (1998) (hep-ph/9712225).

[62] M. Neubert, *Phys. Lett.* B **424**, 152 (1998) (hep-ph/9712224).

[63] D. Atwood and A. Soni, Phys. Rev. D **58**, 036005 (1998) (hep-ph/9712287).

[64] M. Neubert, *JHEP* **9902**, 014 (1999) (hep-ph/9812396).

[65] M. Beneke *et al.*, *Nucl Phys.* B **606**, 245 (2001) (hep-ph/0104110).

[66] R. Fleischer, *Phys. Lett.* B **459**, 306 (1999) (hep-ph/9903456).

[67] I. Dunietz, "Extracting CKM Parameters from B Decays," in Proceedings of the Workshop on B Physics at Hadron Accelerators, ed. P. McBride and S. Mishra, Snowmass, Co, June (1993), Fermilab-Conf-93/90-T.

[68] For a recent calculation of $\Delta\Gamma_s$, see M. Beneke, G. Buchalla, C. Greub, A. Lenz and U. Nierste, *Phys. Lett.* B **459**, 631 (1999) (hep-ph/9808385).

[69] A. Dighe, I. Dunietz, and R. Fleischer, *Eur. Phys. J.* C**6**, 647 (1999) (hep-ph/9804253).

[70] R. Fleischer and I. Dunietz, *Phys. Rev.* D **55** 259 (1997); R. Fleischer, "Extracting CKM Phases from Angular Distributions of $B_{d,s}$ Decays into Admixtures of CP Eigenstates hep-ph/9903540 (1999).

[71] I. Dunietz, *Phys. Lett.* B **427** 179 (1998) (hep-ph/97124).

[72] Another method of measuring $|V_{td}|$ is to measure the branching ratio of $K^+ \to \pi^+ \nu\bar\nu$. A precise measurement would still be subject to theoretical uncertainties mostly arising from the uncertainty in the charmed quark mass and $|V_{cb}|$ See G. Buchalla, A. J. Buras, and M. E. Lautenbacher, *Rev. Mod. Phys.*, **68**, 1125 (1996) (hep-ph/9512380). A Brookhaven experiment, E787, has claimed to see two events and hopes to obtain substantially more data. See S. Adler, *et al.* (E787), *Phys. Rev. Lett.* **88**, 041803 (2002).

[73] K. Lingel, T. Skwarnicki and J. G. Smith, *Ann. Rev. Nucl. Part. Sci.* **48** 169 (1998) (hep-ex/9804015).

[74] M. Bander, D. Silverman and A. Soni, *Phys. Rev. Lett.* **43**, 242 (1979).

[75] M. S. Alam *et al.* (CLEO), *Phys. Rev. Lett.* **74**, 2885 (1995).

[76] R. Ammar *et al.* (CLEO), *Phys. Rev. Lett.* **71**, 674 (1993).

[77] S. Glenn *et al.* (CLEO), "Improved Measurement of $\mathcal{B}(b \to s\gamma)$," submitted to XXIX Int. Conf. on High Energy Physics, Vancouver, Canada, July 1998 paper ICHEP98 1011 (1998).

[78] B. Barate *et al.* (ALEPH), "A Measurement of the Inclusive $b \to s\gamma$, Branching Ratio," *Phys. Lett.* B **429**, 169 (1998).

[79] H. Tajima, "Belle B Physics Results," to appear in Proceedings of the XX Int. Symp. on Lepton and Photon Interactions at High Energies, July, 2001, Rome, Italy, (hep-ex/0111037).

[80] A. Ali and C. Greub, *Phys. Lett.* B **259**, 182 (1991). The parameters for this fit are $< m_b > = 4.88$ GeV and $P_F = 250$ MeV/c.

[81] T. Hurth, "Inclusive Rare B Decays," CERN-TH/2001-146, (hep-ph/0106050); A. Czarnecki and W. J. Marciano, "Electroweak Radiative Corrections to $b \to s\gamma$," submitted to XXIX Int. Conf. on High Energy Physics, Vancouver, Canada, July 1998 paper ICHEP98 714 (1998); ibid *Phys. Rev. Lett.* **81**, 277 (1998); see also see also M. Neubert, "Theoretical Status of $b \to X_s\gamma$ Decays," hep-ph/9809377 (1998); A. Ali, "Theory of Rare B Decays," DESY 97-192 (hep-ph/9709507) (1997); N. G. Deshpande, "Theory of Penguins in B Decays," in *B Decays Revised 2nd Edition*, ed. by S. Stone, World Scientific, Singapore, (1994).

[82] J. L. Hewett, "B Physics Beyond the Standard Model," (hep-ph/9803370) (1998).

[83] S. Abachi *et al.* (D0), *Phys. Rev.* D **56**, 6742 (1997); F. Abe *et al.* (CDF), *Phys. Rev. Lett.* **78**, 4536 (1997).

[84] R. Ammar *et al.*, "Radiative Penguin Decays of the B Meson," CLEO-CONF 96-6 (1996).

[85] B. Aubert *et al.*, BABAR-PUB-01/04, SLAC-PUB-8952, (hep-ex/0110065) (2002).

[86] D. Atwood, B. Blok & A. Soni, *Int. J. Mod. Phys.* **A11**, 3743 (1994) and *Nuovo Cimento* **109A**, 873 (1994); N. Deshpande, X. He & J. Trampetic, *Phys. Lett.* B **362**, 1996 (;) see also J. M. Soares, *Phys. Rev.* D **53**, 241 (1996); G. Eilam, A. Ioannissian & R. R. Mendel, *Z. Phys.* C **71**, 95 (1995).

[87] S. Fukae, C.S. Kim , T. Morozumi, and T. Yoshikawa, "A Model Independent Analysis of the Rare B Decay $B \to X_s\ell^+\ell^-$, *Phys. Rev.* D **59**, 074013 (1999) (hep-ph/9807254), and references cited therein.

[88] A. Ali, C. Greub and T. Mannel, "Rare B Decays in the Standard Model, " in Hamburg 1992, Proceedings, ECFA Workshop on a European B-meson Factory, Eds. R. Aleksan and A. Ali, p155 (1993).

[89] C. Albajar *et al.*, *Phys. Lett.* B **262**, 163 (1991).

[90] R. Godang *et al.*, "Search for Electroweak Penguin Decays $B \to K\ell^+\ell^-$ and $B \to K^*\ell^+\ell^-$ at CLEO," CLEO-CONF 98-22 (1998).

[91] B. Aubert *et al.*, BABAR-PUB-01/22, SLAC-PUB-9096 (2002) (hep-ex/0201008).

[92] T. Affolder *et al.* (CDF), *Phys. Rev. Lett.* **83**, 3378 (1999).

[93] K. Abe *et al.*, *Phys. Rev. Lett.* **88**, 021801 (2002) (hep-ex/0109026).

[94] R. Ammar *et al.*, *Phys. Rev.* D **49**, 5701 (1994); M. Artuso, *et al.*, *Phys. Rev. Lett.* **75**, 785 (1995).

[95] F. Abe *et al.* (CDF), *Phys. Rev.* D **57**, R3811 (1998).

[96] D. Buskulic *et al.*, *Phys. Lett.* B **343**, 444 (1995).

[97] M. Acciarri *et al.*. (L3),*Phys. Lett.* B **396** 327 (1997).

[98] A. Ali and T. Mannel, *Phys. Lett.* B **264**, 447 (1991). Erratum, ibid, **274**, 526 (1992).

[99] E. M. Aitala *et al.*, *Phys. Rev. Lett.* **77**, 2384 (1996).

[100] G. Burdman, "Potential for Discoveries in Charm Meson Physics," (hep-ph/9508349).

[101] H. Georgi, *Phys. Lett.* B **297**, 353 (1992); T. Ohl *et al.*, *Nucl. Phys.* B **403**, 603 (1993).

[102] I. I. Bigi and H. Yamamoto, *Phys. Lett.* B **349**, 363 (1995).

[103] M. B. Gavela, P. Hernández, J. Orloff and O. Pène O, *Mod. Phys. Lett. A* **9**, 795 (1993) (hep-ph/9312215).

[104] J. Ellis, *Nucl. Phys. Proc. Suppl.* **99A**, 331 (2000) (hep-ph/0011396).

[105] F. J. Greub, A. Ioannissian and D. Wyler, *Phys. Lett.* B **346**, 149 (1995) (hep-ph/9408382).

[106] J. P. Silva and L. Wolfenstein, *Phys. Rev.* D **55** 5331 (1997) (hep-ph/9610208).

[107] I. I. Bigi and A. I. Sanda, "On the Other Five KM Triangles," (hep-ph/9909479).

[108] M. E. Peskin, "Theoretical Summary," in "High Energy Physics 99," proceedings of the Int. Europhysics Conf. on High Energy Physics, Tampere, Finland, July, 1999, ed. K. Huitu, H. Kurki-Suonio and J. Maalampi, Inst. of Physics Publishing (Bristol) p319 (hep-ph/0002041).

[109] A. Masiero and O. Vives, "New Physics Behind the Standard Model's Door?," Int. School on Subnuclear Physics, Erice, Italy, 1999 (hep-ph/0003133).

[110] Y. Nir, "CP Violation In and Beyond the Standard Model," IASSNS-HEP-99-96 (1999) (hep-ph/9911321).

[111] I. Hinchliff and N. Kersting, "Constraining CP Violating Phases of the MSSM," *Phys. Rev.* D **63**, 015003 (2001) (hep-ph/0003090).

[112] R. A. Briere *et al.*, *Phys. Rev. Lett.* **86**, 3718 (2001) (hep-ex/0101032).

[113] B. Aubert *et al.*, *Phys. Rev. Lett.*, **87**, 151801 (2001) (hep-ex/0105001).

[114] L. Wolfenstein and Y.L. Wu, *Phys. Rev. Lett.* **74**, 2809 (1994) (hep-ph/9410253).

[115] G. Buchalla, G, Hiller, and G. Isidori, *Phys. Rev.* D **63**, 014015 (2000) (hep-ph/0006136).

[116] G. Barenboim, F. J. Botella, and O. Vives, *Phys. Rev.* D **64**, 015007 (2001) (hep-ph/0012197).

[117] I. Hinchliff and N. Kersting, "CP Violation from Noncommutative Geometry," LBNL-47750 (hep-ph/0104137).

[118] A. Bartl, *et al.*, *Phys. Rev.* D **64**, 076009 (2001) (hep-ph/0103324).

[119] A. Ali, G. Kramer and C. D. Lu, *Phys. Rev.* D **59**, 014005 (1999) (hep-ph/9805403).

[120] K. Agashe, N. G. Deshphande and G. H. Wu, "Universal Extra Dimensions and $b \rightarrow s\gamma$," *Phys. Lett.* B **514**, 309 (2001) (hep-ph/0105084); G. Barenboim, F. J. Botella and O. Vives, "Constraining Models With Vector-Like Fermions from FCNC in K and B Physics," *Nucl. Phys.* B **613**, 285 (2001) (hep-ph/01050306); G. C. Branco, A. de Gouvea and M. N. Rebelo, "Split Fermions in Extra Dimensions and CP Violation," *Phys. Lett.* B **506**, 115 (2001) (hep-ph/0012289); D. Chang, W. Y. Keung and R. N. Mohapatra, "Models for Geometric CP Violation With Extra Dimensions," Phys. Lett. B **515**, 431 (2001) (hep-ph/0105177); J. Papavassiliou and A. Santamaria, "Extra Dimensions at the One Loop Level: $Z \rightarrow b\overline{b}$ and $B - \overline{B}$ Mixing," *Phys. Rev.* D **63**, 016002 (2001) (hep-ph/016002).

[121] A. Masiero and O. Vives, New Physics in CP Violation Experiments, *Ann. Rev. of Nucl. & Part. Science* **51**, (2001) (hep-ph/0104027).

Chapter 2

Summary of Physics Reach and Comparisons With Other Experiments

The results quoted here are based on the tools described and studies reported in Part III, "Physics Simulations" of the May, 2000 BTeV proposal. (In most case these studies use GEANT3.)

All physics sensitivities and yields quoted here are explicitly for the one-arm version of BTeV. The naive expectation is that the yearly rates would be half of those quoted in the proposal. There are improvements, however, that we have taken advantage of both in hardware and our understanding of the detector that we include that increase our sensitivities. Our lepton identification procedures have been significantly improved by including the RICH detector: a full description of the gains expected are given in section 2.9. We also have investigated flavor tagging much more extensively. In our May 2000 proposal, we used an effective tagging efficiency ϵD^2 of 10% for both B^o and B_s final states, based on a preliminary study. New studies summarized in section 2.10, show that we can indeed achieve ϵD^2 of 10% for B^o decays. This more thorough study shows, as expected, that B_s decays have higher tagging efficiency because of the charged kaon produced to conserve flavor in the b quark fragmentation to a B_s. This "same side" tagging is quite favorable and, as a result, we achieve 13% for ϵD^2 in B_s decays.

Our final improvement results from an increase in our effective trigger and data acquisition bandwidth by a factor of 2.5, due to the fact that we have only one arm and schedule delays will lead to lower costs for the computing equipment used in the trigger. We decided to keep the full bandwidth of the two-arm system in our one arm plan. One reason was to keep the capability to eventually go to two arms and another was that we would have realized only a small (∼10%) savings in the trigger and DAQ cost. Our original plan was to trigger on 1% of the interactions in the Level 1 trigger in the two-arm configuration. We now plan accept 2.5% of the interactions pointing into the instrumented arm by loosening the restrictions on the trigger and thereby increasing its efficiency. Simulations show that we

achieve a 15% gain in the Level 1 trigger efficiencies over those quoted in the proposal, only slightly dependent on decay mode. Fig. 2.1 shows the improvement in the Level 1 acceptance for a typical mode, $\overline{B}^o \to D^{*+}\pi^-$, where $D^{*+} \to \pi^+ D^o$, $D^o \to K^-\pi^+$.
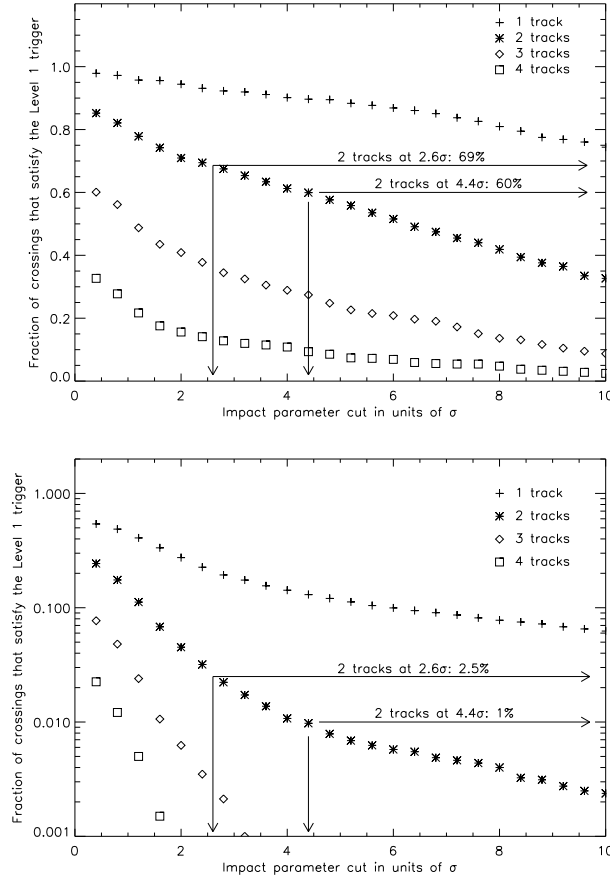
Figure 2.1: a) Trigger efficiencies for $\overline{B}^o \to D^{*+}\pi-$, $D^{*+} \to \pi^+ D^o$, $D^o \to K^-\pi^+$ for various detachment requirments in terms of normalized impact parameter (σ) and the number of detached tracks. b) Trigger response for minimum bias crossing. The arrows indicate two specific requirments, one for 2 tracks at 4.4 σ that shows a 99% rejection of minimum bias crossings (at two interactions per crossing) and 60% trigger efficiency, and other selection being 2 tracks at 2.6 σ that shows a 97.5% rejection and 69% efficiency.

2.1 Sensitivities to CP Violating Angles

BTeV will have outstanding performance in determining CP violating asymmetries. The results of our simulations are summarized in Table 2.1 for a luminosity of 2×10^{32} cm^{-2}s^{-1} and 10^7 seconds of running time.

We briefly discuss each of these measurements:

Table 2.1: Yearly sensitivities for CP violating quantities.

Quantity	Decay Mode(s)	Sensitivity
$\sin(2\beta)$	$B^o \to J/\psi K_S$	± 0.017
α	$B^o \to \rho\pi$	$\sim \pm 4.0°$
γ	$B_s \to D_s^{\pm}K^{\mp}$	$\sim \pm 11.5°$
γ	$B^- \to \overline{D}^o K^-$	$< \pm 13°$
γ	$B \to K\pi$	$< \pm 4°$ (plus theoretical errors)
$\sin(2\chi)$	$B_s \to J/\psi\eta^{(\prime)}$	± 0.024
Asymmetry	$B^o \to \pi^+\pi^-$	± 0.033

- $\sin(2\beta)$ is obtained by fitting the time distribution, which results in a 20% improvement in the error relative to that of the time-integrated asymmetry measurement.

- We use the method originally proposed by Snyder and Quinn to determine α using $B^o \to \rho\pi \to \pi^+\pi^-\pi^o$ [1]. We expect to have ~ 500 effective flavor tagged $\rho^{\pm}\pi^{\mp}$ events and ~ 75 $\rho^o\pi^o$ per year (10^7 s). The signal/background levels are 4.1 and 0.3, respectively. Both the signal efficiences and the background levels were determined by a full GEANT simulation. We have made a study to estimate the error in α described in more detail in Section 2.1.1, and predict an error between $1.8°$ and $6.1°$.

  Quinn and Silva have proposed using non-flavor-tagged rates as input to improve the accuracy of the α determination [2]. We have not yet incorporated this idea.

- Although the $B \to K\pi$ modes provide the smallest experimental error in determining γ, there are model dependent errors associated with this method. On the other hand, two other methods, which use $B_s \to D_s^{\pm}K^{\mp}$ and $B^- \to \overline{D}^o K^-$, provide model independent results and can be averaged. The interplay of the three methods can be used to resolve ambiguities.

- The error in $\sin(2\chi)$ averaged over both $J/\psi\eta$ and $J/\psi\eta'$ decay modes of the B_s is $\pm 3.0\%$. Since this is approximately the value we expect, it will take us a few years to make this important measurement, if it is in the Standard Model range. Including $B_s \to J/\psi\phi$ will reduce the time.

- The asymmetry in $B^o \to \pi^+\pi^-$ may be useful to gain insight into the value of α with theoretical input or combined with $B_s \to K^+K^-$ and theory to obtain γ. This study was done both with MCFast and GEANT. The signal efficiency is 10% higher in MCFast and the background levels the same in both, within statistics.

2.1.1 Sensitivity in Determining α Using $B^o \to \rho\pi$

At the time of the proposal, we used estimates from the literature to get a rough estimate the sensitivity we will have in measuring α using $B^o \to \rho\pi$. This requires the measurement of the tagged, time-dependent CP asymmetry in a particular combination of amplitudes obtained from a Dalitz plot analysis of the decay. The combination of amplitudes causes the Penguin terms to cancel and isolates the tree contribution to the decay, which provides the value of α. We have now performed a Dalitz plot analysis that includes detector resolution and background along with the expected levels of detected signal events.

The decay amplitude may be written as

$$| B^0 \rangle = f_+ a_{+-} + f_- a_{-+} + f_0 a_{00},$$

where $a_{i,j}$ refers to the three distinct final states as

$$a_{i,j} = a(B^0 \to \rho^i \pi^j), \ (i,j) = (+,-),(-,+),(0,0),$$

and f_k parameterizes the ρ decay amplitude. We use

$$f_k(s) = \frac{\cos\theta_k}{s - m_\rho^2 + i\prod(s)},$$

where θ_k is the angle between the direction of the B and the direction of a daughter pion, both viewed in the ρ rest frame, and s is the square of the dipion invariant mass $s = (E_{\pi_1} + E_{\pi_2})^2 - (\overrightarrow{p}_{\pi_1} + \overrightarrow{p}_{\pi_2})^2$; s can be in one of three charge states, s^+, s^- or s^o. In each case

$$\prod(s) = \frac{m_\rho^2}{\sqrt{s}} \left(\frac{p(s)}{p(m_\rho^2)}\right)^3 \Gamma_\rho(m_\rho^2),$$

p being the momentum in the ρ rest frame.

The amplitudes $a_{i,j}$ for B^o and $\overline{B^o}$ decay are written as a sum of Tree (T) and Penguin (P) parts as

$$a_{+-} = -e^{i\gamma}T^{+-} + e^{-i\beta}P^{+-}$$
$$a_{-+} = -e^{i\gamma}T^{-+} + e^{-i\beta}P^{-+}$$
$$a_{00} = -e^{i\gamma}T^{00} + e^{-i\beta}P^{00}$$
$$\bar{a}_{+-} = -e^{-i\gamma}T^{-+} + e^{i\beta}P^{-+}$$
$$\bar{a}_{-+} = -e^{-i\gamma}T^{+-} + e^{i\beta}P^{+-}$$
$$\bar{a}_{00} = -e^{-i\gamma}T^{00} + e^{i\beta}P^{00},$$

where γ and β are the usual CKM angles and $\alpha + \beta + \gamma = \pi$. Using both isospin symmetry and the fact that the Penguin amplitude is a pure $\Delta I = 1/2$ transition leads to the replacement

$$P^{00} = -\frac{1}{2}(P^{+-} + P^{-+}).$$

55

This leaves us with 9 parameters to be fit to the data including α, 3 complex Tree and 2 Penguin amplitudes, where one is defined as purely real and the total rate is used as an independent input. We can also allow the resonant and non-resonant background fractions to be determined by the fit, which adds two additional parameters.

Signal events are generated using the averaged branching ratio for $B^o \to \rho^+\pi^-$ and $B^o \to \rho^-\pi^+$ of 2.8×10^{-5} and a rate of 0.5×10^{-5} for $\rho^o\pi^o$. For this study we generated a data sample corresponding to two years of running (2×10^7s) with the one-arm version of BTeV. The background level is determined by a full GEANT simulation of 4,450,000 generic $b\bar{b}$ events; it is assumed that this background has an exponential time dependence given by the average lifetime of b-flavored hadrons. The background is parameterized with both resonant and non-resonant components. The non-resonant background is distributed uniformly over the Dalitz plot. The resonant background allows for two of the pions to have a Breit-Wigner shaped low mass enhancement. All charged tracks and photons in both signal and background events are smeared by the detector resolution before further analysis. Signal events are generated with an exponential time distribution modified by B^o mixing. The simulation is repeated for different assumptions about the relative size of Penguin and Tree amplitudes and the fraction of resonant and non-resonant background. For each set of data a maximum likelihood fit is performed where the likelihood is given by

$$-2\ln\mathcal{L} = -2\sum_{i=1}^{N_{B^o}} \ln\left[\left(\frac{\mid \mathcal{A}(s_i^+, s_i^-, t_i; \alpha, ..) \mid^2}{\mathcal{N}(\alpha, ..)} \times \varepsilon(s_i^+, s_i^-)+\right.\right.$$

$$R_{non} \times \frac{1}{\mathcal{N}_t} + R_{res} \times \frac{\mid \mathcal{BW}(s_i^+, s_i^-) \mid^2}{\mathcal{N}_{BW}} \times \varepsilon(s_i^+, s_i^-)\bigg)/(1 + R_{non} + R_{res})\bigg]$$

$$-2\sum_{j=1}^{N_{\overline{B}^o}} \ln\left[\left(\frac{\mid \bar{\mathcal{A}}(s_j^+, s_j^-, t_j; \alpha, ..) \mid^2}{\mathcal{N}(\alpha, ..)} \times \varepsilon(s_i^+, s_i^-)+\right.\right.$$

$$R_{non} \times \frac{1}{\mathcal{N}_t} + R_{res} \times \frac{\mid \mathcal{BW}(s_j^+, s_j^-) \mid^2}{\mathcal{N}_{BW}} \times \varepsilon(s_j^+, s_j^-)\bigg)/(1 + R_{non} + R_{res})\bigg],$$

where N_{B^o} and $N_{\overline{B}^o}$ are the total number of B^o and $\overline{B}^o$ events, respectively, and $\mathcal{N}$ is the normalization. It is given by $(\mid \mathcal{A} \mid^2 + \mid \bar{\mathcal{A}} \mid^2) \times \varepsilon$, integrated over the Dalitz plot acceptance, where ε is the detector efficiency. R_{non} and R_{res} are the ratios of non-resonant and resonant background to signal. For one case we show in Fig. 2.2 the χ^2 contours for α and correlations with the fractions of resonant and non-resonant backgrounds. The input value for α in this case was $77.3°$. The fit has no trouble picking out the correct solution.

Table 2.2 shows the results of an ensemble of fits with different assumptions on the fractions of resonant and non-resonant background, and different values of α. The one parameter fit assumes that the non-resonant and resonant background levels are determined from non-flavor tagged data, while in the three parameter fit, these are determined along with α.

These studies show that over a broad range of background models, α is determined with a sensitivity between $1.4°$-$4.3°$ in 2×10^7s of running time. The sensitivity will also depend
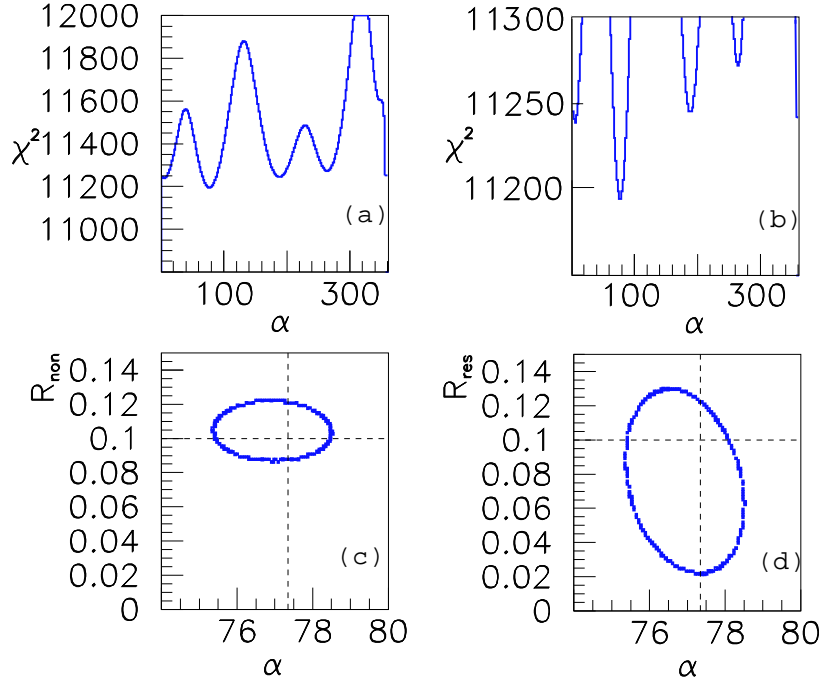
Figure 2.2: Results of a simulation using 1000 $B^o \to \rho\pi$ detected signal events with an input value of $\alpha = 77.3°$. (a) The χ^2 contours as a function of α. (b) same as (a) with the vertical scale enlarged. (c) The correlation of the best fit for α and R_{non} and (d) The correlation of the best fit for α and R_{res}.

on several unknown quantities including the branching ratio for $\rho^o\pi^o$, and the ratio of Tree to Penguin amplitudes.

2.2   Sensitivity to B_s Mixing

BTeV can definitively reach x_s values of 75 in 2×10^7 seconds of running. Put another way, it will take us only 10 days of steady running to reach x_s of 20. These estimates are based on the decay mode $B_s \to D_s^+\pi^-$, with $D_s^+ \to \phi\pi^+$ and $K^{*o}K^+$. "Definitively" is used here to express the ability to make a measurement where the best solution for a fit to the oscillation frequency is better by "5 standard deviations" than the next best fit. Thus BTeV can cover the entire range of x_s values allowed in the Standard Model.

2.3   Reach in Rare Decays

BTeV has excellent reach in rare decays. We have investigated the exclusive decays $B^o \to K^{*o}\mu^+\mu^-$, $B^+ \to K^+\mu^+\mu^-$ and the inclusive decay $B \to X_s\mu^+\mu^-$.

Table 2.2: Results of Determining α with 1000 $B^o \to \rho\pi$ Events.

α MC	Background, % Resonant.	Nonres.	$\langle\alpha\rangle$ 1 parameter	$\langle\sigma_\alpha\rangle$	$\langle\alpha\rangle$ 3 parameters	$\langle\sigma_\alpha\rangle$
77.3	0	0	77.4	1.3	77.3	1.4
	10	10	77.4	1.4	77.3	1.5
	20	20	77.2	1.5	77.2	1.6
	40	0	77.4	1.6	77.2	1.8
	0	40	77.6	1.4	77.1	1.6
93.0	0	0	92.7	1.4	92.8	1.5
	10	10	93.3	1.6	93.4	1.8
	20	20	93.1	1.7	93.3	1.9
	40	0	92.7	1.8	93.2	2.1
	0	40	92.5	1.6	93.3	1.9
111.0	0	0	111.0	1.9	111.7	2.3
	10	10	110.7	2.3	110.6	3.6
	20	20	110.9	2.7	111.7	3.9
	40	0	111.2	2.8	110.4	4.3
	0	40	110.2	2.1	111.1	4.0

We acquire $\sim$2530 $K^{*o}\mu^+\mu^-$ decays in 10^7 seconds, enough to measure the lepton-forward-backward asymmetry and test the Standard Model. Although the asymmetry is expected to be small in $K^+\mu^+\mu^-$, we test the Standard Model expectation, due to our large sample of $\sim$1300 events per year.

We also expect to be able to measure the inclusive rate $b \to s\mu^+\mu^+$ with 20σ significance. This inclusive rate is very important. It could either show non-Standard Model physics or greatly constrain alternative models.

2.4   Sensitivities in New Physics Modes

Precision studies of b decays can bring a wealth of information to bear on new physics, that probably will be crucial in sorting out anything seen at the LHC (see Chapter 1). The BTeV data samples will be large enough to test different scenarios emerging from "New Physics" at the TeV energy scale. In Table 2.3 we show the expected rates in BTeV for one year of running (10^7 s) and an e^+e^- B-factory operating at the $\Upsilon(4S)$ with a total accumulated sample of 500 fb^{-1}, about what is expected before BTeV begins running. More comparisons with e^+e^- are given in the next section.

Table 2.3: Comparison of BTeV and B-factory Yields on Different Time Scales.

Mode	BTeV ($10^7 s$)			B-factory (500 fb^{-1})		
	Yield	Tagged†	S/B	Yield	Tagged†	S/B
$B_s \to J/\psi \eta^{(\prime)}$	12650	1645	>15			
$B^- \to \phi K^-$	6325	6325	>10	700	700	4
$B^o \to \phi K_s$	1150	115	5.2	250	75	4
$B^o \to K^{*o}\mu^+\mu^-$	2530	2530	11	$\sim$50	$\sim$50	3 [3]
$B_s \to \mu^+\mu^-$	6	0.7	> 15	0		
$B_d \to \mu^+\mu^-$	1	0.1	> 10	0		
$D^{*+} \to \pi^+ D^o$; $D^o \to K^-\pi^+$	$\sim 10^8$	$\sim 10^8$	large	8×10^5	8×10^5	large

$\dagger$ Tagged here means that the initial flavor of the B is determined.

2.5 Comparison with e^+e^- B Factories

Much of what is known about b decays has been learned at e^+e^- machines [4]. Machines operating at the $\Upsilon(4S)$ found the first fully reconstructed B mesons (CLEO), B^o-$\overline{B}^o$ mixing (ARGUS), the first signal for the $b \to u$ transition (CLEO), and Penguin decays (CLEO). Lifetimes of b hadrons were first measured by experiments at PEP, slightly later at PETRA, and extended and improved by LEP [4].

The success of the $\Upsilon(4S)$ machines, CESR and DORIS, led to the construction at KEK and SLAC of two new $\Upsilon(4S)$ machines with luminosity goals in excess of 3×10^{33}cm^{-2}s^{-1}. These machines have asymmetric beam energies so they can measure time dependent CP violation. In fact, CP violation in B_d was convincingly demonstrated recently by both the BABAR and BELLE experiments [5]. These machines, however, will investigate only B^o and $B^\pm$ decays. They will not investigate B_s, B_c or Λ_b decays. While, in principle, the e^+e^- machines could run on the $\Upsilon(5S)$, which is likely to be a source of B_s mesons, there are crucial concerns that vitiate any such approach: The predicted cross-section for B_s production is only $\sim$0.1 of that of B production on the $\Upsilon(4S)$. Furthermore the proper time resolution necessary to resolve B_s oscillations cannot be obtained using the relatively slow B_s mesons produced at the $\Upsilon(5S)$

Table 2.4 shows a comparison between BTeV and an asymmetric e^+e^- machine for measuring the CP violating asymmetry in the decay mode $B^o \to \pi^+\pi^-$. The peak luminosity for the e^+e^- machines is set at 10^{34} cm^{-2}s^{-1}, a value higher that what has been achieved. The detection and tagging efficiencies are taken from Aubert et $al.$ [6]. For the B^o branching fraction we use the world average values computed in the "Physics Case" part of this document. In Table 2.5 we show a similar comparison for the final state $B^- \to \overline{D}^o K^-$, a mode that could be used to determine the CKM angle γ. It is clear that the large hadronic b production cross section can overwhelm the much smaller e^+e^- rate. Furthermore, the e^+e^- B factories do not have access to the important CP violation measurements that need to be made in B_s decays. (See Table 2.3 for more comparisons.)

Table 2.4: Number of tagged $B^o \to \pi^+\pi^-$ ($\mathcal{B}=0.45 \times 10^{-5}$).

	$\mathcal{L}(\mathrm{cm}^{-2}\mathrm{s}^{-1})$	σ	# $B^o/10^7$ s	Signal Efficiency	Tagging ϵD^2	# tagged/10^7 s
e^+e^-	10^{34}	1.1 nb	1.1×10^8	0.45	0.26	56
BTeV	2×10^{32}	100μb	1.5×10^{11}	0.021	0.1	1426

Table 2.5: Number of $B^- \to \overline{D}^o K^-$ ($\mathcal{B}=1.7 \times 10^{-7}$).

	$\mathcal{L}(\mathrm{cm}^{-2}\mathrm{s}^{-1})$	σ	# $B^-/10^7$ s	Signal Efficiency	Events/10^7 s
e^+e^-	10^{34}	1.1 nb	1.1×10^8	0.4	5
BTeV	2×10^{32}	100μb	1.5×10^{11}	0.007	176

2.5.1 Comments on Upgrades to KEK-B and PEP-II

In 2001 PEP-II and KEK-B delivered 40 fb^{-1} and 36 fb^{-1}, respectively. This corresponds to about 4×10^7 B^o mesons and 4×10^7 $B^{\mp}$ mesons produced for each experiment. The peak luminosities for both machines are about 5×10^{33}cm^{-2}s^{-1}.

KEK-B is planning on how to upgrade to a luminosity of 10^{35}cm^{-2}s^{-1}, ten times their original design using the same machine configuration, with a target date of 2007. (Much of the reference material in this section comes from the E2 Snowmass working group report [7].) However, as pointed out in the E2 report, the higher luminosity can cause problems for the detector: "Operation at 10^{35} has implications for the detector and the IR. The rates from collisions will be significantly higher which will lead to larger occupancy. Trigger rates and rates through the data acquisition system will be higher. There will be more synchrotron radiation, which will have to be removed by masking. There may be larger vacuum pressure resulting in higher background rates from Touschek scattering. There may need to be a larger crossing angle which may make it harder to shield backgrounds efficiently. The final quads may be moved closer to the IP to reduce β^*. And finally, the background at injection might be significantly worse...the first few layers of the silicon vertex detector will have high occupancy and will be replaced by pixel detectors. Beampipe heating due especially to Higher Order Modes (HOM) requires that the beam pipe be water cooled. The Central Drift Chamber is undergoing a modification in 2002 to replace the two inner layers with a small cell chamber. It is expected to be able to handle super-KEK rates. The CsI(Tl) calorimeter is slow and something may need to be done to it. The RPCs in the muon system already suffer from inefficiency due to local deadtime and will probably need to be replaced with wire chambers. The data acquisition system will also have to be upgraded."

The Super-BABAR concept requires a new machine operating in either the PEP tunnel

60

or the SLC arcs that achieves a luminosity of $10^{36}\text{cm}^{-2}\text{s}^{-1}$. According to the E2 Snowmass summary: "The goal is to be competitive with the next generation hadron collider experiments, at least in the area of B_d and B_u physics." However, in order to reach this goal, the machine must be successfully built and the detector essentially completely rebuilt to withstand the high rates and radiation load. The challenges for both the detector and the accelerator are enormous. Stu Henderson in his Snowmass summary talk said about machine: "Every parameter is pushed to the limit-many accelerator physics and technology issues [8]."

Concerning the detector, the E2 summary states: "Most of the BABAR subsystems will have to undergo some modification or replacement to handle the much higher rates of the new machine. To carry out the program, the overall performance, in terms of resolution, efficiency, and background rejection, must be similar to that of BABAR. The detector must retain its high degree of hermeticity as well.

"There are many questions about the cost and availability of suitable detector technologies which will need to be studied before the detector design can be finalized. We give four examples. (1) To maintain the vertex resolution of BABAR and withstand the radiation environment, pixels with a material budget of 0.3% X_o per layer are proposed. Traditional pixel detectors which consist of a silicon pixel array bump-bonded to a readout chip are at least 1.0% X_o. To obtain less material, monolithic pixel detectors are suggested. This technology has never been used in a particle physics experiment. (2) As a drift chamber cannot cope with the large rates and large accumulated charge, a silicon microstrip tracker has been proposed. At these low energies track parameter resolution is dominated by multiple Coulomb scattering. Silicon microstrip technology is well tested but is usually used at this energy for vertexing, not tracking. Realistic simulations need to be performed to establish if momentum resolution as good as BABAR can be achieved with the large amount of material present in the silicon tracker. If not, we suggest a TPC, possibly readout with a Gas Electron Multiplier, or MICROMEGAS, be explored as an alternative to the silicon tracker (3) There is no established crystal technology to replace the CsI(Tl). There are some candidate materials but the most attractive have not been used in a calorimeter previously. (4) There is no known technology for the light sensor for the SuperDIRC.

"Since the goal of the SuperKEK and SuperBABAR upgrades are to enable the e^+e^- machine to compete with future hadron collider experiments, it is important to make a realistic evaluation of the sensitivities of all these experiments over a wide range of final states. Such projections are, of course, somewhat uncertain. The sensitivities of future hadron collider experiments have been determined from detailed and sophisticated simulations of signals and backgrounds. As these simulations are an approximation to reality, the performance of LHCb and BTeV may be somewhat better or somewhat worse than the simulations predict. Projections for SuperBABAR are, at this point, mainly done by scaling from BABAR experience assuming that the new detector, which still has many open R&D issues, will achieve the same efficiency that BABAR now achieves even though the luminosity will be a factor of 300 higher. More realistic studies need to be performed before a full comparison between SuperBABAR and the hadron collider experiments is made. With these caveats a compari-

Table 2.6: Comparison of CP Reach of Hadron Collider Experiments and SuperBABAR. The last column is a prediction of which kind of facility will make the dominant contribution to each physics measurement. (From the E2 summary [7].)

	BTeV[†] 10^7s	LHCb 10^7s	BABAR Belle (2005)	e^+e^- 10^{35} 10^7s	e^+e^- 10^{36} 10^7s	e^+e^- at 10^{36} vs hadron collider
$\sin 2\beta$	0.017	0.02	0.037	0.026	0.008	Equal
$\sin 2\alpha$	0.05	0.05	0.14	0.1	0.032	Equal
$\gamma [B_s(D_sK)]$	$\sim 11.5^o$					Had
$\gamma [B(DK)]$	$\sim 13.2^o$		$\sim 20^o$		12°	Equal
$\sin 2\chi$	0.024	0.04	-	-	-	Had
$\mathcal{B}(B \to \pi^o\pi^o)$	-	-	$\sim 20\%$	14 %	6%	e^+e^-
V_{ub}	-	-	$\sim 2.3\%$	$\sim 1\%$ (sys)	$\sim 1\%$ (sys)	e^+e^-

† We have changed the BTeV numbers to correspond to the one-arm version.

son of BTeV, LHCb, BABAR and Belle in 2005, and the e^+e^- machines at 10^{35} and 10^{36} is given in Table 2.6 for several states of importance to the study of *CP* violation in *B* decays."

This study indeed demonstrates that it will take a $10^{36} cm^{-2}s^{-1}$ e^+e^- collider operating at the $\Upsilon(4S)$ to match the performance of BTeV on B^o and $B^\mp$ mesons, while there will be no competition for the B_s or other b-flavored hadrons. There are serious technical problems that both the machine and the detector would need to surmount. We believe the cost will far exceed that of BTeV. The HEPAP subpanel in their report [9] mentions a 500 M$ number for the detector. That cost has not been subject to review.

We note that the LHCb sensitivity for $\sin 2\alpha$ is quoted as 0.05, the same as BTeV even though BTeV gathers twice as many events and has a much better signal to background (see section 2.7.2). This LHCb number comes from P. Ball *et al.* [10] where these caveats are included: "It should be stressed that the fitting studies are preliminary and are optimistic in the fact that the exact LHCb acceptance has not been used and the backgrounds have not been included..."

2.6   Comparison with CDF, D0, CMS, and ATLAS

Both CDF and D0 have measured the *b* production cross section [11]. CDF has contributed to our knowledge of *b* decay mostly by its measurements of the lifetime of *b*-flavored hadrons [12], which are competitive with those of LEP [13] and recently through its discovery of the B_c meson [14]. CDF also saw the first hint for CP violation in the *b* system [15]. These detectors were designed for physics discoveries at large transverse momentum. It is remarkable that they have been able to accomplish so much in *b* physics. They have shown that it is possible to do *b* physics in the environment of a hadron collider.

However, these detectors, and the new central detectors ATLAS and CMS are very far from optimal for b physics. BTeV has been designed with b physics as its primary goal. To have an efficient trigger based on separation of b decays from the primary, BTeV uses the large $|\eta|$ region where the b's are boosted. The detached vertex trigger allows collection with very high efficiency of interesting purely hadronic final states such as $\pi^+\pi^-$, $\rho\pi$, $D_s^+\pi^-$ and $D_s^+K^-$. It is also efficient on an eclectic mixture of all b decays and is therefore open to decays which may not be considered "interesting" now or at the time of data taking, but may become so as our knowledge improves. It also allows us to collect enough charm to investigate charm mixing and CP violation.

The use of the forward geometry also allows for excellent charged hadron identification over a wide momentum range, with a gaseous RICH detector. This is crucial for many physics issues such as separating $K\pi$ from $\pi\pi$, $D_s\pi$ from D_sK, kaon flavor tagging, etc.

Furthermore an experiment that plans on answering all the open questions in b physics, requires a high quality electromagnetic calorimeter. Installation of such a calorimeter in the CLEO detector made new physics vistas possible and such a device in BTeV allows for the measurement of several crucial final states such as $B^o \rightarrow \rho\pi$, and $B_s \rightarrow J/\psi\eta'$. The only central detector that is planning to have a high quality electromagnetic calorimeter is CMS.

Finally, BTeV has all the crucial elements required to study any newly suggested b or charm process or uncover new physics. The crucial elements are:

- a detached vertex algorithm in the first trigger level,

- highly efficient particle identification across the entire momentum range with good ($\approx$ 100:1) background rejection,

- an electromagnetic calorimeter with sufficiently good energy resolution and efficiency to fully reconstruct rare B decay final states with single photons or neutral pions.

BTeV will have a physics reach substantially beyond that of CDF, D0, CMS, and ATLAS. The sensitivities of CDF and D0 are summarized in Anikeev et $al.$ [16] and those of CMS and ATLAS in Ball et $al.$ [10].

2.7   Comparison with LHCb

2.7.1   General Comparisons

LHCb [17] is an experiment planned for the LHC with almost the same physics goals as BTeV. Here we show how BTeV can compete with LHCb in many areas and why it is a superior experiment in some very important areas. Both experiments intend to run at a luminosity of 2×10^{32} cm^{-2}s^{-1}. There are several inherent advantages and disadvantages that LHCb has compared with BTeV. The issues that favor LHCb are:

- The b production cross-section is expected to be about five times larger at the LHC than at the Tevatron, while the total cross-section is only 1.6 times as large.

- The mean number of interactions per bunch crossing is expected to be about 3 times lower at the LHC than at the Tevatron.

The issues that favor BTeV are:

- The seven times larger beam energy at the LHC makes the momentum range of particles that need to be tracked and identified much larger and therefore more difficult. The larger energy also causes a large increase in track multiplicity per event, which makes pattern recognition and triggering more difficult.

- The interaction region at the Tevatron is three to six times longer along the beam direction than at LHC ($\sigma_z = 5$ cm), which allows BTeV to be able to accept collisions with a mean of two interactions per crossing, since the interactions are well separated in z. LHCb plans to veto crossings with more than one interaction.

- The short bunch spacing at the LHC, 25 ns, has serious negative effects on all their detector subsystems. There are occupancy problems if the sub-detector integration times are long. This can be avoided by having short integration times, but that markedly increases the electronics noise. For example, in a silicon detector these considerations make first level detached vertex triggering more difficult than at the Tevatron; BTeV has a more relaxed 132 ns bunch spacing, 5.3 times longer. In fact, the current plan of LHCb is to trigger in their first trigger level on muons, electrons or hadrons of moderate p_t, and detect detached vertices in the next trigger level.

- BTeV is designed to have the vertex detector in the magnetic field, thus allowing the rejection of low momentum tracks at the trigger level. Low momentum tracks are more susceptible to multiple scattering which can cause false detached vertices leading to poor background rejection in the trigger.

- BTeV is designed with a high quality $PbWO_4$ electromagnetic calorimeter, that provides high resolution and acceptance for interesting final states with γ's, π^o's, and $\eta^{(\prime)}$'s. The BTeV electromagnetic calorimeter is superior in energy resolution and segmentation to LHCb's. LHCb has a Shaslik-style Pb-scintillating fiber device, following a preshower detector. The LHCb energy resolution is $10\%/\sqrt{E} \oplus 1.5\%$, which compares poorly with BTeV's $1.7\%/\sqrt{E} \oplus 0.55\%$. The LHCb detector segmentation is 4 cm $\times$ 4 cm up to ~90 mr, 8 cm $\times$ 8 cm to ~160 mr and 16 cm $\times$ 16 cm at larger angles. (The distance to the interaction point is 12.4 m.) Thus the segmentation is comparable to BTeV only in the inner region. (BTeV has 2.8 cm $\times$ 2.8 cm crystals 7.4 m from the center of the interaction region.)

- Use of a detached vertex trigger at Level 1 allows for an extensive charm physics program absent in LHCb. It also accepts a more general collection of b events, which are less oriented towards particular final states.

- The LHCb data acquisition system is designed to output 200 Hz of b decays, while BTeV is designed for larger output bandwidth of 1,000 Hz of b's and 1,000 Hz of charm, and an additional 2000 Hz for contingency, calibration events, and other physics. Therefore, BTeV has access to a much wider range of heavy quark decays.

We have compensated for LHCb's initial advantages in b cross-section due their higher center-of-mass energy. In fact, the high energy actually works in many ways as a disadvantage. For example, LHCb needs two RICH counters to cover the momentum range in their one arm. Particle identification and other considerations force LHCb to be longer than BTeV. Its single arm is twice as long as one of BTeV arms. As a result, LHCb's transverse size is twice that of BTeV (linear dimension), in order to cover the same solid angle. It is expensive to instrument all of this real estate with high quality particle detectors. Thus, the total cost for LHCb based only on instrumented area, (a naive assumption) would be four times the total cost for BTeV.

We have done a detailed comparison between BTeV and LHCb using two modes of great importance because they give direct determinations of the CP violating angles α and γ, and report our results here.

2.7.2   A Specific Comparison: $B^o \to \rho\pi$

We base our comparison on the total number of untagged events quoted by both experiments. The BTeV numbers come from Part III of this document. The LHCb numbers are found in their Technical Design Report [17]. Both sets of numbers are calculated for 10^7 seconds at a luminosity of 2×10^{32} cm^{-2}s^{-1}. We have corrected the LHCb numbers by normalizing them to the branching ratios used by BTeV. In Table 2.7 we compare the relevant quantities [18].

Table 2.7: Event yields and signal/background for $B^o \to \rho\pi$.

Mode	Branching Ratio	BTeV		LHCb	
		Yield	S/B	Yield	S/B
$B^o \to \rho^{\pm}\pi^{\mp}$	2.8×10^{-5}	5400	4.1	2140	0.8
$B^o \to \rho^o\pi^0$	0.5×10^{-5}	776	0.3	880	-

LHCb has done a background estimate based on a heavily preselected sample of events [19]. These include:

- a preselection for charged pions and photons which required the momentum or energy to exceed a value depending on the polar angle of the candidate. For charged pions, the momentum cut varied between 1 and 2 GeV/c and for photons the energy cut varied between 2 and 6 GeV;

- selection of signal-like events based on a discriminant variable built from kinematic variables of the π, ρ and B^o;

- selection based on the reconstructed secondary vertex for a $\pi^+\pi^-$ combination; and

- Dalitz plot cuts to eliminate low energy π^o combinatorial background due to particles from the primary vertex.

These cuts are applied to the generator event sample before the events are processed through GEANT [20]. The BTeV simulation was carried out without any preselection cuts. We were worried that the preselection would bias us to lower background rates. For example, if two photons overlapped or interactions of charged tracks put energy into photon clusters these can well become part of our background sample. Thus the LHCb background estimate may well be only a lower limit.

We note that their π^o mass resolution varies between 5 and 10 MeV/c^2 (r.m.s.) and their B^o mass resolution is 50 MeV/c^2 (r.m.s.). The corresponding numbers for BTeV are 3.1 MeV/c^2 and 28 MeV/c^2.

With this analysis, LHCb claims signal/background (S/B) of 1.3 for $\rho^\pm\pi^\mp$, where they have assumed a branching ratio of 4.4×10^{-5}. For our assumed branching ratio, S/B is 0.8; The S/B for BTeV is 4.1. Furthermore, the BTeV background analysis was done without preselection and therefore is likely to be more realistic. For the final state $\rho^o\pi^o$ LHCb has not produced a background estimate; in our experience it is difficult to estimate signal efficiencies without evaluating how restrictive the selection criteria need to be to reduce backgrounds.

It is not surprising that BTeV's superior crystal calorimeter and detached vertex trigger produce a large advantage in this final state over LHCb, even using LHCb's optimistic numbers. BTeV has a factor of 2.2 advantage in signal yield in $\rho^\pm\pi^\mp$ and a better S/B by a factor of 5. This results in an advantage to BTeV in the number of "effective events" (events weighted by dilution due to background) of almost a factor of 4.

2.7.3 $B_s \to D_s^\pm K^\mp$

A comparison of the estimated total efficiencies (excluding D_s decay branching ratios), B_s mass resolutions, and S:B ratios are given in Table 2.8. Here $D_s^+ \to K^+K^-\pi^+$ can be reconstructed via either $\phi\pi^+$ or $K^{*o}K^-$. Here BTeV and LHCb differ somewhat. LHCb has the same efficiency in both modes, whereas BTeV analyzes them somewhat differently. For $K^{*o}K^-$ BTeV requires both charged kaons to hit the RICH detector, while for $\phi\pi^+$ only one charged kaon is required to be identified in the RICH. (The reconstruction efficiency for $\phi\pi^+$ is 2.3%, while for $K^{*o}K^-$ it is 1.3%).

Table 2.8: Comparison of BTeV and LHCb sensitivities for $B_s \to D_s^\pm K^\mp$.

Branching Ratio	BTeV		LHCb	
	Yield	S/B	Yield	S/B
3×10^{-4}	7,530	7	7,660	7

The yields and signal/background are about the same in this mode. This is not unexpected. The LHCb trigger efficiency is 4.1 times lower than BTeV and the acceptances are about equal. This factor of 4 should neutralize the LHCb cross-section advantage, of a factor of 5, and in this study it has.

2.8   Summary

BTeV is far superior to current e^+e^- colliders operating on the $\Upsilon(4S)$ because of the enormous difference in the b rate. For reconstructed B^+ and B^o decays, BTeV has a factor of $\sim$200 more rate. Furthermore, the important B_s physics cannot be done at the e^+e^- machines. A luminosity on the order of $10^{36}\mathrm{cm}^{-2}\mathrm{s}^{-1}$ would need to be achieved before these machines would be competitive in B^o and $B^\pm$ physics with BTeV.

CDF, D0, CMS, and ATLAS cannot compete in areas where particle identification or photon detection are important; as a result, the b-physics reach of BTeV is substantially greater.

BTeV is competitive with LHCb in 'high-priority' final states with all charged particles. For final states with γ's, π^o's, η's or η''s, BTeV has a factor of $\approx$3.5 advantage. Furthermore, BTeV will write to tape a factor of 5 more b events than LHCb, allowing for more physics studies.

BTeV has all the components necessary to measure the most important quantities in heavy quark decays. These include spectacular vertex detection, triggering, particle identification, photon detection, and electron and muon identification. It is of crucial importance the decay time resolution in BTeV is about 45 fs, for most final states, which compares most favorably to the 900 fs in asymmetric e^+e^- colliders. The studies presented here were done on what is currently believed to be the most important modes. What's in fashion, however, changes. BTeV is a powerful enough detector to be able to test new and interesting ideas for all b species.

2.9 Appendix I: Update of Lepton Identification Techniques

In the proposal muon identification was taken from the muon detector alone and electron identification was ignored. In this update we now include muon and electron from the RICH detector and electron identification in the calorimeter.

Though it might seem that the mass difference between muons and pions is too small to provide useful separation using a Cherenkov based detector, because the Cherenkov angle goes as $(\cos\beta)^{-1}$, in fact there is significant separation over an interesting part of the momentum spectrum. More importantly, the RICH detector subtends a significantly larger solid angle than either the muon detector or the EM calorimeter.

Fig. 2.3 (left) shows the Cherenkov angle for different particle species as a function of momentum. The RICH angular resolution per track is expected to be 0.1 mr, as determined by a full simulation. In Fig. 2.3 (right) we have divided the difference in Cherenkov angles by the angular resolution.
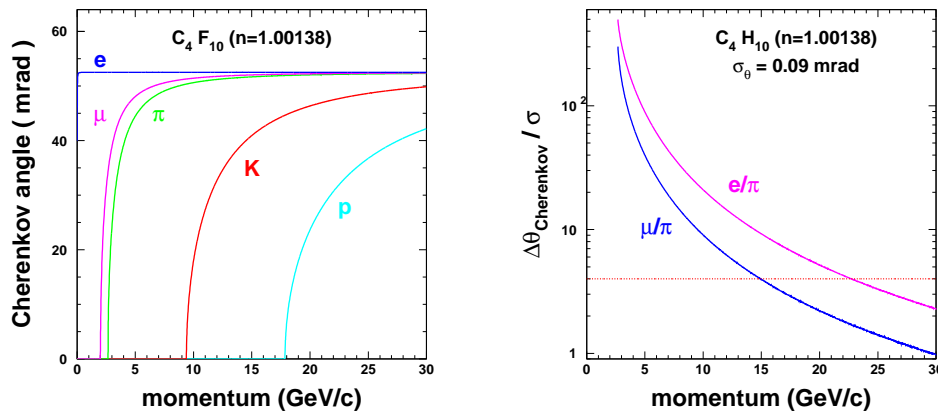
Figure 2.3: (left) The Cherenkov angle for the various particle species as a function of momentum. (right) The number of standard deviation separation for μ/π and e/π as a function of momentum. The dashed horizontal line is drawn at "4σ" separation.

To make a conservative estimate of the useful range of lepton identification from the RICH we require 4σ separation, i.e. the ratio of the difference in Cherenkov angles to the resolution be 4 or greater. For a 4σ separation requirement, the RICH detector can distinguish between muons and pions with momenta up to 15 GeV/c, and between electrons and pions up to 23 GeV/c.

To quantify our efficiency estimates we use the $B^o \to J/\psi K_s$, $J/\psi \to \ell^+\ell^-$ mode, because this is a bench mark mode. The J/ψ can be reconstructed both in the $\mu^+\mu^-$, and the e^+e^- modes. To illustrate the coverage of BTeV for lepton identification, we simulated only $\mu^+\mu^-$ mode; the e^+e^- mode is similar except for bremsstrallung, which we have ignored for now.

Figure 2.4 shows the polar angle distribution of the muons at the J/ψ decay vertex versus their momentum. Also shown are rough estimations of the angular coverage of the three detectors. Tracks at large angles, that are beyond detection in some systems, are at mostly lower energies. A significant number of high momentum tracks are not detected in the muon system because they have small angles. In this plot, each track passes a quality selection defined by requiring more than 20 hits, at least 4 of which must be in the pixel detector.
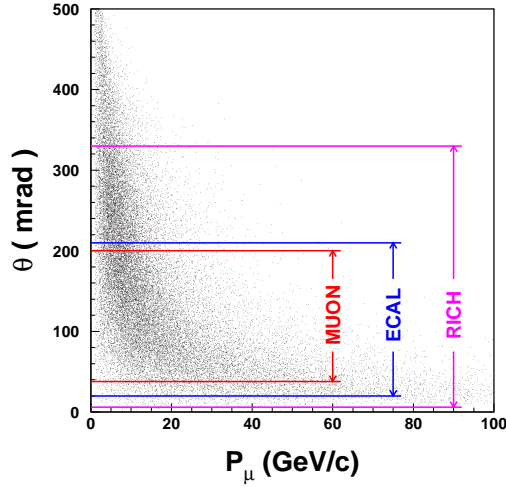
Figure 2.4: The momentum of muons from J/ψ decay versus their laboratory production angle. The lines indicate the geometric acceptance of the indicated detector elements in the absence of a magnetic field taking the origin as the center of the magnet ($z{=}0$).

For good tracks, the RICH detector has an acceptance of 95% for ±300 mr; the 5% loss results from magnetic field bending, the spread of the primary interaction position in z, and our requirement that the track be at least 10 cm within the aperture, a conservative requirement imposed to ensure that every track has a full Cherenkov ring. The ECAL detector has smaller angular coverage and the resulting acceptance is only about 66%.

The MUON detector also covers a smaller than ideal solid angle and has a relatively big hole around beam line. It also cannot detect tracks below 5 GeV/c The total acceptance is 48%. The missing tracks in MUON and ECAL are dominated by lower energy tracks at large polar angles. It is just these tracks that the RICH is capable of identifying.

We assume that the MUON detector has 100% identification efficiency within the acceptance. For ECAL, we use the efficiency curve as function of radius from $B^o \to K^*\gamma$ simulation (Figure 7.6 in the BTeV proposal). For RICH detector, we assume it has 100% efficiency in identifying muons between 2 GeV/c and 15 GeV/c, and electrons below 22.7 GeV/c. Although the RICH can still provide identification at somewhat higher momenta, for simplicity we just assume the efficiency is zero.

Different methods have been used to reconstruct $J/\psi \to \mu^+\mu^-$ in the proposal. One method is to simply identify both muons. This has an advantage of reducing backgrounds but can have low efficiency. (This method was used in the proposal for the $J/\psi K_s$ final state.) Another method is to require good muon identification for only one of the two muon tracks from a two-track detached vertex. (This method was used for the $J/\psi \eta^{(\prime)}$ studies.) Listed in Table 2.9 are J/ψ reconstruction efficiencies for different muon identification methods for the two J/ψ detection methods. Adding the RICH increases the efficiency by 19% when only one of two tracks is required to be a muon and a whopping 96% when both tracks are required to be identified. Using the RICH and MUON systems the difference between identifying one or two leptons is not as large, between 71% and 96%.

Table 2.9: Lepton identification efficiency for $J/\psi \to \mu^+\mu^-$.

	muon identification	
	single track	both tracks
MUON only	80.6 %	36.4%
MUON + RICH	96.0%	71.3%
Ratio	1.19	1.96

Although electron identification efficiency in ECAL is about 80% at large radii, the efficiency is much less at small radii where the density of tracks is high. The identification efficiency of $J/\psi \to e^+e^-$ is quite small using only ECAL identification as shown in Table 2.10. The RICH detector boosts the efficiency by 37% in the case where only one identified track is required. When both tracks are required to be identified, it boosts the efficiency by a factor of 3.

Table 2.10: Lepton identification efficiency for $J/\psi \to e^+e^-$.

	electron identification	
	single track	both tracks
ECAL only	69.3 %	21.6%
ECAL + RICH	94.9%	67.5%
Ratio	1.37	3.12

For lack of space in the hall the MUON detector is smaller than we like. For lack of money the ECAL is also smaller. However, the identification of muons and electrons is brought back to essentially full acceptance by use of the RICH. In summary, for dilepton final states, using both electrons and muons we increase the efficiency from the proposal by a factor of 2.4, for single lepton identification and 3.9 when positive identification of both leptons is insisted on.

2.10 Appendix II: Update on Flavor Tagging

2.10.1 Flavor Tagging Summary

Flavor tagging, determination of the flavor of the signal B hadron at the time of its production, is an essential component of the study of mixing and CP violation in B decays. It is also an area in which considerable sophistication is required. At the time of our proposal, we used a relatively simple approach. We have now completed a new study of the effective tagging power for B^o and B_s. These results, which will be discussed briefly here, supersede those presented in the May 2000 BTeV proposal. A complete discussion is available at *http://www-btev.fnal.gov/tagging.ps.*

We wish to optimize the flavor tagging "power", given by ϵD^2, where ϵ is the efficiency for obtaining a flavor tag and D is the dilution.

$$\epsilon = \frac{N_R + N_W}{\text{Total}}, \qquad D = \frac{(N_R - N_W)}{(N_R + N_W)}, \tag{2.1}$$

where N_R and N_W are the number of correct and incorrect tags, respectively, and "Total" refers to the sample of fully reconstructed neutral B mesons in the mode of interest.

The determination of the flavor tagging ϵD^2 takes advantage of the precision tracking provided by the pixel detector and excellent particle identification afforded by the RICH. We have studied the performance of the BTeV detector using four quasi-independent flavor-tagging methods. They are:

- Same Side Tagging (Kaon for B_s and Pion for B^o)

- Away Side Kaon Tagging

- Away Side Lepton Tagging

- Jet Charge Tag

Same Side Tagging algorithms utilize the correlation which emerges between a neutral B meson, called B_{CP} here, and the charge of nearby tracks produced in the fragmentation chain. Because these tracks are produced in the fragmentation of the b quark (not the decay), same side tag candidates emerge from the primary interaction vertex.

First let us discuss B_s tagging. When a B_s ($\overline{b}s$) forms, an extra $\overline{s}$ is available to form a K meson. About half of the time, it will produce a K^+ (the other half being K^0, which is not useful) which is 100% correlated with the flavor of the B_s at production. One nice feature of this tag is that it is not affected by the mixing of the tagging b, as in away side tagging.

For B^o mesons, the same analysis holds, except the particle tag is a charged pion. Unfortunately, there are a large number of charged pions from the interaction vertex, and hence the pion tag will have lower dilution than the kaon tag used for B_s. However, pion rates are somewhat enhanced because of the presence of B^{**} resonances. About $\sim$23% of B^o mesons

come from B^{**} [21], where the B^{**} decays into either a B^{*o} or B^o by emission of a single pion. Because of isospin, 2/3 of these are charged.

Away Side Tagging exploits the fact that in the strong interaction, b quarks are produced in pairs, and therefore the second (away side) b-quark in the event must have opposite flavor to B_{CP}. Therefore tagging the flavor of the away side b quark at production is a clean tag of the flavor of B_{CP}. Generally, this is done by examining the charge of kaons or leptons from the away side b-hadron decay or the charge of its associated jet. Since these particles come from the decay of the away side b hadron, away flavor tag algorithms usually exclude tracks which point back to the primary vertex. Because we examine the decay products, this method of flavor tagging is affected by mixing of the away side b. About 20% (50%) of B^o (B_s) mesons on the away side mix before decaying, and there are other factors that reduce the dilution. Away Side Kaon Tags exploit the fact that the away side b hadron usually undergoes the cascade $b \to c \to s$, of which half of these produce a K^-. Backgrounds which produce a K^+ include mixing, D_S decays, ϕ decays, etc. Despite these factors, the away side kaon tag has a very large dilution, as will be shown later.

Away Side Lepton tags are also useful. However, unlike the nearly 50% branching ratio for $\overline{B} \to K^- X$, the branching ratio of $b \to \ell^- X$ is about 10% each for electrons and muons. Lepton tags also have lower dilution than away side kaon tags because of the wrong sign leptons tags which arise from $b \to c \to \ell^+ X$. In the rest frame of the decaying b hadron, there is very nice kinematic separation between leptons from bottom and charm decays. However, without knowing the three momentum of the decaying b hadron, the separation is less effective. Nevertheless, leptons from b-hadron decay generally have significantly higher transverse momentum than those from charm, and this can be used to reduce the charm contamination. From the viewpoint of lepton production, electrons and muons should be nearly equally useful in flavor tagging. However, use of electrons for flavor tagging requires more sophistication in order to reject the large background from photon conversions (this problem clearly improves at large transverse momentum). We therefore will discuss in detail the away side muon tagging, and assume we can get about half the performance from the away side electron tags.

The idea behind the Jet Charge Tag is to reconstruct the location and decay products of the $b \to cW^-$ vertex. The particles associated with the W^- decay have a charge which is 100% correlated with the flavor of the parent b hadron. If we can reconstruct all the charged particles from the W decay, we would have a very clean flavor tag. As with other methods, the effectiveness of the jet charge tag is reduced, mainly by two factors. First, we do not reconstruct all the charged tracks from the W decay. Second, the charm decay vertex is often too close to the B decay vertex to separate the two vertices, resulting in a vertex that contains decay tracks from both the bottom and charm decay. Nevertheless, the jet charge algorithm does provide useful flavor tagging power. For all these tagging methods, except for jet charge and same side pion tags, excellent particle identification is required. Because there are ∼6-8 times as many pions as kaons in the momentum range of interest, excellent K/π separation is essential. Despite the proton/kaon ratio being less than one, substantial gains can be achieved with effective p/K separation.

2.10.2   Simulation and Event Selection

Two event samples are used in this analysis, both generated Pythia. For B_s, a sample of $B_s \to J/\psi K^{*0} \to \mu^+\mu^- K^+\pi^-$ events were generated. For B^o, a sample of $B^o \to J/\psi K_S^0 \to \mu^+\mu^-\pi^+\pi^-$ were generated. For the latter sample, we modified the default Pythia parameters in order to produce B^{**}'s which are not normally produced [22]. For both B_s and B^o, we include the effects of mixing. Long-lived particles were decayed using the QQ package [23]. The events were then passed through the *mcfast* detector simulation with a geometry that describes the BTeV detector components. The detector simulation includes the effects of secondary interactions, multiple scattering, conversions, decays in flight and energy loss in material.

Events which had a fully reconstructed B_{CP} (B_s or B^o) hadron were passed on to the flavor tagging analysis. To be considered for a kaon or lepton tag, tracks were required to have at least 4 pixel hits and at least three three-dimensional hits in the downstream tracking chambers. In addition, tracks were required to be within the acceptance of the RICH. To be considered for the same side tag analysis, a track was required to have D/ σ < 3 [24]. For the away side analysis, kaon candidate tracks were required to have D/σ >3, but muon candidates were not subject to this requirement.

2.10.3 B_s Flavor Tagging

Here, we discuss in some detail the B_s analysis, using all four tagging methods described above. Later, we give a briefer description of the B^o analysis which focuses on the differences with the B_s analysis.

2.10.3.1   Same Side Kaon Tag

One important task is to make sure that the tagging particle is indeed a kaon. The C_4F_{10} gas radiator section of the RICH has outstanding K/π discrimination over this momentum range so pion contamination is negligible. To discriminate against proton background, we use both the liquid and gas radiator sections of the RICH and require that

1. The track is in acceptance of the RICH system.

2. If p $\leq$ 3 GeV/c, the track must be inside the active area of the liquid radiator.

3. If p $\leq$ 9.5 GeV/c and the candidate is in the liquid radiator acceptance, there must be at least two reconstructed photons for the kaon hypothesis from the liquid radiator.

4. If 9.5 < p $\leq$ 10.5 GeV/c, the kaon hypothesis must have a non-zero likelihood determined by the gas system.

5. For p > 10.5 GeV/c, there must be at least 5 reconstructed photons from the gas radiator for the kaon hypothesis.

We use the particle ID likelihoods to form signal and background distributions of $\Delta\chi^2 = -2 \times log(L_{pr}/L_{ka})$, where L_{pr} and L_{ka} are the likelihoods for the proton and kaon hypotheses respectively.

There are several sources of background kaons that cause errors in determining the flavor. We have found three relatively uncorrelated kinematic variables which have some power to discriminate the fragmentation kaons we want to use from other sources of kaons. These variables are:

- $\Delta\phi$, the difference in azimuthal angle between the reconstructed B_s and the kaon candidate,

- $\Delta\eta$, the difference in pseudorapidity between the B_s and the kaon candidate, and

- Q, the difference in invariant mass between the B_s + kaon candidate and the B_s itself.

Since each event may contain multiple kaon candidates, we need a method by which to determine an "event charge" associated with the same side kaon, which in turn determines the flavor of the B_s. This is done in the following manner. For each kaon candidate in an event, we calculate the signal probability (P_{sig}) and background probability (P_{bak}), determined from Monte Carlo. Each of these is given by a product of probabilities from the signal and background distributions in $\Delta\phi$, $\Delta\eta$, Q and $\Delta\chi^2$. We then define a discriminant, X_{tag} given by:

$$X_{tag} = \frac{1 - \prod_{i=1}^{4}(P_{sig}^i/P_{bak}^i)}{1 + \prod_{i=1}^{4}(P_{sig}^i/P_{bak}^i)}$$

The index i runs over the four input variables. By definition, $-1 \leq X_{tag} \leq 1$. Signal kaons peak at low values of X_{tag} and background kaons tend to be flat or peak toward positive values of X_{tag}. We select kaon candidates with $X_{tag} < X_{cut}$, where X_{cut} is between -1 and 1. In Fig. 2.5 we show the distribution in X_{tag}. A clear peak toward negative values for signal kaons is evident, and the background is nearly flat. The spike at $X_{tag} = 1$ consists of protons which have low probability for being a kaon.

For a given cut on X_{tag}, we divide the sample into events in which the event weighted charge gives the correct B_s flavor (N_R), and the incorrect flavor (N_W). We compute the efficiency as the sum of N_R+N_W divided by the total reconstructed B_s sample and dilution according to equation 2.1. We find that the maximum tagging power is obtained for a cut on $X_{tag} < -0.2$ for which $\epsilon D^2 = 5.7\%$, with a corresponding efficiency of 36% and a dilution of 40%.

2.10.3.2 Away Side Kaon Tagging

As discussed above, Away Side Kaon Tags rely on detecting the kaon associated with the $b \rightarrow c \rightarrow s$ cascade which produces a charged kaon about half the time. Because the away side kaon tag is a high purity sample for flavor tagging, proton contamination must be minimized using the RICH information. The tagging method follows much of the same formalism as
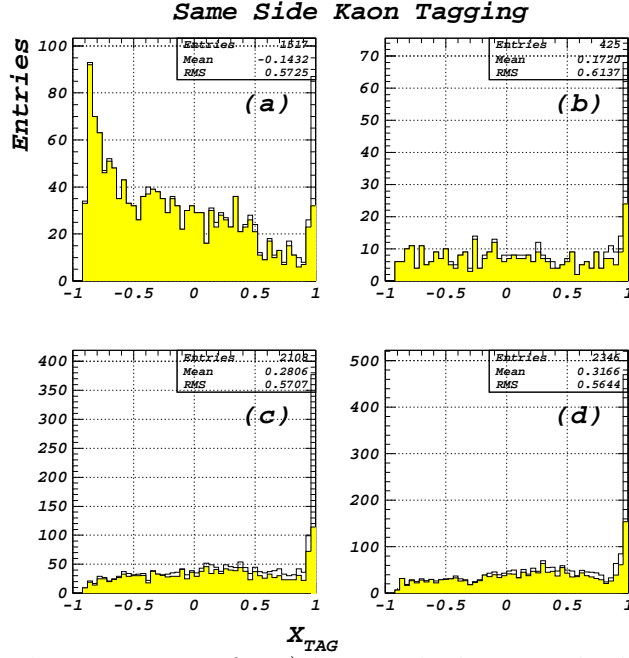
Figure 2.5: The distribution in X_{tag} for a) kaons which correctly determine the B_s flavor and are part of the B_s fragmentation, (b) kaons which incorrectly determine the B_s flavor and are part of the B_s fragmentation, (c) kaons which correctly determine the B_s flavor but are not part of the B_s fragmentation, (b) kaons which incorrectly determine the B_s flavor and are not part of the B_s fragmentation. The unfilled histogram shows the distribution for all kaon candidates and the shaded histogram shows the distribution for true kaons.

the same side kaon tag analysis, except that the track is required to have $D/\sigma > 3$. We also require that the impact parameter to the primary vertex is less than 2 mm which is $\sim 97\%$ efficient for particles from b-hadron decay. Furthermore, we use only the $\Delta\phi$ and $\Delta\chi^2$ information in our discriminant, since there is little or no correlation in $\Delta\eta$ and Q of the away side kaon candidate with the reconstructed B_s.

Kaons which give the wrong flavor tag are mostly due to B mixing, D_s, and ϕ decays. The wrong sign kaons are about 25% of the right sign. This source of tagging dilution is unavoidable, since it is from genuine B decays. There is also a contamination from protons, which is significant because of the non-negligible rate for $B \to p/\overline{p}$ ($\sim 8\%$). The particle identification information from the RICH can eliminate the false tags due to protons.

Using the same procedure as described for the same side tags, we form an event charge, and categorize events according to whether the event charge gives the correct or the incorrect flavor for the B_s. As expected, we do not gain much by making a tight requirement on X_{tag} since the background is largely from wrong sign kaons from B decays which have a similar shape in X_{tag} to right sign kaons. However, some events have multiple kaon candidates, so the charge weighting procedure is useful. We achieve an $\epsilon D^2 = 5.8\%$, corresponding to $\epsilon \sim 16.5\%$ and $D \sim 59\%$.

2.10.3.3   Away Side Muon Tagging

The Away Side Muon Tagging follows the same procedure as the away side kaon tagging, except we remove the requirement that the muon have $D/\sigma < 3$, since we expect the prompt muon background in events with a reconstructed b hadron to be small. We assume perfect muon identification using the RICH and muon systems. Decays in flight are modeled in

our simulation, but they generally have much larger impact parameter than muons from B decay, and hence do not have pixel and/or downstream tracks. For muon tags, the correct flavor tag is mainly from the $\overline{B} \to \mu^- X$ decay. A small fraction of right sign tags come from $D \to \mu^- X$ where the B^o has mixed. B mixing and leptons from the semileptonic decay of charm constitute the main source of wrong sign muons. Because of the latter, we expect the dilution to be worse for away side muon tags than away side kaon tags. In addition, the branching fraction for $B \to \mu^{\pm} X$ (including $b \to c \to \mu X$) is about 40% of $B \to K^{\pm} X$.

The right sign muons, from $B \to \mu X$, have a much stiffer P_T distribution than do the wrong sign, predominantly from $D \to \mu X$. In this analysis, there is a cut on the transverse momentum of the muon at 0.4 GeV/c to reduce the $D \to \mu X$ background . We also find that the acceptance for B muons ($\sim$60%) is larger than D muons ($\sim$37%), mainly due to the stiffer momentum spectrum for B muons. Non-b decay related backgrounds are negligible.

Just as with the away side kaon tags, an event charge is computed, although only 3% of the events have two reconstructed muons. However, one observes that since most wrong sign muons are from a B-related charm daughter, the maximum value of the tagging power is achieved by not making any cut on X_{tag}. Therefore, the results are essentially identical to having simply counted the number of right sign and wrong sign muons. With no requirement on X_{tag} we obtain an efficiency, $\epsilon = 8\%$, a dilution $D = 40\%$, and $\epsilon D^2 = 1.3\%$.

We have not carried out the more complicated study of Away Side Lepton Tagging using electrons/positrons, but plan to do so soon.

2.10.3.4 Jet Charge Tagging

Jet charge tagging has been successfully used in hadron collider experiments [25]. The philosophy behind the jet charge is to reconstruct the tracks associated with the W decay in $b \to W^{\pm} c$ for the away side b hadron. The total charge of the tracks associated with the W give the flavor of the decaying b hadron, and hence of B_{CP}.

First, we utilize only charged tracks with $D/\sigma > 3$ and $D < 5$ mm (i.e., "secondary tracks") to search for displaced (or secondary) vertices. Because of the high purity of secondary kaons and muons, they are only required to have a $P_T > 0.1$ GeV/c, whereas all other particles are required to have $P_T > 0.2$ GeV/c. The procedure loops over all track pairs, and fits them to a common vertex. If the χ^2 probability is greater than 1%, the vertex is kept. The algorithm then attempts to attach other tracks which have $D/\sigma < 2.5$ with respect to the candidate decay vertex. If the addition of the track results in a $\chi^2/dof < 2.5$ for the vertex fit, the track list for the vertex is updated and the new vertex parameters stored. The process continues until all track pairs have been used as "seed tracks" for a vertex. This is done to avoid order dependence of the vertexing. As new vertices are formed, they are compared to the existing ones, and duplicates are removed. If no vertex is found, we take the highest P_T secondary track, as long as $P_T > 1$ GeV/c. For each secondary vertex, we compute the jet charge (JETQ), defined as:

$$JETQ = \frac{\sum r_i(P_T)(p_i \cdot \hat{n})^k \times Q_i}{\sum r_i(P_T)(p_i \cdot \hat{n})^k}$$

The weights, $r_i(P_T)$ are functions of P_T and give the relative probabilities for π, K, P, e, and μ to give the correct flavor of the parent B. Usage of this factor is enabled by the excellent particle identification provided by the RICH. In determining the weights, we flip the charge of all protons, as their charge is anti-correlated with the b flavor [26], and flip the charge of electrons and muons with $P_T < 0.8$ GeV/c, since it is more probable that these are from charm decay, in which case the charge is anti-correlated.

The term $p_i \cdot \hat{n}$ gives the component of the track's momentum (p_i) along the axis of the jet ($\hat{n}$), and k is an exponent which is generally varied between 0 and 1 to optimize the performance of the jet charge tag. The "jet" axis is defined using the tracks in the secondary vertex. We compared three values for the exponent, 0, 0.5, and 1.0, and we find that the highest flavor tagging efficiency is obtained for $k = 0$. Given a list of vertices, we choose the one with the highest track multiplicity as this gives the largest dilution [27]. In Fig. 2.6, we compare the tagging power as a function of the number of tracks in the vertex for the $k = 0$ case. In this case, the correct charge corresponds to JETQ$=$-1. For the case where only a single track was found, we reject events in which the track is a $\pi^{\pm}$ because it is ineffective (i.e., $D \sim 0$). Also, to improve the dilution for 3 track vertices, we have required $|JETQ| > 0.2$. While the jet charge tag is highly correlated with the away side kaon and away side muon tags, as a stand-alone tagger, we achieve $\epsilon D^2 = 4.5\%$, with a corresponding efficiency of about 33% and a dilution of $\sim$37%.

2.10.4 B^o Flavor Tagging

Flavor tagging for the B^o uses the same techniques as B_s for away side kaon tagging, away side muon tagging and jet charge tagging. These results compare well with those derived from the independent sample of B_s events. Same Side Tagging is less effective for B^o than for B_s.

2.10.4.1   Same Side Pion tagging

For the same side tag, we search for charged pions which are consistent with being from the fragmentation of the b-quark. As mentioned above, we tune the MC to produce the correct rate of B^{**} relative to B [21]. If the correct $\pi^{\pm}$ is reconstructed and selected, such combinations produce a pronounced peak in the $Q = M(B^o+\pi)-M(B^o)-M(\pi)$ distribution at about 300 MeV. Since these pions point back to the interaction vertex, there is a very large pion background. We find that the $\Delta\eta$ distribution degrades the results for ϵD^2, so we do not use this in computing signal and background probabilities. Otherwise, we use the same procedure as was done for same side kaon tags. For the same side pion tag, we find and $\epsilon D^2 = 1.8\%$, which corresponds to an efficiency of 90% and a dilution of 14%.

2.10.4.2   Away Side Kaon and Muon Tagging and Jet Charge Tagging

The analysis of the Away Side Kaon tagging for B^o is exactly the same as for B_s. Following the same procedure, we find $\epsilon D^2 = 6.0\%$ with an efficiency of 19% and a dilution of 57%. For
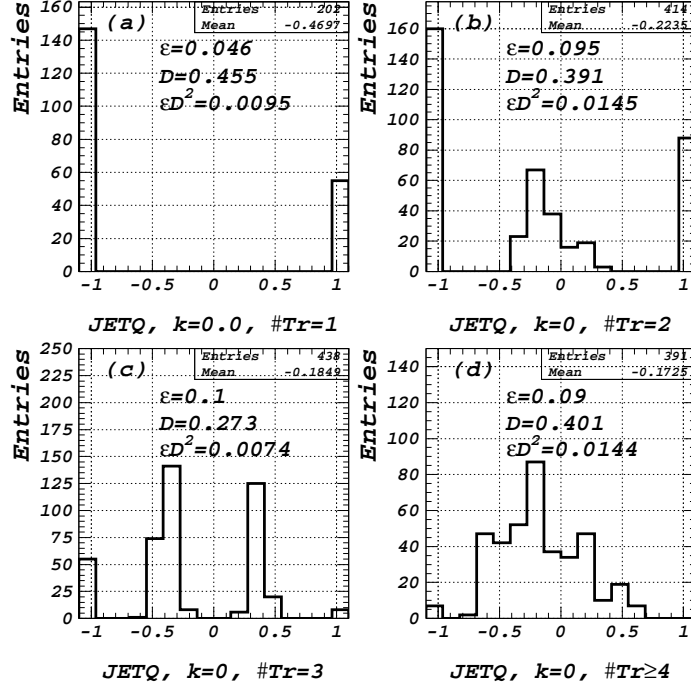
Figure 2.6: The distribution of jet charge for different number of tracks, using $k = 0.0$ as described in the text: (a) single track (b) 2 track vertices, (c) 3 track vertices, and (d) 4 or more track vertices. Also shown in each figure are the efficiencies, dilutions and tagging power values.

Away Side Muon Tagging, using the same procedure as was done for B_s, we find $\epsilon D^2 = 1.2\%$. Finally, for Jet Charge Tagging we find $\epsilon D^2 = 4.8\%$.

2.10.5 Combining Flavor Tags

We have used a simple approach to combining the tagging algorithms. We simply rank the algorithms in order of decreasing dilution, and the algorithm highest on the list determines the flavor tag for a given event. If an event is not tagged by the first algorithm, we check the second, and so on. In this way, the flavor determination comes from a single tag algorithm, the one with the highest dilution. For B_s, the hierarchy is: away side kaon tag, away side muon tag, same side kaon tag, and jet charge tag. For B^o, the jet charge has higher dilution than the same side pion tag, so the order is reversed.

2.10.6 Final Results

The final results for ϵD^2 for B_s are shown in Table. 2.11 and for B^o in Table 2.12. The second column shows the results if the taggers are treated independently, and the third

column shows the results when overlaps are removed. For B_S, the high degree of correlation between the away-side tags and the jet charge tag is evident, as only 1/3 of the events tagged by jet charge are not tagged by one of the three other algorithms. Also, the average dilution of the jet charge drops to 37%, when all events are used, to 20%, when overlaps are removed. We have not yet performed a sophisticated likelihood analysis in which the correlations are used to improve the combined ϵD^2. Also, note that the away-side electron tags are not explicitly treated, and we might expect to get another 0.7% in ϵD^2. Therefore, we expect to achieve an ϵD^2 of 13% for B_s decays and 10% for B^o decays.

Table 2.11: Results on ϵD^2 for the four tagging algorithms for B_s. Shown are the results of the individual taggers, and the results when overlaps are removed.

Sample	Independent Tag $\epsilon D^2(\%)$	Overlaps removed $\epsilon D^2(\%)$
Away side Kaon Tag	5.8	5.8
Away side Muon Tag	1.3	1.3
Same side Kaon Tag	5.7	4.5
Jet Charge Tag	4.5	0.4
Sum	-	12.1
Electrons + Likelihood Fit	-	0.9
BTeV Expected		13

Table 2.12: Results on ϵD^2 for the four tagging algorithms for B^o. Shown are the results of the individual taggers, and the results when overlaps are removed.

Sample	Independent Tag $\epsilon D^2(\%)$	Overlaps removed $\epsilon D^2(\%)$
Away side Kaon Tag	6.0	6.0
Away side Muon Tag	1.2	0.8
Jet Charge Tag	4.8	1.4
Same side Pion Tag	1.8	1.0
Sum	-	9.2
Electrons + Likelihood Fit	-	0.8
BTeV Expected		10

Bibliography

[1] A. E. Snyder and H. R. Quinn, *Phys. Rev. D* **48** (1993) 2139.

[2] H. R. Quinn and J. P. Silva, "The Use of Early Data on $B \rightarrow \rho\pi$ Decays," hep-ph/0001290 (2000).

[3] K. Abe *et al.*, *Phys. Rev. Lett.* **88**, 021801 (2002) (hep-ex/0109026).

[4] See *B Decays, revised 2nd Edition* ed. S. Stone, World Scientific, Singapore, (1994).

[5] B. Aubert *et al.*, *Phys. Rev. Lett.* **87**, 091801 (2001), *ibid.* **86**, 2525 (2001), and B. Aubert *et al.*, "A Study of Time-Dependent CP-Violating Asymmetries and Flavor Oscillations in Neutral B Decays at the Upsilon(4S)," (hep-ex/0201020) (2002); K. Abe etal, *Phys. Rev. Lett.* **87**, 091802 (2001).

[6] B. Aubert *et al.* (BABAR), "Study of CP-violating asymmetries in $B^o \rightarrow \pi^+\pi^-$, $K^+\pi^-$ decays," (hep-ex/0110062) (2001).

[7] Z. Zhao *et al.*, "Report of Snowmass 2001 Working Group E2: Electron-positron Colliders from the ϕ to the Z," to appear in the proceedings (hep-ex/0201047).

[8] S. Henderson, "M2: Summary -Electron-Positron Circular Colliders," presented at Snowmass 2001, to appear in the proceedings, http://vmsstreamer1.fnal.gov/VMS _Site_02/Lectures/Snowmass2001/720M2Henderson/sld016.htm

[9] DOE/NSF HIGH-ENERGY PHYSICS ADVISORY PANEL SUBPANEL ON LONG RANGE PLANNING FOR U.S. HIGH-ENERGY PHYSICS, available at http://doe-hep.hep.net/.

[10] P. Ball *et al.*, "B decays at the LHC," CERN-TH/2000-101 (hep-ph-0003238).

[11] K. Abe *et al.*, (CDF), *Phys. Rev. Lett.* **75**, 1451 (1995); S. Abachi *et al.*, (D0), *Phys. Rev. Lett.* **74**, 3548 (1995). See also the UA1 measurement C. Albajar *et al.*, *Phys. Lett.* B**186**, 237 (1987); B**213**, 405 (1988); B**256**, 121 (1991).

[12] K. Abe *et al.*, (CDF), *Phys. Rev. Lett.* **76**, 4462 (1996); ibid **77**, 1945 (1996); K. Abe *et al.*, (CDF), *Phys. Rev. D* **57**, 5382 (1998).

[13] T. Junk, "A Review of B Hadron Lifetime Measurements from LEP, the Tevatron and SLC," in Proceedings of the 2nd Int. Conf. on *B Physics and CP Violation*, Univ. of Hawaii, (1997), ed. T. E. Browder *et al.*, World Scientific, Singapore (1998).

[14] K. Abe *et al.*, (CDF), "Observation of B_c Mesons in $p - \overline{p}$ Collisions at $\sqrt{s} = 1.8$ TeV," hep-ex/9804014 (1998).

[15] M. Paulini, "B Lifetimes, Mixing and CP Violation at CDF," Review article to appear in the Int. Journal of Modern Physics A, hep-ex/9903002 (1999).

[16] K. Anikeev *et al.*, "B Physis at the Tevatron: Run II and Beyond, "FERMILAB-PUB-01/197 (hep-ph/0201071) (2001).

[17] "LHCb Technical Proposal," CERN/LHCC 98-4, LHCC/P4 (1998), available at http://lhcb.cern.ch .

[18] We have confirmed with T. Nakada, the LHCb spokesperson, that the yields for this mode as quoted in their Technical Proposal are their current values that we should use in our comparisons. The branching ratio numbers used by LHCb were taken from Table 15.11 on page 157. The number of events were taken from Table 15.12. Since these numbers are quoted as being "tagged," we divided by the 0.40 tagging efficiency given on page 145. The two final states $\rho^+\pi^-$ and $\rho^-\pi^+$ are given separately by LHCb; we added them together. The same procedure was followed for $B_s \to D_s K$.

[19] P. Ball *et al.*, "B Decays at the LHC," CERN-TH/2000-101, hep-ph/0003238.

[20] Although they state a 1% efficiency here, this is only a partial efficiency according to T. Nakada.

[21] T. Affolder *et al.*, (CDF), *Phys. Rev. D.* **64**, 072002 (2001); N. Harnew, P.E. Schlein, BEAUTY 95, Proceedings of the Third International Workshop on B Physics at Hadron Machines, University of Oxford, UK, July 10-14, 1995; R. Akers *et al.*, (OPAL Collaboration) *Z. Phys. C.* **66**, 19 (1995).

[22] The parameters PARJ(14) - PARJ(17) were change from 0.0 to 0.05, which allows for the production of higher spin and angular momentum states.

[23] For a description of the QQ generator see http://www.lns.cornell.edu/public/CLEO/soft/QQ (unpublished).

[24] The quantity D/σ is the distance of closest approach of the track to the primary vertex divided by the uncertainty in that distance.

[25] T. Affolder *et al.*, (CDF), *Phys. Rev. D.* **60**, 072003 (1999).

[26] Protons from b decay frequently come from $b \to \Lambda_b \to \Lambda_c + X$, with $\Lambda_c \to p + X$. So the positively charged proton is correlated with the negatively charged b quark, and visa versa.

[27] Strictly speaking, the single-track sample has a larger dilution, but we expect these are only used when there are no multi-track vertices in the event. Also, we expect that many of the single-track candidates will be accounted for in the away side tag analyses.

Chapter 3

Detector Requirements

In this section, we present the main requirements on the design of the BTeV detector and provide an overview of the spectrometer design that we have developed to satisfy these requirements.

We begin with a discussion of the key "drivers" of the detector design:

- the physics of B production at $\sqrt{s}$ of 2 TeV;

- the final states we want to detect and study, based on the physics goals described above, and the associated backgrounds that must be suppressed;

- the characteristics of the Tevatron and the C0 collision region; and

- the required statistical precision.

After explaining the requirements of the design, we describe the baseline detector, which achieves BTeV's currently stated physics goals. A further requirement is that the detector be flexible – that it have the capability to study topics which may not be considered interesting today but which may be recognized to be important in the future.

In our original June 2000 proposal, the detector covered the angular region from 10 mr to 300 mr relative to the proton beam and from 10 mr to 300 mr relative to the anti-proton beam. We referred to each region of angular coverage as an "arm" of the spectrometer and described this as a "two arm" detector. Here we define a descoped version of the detector, which we call Phase 1, which covers only one of these two angular regions and is, therefore, a "single arm" detector. Figure 3.1 shows the full detector as originally proposed. A schematic of the Phase 1 detector is shown in Fig. 3.2. The new design is capable of carrying out the full program of measurements albeit on a longer time scale. The new design also permits the installation of components on the "uninstrumented side" later on.

The key design features of BTeV include:

- A dipole located on the IR, which permits BTeV to have an effective "two arm" acceptance. In Phase 1, only one arm is instrumented.
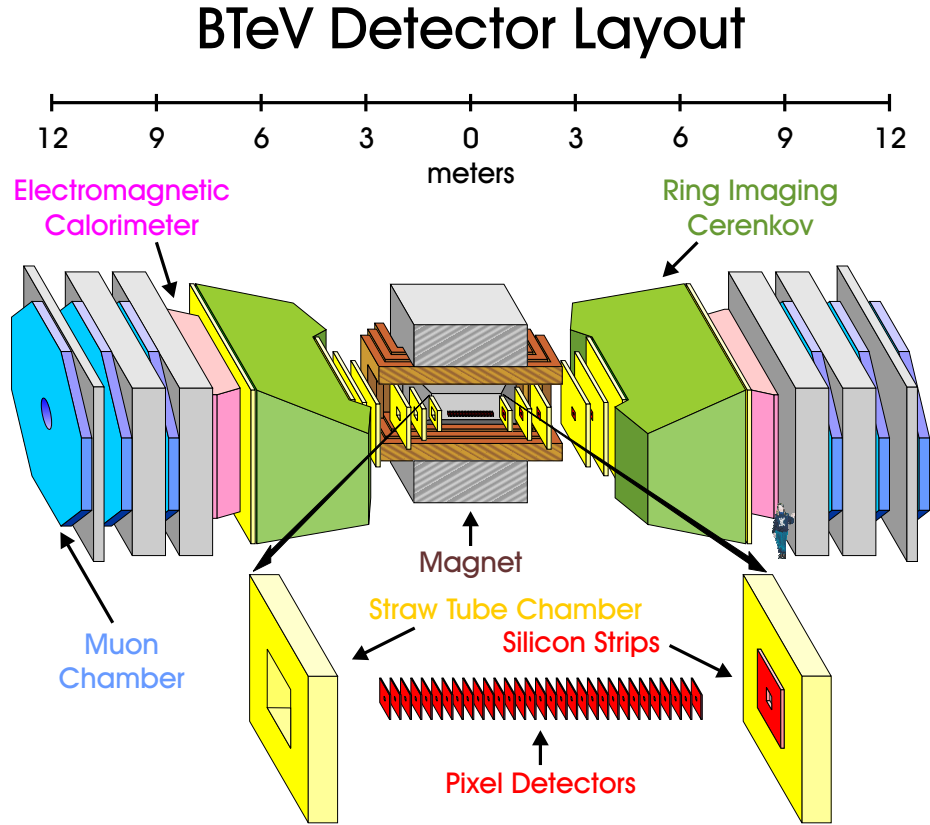
BTeV Detector Layout

Figure 3.1: Layout of original BTeV/C0 detector (both arms fully instrumented)

- A precision vertex detector based on planar pixel arrays;

- A detached vertex trigger at Level 1 which makes BTeV efficient for most final states, including purely hadronic modes;

- Precision tracking using straw tubes and silicon microstrip detectors, which provide excellent momentum and mass resolution out to 300 mr;

- Excellent particle identification using a Ring Imaging Cherenkov Detector (RICH). The RICH provides hadron identification from 3-70 GeV and lepton identification from 3-20 GeV, out to the full aperture of 300 mr, which is crucial since the muon detector and calorimeter do not cover the full solid angle.

- A high quality $PbWO_4$ electromagnetic calorimeter, covering 200 mr, capable of reconstructing final states with single photons, π^o's, η's or η''s, and identifying electrons;

- Excellent identification of muons out to 200 mr using a dedicated detector consisting

BTeV Detector Layout
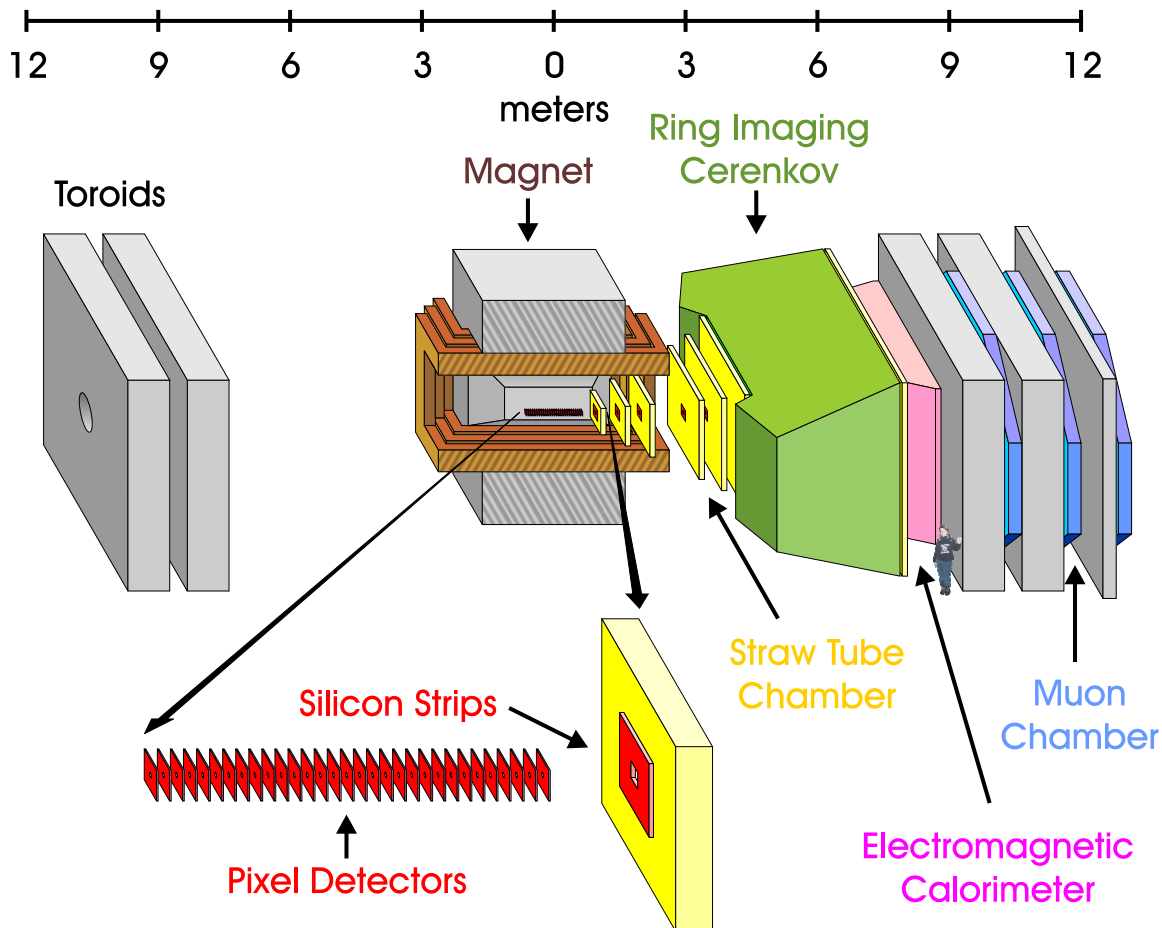
Figure 3.2: Layout of BTeV Phase 1 Detector (only one arm instrumented)

of a steel toroid instrumented with proportional tubes. This system has the ability to supply a dimuon trigger; and

- A very high speed and high throughput data acquisition system which eliminates the need to tune the experiment to specific final states.

After reviewing the requirements that led us to these design principles, we provide, in the next chapter, a brief description of each major detector component. The level of detail is sufficient to provide the reader with a good overview of the experimental apparatus and a reasonable understanding of the solution to all the various problems associated with carrying out our ambitious program of studying B decays. However, we do not present every detail which an expert might need to understand the implementation and status of development of each detector technology, nor do we discuss the many calculations that went into the

optimization of the design. Additional information may be found in the proposal and in many writeups and reports, which are referenced in the text.

3.1 Requirements Based on the Physics of B Production at $\sqrt{s}$ of 2 TeV

The physics of hadronic beauty and charm production plays a major role in the design of BTeV. We review the most important features here. In hadron colliders all B species, B_d, B_u, B_s, b-baryons, and even B_c mesons, are produced at the same time. This allows one to carry out a very large number of interesting studies and to look for unexpected phenomena provided the detector is both powerful and flexible, especially in the area of triggering.

3.1.1 The $b\overline{b}$ Production Cross-Section

It is customary to characterize heavy quark production in hadron collisions with two variables, the momentum transverse to the beams, p_t, and the rapidity,

$$y = \frac{1}{2} \ln \left(\frac{E + p_{\parallel}}{E - p_{\parallel}} \right) , \tag{3.1}$$

where E is the particle's energy and $p_{\parallel}$ is its longitudinal momentum. Often, the pseudorapidity η

$$\eta = -ln \left(\tan \left(\theta/2 \right) \right) \quad , \tag{3.2}$$

where θ is the angle of the particle with respect to the beam direction, is used for the longitudinal variable since this variable is independent of the particle's mass.

The $p\overline{p}$ production of b quarks has been measured in the Tevatron at a center-of-mass energy of 1.8 TeV in the central rapidity region $|\eta| < 1$ by CDF [1] and D0 [2], and in the forward region $3.2 > y > 2.4$ by D0 [3]. Both CDF and D0 find that the $b\overline{b}$ production cross-section in the central region is underestimated by the Mangano, Nason and Ridolfi (MNR) next-to-leading order QCD calculation [7] by a factor of approximately two. Since the QCD calculation predicts a cross-section of 50 μb, when integrated over η and p_t, using the data in the central regions leads to a total $b\overline{b}$ production cross-section of 100 μb. The D0 central and forward data are shown in Fig. 3.3.

The measured cross-section in the higher y region is 3.6 ± 0.8 times higher than the QCD calculation, leading to a total estimated $b\overline{b}$ production cross-section of 180 μb. BTeV will operate in the range $1.9 > \eta > 4.5$. While we have no reason to dispute the D0 measurement, we will conservatively normalize our estimates to a $b\overline{b}$ production cross-section of 100 μb.

There is some evidence from HERA that the fragmentation of charmed particles is influenced by the leading quarks in the beam so that the fragmentation produces, in some cases, faster D's than the parent c-quarks [4]. This effect is expected to be smaller for b quarks at the center-of-mass Tevatron. If such an effect were present it would increase BTeV's acceptance in the forward direction.
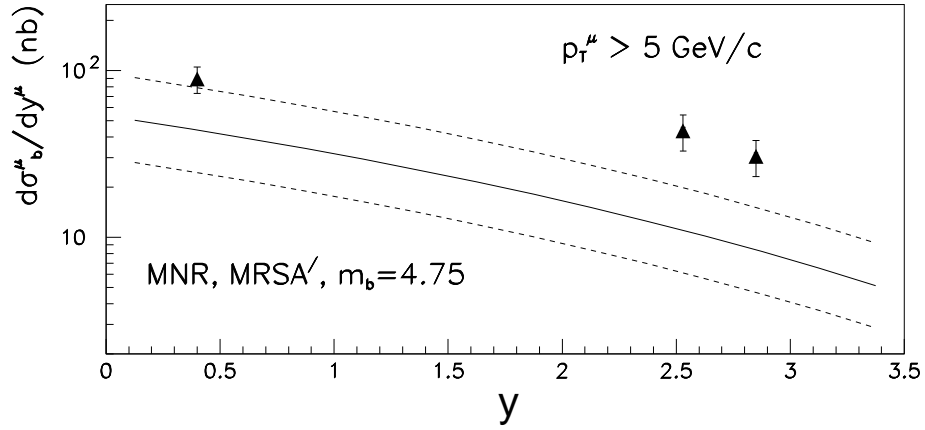
Figure 3.3: The $b\bar{b}$ cross-section as a function of the rapidity of muons from b decay, y^{μ}, measured by D0 for both the forward and central rapidity regions, using muons from b decays with $p_t > 5$ GeV/c. The solid curve is the prediction of the next-to-leading order QCD calculation for a b-quark mass of 4.75 GeV. The dashed curves represent the estimated theoretical 1σ error band.

The fact that the production cross section for states containing b-quarks is $\approx 1/500$ of the total cross section has strong implications for the design of the experiment. It means that the experiment must have a very good trigger to reject the very large number of typical interactions which involve only light quarks. It further means that the experiment will have to handle very high particle fluxes, and tolerate very high radiation doses, if it is going to get reasonable samples of the key decay modes it wants to study, especially given the well-known fact that the B decay modes most interesting for CP studies have rather small branching fractions.

3.1.2   Characteristics of Hadronic b Production

The dominant mechanism for b quark production at the Tevatron is believed to be gluon-gluon fusion. Whenever the two gluons have different Feynman-x, the center of mass of the produced $b - \bar{b}$ pair is boosted along the direction of the higher momentum gluon. Thus, we have an intrinsically asymmetric energy gluon-gluon collider. According to both simple arguments and detailed QCD calculations, the b's are produced approximately "uniformly" in η and have a truncated transverse momentum, p_t, spectrum, characterized by a mean value approximately equal to the B mass [5]. The distribution in η is shown in Fig. 3.4.

There is a strong correlation between the B momentum and η. Shown in Fig. 3.5 is the $\beta\gamma$ of the B hadron versus η from the Monte Carlo physics generator Pythia at $\sqrt{s} = 2$ TeV. It can clearly be seen that near η of zero, $\beta\gamma \approx 1$, while at larger values of $|\eta|$, $\beta\gamma$ can easily reach values of 6. This is important because the observed decay length varies with $\beta\gamma$ and, furthermore, the absolute momenta of the decay products are larger allowing for a suppression of the multiple scattering error.
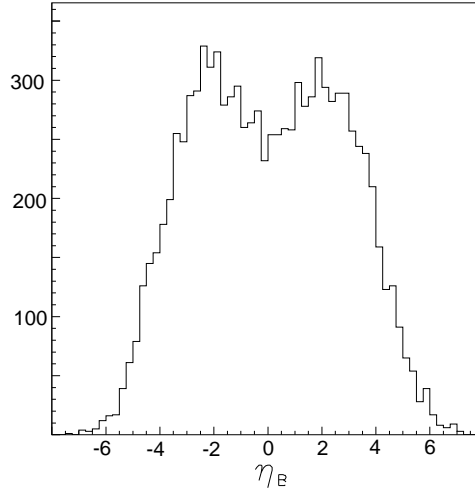
Figure 3.4: The B yield versus η.
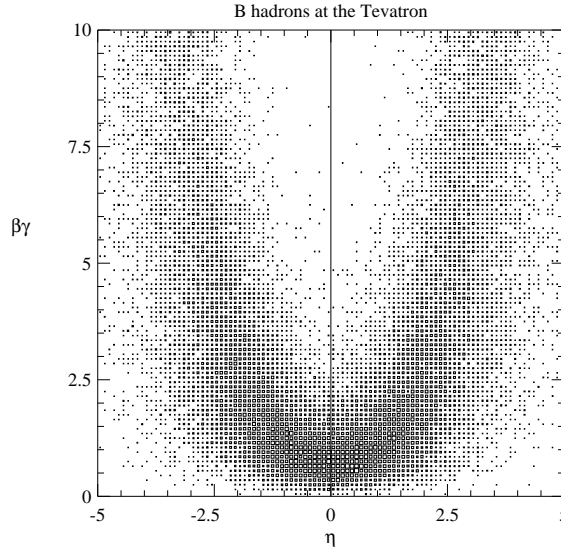
Figure 3.5: $\beta\gamma$ of the B versus η.

Since the detector design is somewhat dependent on the Monte Carlo generated b production distributions, it is important to check that the correlations between the b and the $\bar{b}$ are adequately reproduced. Fig. 3.6 shows the azimuthal opening angle distribution between a muon from a b quark decay and the $\bar{b}$ jet as measured by CDF [6] and compares it with the MNR next-to-leading order QCD predictions [7].

The MNR model does a good job representing the shape, which shows a strong back-to-back correlation. The normalization is about a factor of two higher in the data than the theory, which is generally true of CDF and D0 b cross-section measurements.

The "flat" η distribution hides an important correlation of $b\bar{b}$ production at hadronic colliders. In Fig. 3.7 the production angle of the hadron containing the b quark is plotted versus

Figure 3.6: The differential $\delta\phi$ cross-sections for $p_T^\mu > 9$ GeV/c, $|\eta^\mu| < 0.6$, $E_T^{\bar{b}} > 10$ GeV, $\left|\eta^{\bar{b}}\right| < 1.5$ compared with theoretical prediction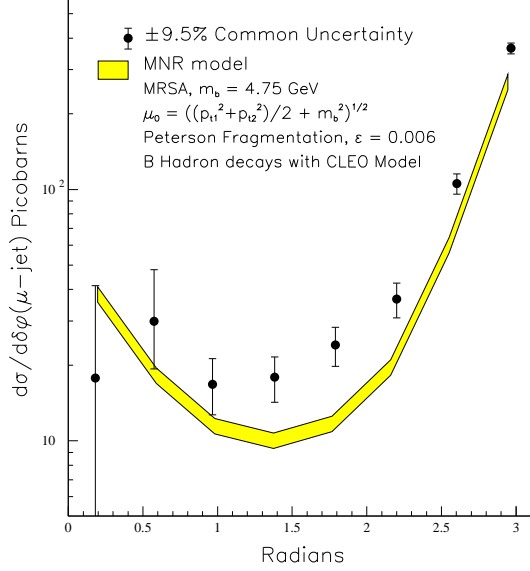s. The data points have a common systematic uncertainty of $\pm 9.5\%$. The uncertainty in the theory curve arises from the error on the muonic branching ratio and the uncertainty in the fragmentation model.

the production angle of the hadron containing the $\bar{b}$ quark. Here zero degrees represents the direction of the incident proton and 180 degrees, the incident anti-proton. There is a very strong correlation in the proton or the anti-proton directions: when the B is forward the $\overline{B}$ is also forward. (We call both the proton and anti-proton directions forward.) This correlation between B and $\overline{B}$ production is not present in the central region (near 90 degrees). This is a result of the underlying physics of gluon-gluon collisions described above.

In the forward direction, this correlation is crucial to carrying out studies that involve flavor tagging. For many B decay studies that involve mixing, it is necessary to determine the flavor of the signal B hadron at the moment of production. One way to do this is to determine the flavor of the "other" B hadron. Because of the correlated nature of the b-quark production, both B hadrons will be boosted in the same direction and therefore the signal and the tagging decay products will appear in the same "arm". Were this not true, it would be impossible to do these measurements with a single arm detector.

Thus, the forward direction at the Tevatron presents us with a number of striking advantages. First of all, there is a large cross-section for the production of correlated $b\bar{b}$ pairs. Secondly, the B hadrons that are formed have relatively large momenta, on average 30 GeV/c, and their decay products are not too badly affected by Multiple Coulomb Scattering. This allows us to make precision measurements of their spatial origins; so we can determine if they arise from B hadrons that traveled on the order of several mm prior to their decay. Furthermore the geometry is very natural for certain aspects of detector technology that significantly enhance the physics performance. For example, a Ring Imaging
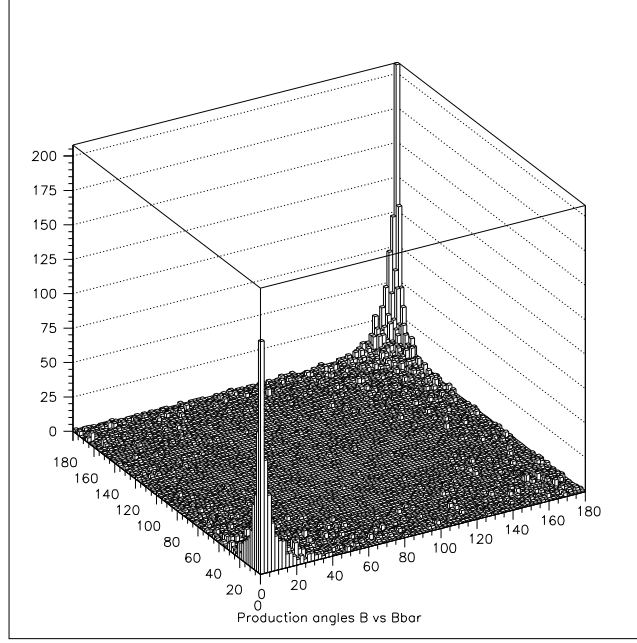
Figure 3.7: The production angle (in degrees) for the hadron containing the b quark plotted versus the production angle for the hadron containing the $\bar{b}$ quark in the same event, from the Pythia Monte Carlo generator.

Cherenkov detector using a gas radiator matches the 3-70 GeV/c momentum range for B decay products. The Cherenkov photons can be detected using a relatively small area array of photomultiplier tubes or Hybrid PhotoDiodes(HPDs). Powerful particle identification is essential for high sensitivity b experiments. Another example is the ability to put the silicon pixel vertex detector inside the main beam vacuum. Precision detection of the B decay vertices is crucial for the trigger and in rejecting backgrounds. For these reasons, we have designed a detector with "forward coverage."

Charm production is similar to b production but has a much larger cross section. Current theoretical estimates are that charm is 1-2% of the total $p\bar{p}$ cross-section. The cross section is even more strongly peaked in the forward direction because the average transverse momentum is of the order of only 1.5 GeV/c. The charm cross section has never been measured because experiments with good acceptance in the central region have very low efficiency for triggering and reconstructing charm. The favorable kinematics in the forward direction gives BTeV a very high efficiency for reconstructing charm.

3.2 Requirements Based on the Characteristics of B Decay Modes

The physics case described above involves reconstructing a variety of different decay modes of the B, B_s, and other B hadrons and, in many cases, following their time evolution, and tagging the flavor of the parent B at production and at the moment of decay. These decay modes may involve charged hadrons, charged leptons, photons (prompt or from π^o's), and tertiary vertices from the $b \to c$ decay chain. In some cases, there are substantial backgrounds from minimum bias (typical hadronic) events, charm decays, or other B decays. In many cases, the branching fractions, including any tertiary decays, are quite small, typically 10^{-5} to 10^{-7}. This, together with the large background of minimum bias events, demands that BTeV be able to reconstruct multibody final states, with good resolution in invariant mass, and to handle very high rates. In order to carry out the physics program described above, the detector must have the ability to separate decay vertices from the primary interaction vertex and to reconstruct secondary B vertices and daughter charm vertices. This requires a precision vertex detector. It also must be able to measure the time evolution of decays for time-dependent asymmetry studies. The most demanding requirement is to be able to follow the very rapid oscillations of the B_s meson in order to study CP violation. It must have the ability to distinguish pions, kaons, and protons from each other to eliminate kinematic reflections that can contaminate signals and make them difficult to observe. Many key decay modes have π^o's, γ's, or particles that decay into them, such as ρ's or η's. Leptons, muons and electrons (positrons), appear in many key final states so good lepton identification is also required. Finally, many of the detector properties which are needed to isolate and reconstruct signals are also needed to perform "flavor tagging."

We illustrate the full range of capabilities required for BTeV by choosing a particular menu of physics measurements related to CP violation in B decays. These by no means constitute the full range of measurements that we plan to make but comprise a basic set of very crucial measurements which do constrain the CKM triangle. These translate into a basic set of requirements for the detector, shown in Table 3.1. In the table, we list physics topics, a particular decay mode that can be used to study it, and then tabulate the key features necessary to reconstruct the signal and perform flavor tagging where required. It can be seen that in order to carry out this program, the detector must make a complete characterization of the final state particles. A table prepared to address the topic of rare decays would have similar characteristics. It should be clear that a device with these properties, combined with a very powerful and inclusive trigger system for B decays and a high speed data analysis system, can address a very large range of topics.

91

Table 3.1: Some crucial measurements and corresponding detector requirements. In order to separate signals and background, all studies in BTeV need good primary and secondary vertex resolution, which is equivalent to a requirement on the resolution in proper time, τ, of a small fraction of the B lifetime. The requirement of "superb τ resolution", referred to in this table, means resolution which is a small fraction of the expected period for B_s mixing and is a much more stringent requirement. The "lepton id" is checked where it is used to extract the signal decay, although it participates in most of the other studies via lepton flavor tagging.

Physics Quantity	Decay Mode	Detector Property				
		Vertex trigger	K/π separation	γ detection	superb τ resolution	lepton id
$\sin(2\alpha)$	$B^o \to \rho\pi \to \pi^+\pi^-\pi^o$	$\checkmark$	$\checkmark$	$\checkmark$		
$\cos(2\alpha)$	$B^o \to \rho\pi \to \pi^+\pi^-\pi^o$	$\checkmark$	$\checkmark$	$\checkmark$		
$\text{sign}(\sin(2\alpha))$	$B^o \to \rho\pi, B^o \to \pi^+\pi^-$	$\checkmark$	$\checkmark$	$\checkmark$		
$\sin(\gamma)$	$B_s \to D_s K^-$	$\checkmark$	$\checkmark$		$\checkmark$	
$\sin(\gamma)$	$B^+ \to D^o K^+$	$\checkmark$	$\checkmark$			
$\sin(\gamma)$	$B \to K\pi$	$\checkmark$	$\checkmark$	$\checkmark$		
$\sin(\gamma)$	$B \to \pi^+\pi^-, B_s \to K^+K^-$	$\checkmark$	$\checkmark$		$\checkmark$	
$\sin(2\chi)$	$B_s \to J/\psi\eta', J/\psi\eta$	$\checkmark$	$\checkmark$	$\checkmark$	$\checkmark$	$\checkmark$
$\sin(2\beta)$	$B^o \to J/\psi K_s$					$\checkmark$
$\sin(2\beta)$	$B^o \to \phi K_s, \eta' K_s, J/\psi\phi$	$\checkmark$	$\checkmark$	$\checkmark$		$\checkmark$
$\cos(2\beta)$	$B^o \to J/\psi K^*, B_s \to J/\psi\phi$					$\checkmark$
x_s	$B_s \to D_s\pi^-$	$\checkmark$	$\checkmark$		$\checkmark$	
$\Delta\Gamma$ for B_s	$B_s \to J/\psi\eta', K^+K^-, D_s\pi^-$	$\checkmark$	$\checkmark$	$\checkmark$		$\checkmark$

3.3 Requirements Due to Characteristics of the Tevatron and the C0 Interaction Region

For reasons related to radiation damage and triggering, among others, we have concluded that BTeV will become rate limited somewhere between 2 and 5×10^{32}cm^{-2}s^{-1}. (This depends on many technology and budget issues). Since BTeV would begin after many years of Tevatron operation for Run 2, we assume that a luminosity of 2×10^{32} will be available to us. We have designed BTeV to run at that luminosity (with the ability to handle at least another factor of two with increased triggering hardware and possible limited detector upgrades). We also have made sure that the design permits the full instrumentation of the second arm.

Table 3.2 gives the Tevatron parameters which are especially relevant to BTeV design and physics reach. We expect to start serious data taking with a luminosity of about $5 \times$

10^{31} cm^{-2}s^{-1}; our design luminosity goal is 2×10^{32} cm^{-2}s^{-1}. At the higher luminosity we expect an average of 2 total interactions per crossing, 1.3 of which are not elastic or quasi-elastic.

Table 3.2: The Tevatron as a b and c source for BTeV

Luminosity (BTeV design)	2×10^{32} cm^{-2}s^{-1}
$b\bar{b}$ cross-section	100 μb
# of b's per 10^7 sec	4×10^{11}
$\frac{\sigma(b\bar{b})}{\sigma(total)}$	$\sim 0.15\%$
$c\bar{c}$ cross-section	$> 500\ \mu$b
Bunch spacing	132 ns
Luminous region length	$\sigma_z = 10\text{-}20$ cm (crossing angle dependent)
Luminous region width	$\sigma_x, \sigma_y \approx 50\ \mu$m
Interactions/crossing	$< 2.0 >$

3.4 Summary

BTeV will be a second generation study of CP violation in B decays. The experiments at the asymmetric B-factories, BABAR at PEPII and BELLE at KEKB, will have made many measurements of CP violation and rare decays of the B_d and B_u hadrons. CDF and D0, running at the Tevatron, will also carry out some of these measurements and will begin to study the decays of the B_s and other B hadrons. BTeV will do these studies at much higher precision and will augment them with crucial high-precision studies of B_s decays along with a program of studies of B_c and b-baryon decays. On about the same time scale as BTeV, LHCb will go into operation with similar capabilities for all-charged states, although without a high quality calorimeter or as inclusive a trigger. ATLAS and CMS will also be capable of doing some B-physics, especially for states containing leptons which are easy for them to trigger on.

In order make the best measurements on a wide range of B decays, we must accumulate large samples of reconstructed B decays. The Tevatron operating as described above produces enough B-hadrons for us to achieve our physics goals. The detecter must be able to operate at the high radiation levels implied by the high luminosity, must have excellent triggering capability, and be able to reconstruct B hadrons and tag their flavor with very high efficiency. The detector we describe in detail in the next chapter, whose design was driven by all the requirements and considerations we have discussed, achieves this goal.

Bibliography

[1] F. Abe *et al.*., "Measurement of the B Meson Differential Cross-Section in $p\overline{p}$ collisions at $\sqrt{s} = 1.8$ TeV," CDF/PUB/BOTTOM/PUBLIC/3759 submitted to ICHEP '96 and references therein; F. Abe *et al.*., *Phys. Rev. Lett.* **75**, 1451 (1995).

[2] R. Abbott *et al.*., "The $b\overline{b}$ Production Cross Section and Angular Correlations in $p\overline{p}$ collisions at $\sqrt{s} = 1.8$ TeV," FERMILAB-Pub-99/144-E; S. Abachi *et al.*, *Phys. Rev. Lett.* **74**, 3548 (1995).

[3] D. Fein, "Tevatron Results on b-Quark Cross Sections and Correlations," presented at Hadron Collider Physics (HCP99) (Bombay), January 1999.

[4] I. Redondo, "ZEUS Results on Charm in DIS as aN Indication of Beam Drag Effects," and E. Norrbin and T. Sjostrand, "Drag Effects in Charm Photoproduction," both in Proceedings of the workshop for **Monte Carlo Generators for HERA Physics**, 1998/99, ed. by A. T. Doyle et al., http://www.desy.de/ heramc/proceedings/wg60.

[5] M. Artuso, "Experimental Facilities for b-Quark Physics," in *B Decays* revised 2nd Edition, Ed. S. Stone, World Scientific, Singapore (1994).

[6] F. Abe *et al.*., *Phys. Rev.* D **53**, 1051 (1996).

[7] M. Mangano, P. Nason and G. Ridolfi, *Nucl. Phys.* B **373**, 295 (1992).

Chapter 4

Detector Description

4.1   Detector Overview

A schematic of the detector was given in chapter 3. Figure 4.1 gives a layout with more mechanical detail such as a profile of the analysis magnet and its coils, the vacuum pipes and flanges, etc. The best way to understand the detector is to follow what happens to a charged particle produced in a proton-antiproton collision near the center of the C0 Interaction Region (IR) traveling into the instrumented arm. Below, we give a brief description of its trip. We also describe briefly two important elements of BTeV: the trigger and the data acquisition system. In the following subsections, each detector element the particle traverses is discussed with enough detail to explain how it contributes to the physics capability of BTeV.

The particle is produced near the middle of the BTeV analysis magnet, which is centered on the IR. The magnet deflects the particle vertically with a field of approximately 1.5 T. The first detector it intercepts is the silicon pixel detector which is inside the magnet. The detector is centered on the IR and has a total of 30 "doublets" of pixel planes, oriented perpendicular to the beam. Each doublet consists of two planes of pixels of 50 μm$\times$400 μm. One plane of each doublet has the high precision dimension of the pixel oriented to measure the horizontal coordinate of the track and the other plane has the high precision dimension oriented to measure the vertical coordinate of the track. The high precision tracking permits us to cleanly separate primary interaction vertices from secondary and tertiary vertices associated with B decays. The measurement of the separation, L, has a resolution of about 140 μm, compared to an average separation of about 4000 μm for a B decay. Another way to look at this is that we measure the decay proper time with a resolution of about 45 fs, compared to a typical B hadron lifetime of over 1500 fs.

After passing through the pixel planes, the tracks pass through the first six "stations" of the "forward trackers." The first three are in the analysis magnet. The next three are in the relatively low field region downstream of the analysis magnet. These chambers measure the track after it has passed through all of the magnetic field. The forward tracker improves the momentum resolution with respect to the measurement using the pixel detector alone and
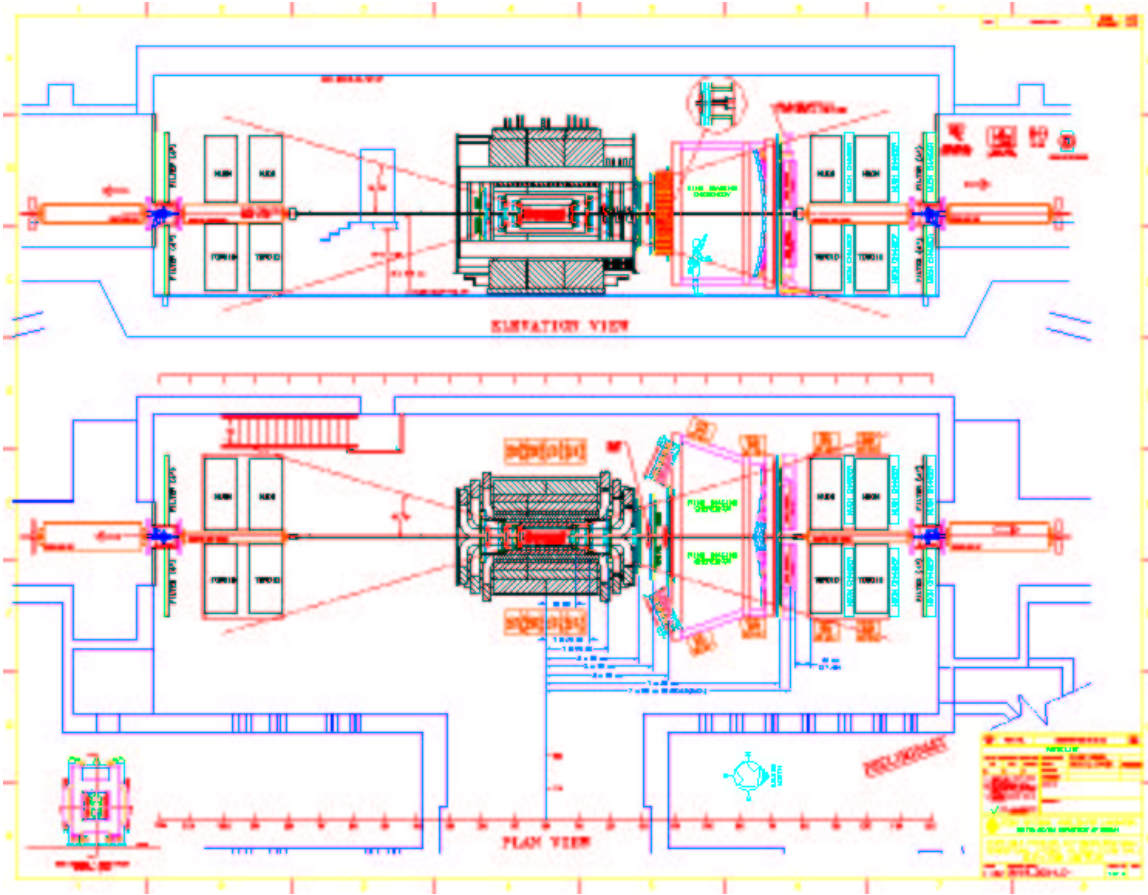
Figure 4.1: Layout of Phase 1 BTeV/C0 Detector – anti-Proton Arm Instrumented

provides us with excellent mass resolution for B decay candidates. It also serves to confirm that the track enters the Ring Imaging Cherenkov counter (RICH) and provides the best measurement of the coordinates of the particle within it. The forward tracker consists of two sections, an "inner" section of silicon microstrips in the high occupancy region near the beam and an "outer" section of straw tubes in the lower occupancy region at larger angles with respect to the beam.

The particle next enters the RICH, where it encounters first the 1 cm thick liquid-freon, followed by 3 m of gaseous-freon radiator. Cherenkov photons generated in the liquid pass into the gas volume of the RICH and are detected in photomultipliers arrayed along the outside of the gas containment vessel. The Cherenkov photons generated in the gas travel forward to a spherical mirror at the downstream end of the gas volume. The mirror reflects the photons towards the upstream face of the RICH and sideways out of the spectrometer's aperture, and focuses them on arrays of Hybrid Photodiodes. The two RICH systems provide charged particle identification over the energy range from 3-70 GeV/c.

The particle then traverses the 7th station of the forward tracker. This station confirms that the particle traversed the RICH and helps determine its position and angle at the RICH

96

mirror. It also defines the trajectory of the charged particle as it moves towards the most downstream elements of the spectrometer.

Next, the particle enters the electromagnetic calorimeter. This detector is composed of lead tungstate crystal blocks which measure the energy and position of electrons and photons striking it. While we have been describing a charged particle, a photon produced in the collision will, if not converted in the material of the upstream elements of the detector, travel in a straight line until it strikes the calorimeter. The calorimeter provides the only information we have about the photon. For electrons and photons, nearly all the energy of the particle is absorbed in the calorimeter. Muons will traverse the entire calorimeter losing only a little energy through ionization. Charged hadrons may begin to shower in the calorimeter or may pass through it losing energy only through ionization. Even if a hadron showers, the energy deposition will typically be only a fraction of the total energy.

The last detector in the system is the muon detector. This consists of two sections of steel toroids, interspersed and followed by stations of proportional tube arrays. Hadrons escaping the calorimeter are absorbed in the first steel toroid. Muons traverse the toroid steel, bending in the field, and their momenta and angles are measured with the proportional tubes. Muons eventually enter the earth berm outside C0 where they loss all their energy.

The BTeV trigger is based on the property that most distinguishes all events containing b-flavored hadrons from events involving only light quarks: decay vertices separated from the primary vertex by distances consistent with lifetimes of ≈ 1.5 ps. We use this in the lowest level trigger, which we call Level 1, to select an eclectic mix of b decays. This eliminates the need to use characteristics of specific final states which bias the experiment's sensitivity. To accomplish this, we must find both primary and secondary vertices at the lowest level of the trigger for every beam crossing of the Tevatron. These occur at a rate of 7.5 million per second. To do such sophisticated computations at such a high rate requires a massively parallel system of several thousand computational elements: Field Programmable Gate Arrays (FPGAs), Digital Signal Processors (DSPs), and microprocessors. While the Level 1 decision is being made, sparsified data for each crossing is stored in a large, multi-terabyte buffer memory made from commodity parts. There is no fixed latency for the Level 1 trigger. Whenever a decision is reached for a given beam crossing, data are either (effectively) deleted from the memory or (effectively) transferred to another memory to await subsequent processing. The events selected by the Level 1 trigger are further refined by the Level 2/3 trigger which is implemented with a system of several thousand conventional LINUX processors.

The data acquisition system includes the buffer memory system and the data highways over which events flow between the experiment front ends, the buffer memories, and the trigger processing elements. It also includes facilities to move data to large output disk buffers and eventually to record them on permanent media. It must also supervise the data flow, and control, monitor, and facilitate the troubleshooting of the entire system. It contains the "slow control system," which initializes and changes the parameters of the front-end systems. It also records non-event data, such as temperatures and pressures, provides the operator interface to the experiment, and maintains logs of all problems. It includes

many databases required to support all these activities.

4.2 The C0 Experimental Area

The experiment will be carried out in the newly constructed C0 collision hall, shown in Figure 4.2. The hall is a 216 m^2 (9 m wide by 24 m long) enclosure centered on the C0 straight section of the Tevatron. The Tevatron beam is 2.5 m above the floor slab and 4.25 m below the roof of the hall. The enclosure specifications and dimensions are compatible with the detector described in this document.

Figure 4.2: "Fish Eye" View of the C0 Collision Hall

To the east of the collision hall is the C0 assembly building, a steel framed, industrial type structure containing a 150 m^2 assembly hall at the collision hall elevation. The final assembly of detector components will occur in the assembly hall. They will then be moved into the collision hall through the 6 m × 6 m "shield door" opening. Figure 4.3 shows a layout of the assembly building and collision hall with the vertex magnet and the muon toroids of the proposed BTeV detector superimposed.

Detector elements are brought into the area at a ground level loading dock and lowered to the assembly floor using the 30 ton crane which covers the loading dock and assembly hall. A large movable shielding wall separates the assembly area from the experiment enclosure. There are cable ducts from the experiment enclosure to a 150 m^2 equipment room at grade level on the north end of the assembly building. There will be a three level electronics/counting room and office area for experimenters.
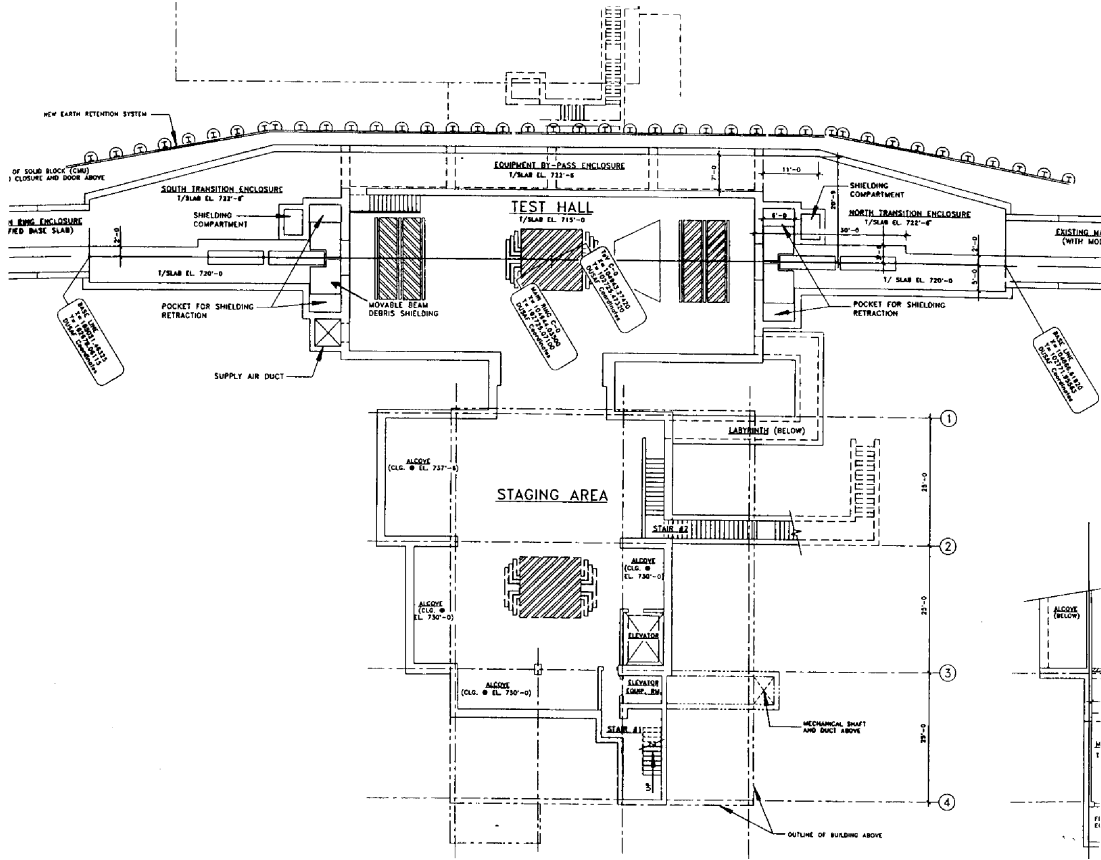
Figure 4.3: Layout of C0 Collision Area

4.3 BTeV Analysis Magnet

The vertex magnet in the proposed BTeV spectrometer is based on an existing magnet, the SM3 magnet, which is currently part of the decommissioned Fermilab MEast Spectrometer. It is shown, after modification, on the proposed layout, Figure 4.1, of the BTeV/C0 spectrometer. The magnet operated in MEast from 1982 until 1997, at a central field of about 0.8 Tesla, serving experiments E605, E772, E789, and E866.

The SM3 magnet was assembled by welding together, in place, various blocks of iron recovered from the Nevis Cyclotron. It has a total weight of 500 metric tons. After transportation to C0, the modified magnet will be reassembled in the C0 assembly hall and rolled into the C0 collision hall, as shown in Figure 4.3.

Studies with the magnetostatic modeling programs POISSON and OPERA have led to a design for a new pole-piece for SM3. This pole-piece, indicated in Figure 4.4, yields a central field of 1.5 Tesla, and an integrated dipole field of 5.0 T-m. The magnet will be oriented so that charged particles are deflected in the vertical plane. The properties of the magnet, with the pole faces shimmed to the BTeV requirements, are listed in Table 4.1. The vertical deflection of the Tevatron beam by the vertex magnet is compensated by two conventional dipoles at each end of the spectrometer.

The magnet is centered on the interaction region thus creating the potential for two forward spectrometers. In quark-antiquark production at 1.8 TeV, the quark and antiquark are usually either both boosted in the proton beam direction, or both boosted in the an-
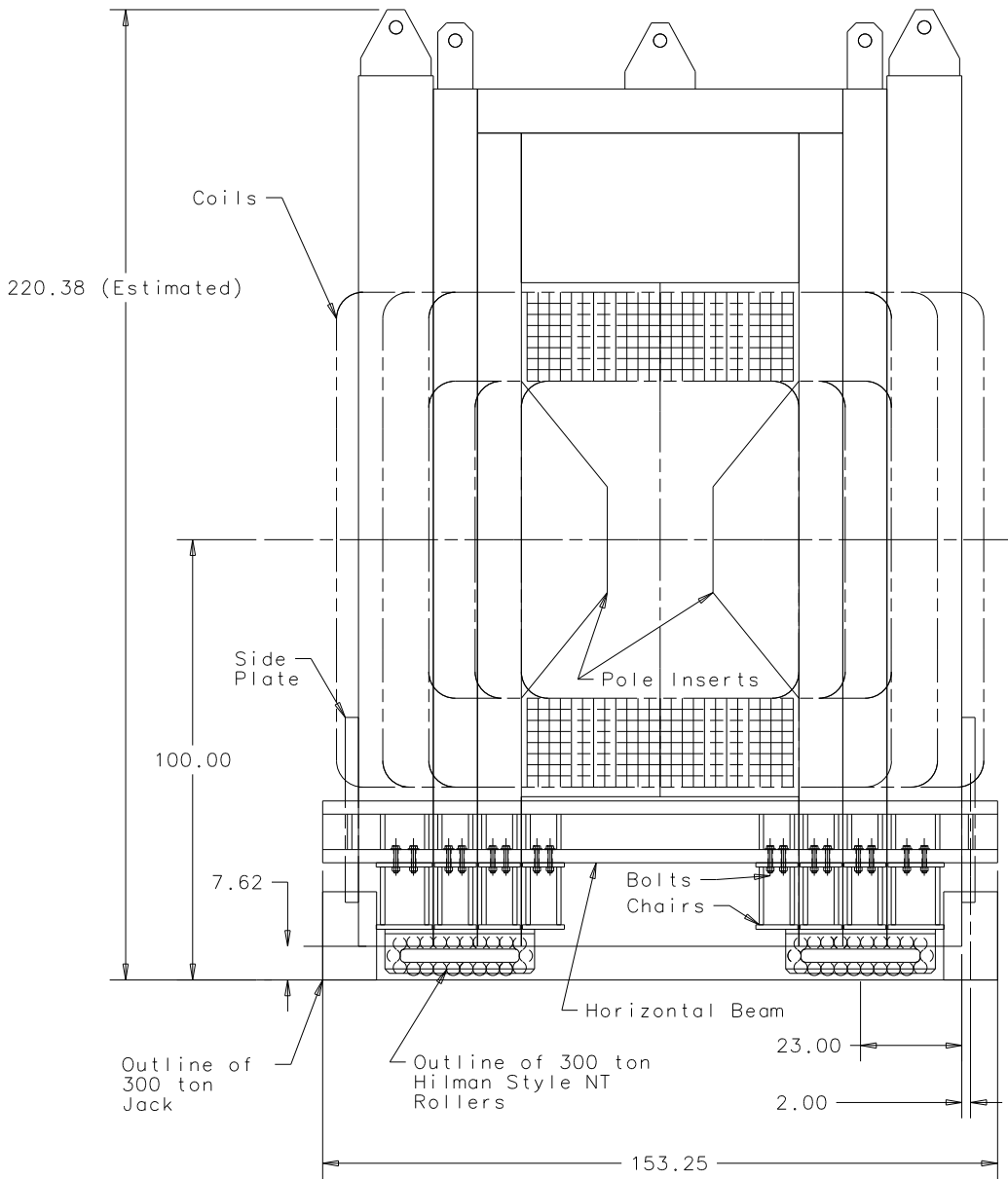
Figure 4.4: Cross section of the modified SM3 dipole with rollers and pole piece inserts. All dimensions are in inches.

Table 4.1: BTeV/C0 Vertex Dipole Properties

Property	Value	Comment
$\int B \times dl$	5.0 T-m	2.5 T-m on each side of center of IR
Central Field	1.5 Tesla	
Steel Length	3.2 m	
Overall length	5.3 m	
Magnet Vert. aperture	± 0.3 rad	
Magnet Horz. aperture	± 0.3 rad	

tiproton beam direction. Thus, having two spectrometers would double the acceptance of the experiment for tagged decays. Nevertheless, we initially plan to construct a single arm spectrometer only. Note that the second uninstrumented side can be used to test new detector concepts or prototypes of production components under actual beam conditions until it becomes possible to instrument the second arm.

In this central dipole geometry, there is a strong magnetic field at the vertex detector. Because of the excellent spatial resolution of the vertex detector, it is possible to get a crude measurement of the track momentum using the vertex detector alone, as outlined in the Pixel Detector section below.

4.4 Pixel Vertex Detector

4.4.1 Introduction

The vertex detector is critical to the success of BTeV. The key goals of the detector are excellent spatial resolution, ease of tracking pattern recognition, radiation hardness, material thinness, and readout of data fast enough for use in the lowest-level BTeV trigger system. The detector design has been guided by these goals, as will be described in the sections below. (This section is organized around these goals.) Many test results and details mentioned breifly here, are described in more detail in the R&D chapter.

4.4.2 Overview of Vertex Detector

The baseline vertex detector consists of a regular array of 30 "stations" of "planar" silicon pixel detectors distributed along the interaction region (Fig. 4.5). Each station contains one plane with the narrow pixel dimension vertical, and one with the narrow dimension horizontal. The stations are split, having a top half and a bottom half. Each half-station contains one (approximately) 5 cm × 10 cm precision vertical-position-measuring half-plane, and a smaller, (approximately) 3.8 cm × 7.3 cm horizontal-position-measuring half-plane. The top half-stations are positioned at regular intervals along the beam, and the bottom halves are similarly positioned, but midway between the top stations. This allows for possible overlap of half-planes with a variable-sized, small hole left for the beams to pass through. Table 4.2 summarizes the properties of the pixel detector.

The vertex detector contains nearly twenty-two million rectangular pixels, each 50 μm × 400 μm. Each sensor pixel is read out by a dedicated electronics cell. The sensor pixel and the readout cell are connected by a "bump bond." The basic building block of the detector is a hybrid assembly consisting of a sensor, a number of readout chips, and a flexible printed circuit (a high-density interconnect, HDI) which carries I/O signals and power. The sensors are variously sized to accept variable numbers of readout chips to make the required half-plane shape. Each readout chip is "flip-chip" mated to 22 columns of 128 rows of pixels on the sensors, corresponding to 2,816 active channels per readout chip. Each readout chip covers an active area approximately 0.64 cm × 0.92 cm. To avoid any dead space between adjoining read out chips, the pixels on the sensors corresponding to the edge of the readout chip (first and last column) are extended to 600 μm. These hybrid assemblies are supported by a movable carbon substrate that allows the pixel sensors to be positioned a safe distance away from the beam-line until stable conditions have been established in the Tevatron, at which point they are moved as close to the beam-line as radiation damage considerations will allow. This substrate also provides cooling for the readout electronics.

Fig. 5.8 shows a conceptual design for the aluminum vacuum vessel and carbon support structure for the pixel detector. The vessel is a rectangular box with a length of $\sim$ 165 cm and a height of $\sim$ 83 cm. Particles within the 300 mrad acceptance of the spectrometer traverse only the pixel stations and the 0.75 mm thick exit window. The carbon substrate
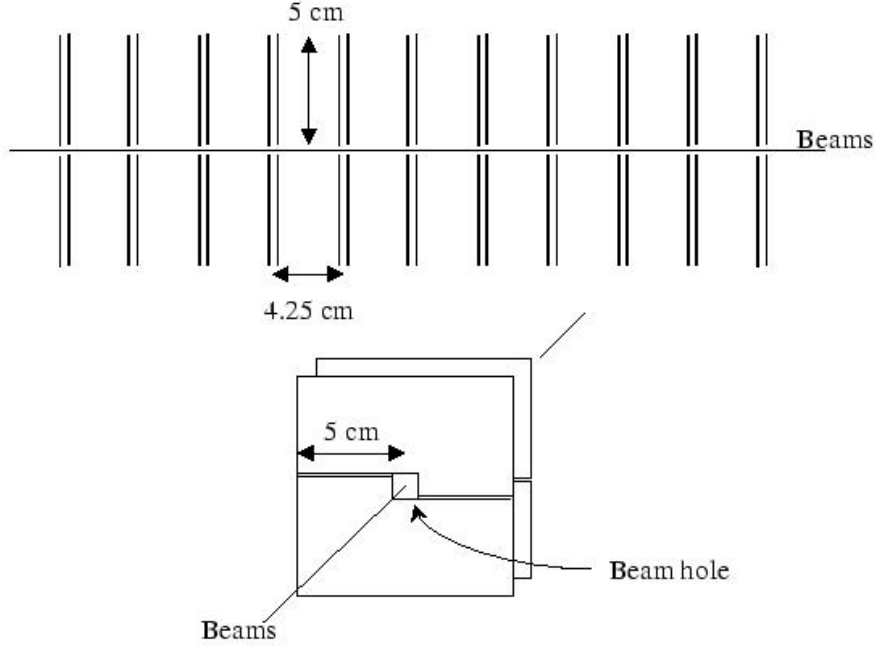
Figure 4.5: Schematic drawing of part of the pixel detector.

will be attached to a support frame made out of carbon fibers. Its position will be controlled by motors located just outside the vacuum vessel.

4.4.3 Spatial Resolution

BTeV test beam studies, performed with prototype sensors and readout having pixel sizes of 50 μm by 400 μm, have demonstrated a spatial resolution between 5 and 9 μm in the narrow dimension, depending on the track angle of incidence (see Fig. 4.7). The solid line shows the resolution function (Gaussian) used for the Monte Carlo studies presented in the BTeV proposal. The figure shows both the resolution obtained using 8-bit charge information directly, and also the resolution obtained by degrading the pulse height to 2-bits of information. This result confirms the prediction of our simulations:that excellent resolution can be obtained using charge sharing, even with very coarse digitization. Based on these results it has been decided that the BTeV readout chip will have a 3-bit FADC in each pixel cell. This will provide excellent spatial resolution. In addition, the actual pulse heights may be used to indicate the presence of δ-rays or γ conversions.

The single hit resolution is made possible by the choice of pixel size and a relatively low threshold for readout (approximately 2500 input electrons equivalent compared to about 24000 electrons for a minimum ionizing track at normal incidence for the devices tested).
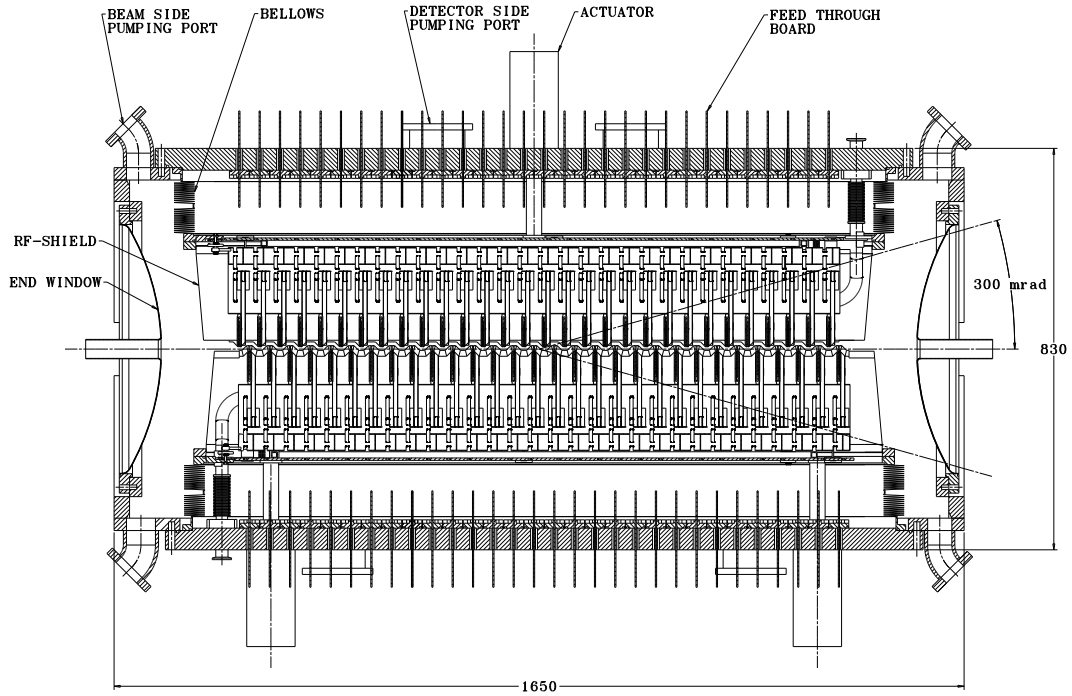
Figure 4.6: Side view of the vacuum vessel and support structure for the pixel detector. The pixel stations are mounted in two halves. Each half sits in a vacuum enclosure separated from the beam by a thin rf shield. Signals are fed through the vacuum vessel via printed circuit boards with high density connectors. Also shown in the figure are actuators and a bellows structure to allow the detectors to be moved in and out of the beam during data-taking and beam refill.

Relatively low dispersion of the thresholds across the chip and low noise in each pixel make the low readout threshold possible. Given the 132 ns beam crossing interval of the Tevatron, time slewing in the chips will not be a problem. While the above performance is for unirradiated devices, we anticipate operation at about -5 °C to minimize effects of radiation damage during the lifetime of the detectors. Mounting stability and the necessary pixel alignment, using actual tracks in the final location, will be important to avoid serious degradation of this good resolution.

While single hit resolution is important, it is not the whole story. We have worked to minimize the multiple scattering due to the material in all the components of the system. In addition to making the components of the detector proper as thin as possible (see Table 4.2), we allow only a thin membrane between the pixel detector and the beams. Thus, the pixel detector will sit in a secondary vacuum with only a thin aluminum rf shield between that vacuum and the accelerator vacuum. The very close proximity to the interaction region and the spacing between pixel planes is kept to a minimum to reduce the extrapolation distances to vertices, both primary and secondary. All these parameters have been optimized using

Table 4.2: Pixel Vertex Detector Properties

Property	Value
Pixel size	rectangular: 50 μm $\times$ 400 μm
Outer Plane Dimensions	10 cm $\times$ 10 cm
Central Square Hole (adjustable)	nominal setting: 12 mm $\times$12 mm
Total Planes	60
Total Stations	30
Pixel Orientations (per station)	one with narrow pixel dimension vertical & the other with narrow dimension horizontal
Separation of Stations	4.25 cm
Sensor Thickness	250 μm
Readout Chip Thickness	200 μm
Total Station Radiation Length (incl. rf shielding)	2.5%
Total Pixels	2.2×10^7
Total Silicon Area	$\approx$0. 6m^2
Readout	analog (almost 3 bits, i.e., 7 thresholds)
Trigger	Signals are used in Level I trigger.
Rate Requirements	Time between beam crossings is 132 ns.
Noise Requirement	desired: $< 10^{-6}$ per channel/crossing required: $< 10^{-5}$ per channel/crossing
Resolution	better than 9μm
Radiation Tolerance	$> 6 \times 10^{14}$ particles/cm^2
Power per Pixel	$\sim$60 μWatt
Operating Temperature	$\sim$-5 °C

detailed (MCFast and GEANT) simulations of our experiment and representative physics measurements.

4.4.4 Pattern Recognition Capability

The early choice of pixel technology for the BTeV vertex detector was based, in part, on the space point information that it provides which will help in pattern recognition. Fig. 4.8 comes from a beam test of BTeV prototype pixel detectors, and shows the power of space points in reconstructing high density tracks. There, an interaction in a carbon target a few mm upstream of the first pixel plane leads to seven tracks reconstructed in much less than 1 cm^2, a density an order of magnitude more than typical for BTeV.

The pattern recognition capability benefits enormously from the low occupancy, averaging slightly above 1 track per B event in the highest rate readout chip. In addition, the stretching
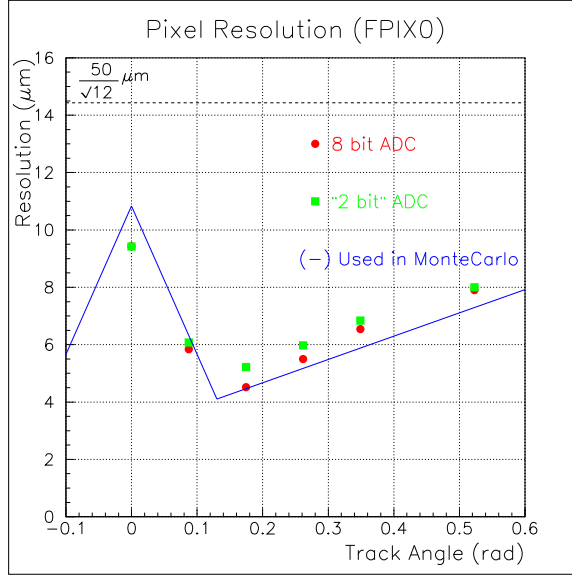
Figure 4.7: Resolution as a function of the angle of the incident beam for both 2-bit and 8-bit ADC readouts. The lines are piecewise linear fits to a simulation of the resolution.

of edge pixels and the shingled mounting (like the lapped wooden siding on a house) of the multichip pixel modules provide complete coverage within the nominal plane acceptance. The regular spacing of planes along the beam also eases the job of the Level 1 trigger.

4.4.5 Radiation Hardness

Solid-state device technology developments since the start of our BTeV efforts have eased concerns substantially in the area of radiation hardness. Our silicon sensors are based on n+/n/p technology as developed by LHC experiments. Our latest readout chips are manufactured with deep sub-micron (0.25 μm) CMOS technology, an inherently radiation-tolerant process, once enclosed-geometry transistors and appropriate guard ring designs are used. No redesign for military radiation-hard technologies, as planned in the past, is required.

Our tests have been made with irradiations up to 0.4×10^{15} 200 MeV protons per cm^2 equivalent for our sensors (about 20 MRad) and 0.74×10^{15} 200 MeV protons per cm^2 (equivalent to 43 MRad) for our readout chips. These tests show acceptable operation of sensors based on current and capacitance curves vs applied bias voltage, in terms of leakage current, required depletion voltage, and breakdown voltage. The readout chips in deep sub-micron technology appear to be even more radiation-hard. Radiation damage does not seriously affect noise, threshold dispersion, etc. up to these irradiation levels. These irradiation results will be augmented with charge collection and other tests in a Meson120 beam as soon as it is available this year. In addition, the measured rates of single event upset are low enough to be handled easily. No evidence of more serious single event effects has been seen. In addition, the plan is to operate the pixel detector at about -5 °C. This will
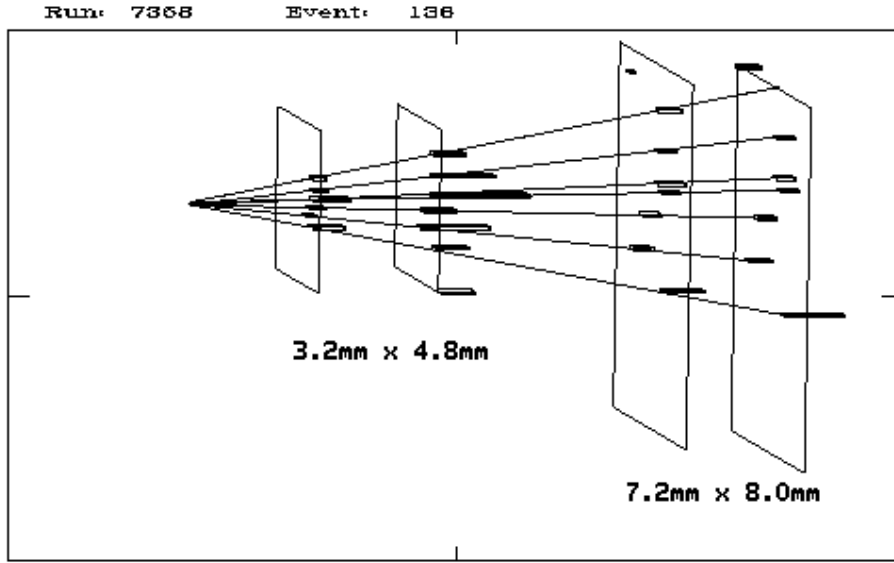
Figure 4.8: Multiparticle interaction observed in Fermilab beam test. The length of each hit is proportional to the pulse height. The straight lines represent fits to the outgoing tracks.

mitigate problems with charge trapping and reverse annealing (the variation in depletion voltage with time).

Finally, we will be testing all components (high density interconnects, adhesives, etc.) in high radiation environments before certification for use in the final detector.

4.4.6   Material Thinness

In order to prevent multiple scattering from decreasing the utility of our precision spatial resolution, we are keeping the material budget as low as possible. Table 4.3 lists the various contributions to our material budget. Note that the sensors and readout chips are thinned relative to what is typically used in high-energy physics today. The high-density interconnects and attached cables are minimal, with decoupling of signal and power cables so that the materials in each can be separately optimized. Both horizontal and vertical measuring half-planes share a single support substrate. The cooling is incorporated into this substrate, its design based on a system of glassy-carbon cooling tubes covered in highly thermally conductive "fuzzy carbon" to transmit heat to the water/glycol cooling fluid. This proprietary technology is required to reach the level of support material listed in Table 4.3. Given the risk in this approach, we are also working on fall-back solutions as described in the R&D chapter.

Table 4.3: Material budget of a BTeV pixel plane. The "Coverage" column shows the factors applied to account for overlaps of the sensors and readout chips, and for geometric coverage (e.g. area covered by bump bonds/total area); substrate coverage is listed as 0.50, because one substrate is shared by two planes. The numbers given for components on the HDI and for adhesive are derived from the ATLAS Pixel Detector TDR [1].

$Item$	$Thickness(mm)$	$X_0(mm)$	$Coverage$	$X/X_0(\%)$
$Sensor$	0.25	93.6	1.46	0.39
$Readout\ chip$	0.20	93.6	1.47	0.31
$Bumps\ and\ wire\ bond$	0.02	10.0	0.02	0.004
HDI	0.224	284	1.00	0.20
$Components\ on\ HDI$				0.02
$Adhesive$				0.02
$Substrate(C-C)+coolant$	0.5	427	0.50	0.15
$Shielding(Al)$	0.15	89.0	1.00	0.16
$Total$				1.25

4.4.7   Readout Speed

Our pixel readout is data-driven. That is, the readout occurs as soon as data is ready on the readout chip. The token passing from row to row, which is an important part of the potential readout speed, is very fast (0.125 ns per row), and this starts in parallel in all columns. The readout rate allows us to move all the data off chip with negligible loss of data, even if the amount of data is three times that projected for our nominal luminosity of 2×10^{32} cm^{-2}s^{-1}. Data output is serialized, but uses a number of parallel readout paths selectable for each readout chip. The bandwidth of each serial path is 140 Mbps. The chips located closest to the beam are each read out using 6 serial paths (840 Mbps total). Other chips are read out using 1, 2, or 4 serial paths. Most of the readout chips in the pixel system require only 1 serial output path. The readout bandwidth summed over the entire pixel detector is approximately 2 Tbps (terabits per second). The data coming off the chip is already highly sparsified, since only pixels above threshold are read out. Sorting out the data and assembling events is done external to the detector in large buffer memories.

4.4.8   Physics Capability

Figure 4.9 shows the distribution of L/σ(L), which is the normalized detachment between the primary vertex and the B decay vertex, for reconstructed decays $B_s \rightarrow D_s^- K^+$, where, $D_s^- \rightarrow \phi\pi^-$ and $\phi \rightarrow K^+K^-$. The mean value is 44 standard deviations! Figure 4.10 shows the L-resolution and the proper time resolution for the B_s decay. The resolution in proper time is 46 fs even for this complex multibody decay containing a tertiary vertex (the D_s^-

decay). This can be compared with the B_s lifetime of ~1500 fs or the B_s mixing period of ~400 fs if x_s is about 25. It is clear that the BTeV vertex detector has abundant resolution to carry out detailed time-dependent analyses even if the B_s were to have a surprisingly high oscillation frequency.
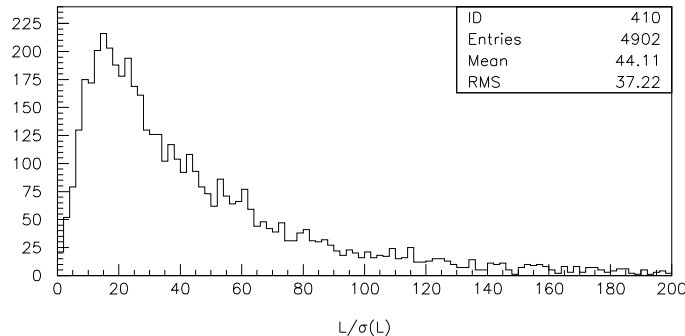

Figure 4.9: Normalized detachment, $L/\sigma(L)$, between the primary vertex and the decay vertex for the decay $B_s \to D_s^- K^+$.

4.4.9 Summary

Over the last four years, BTeV collaborators have been working vigorously to establish a pixel detector capability for Fermilab, tuned to the unique features of the Tevatron crossing time and BTeV trigger needs. Since the earliest concerns were related to sensors, readout, and bump bonding, the primary focus has been on those issues. Progress has been gratifyingly rapid. This progress is evident in the success of the test beam effort at Fermilab, the results of which validate the ideas used for the BTeV proposal. The proposal to use a "shingled" fuzzy carbon support and cooling structure is undergoing mechanical and cooling capacity tests, as is a beryllium alternative.

Yields of all pixel-related components have been high enough that thus far we have made working prototypes without major production duplications. Thus, we may hope that our focus on simplicity within our aggressive technical approach will succeed. This approach, combined with the early implementation of a significant subsample (~10%) of final-design detectors, should allow reliable planning and achievment of the goals of the experiment.
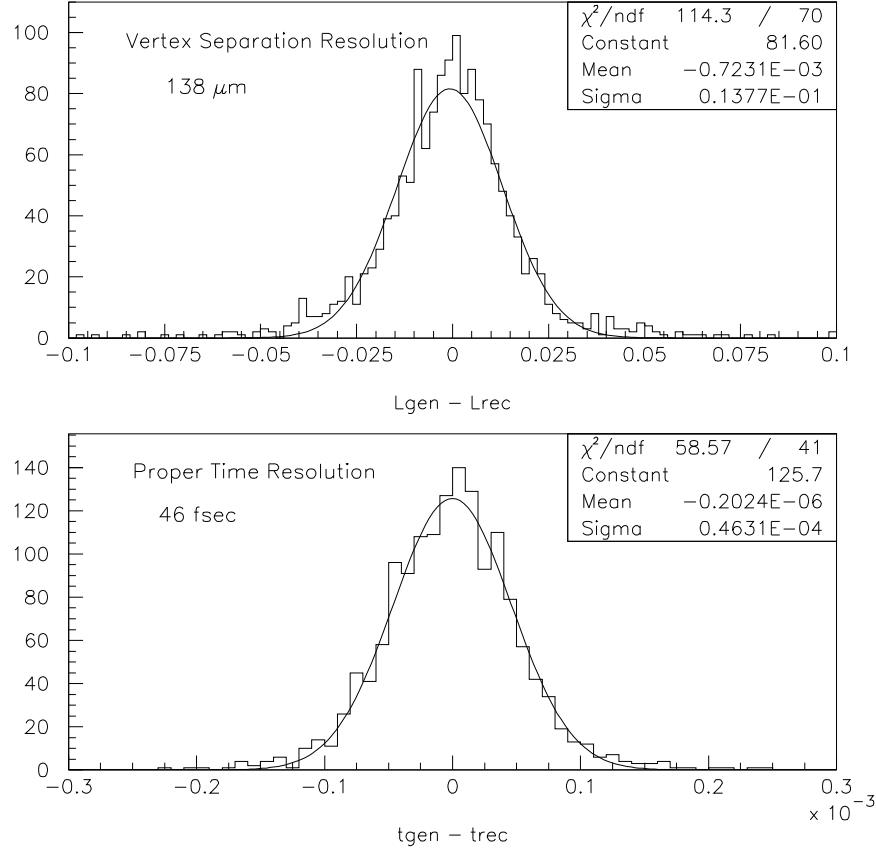
Figure 4.10: Top) The resolution in L, the separation between the primary and secondary vertex. The quantity plotted is the difference between the Monte Carlo generated separation L_{gen} and the reconstructed separation L_{rec}, for the B_s decay. The X- axis is in cm. The L resolution is 138 μm; and bottom) resolution in proper time. The quantity plotted is the Monte Carlo generated proper time t_{gen} minus the reconstructed proper time, t_{rec} of the B_s decay. The X-axis is picoseconds (10^{-3} nanoseconds). The proper time resolution is 46 fs.

4.5   Forward Tracking System

4.5.1   Introduction

The major functions of the forward charged particle tracking system are to provide high precision momentum measurements for tracks found in the pixel system, to reconstruct and measure all parameters for tracks which do not pass through the vertex detector (such as K_s and Λ^o daughter tracks), and to project tracks into the RICH counters, EM calorimeters, and Muon detectors. Measurements from the forward tracking system are also used online in the Level 3 trigger, as explained below.

4.5.1.1   General Description

The baseline forward tracking system consists of 7 stations in one arm, placed transversely to the beam at various distances from the interaction point. Three stations are placed inside the dipole magnet, three stations in the low field region just upstream of the RICH, and one station just downstream of the RICH. The entire system extends over a distance of $\sim$7 m and provides polar angle coverage from approximately 10 mr up to 300 mr.

The design of the forward tracking system has been driven by the high density of tracks produced in the forward direction, especially with multiple interactions per crossing. Two different types of detectors are used. Most of the solid angle is instrumented using straw tube drift chambers. Straws have been chosen because they can be used to make large chambers with small cell size, and because they are immune to catastrophic failure of an entire detector from a single wire break. The track density very close to the beam requires detectors with even higher granularity; we have chosen to instrument the central section of each station with silicon microstrip detectors.

Tables 4.4 and 4.5 list all the geometric parameters and the main characteristics of the forward tracker. This forward tracking system configuration has sufficient segmentation to handle the high hit multiplicities that are expected when $b\bar{b}$ events are produced in the forward region along with minimum bias events. Fig. 4.11 shows occupancies in the straw tracker predicted by BTeVGeant for the case in which a $b\bar{b}$ event is produced at the design luminosity of 2×10^{32} cm^{-2} s^{-1}. The maximum occupancy is 4% in the silicon strip detectors, which have 40 times finer pitch than the straw chambers.

4.5.1.2   Forward Tracker Performance

The system just described ensures excellent tracking performance over the full acceptance of the forward spectrometer. Figure 4.12 show the expected average fractional momentum resolution for b decay products as a function of track momentum and of the track production angle with respect to the beam axis. For these histograms, an effective position resolution of $\sigma_{X,U,V} = 150$ μm was assumed for each view of the straws and a resolution of $\sigma_{X,U,V} = 29$ μm assumed for the silicon strip detectors.

Table 4.4: Properties of the baseline forward straw tracker (1 arm)

Property	Value
Straw size	4 mm diameter
Central hole	27 cm × 27 cm
Total Stations	7
Z positions (cm)	95, 138, 196, 288, 332, 382, 725
Half size (cm)	27, 41, 61, 88, 102, 116, 204
Views per station	3 (X,U,V)
Layers per view	3
Total number of straws	29,088
Total station thickness	0.6% X_0
Total channels	58,176
Readout	ASD + timing chip (6 bits), sparsified

Table 4.5: Properties of the baseline forward silicon tracker (1 arm)

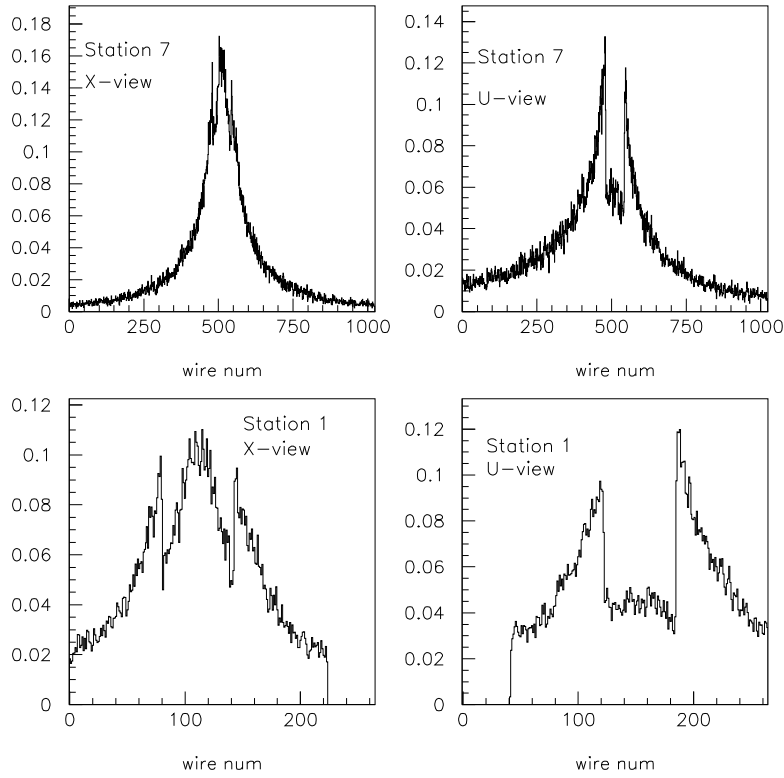| Property	Value
Si-sensors	$\sim 7 \times 7$ cm^2, p-on-n type
Pitch	100 μm
Thickness	200 μm
Sensor configuration	4 ladders of 4 sensors
Coverage	27cm × 27cm
Central hole	5.4 cm × 5.4 cm (7 cm × 7 cm in last station)
Total stations	7
Z positions (cm)	99, 142, 200, 292, 336, 386, 729
Views per station	3 (X, U, V)
Channels per view	$\sim$5,600
Total channels	$\sim$127,600
Readout	sparsified binary

Figure 4.11: Occupancies in the first station of straws, Station 1, and the station just upstream of the EM Calorimeter, Station 7, when a $b\overline{b}$ event is produced at the design luminosity of 2×10^{32} cm^{-2} s^{-1}. The two histograms on the left are for X-view straws, while those on the right are for U-view straws. The V-views have identical occupancies to the U-views.
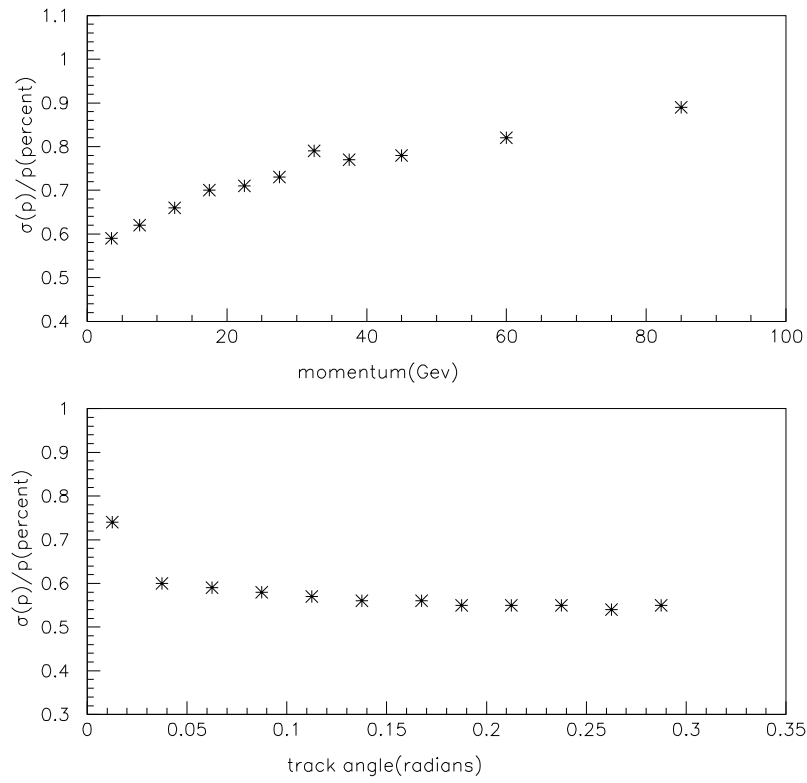
Figure 4.12: Momentum resolution as a function of track momentum (upper plot) and as a function of polar production angle (lower plot) for b decay products.

114

4.5.2 Forward Silicon Tracker

4.5.2.1 Detector Description and Layout

Our design consists of stations with three planes of 200 μm thick single-sided silicon microstrip detectors with 100 μm pitch. The silicon sensors, which have an area of 7×7 cm^2, are arranged in ladders of 4 daisy-chained sensors each in such a way that four adjacent ladders form a plane as illustrated in Fig. 4.13. The ladders are mounted on a low mass carbon fiber support which is designed to ensure a relative proper alignment among all the elements of the plane and also among different planes of the same station as described in the R&D section of this document.
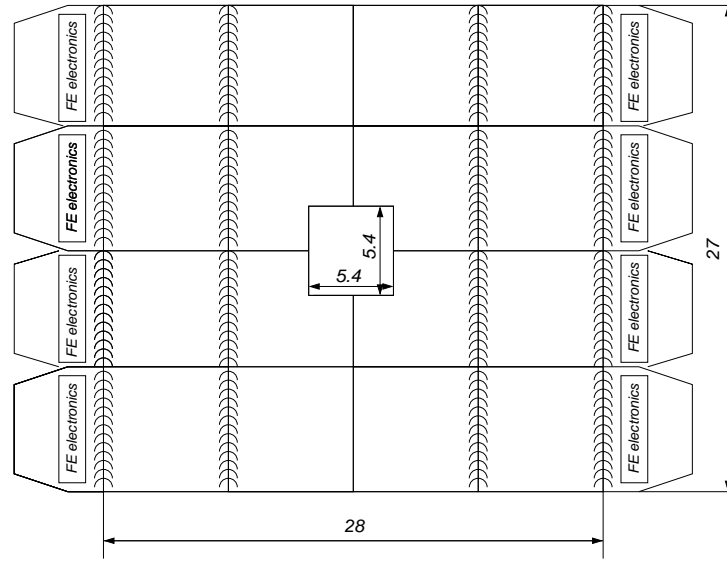

Figure 4.13: Sketch of a silicon detector plane. It consists of 4 ladders of four daisy-chained Si-sensors. The two pairs of sensors on each ladder are read-out separately by the front-end electronic chips placed at the two ends of the same ladder. There is some overlap between adjacent ladders to ensure good efficiency over the entire plane. Dimensions are in centimeters.

Three views, called X, U and V, are provided by rotating two of the planes. The two stereo views, U and V, are at $\pm$ 11.3^o around the Y bend coordinate. Each plane consists of about 5,600 readout channels; the entire system of 7 stations has about 128,000 channels in total (1 arm).

The Si-sensors are of the standard p-on-n type, with multiple guard rings to allow high voltage operation. The front-end electronics is distributed along the two opposite edges of each plane where it is cooled by a fluid circulating in a duct embedded in the support structure around the periphery of the plane.

The preamplifier chips are AC coupled to the strips by means of capacitors directly

integrated on the sensors. Each channel is read out in binary mode providing a $\sigma = 100$ $\mu\mathrm{m}/\sqrt{12}= 29$ μm resolution, adequate for our physics goals.

We do not foresee any major problems in building these detectors since we can profit from the enormous experience accumulated in CDF and D0 at the Tevatron, as well as other experiments, and from the ongoing R&D programs for LHC.

4.5.2.2   Radiation Issues

It is well known that the exposure of silicon detectors to high radiation doses causes damage that limits their useful lifetime. Thanks to the enormous progress accomplished during the last few years, we can now build detectors that can be operated after exposure to fluences in excess of 10^{14} particles/cm^2 [5].

In BTeV, we expect a radiation level at the silicon detectors that decreases rapidly with increasing distance from the beam. Important radiation damage effects, if any, will be confined to a small region closest to the beam line.

The highest levels of radiation occur at the station closest to the interaction region. As shown in Fig. 4.14, the maximum value of the fluence is expected to be $\sim 1.6 \times 10^{13}$ particles/cm^2/year, given a luminosity of 2×10^{32} cm^{-2} s^{-1}. This is slightly less than the dose expected for Layer 0 of the CDF silicon tracker at the same luminosity [6]. With a proper choice of sensors, we will operate our detectors with a safety margin superior to that of CDF and those of LHC experiments. In the worst case scenario, we can expect serious radiation damage effects only on a minor portion of our detectors close to the beam after several years of operation.

4.5.2.3   Readout Electronics

Even given the low occupancy expected in the Forward Silicon Tracker, the output bandwidth required to read out all hit information from every crossing is higher than is provided by any silicon strip detector (SSD) readout chip, either already fabricated or being developed for another experiment. For this reason we have decided to develop a new readout chip with very high readout bandwidth. We will also take the opportunity to design a continuous-time-filter preamplifier capable of exploiting all the advantages offered by the relatively long bunch-crossing period of the Tevatron collider (T = 132 ns). We are designing a new preamplifier which should feature an ENC $\sim$1000 e^- for semi-Gaussian shaping with 100 ns peaking time and a capacitive load at the input of $\sim$20 pF, as expected for our longest strips. This noise performance represents in our view "the state of the art" for silicon strip preamplifiers.

The binary readout we are presently considering is a simplified version of the readout scheme implemented in the FPIX2 pixel readout chip. It is very fast and employs a flexible scheme for zero-suppression and readout, that can be easily adapted to strips. The SSD readout chips will be designed to interface to the same electronics we will employ to read out pixel chips.

The new read-out chip will be implemented using 0.25 μm CMOS technology, following the radiation tolerant design rules developed for the FPIX2 design.
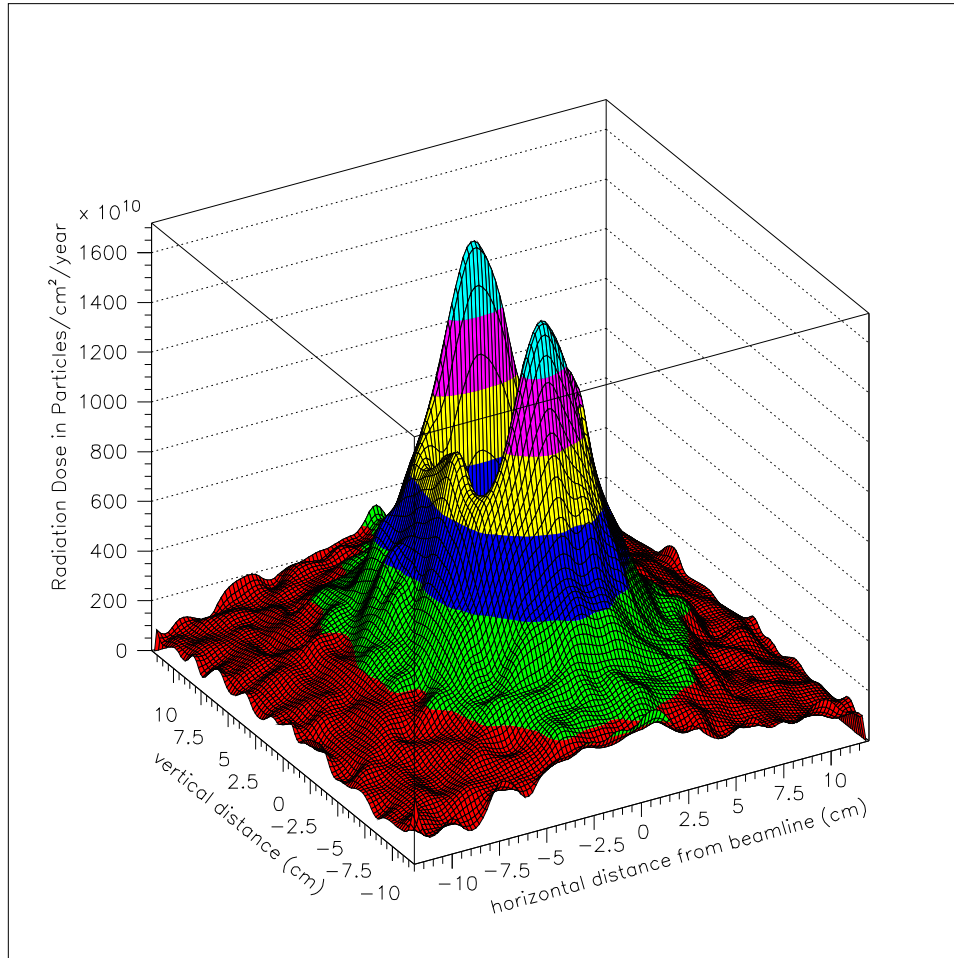
Figure 4.14: Radiation dose as a function of position in Forward Silicon Tracker Station # 1. The horizontal magnetic field concentrates more particles above and below the square central beam hole than on either side.

Figure 4.15: A photograph of one of the BTeV 3.97mm diameter × 8mm length twisters. The material is Ultem plastic. Of key importance is the smooth cut edges, which prevent the sense wire from snagging during the stringing process. The depth of the spiral groove is 2.00 mm, which nominally centers the 25 micron sense wire along the longitudinal axis of the twister.

4.5.3 Forward Straw Tracker

4.5.3.1 Detector Description and Layout

The forward straw tube tracker consists of stations that provide 3 coordinate measurements, X, U and V, where the two stereo views, U and V, are at $\pm$ 11.3^o around the Y bend coordinate, same as in the forward silicon detector. With three layers per view, this configuration provides excellent resolution in the bend plane while maintaining a robust ability to reject ghost combinations of hits. It has sufficient redundancy to achieve a high detection efficiency and to resolve the left/right ambiguity a very large fraction of the time. The unit of construction is the "half-view", itself composed of a number of 48 straw modules. Two half-views fit around the beampipe to make up a single view.

All the sense wires for the straw cells that do not terminate at the central hole are divided electrically using a small glass capillary bead following the technique used for the ATLAS TRT [3]. This cuts the occupancy rates in half. In addition, within a 27 cm square region of the beam pipe, all straw sense wires are deadened by using two glass capillary beads to isolate the central section of the sense wire. This is done to lower the straw occupancy rates. This region is covered by the Silicon Strip tracker. The sense wires in straws that span more than 80 cm have additional supports (twisters), which are realized following the helical design developed for the SDC Straw Prototype. One of our twisters is shown in Fig. 4.15.

The smooth edges avoid any sense wire snags during the stringing process.

The time between bunch crossings in the Tevatron will be 132 ns by the time BTeV is operational. This time allows the use of standard gases like Argon-Ethane or Argon-CO_2, which have drift times in our 4mm straws on the order of 60 ns. We are undertaking an extensive R&D program on the aging properties of these and other gases.

4.5.3.2   Front End Electronics and Drift Time Measurement

The straw tube chambers will be instrumented using electronics developed by the University of Pennsylvania [4], initially for the SDC straw chambers, the CDF Central Outer Tracker and more recently for the ATLAS TRT. These radiation hard integrated circuits include high gain preamplifiers, pole-zero networks for pulse shaping and ion-tail cancellation, and leading edge discriminators.

The drift time will be measured using digital TDC's. The information from the straw tracker, like all information from every subsystem in the BTeV spectrometer, must be digitized and read out for every crossing. This means that a new TDC must be designed for BTeV. The small diameter of the straws makes the specifications of this TDC easy to achieve. A six-bit single-hit TDC, with 1.5 ns wide bins covering 96 ns, is sufficient to provide a drift distance measurement precision better than 100 μm. It is worthwhile recalling that even without a TDC, we can locate the track in a particular view with an rms uncertainty of 600 μm.

4.5.3.3   Technical issues

We are developing a prototype straw tube which places an aluminum conduction layer between two Kapton films, the inner one next to the gas volume being a carbon loaded, low resistivity film. The idea is that the Kapton forms a protective barrier, similar to the graphite layers deposited on the inner surface of the ATLAS TRT straws. Without this protective barrier, there is a danger that the aluminum layer may be etched away, limiting the lifetime of the straw. We measured the surface resistivity of the aluminum coated, carbon loaded Kapton film of our prototype to be 6.5 ± 1.0 Ω/square, which is comparable to the specified value for the TRT straw tube. The details of the prototype straw material are listed in Table 4.6.

Currently we have built multiple single straw prototypes using this straw. We have measured gas gains and gain uniformity along the straw, with the straw straightness provided by tensioning the straw. A one meter, two-module (96 straws in total) prototype detector (Fig 4.16) is under construction. It will be tested in the Fermilab Test Beam this year.

Description	BTeV Straw Prototype
Kapton film	Inner: Polyimide type XC
	25 ± 2.5 μm thickness
	Outer: Polyimide type 100 VN
	25 ± 2.5 μm thickness
Density	1.42 g/cm^3
Aluminum layer	$(0.2 \pm 0.08)\mu m$ thickness
Resistivity of inner Kapton layer	6.5 ± 1.0 Ω/square

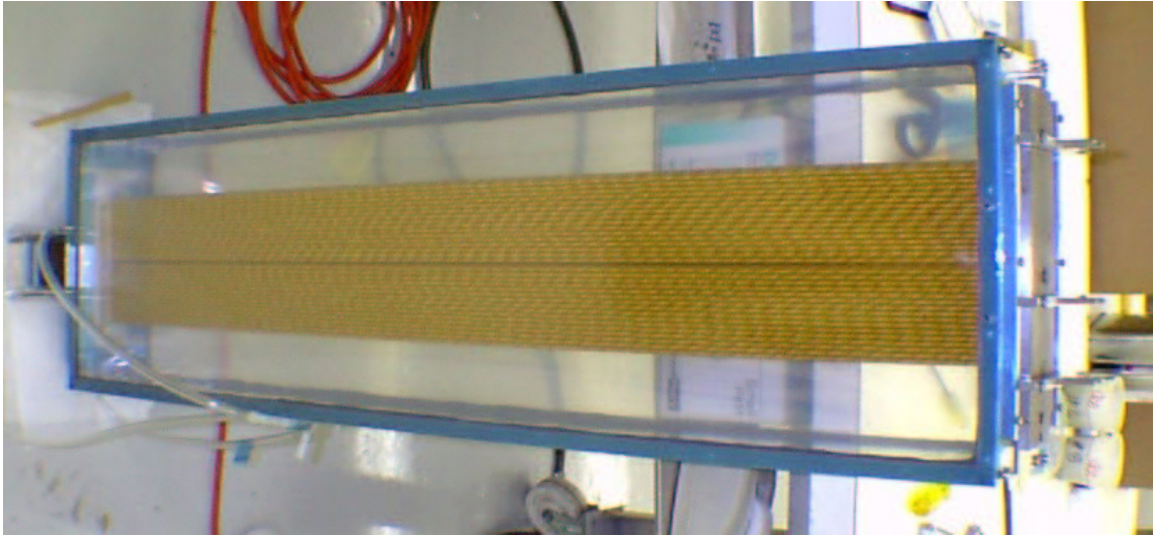Table 4.6: Summary of material specifications for the BTeV prototype straw tubes

Figure 4.16: The BTeV Straw Prototype Detector (under construction) showing the modularity which is anticipated for the actual detector. Each module contains 48 straws, in three close-packed planes.

4.6 Charged Particle Identification

Excellent charged hadron particle identification is a critical component of a heavy quark experiment. Even for a spectrometer with the excellent mass resolution of BTeV, there are kinematic regions where signals from one final state will overlap those of another final state. For example, $B_s \rightarrow D_s K^-$ signal must be distinguished from $B_s \rightarrow D_s \pi^-$ background in order to measure the CKM phase γ. These ambiguities can be eliminated almost entirely by an effective particle identifier. In addition, many physics investigations involving neutral B-mesons require "tagging" of the flavor of the signal particle by examining the properties of the "away-side." Our studies show that kaon tagging is a very effective means of doing this. "Same-side" kaon tagging is also very effective for B_s mesons.

4.6.1 Requirements

In the design of any particle identification system, the dominant consideration is the momentum range over which efficient separation of the various charged hadron types – π, K, and p – must be provided. In BTeV, the physics goal which sets the upper end of the momentum requirement is the desire to cleanly separate $B_d^o \rightarrow \pi^+ \pi^-$ from $B_d^o \rightarrow K^+ \pi^-$ and $B_s^o \rightarrow K^+ K^-$. These two-body decays produce reasonably high momentum pions and kaons. Fig. 4.17 shows the momentum distribution of pions from the decay $B_d^o \rightarrow \pi^+ \pi^-$ for the case where the two particles are within the spectrometer's acceptance. The low momentum requirement is defined by having high efficiency for "tagging" kaons from generic B decays. Since these kaons come mainly from daughter D-mesons in multibody final state B-decays, they typically have much lower momentum than the particles in two body decays. Fig. 4.18 shows the momentum distribution of tagging kaons for the case where the signal particles are within the geometric acceptance of the spectrometer. About 1/5 of the tagging kaons never exit the end of the spectrometer dipole. Almost all kaons exiting the dipole have momenta above 3 GeV. Based on these plots, we have set the momentum range requirement for the particle identification system to be

$$3\,\mathrm{GeV/c} \quad < \quad P_{particle\ id} \quad < \sim 70\,\mathrm{GeV/c} \tag{4.1}$$

Finally, kaons and pions from directly produced charm decays have momenta which are not very different from the kaons from B-decays. The range set by the B-physics requirements is a reasonable, if not optimal, choice also for charm physics.

4.6.2 RICH radiators

Because of the large particle momenta there is really only one choice of detector technology – a gaseous ring-imaging Cherenkov counter. Pions and kaons can be separated in the required momentum region with a single gas radiator. We choose C_4F_{10} which has an index of refraction of 1.00138 in the visible range. The momentum dependence of the Cherenkov angle for pions, kaons and protons in this gas is shown in Fig. 4.19. Many other experiments
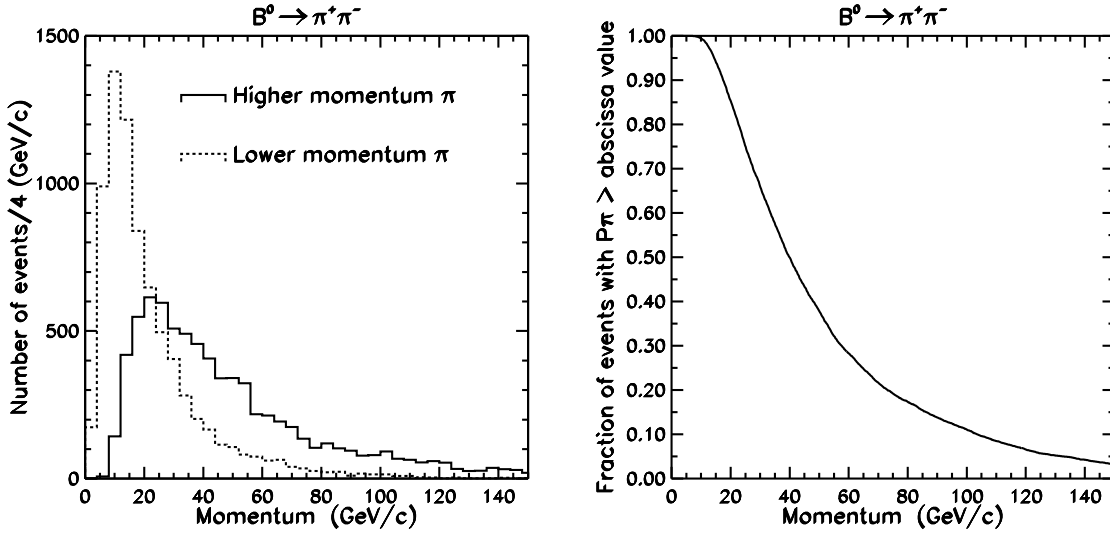
Figure 4.17: The momentum distribution of pions in $B_d \to \pi^+\pi^-$ decays. The left plot shows distributions for the lower (dashed line) and higher (solid line) momentum pion in this decay. The right plot presents the latter distribution in integral form, which gives loss of efficiency as a function of the high momentum cut-off of the particle ID device.

use this gas, including DELPHI (endcap) [7], HERA-B [8] and HERMES [9]. It was also chosen for one of the LHCb RICH detectors [10].

Note that below about 9 GeV, no gas can provide K/p separation and that, since kaons are below threshold, the RICH operates in a threshold mode for (K or p) vs. π separation (except that it has much better noise discrimination than a normal threshold counter because it still measures a Cherenkov ring for pions). K/p separation turns out to be important for b-flavor tagging. In the case of the B_s^o, we use a positively identified kaon for for both "same side" and "away-side" tagging. For the B_d, only the "away-side" case requires kaons. In the "same side" tag, there is a strong correlation between the sign of the fragmentation kaon and the flavor of the B_s. However, the tagging fragmentation kaon comes from the primary vertex which also contains many protons that can cause false tags. In "away-side" tagging, the lack of K/p separation prevents one from distinguishing kaons from $p, \bar{p}$, which occur 8% of the time in B meson decays and a much larger $\sim 50\%$ for Λ_b decays.

In the BTeV proposal, there was a plan to improve identification of low momentum particles by inserting a thin (~ 4cm) piece of aerogel at the entrance to the gas RICH as proposed by LHCb [11] and already implemented by HERMES [9]. The Cherenkov rings were focused by the mirrors of the RICH and fell on the same photon detector array (somewhat enlarged) as the Cherenkov photons emitted in the C_4F_{10}. A study using detailed reconstruction of the Cherenkov rings showed that the relatively low light yield of the aerogel, combined with confusion from the larger number of overlapping rings from higher momentum tracks radiating in the C_4F_{10}, resulted in very little particle discrimination.

Recently, a new plan has bean adopted in which the aerogel radiator is replaced by a
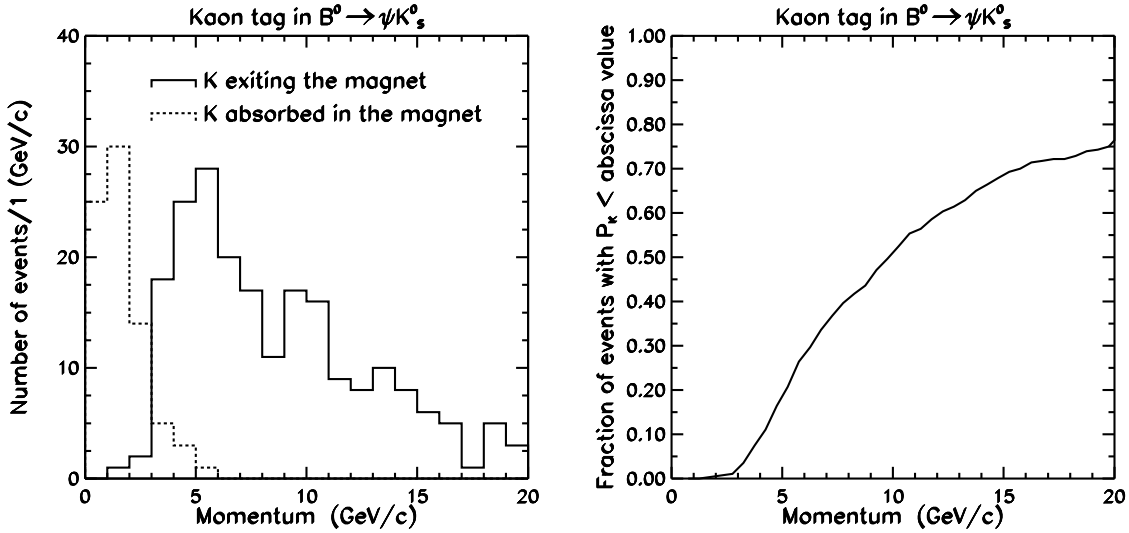
Figure 4.18: The momentum distribution of "tagging" kaons for the case where the signal particles (ψK_S^0) are within the geometric acceptance of the spectrometer. The left plot shows distributions for kaons absorbed in (dashed line) and exiting from (solid line) the magnet. The right plot presents the latter distribution in integral form, which gives loss of efficiency as a function of the low momentum cut-off of the particle ID device.

liquid radiator. The selected liquid, C_5F_{12}, has an index of refraction of 1.24, compared to 1.03 of aerogel. This produces more intense Cherenkov rings even from a very thin layer of liquid. The rings are also larger so that 2/3 of the photons impinge on the side walls of the RICH gas containment vessel, which is covered with photomultipliers to record them. The Cherenkov photons radiated in the gas radiator (C_4F_{10}) are reflected and focused by the RICH mirror and almost never arrive at the side walls. Thus, the two main limitations of the aerogel scheme, the low amount of Cherenkov light and the confusion between Aerogel photons and C_4F_{10} photons are eliminated. At the same time, the refractive index of C_5F_{12} is low enough, that kaon and proton rings have very different radii, even at 9 GeV, and can be distinguished with relatively large diameter photomultiplier tubes (to keep the cost low). Although about 1/3 of the photons from the liquid radiator are focused by the RICH mirror, they are imaged outside the sensor planes which detect the C_4F_{10} photons and thus cause no problem to the RICH pattern recognition.

4.6.3   RICH dimensions

The RICH detector can be located behind the tracking chambers just outside the central dipole magnet, about 4 meters away from the interaction point. The length of the RICH detector must be less than 3 meters to allow sufficient space for the EM calorimeter and the muon system.

The liquid radiator with thickness of about 1 cm will be mounted at the entrance to the
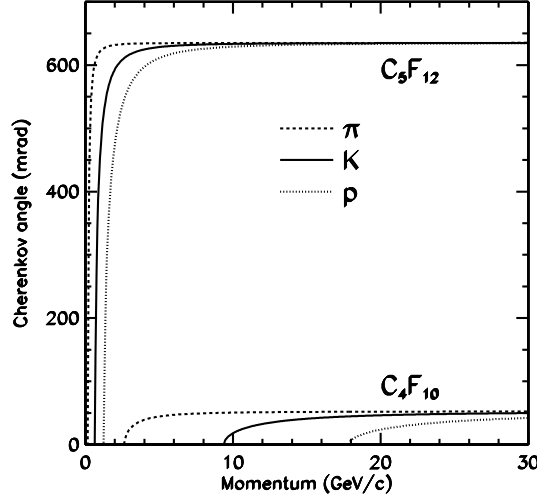
Figure 4.19: Cherenkov angles for various particle species as a function of particle momentum for C_4F_{10} and liquid C_5F_{12} ($n = 1.24$) radiators.

RICH vessel. It will cover the entire RICH entrance window, except for a rectangular square around the beam-pipe. The liquid is supported by a 3 mm thick carbon fiber backplane and a 3 mm thick quartz window (for radiation hardness).

Spherical mirrors at the end of the gas volume reflect Cherenkov photons, radiated in the C_4F_{10} and focus them into rings at the photo-detection surface. The photo-detectors should be located away from the flux of particles exiting the magnet, therefore the mirrors are tilted. In order to minimize geometric aberrations from an off-axis mirror configuration, the mirrors will be split along the mid-line of the detector, reflecting photons to photo-detectors located on each side of the vessel in the non-bend view ($x - z$ plane). The longer the RICH detector the smaller the tilt angle. Since the geometric aberrations due to the mirror tilt are significant for the gas radiator, we plan on the longest RICH detector we can accommodate within the space limitations. This also maximizes the photon yield from the gaseous radiator, again improving the resolution of the device. Thus, the gas radiator will be approximately 3 meters long and the mirror radius will be 7 meters. The mirror tilt angle will be 261 mrad. Note that the mirror tilt angle cannot be further reduced by use of additional flat mirrors at the other end of the detector, as in the designs of HERA-B and downstream LHC-b RICH detectors, since the front of the gas volume must stay transparent to the C_5F_{12} photons. (Such a scheme would be difficult even without the liquid radiator since there is not enough lateral space in the experimental hall.) The transverse size of the mirror will be about 4 m × 4 m. A possible configuration for the mirrors is to make them from an array of individual hexagons. Each mirror half would consist of 18 full hexagons (76.2 cm tip-to-tip) and 6 half hexagons. A reflectance efficiency of about 90% has been achieved in HERA-B detector with 7 mm thick Pyrex coated with 200 nm Al and 30 nm MgF_2. We are investigating lower mass mirror materials.

124

To find the size and optimal position and orientation of the photo-detection surface, we have used a ray tracing Monte Carlo. Even though the true focal plane of a spherical mirror is not planar, non-planar surfaces do not improve resolution significantly and are difficult to realize in practice. Thus, we have assumed that the Cherenkov rings are focused on a plane. Photo-detection systems considered (see the next section) work the best for normal light incidence. Thus the photo-detection plane must be tilted in the $x - z$ plane to follow the mirror tilt. Simulation indicates that a tilt by 442 mrad produces normal incidence on average. Since the actual emission point along the track for Cherenkov photon is unknown, the Cherenkov angle reconstruction assumes emission at the track mid-point. The emission point error contributing to Cherenkov angle resolution is magnified by mirror tilt from 0.2 mrad to 0.53 mrad. This error imposed by geometrical considerations sets the scale for the other two major contributions to Cherenkov angle resolution: chromatic error and photo-detector segmentation error (called also photon position error) which can be controlled by parameters of the photo-detection devices.

The photons generated in the liquid radiator pass through the quartz exit window and enter the C_4F_{10} gas volume. Most of the photons reach the sides of the RICH gas containment box. The sides, top, and bottom of the box contain arrays of 3" diameter photomultipliers to detect these photons.

The geometry of the proposed RICH detector is shown in Fig. 4.20. A 3-dimensional representation is given in Fig. 4.21.
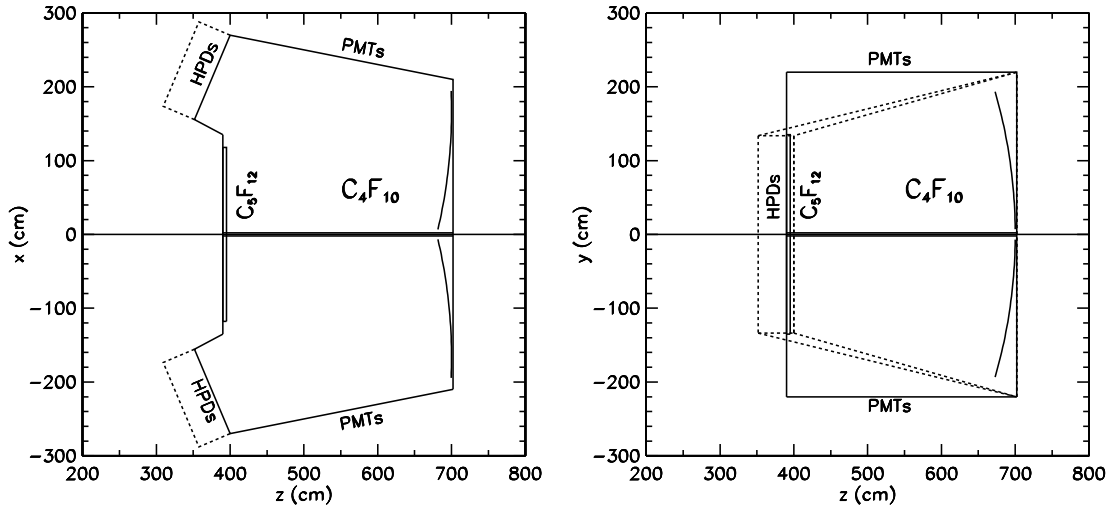

Figure 4.20: BTeV RICH geometry outline. The figure on the left is a plan view and the one on the right is an elevation view. Note the position of the C_5F_{12} on the upstream window and the location of the HPD and photomultiplier sensor planes.
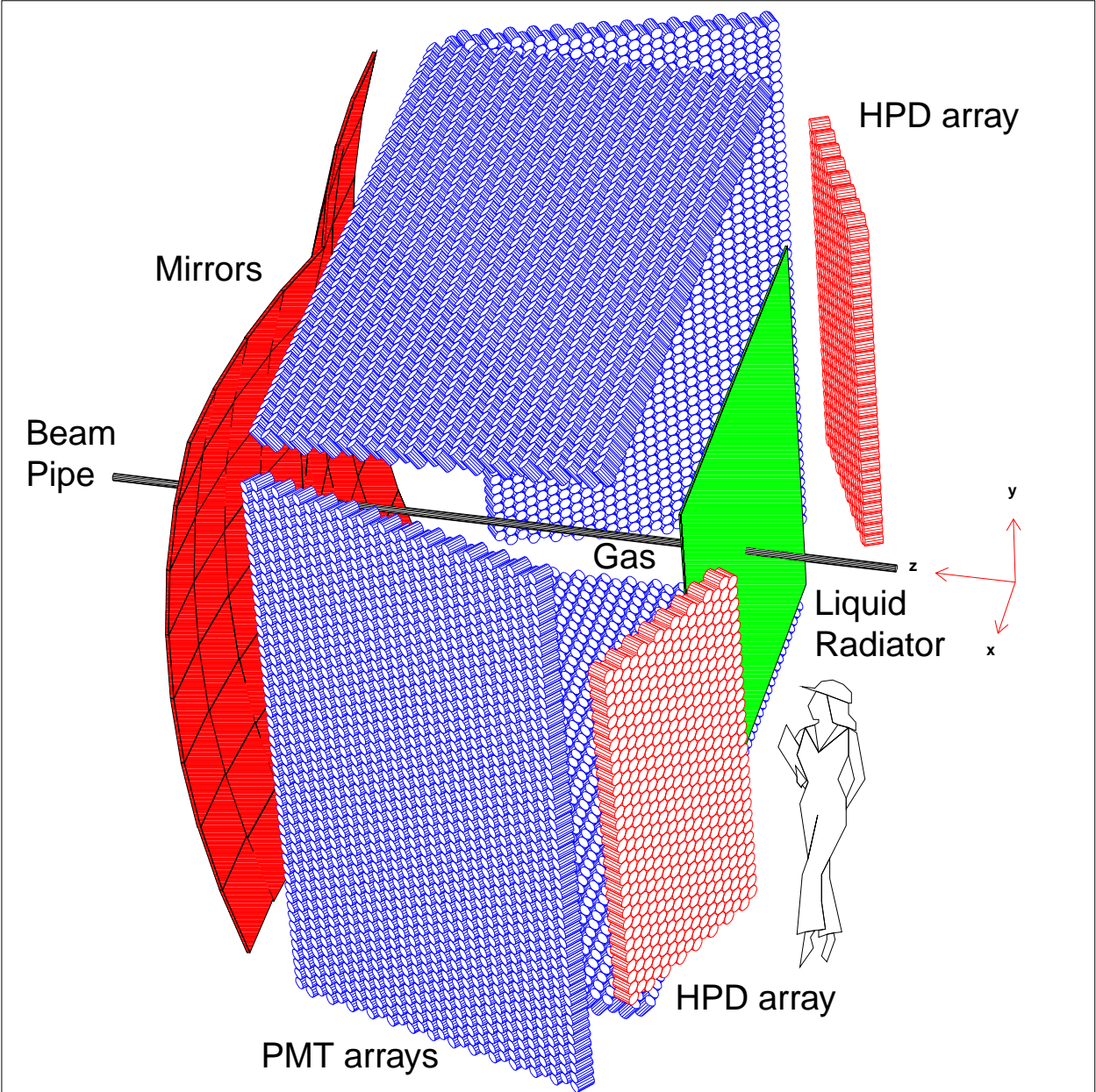
Figure 4.21: Outline of the important RICH components.

4.6.4 Photo-detectors

4.6.4.1 Photodetectors for the C_4F_{10} radiator

We choose to work in the "visible wavelength" regime, above 280 nm, to minimize chromatic aberrations (that arise from the wavelength dependence of the radiator refraction index). Because of the open geometry of the forward spectrometer and the availability of space to install shielding to protect detection elements from the fringe field of the BTeV analysis magnet, arrays of photo-multipliers (PMT) or hybrid photo-diodes (HPD) can be used. We chose to use HPDs which offer a cheaper solution. (Multi-anode PMTs are considered a back-up option.)

HPDs are commercially available from DEP (Delft Electronic Products B.V.) in the Netherlands. DEP can now produce pixelated HPDs as large as 8.3 cm in diameter. A photon incident at a quartz window of the HPD refracts and reaches a photo-cathode deposited on the inner window surface. The window has a spherical shape to provide optical focusing of light onto the photo-cathode. About 80% of the tube area is active. Closely packed tubes will cover 91% of the area they occupy, thus the overall geometrical light collection efficiency is 73%. Therefore, there is no need to use any additional demagnification systems to recover the geometric inefficiency.

A photo-electron emitted by the photo-cathode is accelerated onto a segmented silicon diode array by a high voltage (-20 kV). The segmentation of the diode array into pixels can be adjusted to match specific spatial resolution requirements. This family of HPD tubes was developed by DEP in collaboration with the LHCb group [12]. Development of BTeV version of the HPD is described in Chapter 5. In the BTeV design we will have 163 hexagonal pixels per tube. The corresponding photon position error is 0.45 mrad.

The gain of the device is about 5000 and is proportional to the accelerating voltage. We expect to detect such signals with a signal-to-noise ratio of about 7:1. Development of the front-end readout electronics is carried out in collaboration with IDE AS company from Norway as described in Chapter 5.

The last major factor impacting the RICH performance is the wavelength coverage determined by the photo-cathode and window material. The wavelength sensitivity determines chromatic error and is the major factor in the number of Cherenkov photons detected per track.

Quartz windows are a standard feature in the HPD tubes as they can easily sustain the large high voltage on the photo-cathode. High quality quartz extends the wavelength coverage from the visible range down to 160 nm. Such a large wavelength coverage results in a large chromatic error of 1.2 mrad per photon and in a large number of photons radiated per track (~ 235). When the wavelength coverage is limited, the photon yield drops but the chromatic error per photon improves. These two effects offset each other. The simulations show that a shallow optimum in Cherenkov resolution per track is reached when the wavelengths are limited to about 280 nm. UVT acrylic used in the vessel window will produce such wavelength cut-off. This results in a chromatic error of 0.45 mrad per photon with a photon yield of 63 photons per track. The total Cherenkov angle resolution is 0.83 mrad per

photon and 0.1 mrad per track.

A system with 944 HPDs/arm approaches the full geometrical coverage limit. With 163 pixels per tube, the detector (1 arm) will have 153,872 electronic channels.

We note that with the replacement of the aerogel with the liquid radiator, the number of HPDs has gone down. With the aerogel, photons struck the mirror and were detected on the HPD array, which had to be enlarged by 96 tubes/arm to capture them. Now, the photons from the liquid radiator are detected on the PMTs on the sides, the top, and the bottom of the counter and the HPD plane only needs to be sized to detect the photons radiated in the C_4F_{10} gas volume.

4.6.4.2 Photodetectors for the C_5F_{12} Liquid Radiator

After passing through the quartz window and refracting on the quartz-glass interface, Cherenkov photons generated in the liquid travel towards the PMT arrays. The PMTs are tilted to match the average angle of incidence. The Cherenkov images at the PMTs are not simple rings since they are distorted by light refraction at the interfaces of the various media and by the orientation of the RICH box's walls. The chromatic error for C_5F_{12} is 3.7 mrad per photon. The emission point error is negligible. The photon position error is determined by the size of the photomultiplier tube. Three inch PMTs produce a photon position contribution to the Cherenkov angle resolution of 5.3 mrad. The total error is then 6.2 mrad. (The total error with 2" tubes would be 4.9 mrad) The current design has 5000 3" PMTs covering the most illuminated portions of the two RICH side walls, the top and bottom. With this system, we expect to detect 12.4 photoelectrons/track, resulting in a per track resolution of 1.88 mrad. Since at 9 GeV/c, kaon and proton Cherenkov angles differ by 5.34 mrad, separation would be 2.8 standard deviations. Separation improves substantially for lower momentum tracks.

Because of the large number of PMTs required, minimizing the cost per PMT is very important. Several companies make 3" PMTs with the required quantum efficiency, gain, noise characteristics, and single photo-electron resolution. Preliminary estimates of radiation levels at the position of the PMTs indicate that radiation damage should not be a problem even after many years of operation.

4.6.5 Expected physics performance

In a real environment, Cherenkov rings from different tracks overlap in the detector. A realistic simulation of efficiency and fake rates must take into account ambiguities in track-photon assignment. However, in the new design, the photons from the liquid radiator and the gas radiator fall on separate sensor arrays, which reduces this problem significantly.

We have analyzed simulated data with an algorithm which could be applied to real data. The reconstruction is performed in two steps. In the first pass, all hits within $\pm 3\sigma$ of a mass hypothesis are included in the per track average, excluding those hits which are within $\pm 3\sigma$ of the pion hypothesis for any other track. The second pass is essentially the same except that instead of assuming that all tracks are pions in the hit exclusion, the most likely

Table 4.7: Expected performance of BTeV RICH system. The photon yield and the resolution per track given here do not take into account any reconstruction losses due to overlap of Cherenkov rings from different tracks in the same event. For C_5F_{12}, 3" PMTs are assumed.

	$C_4F_{10}\, n = 1.00138$	$C_5F_{12}\, n = 1.24$
emission point error	0.53 mrad	0.4 mrad
segmentation	0.45 mrad	5.3 mrad
chromatic error	0.45 mrad	3.7 mrad
total error per photon	0.83 mrad	6.2 mrad
number of photons	63	12.4
total error per track	0.10 mrad	1.9 mrad

mass hypothesis based on the first-pass results is used. To discriminate between two mass hypotheses for the same track (e.g. K or π) we cut on the likelihood ratio expressed as a χ^2 difference: $\Delta\chi^2_{K\pi} = -2\log(L_\pi/L_K)$ with $L_h = P(N_h|N_h^{exp})\,G(\theta_{trk\,h}|\theta_h^{exp})$. Here $P(N_h|N_h^{exp})$ is the Poisson probability for observing N_h photons found within $\pm 3\sigma$ of this hypothesis when N_h^{exp} are expected, and $G(\theta_{trk\,h}|\theta_h^{exp})$ is the Gaussian probability density for obtaining Cherenkov angle per track for given mass hypothesis $h(\theta_{trk\,h})$ when θ_h^{exp} is expected. The expected photon yield includes acceptance corrections and loss due to the Cherenkov ring overlaps. For a given cut value on the $\Delta\chi^2_{K\pi}$ we obtain a value for efficiency and fake rate.

To illustrate performance of the C_4F_{10} system we show in Fig. 4.22 the updated simulation of $B_d \to K^\pm\pi^\mp$ background rejection as a function of $B_d \to \pi^+\pi^-$ efficiency. The updated simulations include a better description of the detector components which resulted in the increased photon conversion backgrounds. On the other hand, particle discrimination algorithms have been improved. The net change is a slight improvement over the performance curve included in the BTeV proposal.

The gas radiator will play a useful role in lepton identification at low momenta, as its acceptance is much larger than the ones for the calorimeter and for the muon system. This is discussed in more detail in Chapter 2.

To demonstrate the performance of the liquid radiator, we have analyzed Monte Carlo samples of $b\bar{b}$ to show the efficiency and misidentification probability for kaons of momenta less than 9 GeV/c. These are significant in kaon flavor tagging. Background cross-efficiency, in this case the identification of a proton as a kaon, is plotted as a function of kaon efficiency in Fig. 4.23. It should be recalled that with no liquid radiator or, as we have shown with aerogel, we have no discrimination between kaons and protons at these momenta.
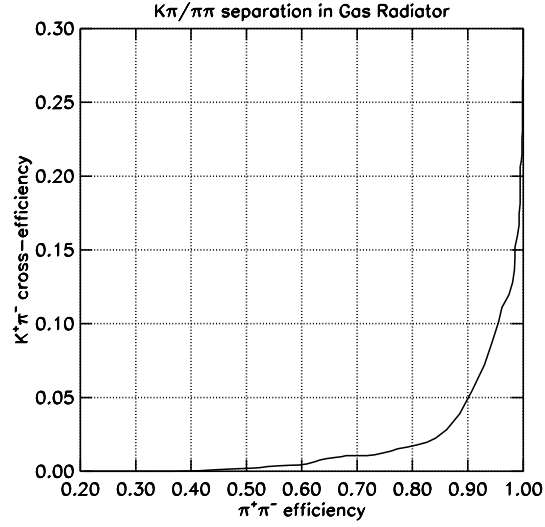
Figure 4.22: Cross-efficiency of particle identification system for $B_d \to K^\pm \pi^\mp$ as a function $B_d \to \pi^+ \pi^-$ PID efficiency. The efficiencies are defined relatively to number of events with both tracks entering the RICH detector. The Monte Carlo simulation included on average two minimum bias interactions in addition to the $b\bar{b}$ production.

Figure 4.23: Proton fake-rate as a function of kaon identification efficiency for tracks with momenta less than 9 GeV/c.

4.7 Electromagnetic Calorimeter

4.7.1 Introduction

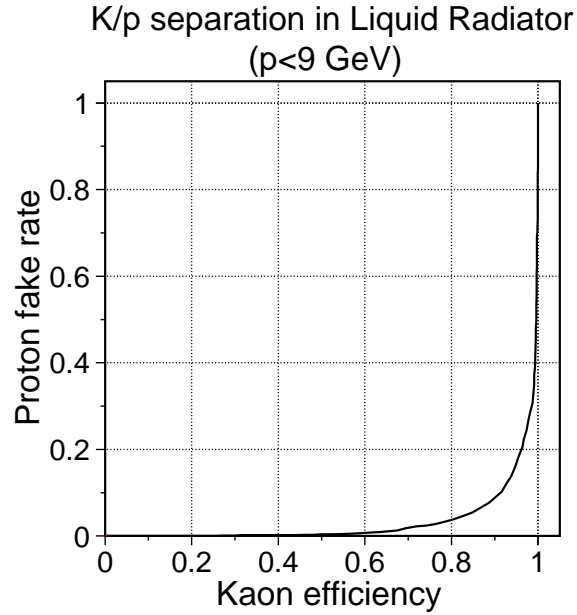A thorough investigation of B decays requires the ability to study decay modes containing single photons, π^o's, η's and electrons. The addition of a high quality crystal calorimeter to the CLEO detector was a first in coupling excellent photon detection to charged particle detection and demonstrated its importance in B decay studies [13]. Furthermore, the identification of electrons is useful to reconstruct J/ψ decays and to identify semileptonic decays, both for their intrinsic physics interest and as "flavor tags" for mixing and CP violation studies.

Some of the important decay modes for BTeV include: $B^o \rightarrow (\rho\pi)^o \rightarrow \pi^+\pi^-\pi^o$, $B_s^o \rightarrow \psi\eta$, and $\psi\eta^{'}$, semileptonic decays, and $B^o \rightarrow K^{*o}\gamma$ and $\rho^o\gamma$.

After an extensive study of various technologies, we chose a calorimeter made of $PbWO_4$ crystals. This technology has been developed for high energy physics by CMS. Our choice of lead tungstate is based on several considerations:

- It satisfies our requirements on energy and spatial resolution. Blocks of appropriate transverse and longitudinal size can be manufactured. CMS expects to achieve a stochastic term of 2.7% and a constant term of 0.55% using Avalanche PhotoDiodes (APDs) for readout. We plan to use photomultiplier tubes (PMTs) and expect to have a smaller stochastic term, $\sim$1.6%-$\sim$1.8%.

- This material is very resistant to radiation damage, especially when doped with either Nb or La. We have verified in test beam runs that these crystals will survive the worst case radiation levels expected in BTeV.

- It is fast – crystals deliver 99% of their light output within 100 ns, which is safely less than the bunch crossing time of 132 ns at the Tevatron.

The properties of $PbWO_4$ which are important for the calorimeter are given in Table 4.8.

4.7.2 Description of the BTeV Calorimeter

Our crystals are 220 mm long and 28 mm$\times$28 mm in cross section at the rear face. They are slightly tapered to point towards the interaction region to provide a projective geometry. (They actually project to a point displaced by 10 cm in both the horizontal and vertical direction from the center of the IR to prevent photons from traversing cracks between the crystals.) The crystals are very similar to the crystals used by CMS.

Figure 4.24 shows a representation of the calorimeter, with the crystal hits displayed, for an event generated with GEANT containing a $B^o \rightarrow \rho^o\pi^o$ decay. The two photons from the π^o decay are indicated by the circles. One photon has 19.3 GeV of energy, while the other has 2.4 GeV. The minimum energy displayed per crystal is 10 MeV. This corresponds to the minimum energy crystal that we use in measuring the shower energy. It can be seen even

Table 4.8: Properties of PbWO$_4$

Property	Value
Density (g/cm^3)	8.28
Radiation Length (cm)	0.89
Interaction Length (cm)	22.4
Light Decay Time (ns):	5(39%)
	15(60%)
	100(1%)
Refractive Index	2.30
Maximum of emission (nm)	440
Temperature Coefficient (%/^{o}C)	-2
Light output/NaI(Tl) (%)	1.3
Light output (pe/MeV into a 2" PMT)	10

Table 4.9: Properties of the BTeV electromagnetic Calorimeter

Property	Value
transverse block size, back	28.0 mm $\times$ 28.0 mm
tapered, smaller in front	27.2 mm$\times$ 27.2 mm
Block length	22 cm
Radiation Lengths	25
Front end electronics	PMT
Digitization/readout	QIE (FNAL)
Inner Dimension	$\pm$ 9.88 cm $\times$ $\pm$ 9.88 cm
Outer Radius	160 cm
Total blocks per arm	10500

from this one event that there is much more activity near the beam line than further out in radius. We will return to this point later.

The light emitted by the crystal peaks at 440 nm. In BTeV, unlike CMS, we are far enough away from magnetic fields, so we can use photomultiplier tubes to read out the calorimeter. BTeV will use modified Hamamatsu R5380 tubes or equivalent equipped with quartz windows to withstand radiation. These are similar to the ones used by KTeV. Using this photomultiplier, we have demonstrated in beam tests conducted at IHEP, Protvino that we can collect approximately 5 photoelectrons per MeV.

The output of the PMT will go to a modified QIE chip [16] located near the photo-multiplier base, but outside the region of intense radiation. This chip provides a digitized charge output for each beam crossing. The expected light output is 5000 photoelectrons at 1 GeV. The detector is far enough away from the BTeV dipole so that there should be no need for special magnetic shielding from that source. Since we will magnetize the iron of the muon filter just downstream of the detector, we will put iron shield plates between the
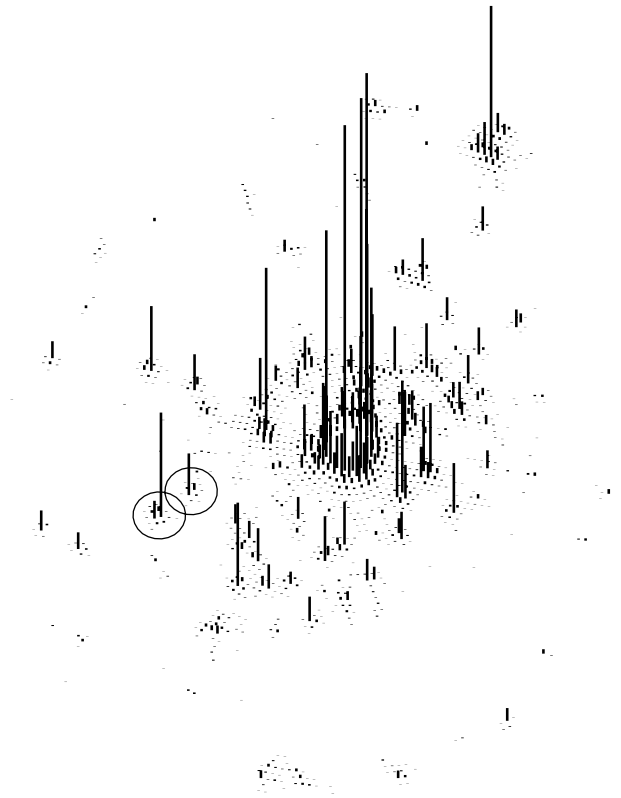
Figure 4.24: The energies in the PbWO$_4$ calorimeter (one arm) for an event containing two photons from the decay sequence $B^o \rightarrow \rho^o \pi^o$, $\pi^o \rightarrow \gamma\gamma$. The photons of energies 19.3 and 2.4 GeV are surrounded by circles. All energies above 10 MeV are shown, with the height of line proportional to the energy.

calorimeter's PMTs and the muon filter.

The detector will be housed in a temperature and humidity controlled hut. There will be a dry air environment. Temperature stabilization is necessary because of the thermal coefficient of the PbWO$_4$ light output. In addition, the gains will be monitored with a light pulsing system based on Light Emitting Diodes.

4.7.3   Radiation Levels and Radiation Tolerance

Radiation damage of PWO crystals is a serious issue. Detailed studies [17] reveal that the light transmission of crystals deteriorates due to formation of color centers by radiation, while the scintillation mechanism itself seems unaffected. When a PWO crystal no longer receives radiation, its color centers (semi-stable excited states) disappear, and it recovers from transmission degradation by natural room-temperature annealing. In fact, this annealing
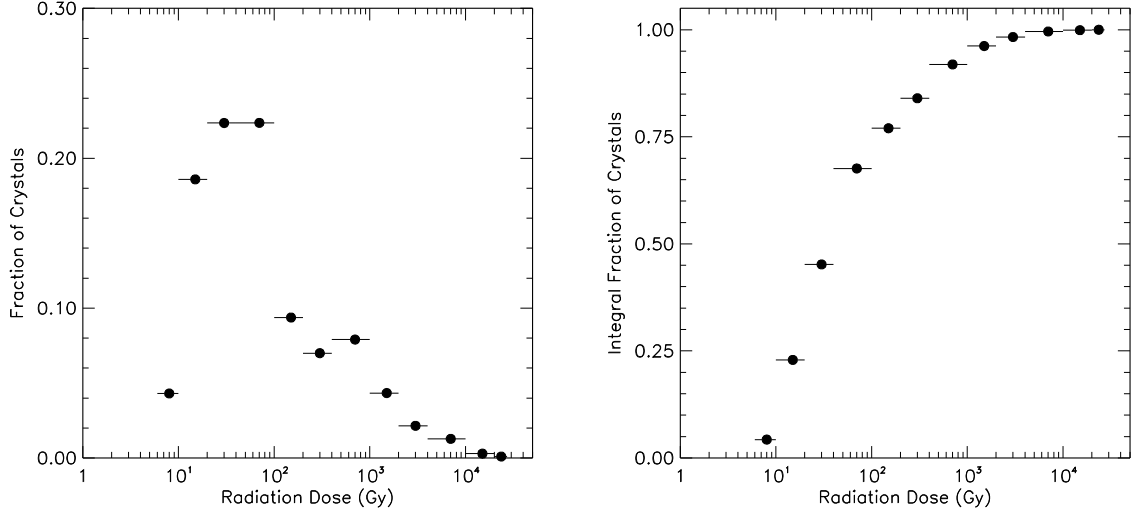
Figure 4.25: (left) The maximum dose distribution in the crystals for for 1 year of running at a luminosity of $2 \times 10^{32}\text{cm}^{-2}\text{s}^{-1}$. (right) The integral of the maximum dose distribution.

goes on even during radiation exposure. Therefore, when crystals are exposed to a constant radiation level, they lose light only up to the point where the rates of radiation damage and natural recovery balance.

The radiation levels at the crystals and phototubes are discussed in Appendix A of the May 2000 proposal. The maximum radiation levels occur close to the beam. There is also a relatively narrow vertical band of higher than average dose caused by the sweeping action of the BTeV dipole.

The simulations shown here were done for a smaller calorimeter of 150 cm radius. The actual outer radius of 160 cm was chosen by weighting the efficiency of a larger calorimeter, up to the spectrometer acceptance of 300 mr, with the cost. The integrated dose rates for most crystals are quite modest. In Fig. 4.25 (left) we show the dose distribution in the crystals (here dose means the maximum dose in any part of the crystals), for 1 year of running at a luminosity of $2 \times 10^{32}\text{cm}^{-2}\text{s}^{-1}$. We also show (right) the cumulative fraction of crystals with doses less than that shown on the horizontal axis. We see that ∼90% of the crystals have a yearly accumulated dose of less than 1000 Gy (0.1 Mrad).

The dose rate into most of the BTeV crystals is less than 0.1 Gy/hour, and only a few crystals receive more than 1 Gy/hour. For the 90% of the crystals that are below the lower rate, there are only few percent changes in light output that are easily monitored. At the higher rate, these changes get to the 10% level, but still can be corrected for.

We plan on injecting light from an LED into the crystals for short term monitoring, and have tested such a system in the beam at Protvino (see Chapter 5). Ultimately, we need to use physics events to calibrate every crystal. We plan to use the electron sample from B semileptonic decays as well as converted photons mainly from minimum bias events to

calibrate every crystal. Monte Carlo studies show that there is one electron candidate in every event we record. This implies that there will be 4×10^6 electrons every hour, or 200 electrons/crystal for "average" crystals. Although the outer crystals will receive only a few electrons, these crystals won't be effected by radiation either. This implies that for crystals which require careful monitoring of radiation effects, we will be able to calibrate them every hour with electrons.

4.7.4 Expected Resolution

The detailed estimates of the expected resolution are given in Appendix A of the May 2000 proposal. Briefly, 22 cm long crystals were selected after a GEANT study determined that length to be optimal. The transverse size was originally chosen to be essentially the same as CMS is already using (26 mm). Making the crystals two mm larger sacrifices little performance and cuts the costs by about 8%, due to a reduced number of photomultiplier tubes and electronics channels.

Using 5 photoelectrons/MeV, we find contributions to the stochastic term in the energy resolution to be $1.5\%/\sqrt{E}$ from photon statistics and $0.7\%/\sqrt{E}$ due to crystal size and clustering (transverse and longitudinal leakage) where E is in units of GeV. For the constant term, we use the CMS estimate of 0.55%. We note that KTeV has achieved a constant term of 0.45% [18]. Overall we expect the energy resolution to be

$$\frac{\sigma_E}{E} = \sqrt{\frac{a^2}{E} + b^2} = \frac{a}{\sqrt{E}} \oplus b, = \frac{1.7\%}{\sqrt{E}} \oplus 0.55\% \tag{4.2}$$

The spatial resolution in both directions transverse to the crystal axis is expected to be

$$\sigma_x = \frac{3500 \ \mu m}{\sqrt{E}} \oplus 200 \ \mu m \ . \tag{4.3}$$

Our test beam results (see Chapter 5) are consistent with these expectations. With these single photon resolutions, the π^o and η mass resolutions are excellent. Fig. 4.26 shows the invariant $\gamma\gamma$ mass for π^o's of 10 GeV energy incident on the calorimeter. The energies and positions are simulated by GEANT and our cluster finder is used to reconstruct the photons. The mass resolution is 2.6 MeV, which compares favorably to that found in CLEO (5 MeV) [19].

4.7.5 Examples: Efficiencies in $B^o \to K^* \gamma$ and $B^o \to \rho\pi$

In the hadroproduction environment, there is great concern that there is so much activity from charged track interactions in the calorimeter and additional photons that the signal photons will be totally obfuscated. As a test case, we use the decay $B^o \to K^* \gamma$. Although we are only concerned with the gamma reconstruction here, we require that the two charged tracks from the K^* decay reach the RICH detector, in order to ensure that the B^o's were
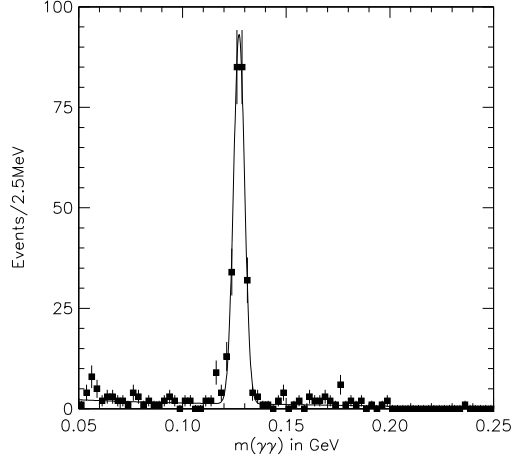
Figure 4.26: The $\gamma\gamma$ invariant mass for 10 GeV π^o's incident on the calorimeter. The fit is to a Gaussian signal function plus a polynomial background.

in the acceptance of the spectrometer. The decay was simulated by GEANT at a mean interaction rate of two per crossing.

To identify photons we find clusters of energy whose shape is consistent with an electromagnetic shower and we require that no charged track extrapolate close to the cluster. In Fig. 4.27 we show the difference between measured and generated photon energy divided by the generated energy.

The BTeV energy resolution is about a factor of two better than CLEO. The CLEO spectrum is absolutely clean; there is a small background in the BTeV distribution. Our concern is a large overlap with fragments from other particles that would cause the photon energies to be shifted high and out of the peak, but this apparently is not the case. In Fig. 4.28 we show radial distribution of generated photons from $K^*\gamma$, the accepted ones, and the efficiency; we define accepted photons as ones with energies within 3σ of the peak that pass the shower shape and isolation cuts. We note that the same number for the CLEO barrel calorimeter, calculated in the same manner using GEANT, is 89%. While our efficiences start out considerably lower than CLEO, they increase rapidly and demonstrate the usefulness of the calorimeter.

We also looked at the π^o efficiency as a function of the radius of the π^o at the z position of the calorimeter for $B \to \rho^o\pi^o$ and $B \to \rho^+\pi^-$ decays. The efficiency, shown in Fig. 4.29 plateaus at a radial distance of about 75 cm. This simulation was run in a larger than proposed calorimeter so we could view the dependence on radius more easily. From such studies the calorimeter radius was chosen.
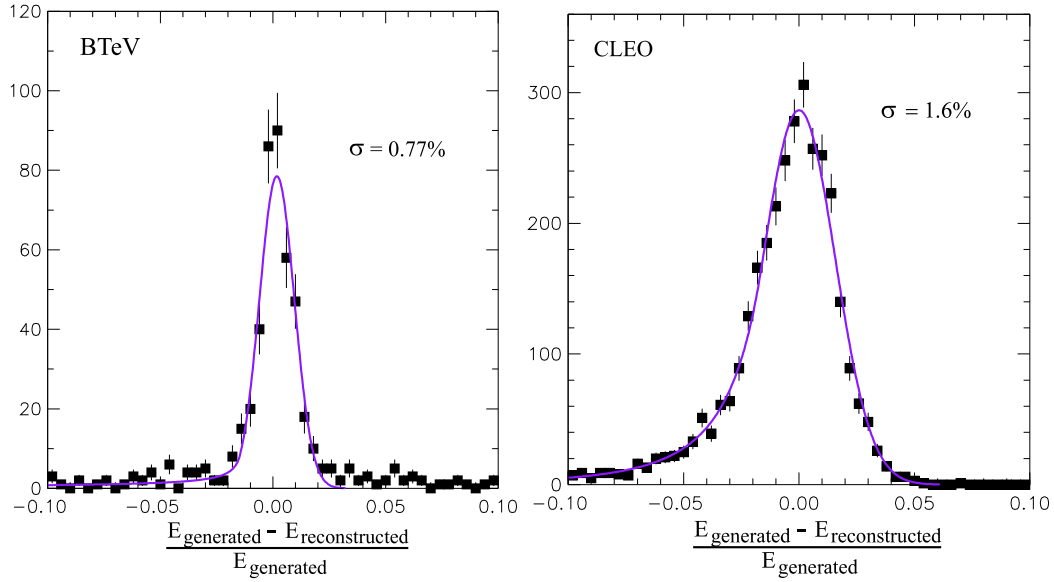
Figure 4.27: The difference between the measured and generated energies, divided by the generated energy, for reconstructed photons as simulated by GEANT for BTeV (left) and CLEO (right). The photons candidate clusters were required to have shower energy shapes consistent with that expected for photons and to be isolated from charged tracks. The BTeV simulation was run at 2 interactions/crossing.

4.7.6 Crystal Acquisition

For PWO crystals to be fast and radiation hard, they need to be produced very carefully. Any impurities and crystal defects, such as Pb or O vacancies, increase both the slower components of the light output and the radiation susceptibility. Therefore, establishing mass production procedures to produce good crystals has been one of the major goals of the R&D program of the CMS calorimeter group and its vendors at the Bogoroditsk Plant in Russia and the Shanghai Ceramic Institute.

They have realized this goal by concentrating on the following five factors:

- economical raw material purification methods

- adjustment of the stoichiometric ratio between PbO and WO_3 in the raw material to compensate for the evaporation of PbO during crystal growth

- environmental gas during the crystal growth

- annealing methods

- doping with Y, La and/or Nb to compensate residual crystal defects.

The Russian manufacturer uses the Czochralski method to grow crystals. They have already succeeded in producing more than 6000 crystals for the CMS barrel calorimeter.
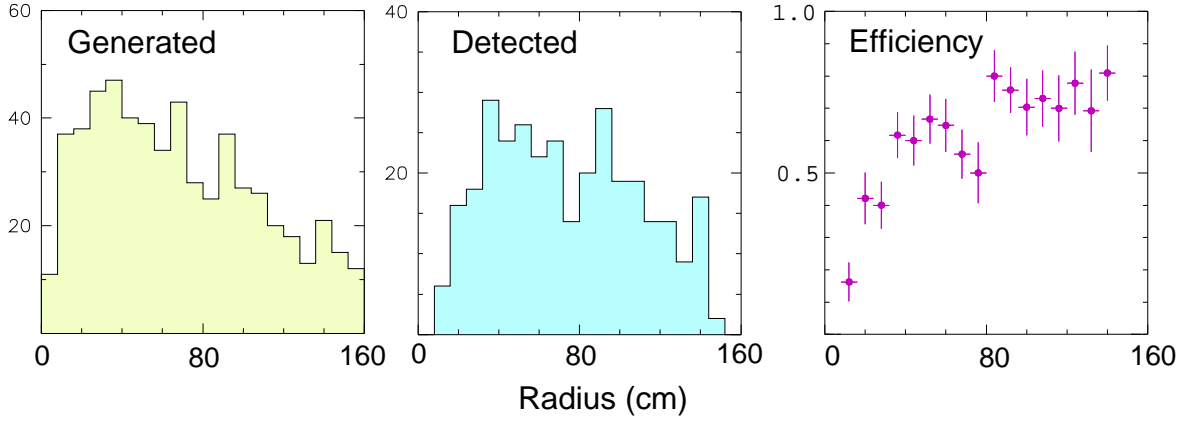
Figure 4.28: The radial distribution of generated and detected photons from $B^o \rightarrow K^* \gamma$ and the resulting γ efficiency. The detector was simulated by GEANT and the resulting crystal energies were clustered by our software. The charged tracks from the K^* were required to hit the RICH. The simulation was run at 2 interactions/crossing.

They have also completed additional R&D to produce larger endcap crystals, as well as large enough crystals to obtain more than one barrel crystal per ingot, which could lead to lower costs.

The Chinese producer uses the Bridgeman method to grow crystals. Due to prior commitments to other HEP experiments, they started R&D on mass production after the Russians. Nevertheless the Chinese have already produced good sample crystals for BTeV and their quality appears to be comparable to the Russian crystals in our test beam studies.

We have visited both the Bogoroditsk and Beijing/Shanghai production facilties, hosted by our Russian IHEP and Chinese colleagues. We purchased and tested 25 crystals each from Shanghai and Bogorodisk and an additional 12 crystals from the Beijing facility, and are in the process of buying four smaller crystals from a second potential Russian vendor at Apertiti. The two leading companies are interested in growing crystals for BTeV. The Russians plan to finish production for CMS by the middle of 2005 by producing more than 10000 crystals per year. This rate is sufficient to produce the BTeV crystals in one year.
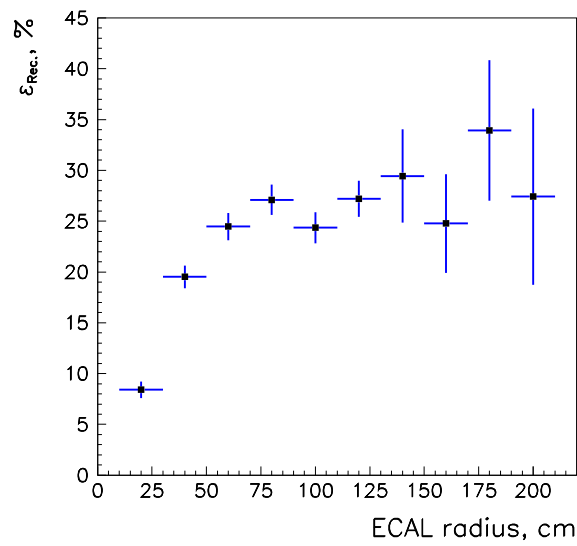
Figure 4.29: The π^o efficiency as a function of the radial distance from the beam line in the calorimeter of π^o's from $B \to \rho\pi$ decays. The simulation was run at 2 interactions/crossing in the "large" calorimeter.

4.8 Muon Detector

The BTeV muon system has two primary functions:

- J/ψ and Prompt Muon Trigger: Besides providing interesting physics (including J/ψ final states of B decays, direct J/ψ production, and semileptonic decays), this trigger performs an important service role by selecting a large enough sample of b events on which the more aggressive and technically challenging vertex trigger can be debugged and its efficiency evaluated.

- Muon Identification: Many of the experiment's physics goals (rare decay searches, CP violation studies which require tagging, studies of beauty mixing, searches for charm mixing, etc.) rely on efficient muon identification with excellent background rejection.

We have selected a toroidal magnet design combined with fine-grained tracking elements. This design permits a "stand-alone" trigger: *i.e.* a di-muon trigger based solely on information from the muon detector. In addition, improved background rejection is possible by comparing this measurement with momentum and tracking information from the rest of the spectrometer. The system design has been chosen to reduce and uniformly distribute occupancies and to minimize confusion in pattern recognition. To provide a viable trigger, the system must obtain a rejection rate at Level 1 of a few hundred. The goal for muon misidentification in the physics analysis is 10^{-3}.

Given the objective of a stand-alone trigger and the size limitations set by the experimental hall, one can make fairly general calculations that place specific (and restrictive) constraints on the design of the system. We first describe these calculations and use them to motivate the overall design of the muon system. We then describe the trigger efficiency and rejection studies we have performed.

4.9 General Design Considerations

The fractional momentum resolution in a magnetic spectrometer can be parameterized as $\sigma_p/p = \sqrt{a^2 + (b\,p)^2}$ where the a term depends on the bending power and multiple scattering environment of the detectors and the b term depends on the bending power and the detector layout and spatial resolution. Figure 4.30a shows that the potential rejection provided by a trigger for low momentum muons significantly degrades once the low momentum fractional resolution exceeds 25%. At $a = 25\%$, the trigger rejects very soft muons at roughly the 4σ level. At higher momentum, where multiple scattering is less important, one becomes sensitive to the b term. The high momentum resolution influences how sharp a momentum threshold one can make in a stand-alone muon trigger. Figure 4.30b illustrates this point by showing the trigger efficiency as a function of momentum for several b values. These considerations suggest minimum performance criteria of $a < 25\%$ and $b < 1\%/GeV$.
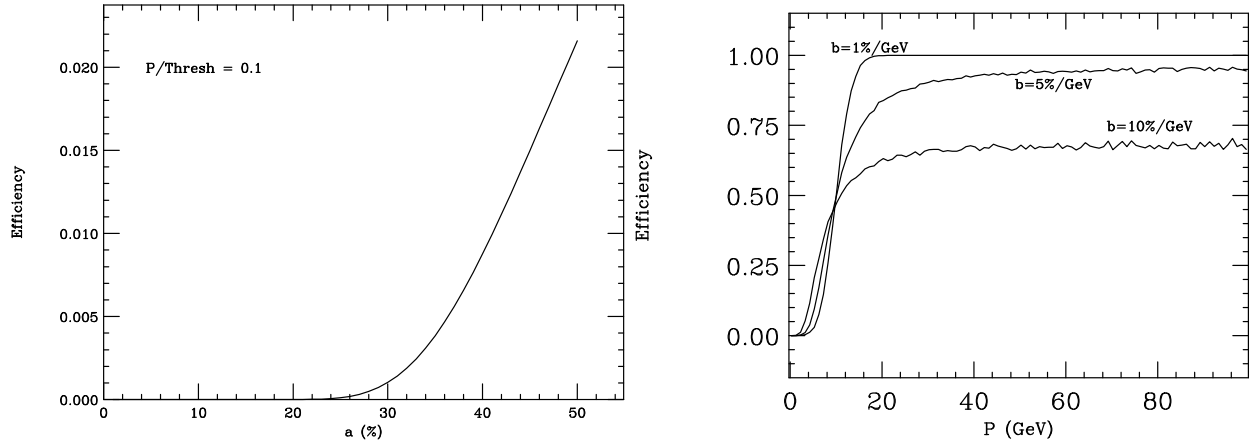
Figure 4.30: (left) Efficiency, calculated in a simple Gaussian model, for a muon with 1/10 the threshold momentum to pass a momentum threshold as a function of a, the MCS term in the resolution formula. (right) Efficiency as a function of muon momentum for a trigger designed to fire with a 50% efficiency at 10 GeV. The multiple scattering dominated term is fixed ($a = 25\%$) while the measurement dominated term varies from $1\%/\text{GeV} < b < 10\%/\text{GeV}$.

4.10 Baseline Muon System

Several measurement and shielding scenarios were studied before reaching the baseline design. In assessing possible layouts, we compute the momentum resolution using an error matrix which incorporates Gaussian models for the detector resolution and multiple Coulomb scattering. The interaction region is modeled as a Gaussian beam spot with $\sigma_x = \sigma_y = 1$ mm and $\sigma_z = 30$ cm. The result of these studies gives us the baseline geometry shown in Fig. 4.31. A cross section of the toriod system is given in Fig. 4.32
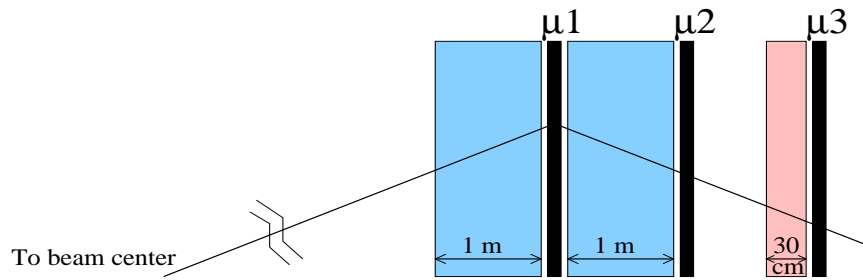
Figure 4.31: Layout of the baseline geometry, shown in elevation view. The three dark boxes, labeled μ_1, μ_2, and μ_3, represent detector stations with 4 measurement views per station. The two lighter boxes with lengths of 1 m represent magnetized steel toroids, which provide bending power for the muon momentum measurement and which also serve as hadron absorbers. The 30 cm long lighter box is an unmagnetized iron shield. The downstream trajectory is measured by μ_2 and μ_3. The upstream trajectory is measured using the nominal beam center with possible help from μ_1. To obtain sufficient bending power, both 1 m steel sections must be magnetized.

141

Figure 4.32:   Sketch of a Muon Toroid

4.10.1   Baseline Geometry

Two toroids, 1 m long with 1.5 T fields, provide the bending power. The muon detectors will be set up in three stations, one between the toroids and two behind the toroids. The momentum can be measured using the two, well shielded, downstream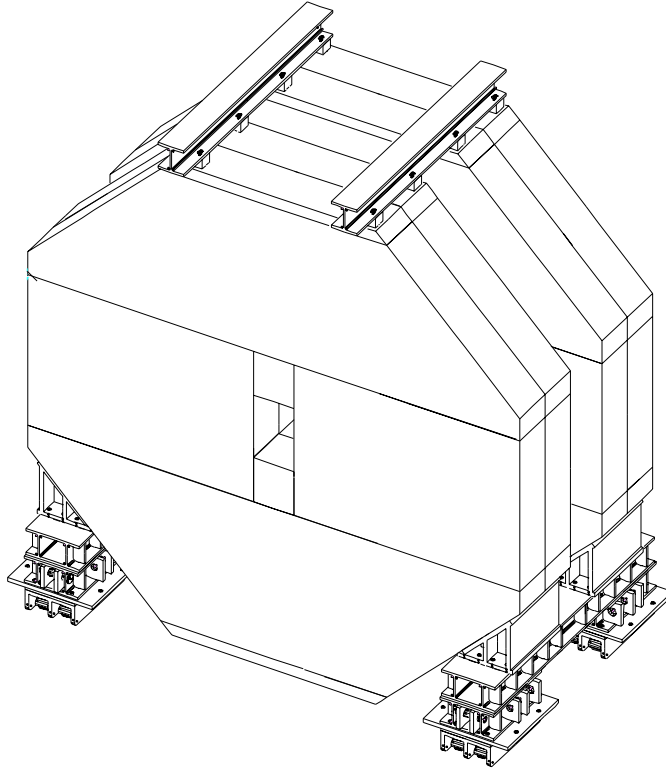 stations and the nominal beam constraint. The station between the two toroids provides a powerful confirming hit to eliminate fake tracks.

The angular acceptance of the muon detector ideally should correspond to the acceptance of the spectrometer, which is 300 mr. However, the physical constraints of the experimental hall do not permit this. The detector radius is chosen to be as large as possible, 240 cm (nearly touching the floor of the enclosure), which corresponds to a polar angle acceptance at the last muon detector station of 200 mr. Fortunately, wider angle muons, which are outside of the acceptance of the muon detector, tend also to have lower energy and can be identified by the Ring Imaging Cherenkov Counter, as discussed above. Muons from B decays which emerge at angles above 200 mr cannot participate in the stand-alone muon trigger described below, but can contribute to the vertex trigger.

There are additional constraints at the inner radius of the detector. The BTeV analysis magnet is part of the Tevatron lattice and deflects the circulating beams. This deflection is compensated by dipole magnets at each end of the C0 enclosure. Moreover, the quadrupoles

142

that focus the beam at the IR must be as close to the IR as possible. To achieve this, it has become necessary to save longitudinal space by actually inserting the compensating dipoles in the muon toroid as shown in Fig. 4.33. This defines the inner radius of the muon detector to be 38 cm, or about 40 mr. The presence of the magnet coils also creates the potential for particle leakage which must be carefully shielded.
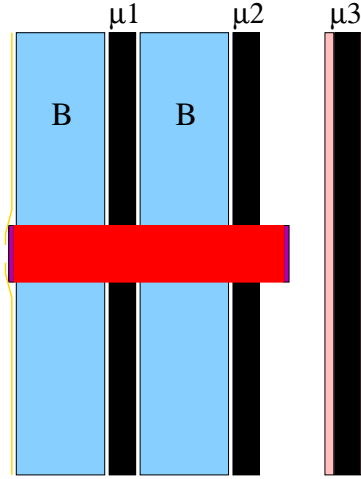

Figure 4.33:   Position of Compensating Dipole inside the Muon Toroids

4.10.2   Baseline Detector

The basic building block in the construction of a detector station is a "plank" of 3/8" diameter stainless steel proportional tubes as shown in Fig. 4.34. Thirty-two tubes are arranged in a double layer with an offset of half a tube ("picket fence" geometry) and will be soldered at each end to a brass gas manifold and supported in the middle by soldering to brass support rib pieces. This provides a sturdy, self-supporting building block which acts as an excellent Faraday cage. Proportional tubes have been selected as the detector technology because they are robust and have the necessary rate capability. We intend to use a fast gas (*e.g.* 88% Ar, 10% CF_4, 2% CO_2 ($v_d \approx 9$ cm/μs) [20]) so the maximum collection time (drift plus charge integration) for a signal should be less than 60 ns, allowing us to gate off hits due to incoming beams which arrive 70 ns before particles from the interaction region. We will use thin walled (0.01") stainless steel tubes. This is a proven technology — it has been used successfully by the CDF collaboration where similar tubes [21] had a long lifetime with low failure rate. The tubes will be strung with 30 μm gold-plated tungsten wire.

The 0.5 cm wire spacing of this design has no dead regions and has an effective spatial resolution of 5 mm/$\sqrt{12} = 1.4$ mm which meets the requirements outlined in Section 4.9. Figure 4.35 shows the momentum resolution for various muon system configurations assuming a 2.5 mm resolution and incorporating the magnetic fields and multiple scattering. The top curves show the result for only one magnetized toroid which is clearly ineffective. The
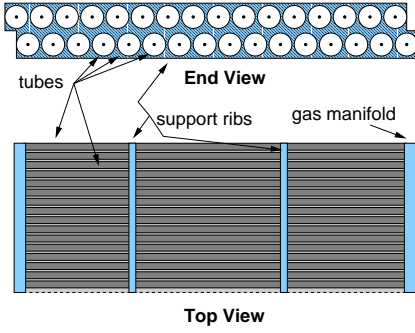
Figure 4.34:   End and top views of one "plank" of proportional tubes.

Table 4.10:   Parameters of the baseline BTeV Muon System.

Radial coverage	38–240 cm
Toroid Z-locations (center)	870, 1010 cm
Average Station Z-location	940, 1080, 1194 cm
Total Length	4 m (includes toroids)
Toroid Length (each)	1 m
Toroidal Fields	1.5 T
Tube cell size	1 cm (diameter)
Wire spacing:	0.5 cm (staggered)
Spatial resolution	1.5 mm
Total channels	36,864 per arm
Momentum resolution	$\sigma_p/p = 19\% \oplus 0.6\% \times p$

bottom curves show results when both steel filters are magnetized. The case where only a beam constraint and μ_2–μ_3 are used is illustrated by the dashed red curves. Including information from μ_1 produces the solid magenta curves. Curves are shown for three different azimuths. The chosen geometry exhibits good performance relative to our criteria on a and b. The importance of μ_1 lies in providing redundant information to eliminate fake tracks and for matching tracks with the inner tracker at higher trigger levels and offline. Its effect on the momentum resolution is less important.

To minimize occupancy at small radii and to minimize pattern recognition confusion, each detector station will consist of eight overlapping pie shaped "octants," as shown in Fig. 4.36a. The four views (r, u, v, and r) in each octant are shown in Fig. 4.36b. The r (radial) view is repeated to provide redundancy for the most important (bend) view and to help reject fake tracks in the trigger. The u and v views are rotated $\pm 22.5^{\rm o}$ from the r view and are used to measure ϕ and to resolve hit ambiguities, thereby reducing the misidentification rate. The views stack on top of each other and are built from the planks described above. There will be 12 planks in each view of an octant. Pairs of octants will be combined into quads which will be the structure moved in and out of the BTeV detector.

A summary of the baseline BTeV muon system is given in Table 4.10.
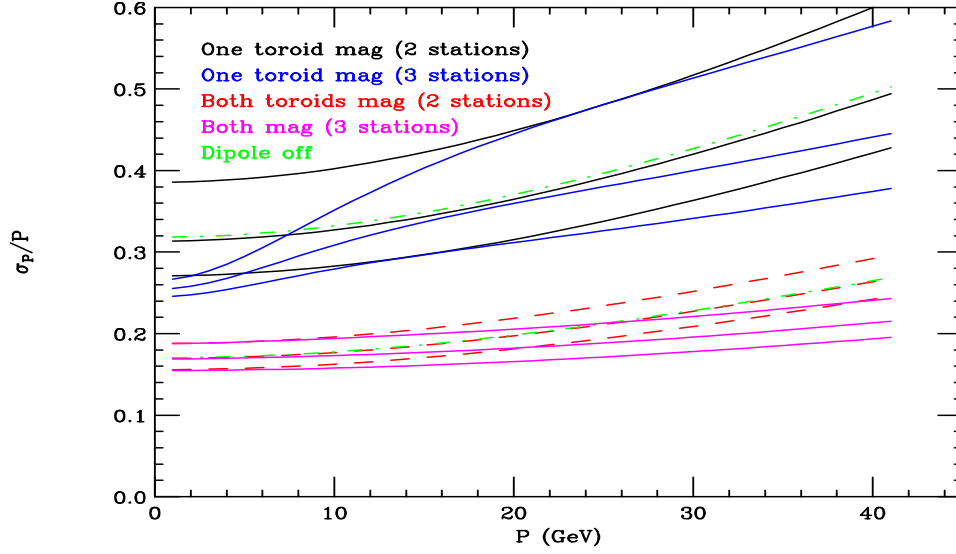
Figure 4.35: Plots of the fractional momentum resolution versus momentum for various muon system configurations. All plots assume 2.5 mm RMS spatial resolution. The plots appear in groups of 3 corresponding to $\phi = 270^o$ (best) 0° and 90° (worst). The ϕ dependence illustrates interference between the central dipole and muon toroids. The top (bottom) curves show the resolution when one (two) toroids are magnetized. The black and red curves illustrate the case where only the two stations after the second toroid are used. In this case the trajectory upstream of the toroid comes entirely from the beam constraint. The blue and magenta curves illustrate the case where the station between the two toroids is used to help determine the trajectory prior to the toroids. The green curves assume only the final two stations are used, and the dipole is turned off.

Figure 4.36: (left) Beams-eye view of one muon detector station, which consists of eight overlapping octants arranged in two layers. One octant is cut away in places to show the overlap between adjacent octants. (right) Arrangement of planks to form the four views in an octant (r view is repeated). There will be 12 planks per view (more than shown).

145

4.10.3 Front-end Electronics
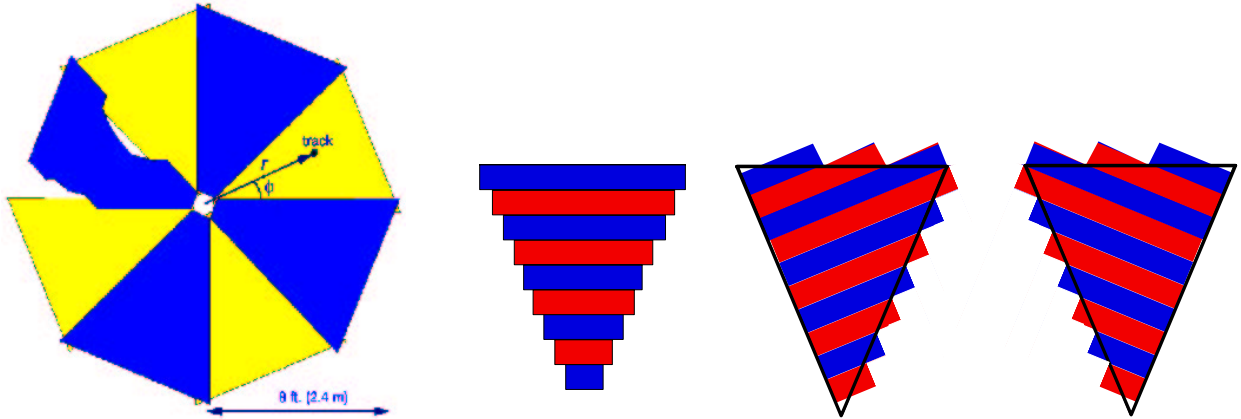
Although we will only be reading out a latch bit and not using TDC's, we are considering gating the system to exclude hits coming from the incoming beam. Therefore the front-end electronics need a double pulse resolution < 30 ns. The electronics should also be low cost and have sufficient gain. We intend to mimic the setup used for the CDF COT. There will be a PC board to deliver high voltage to each proportional tube, and a PC board with electronics to amplify and digitize the tube signal. Both boards will be located directly at the end of a plank.

We plan to utilize the ASDQ integrated circuit developed at the University of Pennsylvania to amplify and digitize the signals coming from the proportional tubes. This chip is being used in the Run-II CDF central outer tracker for a similar purpose. The ASDQ amplifies the first $\sim$8–10 ns of the signal and outputs an LVDS (equivalent) differential logic signal. This chip, when mounted on a PC board, has a low effective threshold of about 2 fC and features a double pulse resolution of $\sim$20 ns. The chip seems to be an ideal choice for the BTeV muon system. Beam tests of the predecessor to the ASDQ, the ASD8B, indicate that it is suitable for our use. Noise problems encountered during the beam test with the ASD8B required creating a Faraday cage out of aluminum, copper plated G10 and copper tape. We will address this problem by completely enclosing the electronics and proportional tube connections in a Faraday enclosure. This is the reason that the gas manifolds (Fig. 4.34) will be made of brass and soldered to the proportional tubes.

The ASDQ digital signals will be sparsified, serialized, and read out using a standard Fermilab readout protocol. Fiber optic cables will transfer the data from the plank to a buffer memory. Slow control and monitoring functions will be performed via fiber optic link as well.

4.11 Trigger Studies

We have studied the triggering performance of our baseline muon system using a full GEANT simulation, which includes additional hits in the muon system due to non-prompt sources, δ-rays, electromagnetic shower debris and hadronic shower leakage. We used minimum bias events to study rejection rates and $B^0 \rightarrow J/\psi\, K_s^0$ and $B_s^0 \rightarrow J/\psi\, K^{*0}$ where $J/\psi \rightarrow \mu^+\mu^-$, to investigate trigger efficiency. The minimum bias events were generated with PYTHIA and include elastic scattering, single and double diffractive, low p_T scattering and semi-hard QCD $2 \rightarrow 2$ processes. The number of events per crossing is generated from a Poisson distribution with average of two. Likewise, in generating the signal events, a Poisson distributed number of minimum bias events (average of 2) were added to the signal event.

4.11.1 Properties of additional "noise" hits

Figure 4.37 shows the characteristics of the hits in the muon detector for $B_s^0 \rightarrow J/\psi\, K_s^0$ events with the original geometry. The noise hits are dominated by low momentum secondaries

coming from interactions with the walls of the beam hole in the muon filters as is evident from the radial position distributions at the downstream faces of the filters. Secondaries spray out of the downstream ends of the holes in both filters. Figure 4.38a documents this problem. The hit distribution in the muon planes can be understood by considering that the percentage of such tracks striking a given plane will increase with the lever arm between the nearest filter and the plane. (All planes go down to the same radial position.) The effect is noticeable in stations 1 and 2 which are just downstream of filters but is largest for station 3. All planes in station 3 receive a large flux due to the long lever arm between this station and the second filter. To reduce this effect we added a 30 cm thick filter with the same radial coverage as the toroids just in front of the third station. The improvement is presented in Fig. 4.38b. Interactions with the beam pipe as well as δ-ray production also contribute significantly to the noise. Additional shielding (8 cm) around the beam pipe is also proposed and the resulting improvement is shown in Fig. 4.38c and 4.38d.
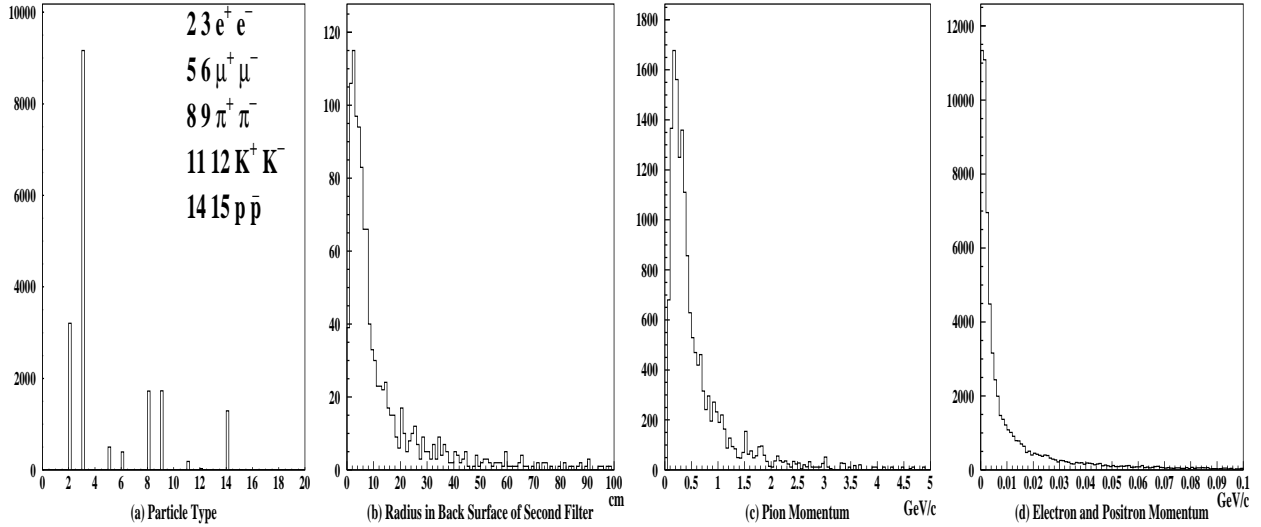
Figure 4.37: Characteristics of muon detector hits for $J/\psi\,K_s^0$ events. (a) Particle type. Each particle type is assigned an integer code, shown in the legend. For example, π^+ is given the code 8. The electromagnetic and hadronic noise is larger than the muon signal. The excess of electrons over positrons is due to δ-ray production. (b) Projected radial position at the downstream face of the second filter for tracks that hit station 3. The large percentage of tracks emanating from the vicinity of the hole in the filter is quite evident. (c) and (d) Momentum of pion and e^+/e^- noise. Noise secondaries have much lower momentum than J/ψ muons.

4.11.2   A muon "tracking" trigger

To establish an "upper" limit on muon trigger performance in the presence of the GEANT generated noise, we studied the performance of a muon "tracking" trigger. This trigger loops over all hits within a given octant to choose the best set of hits using a χ^2 test to the

147

Figure 4.38: Distributions of hits among muon detector planes for different shielding configurations. There are twelve planes per station. (a: upper left) Original design; no extra shielding. (b: lower left) Extra shielding block in front of the third station. (c: Upper right) Extra shielding around the beam pipe. (d: Lower right) Both beam pipe and third station shielded.
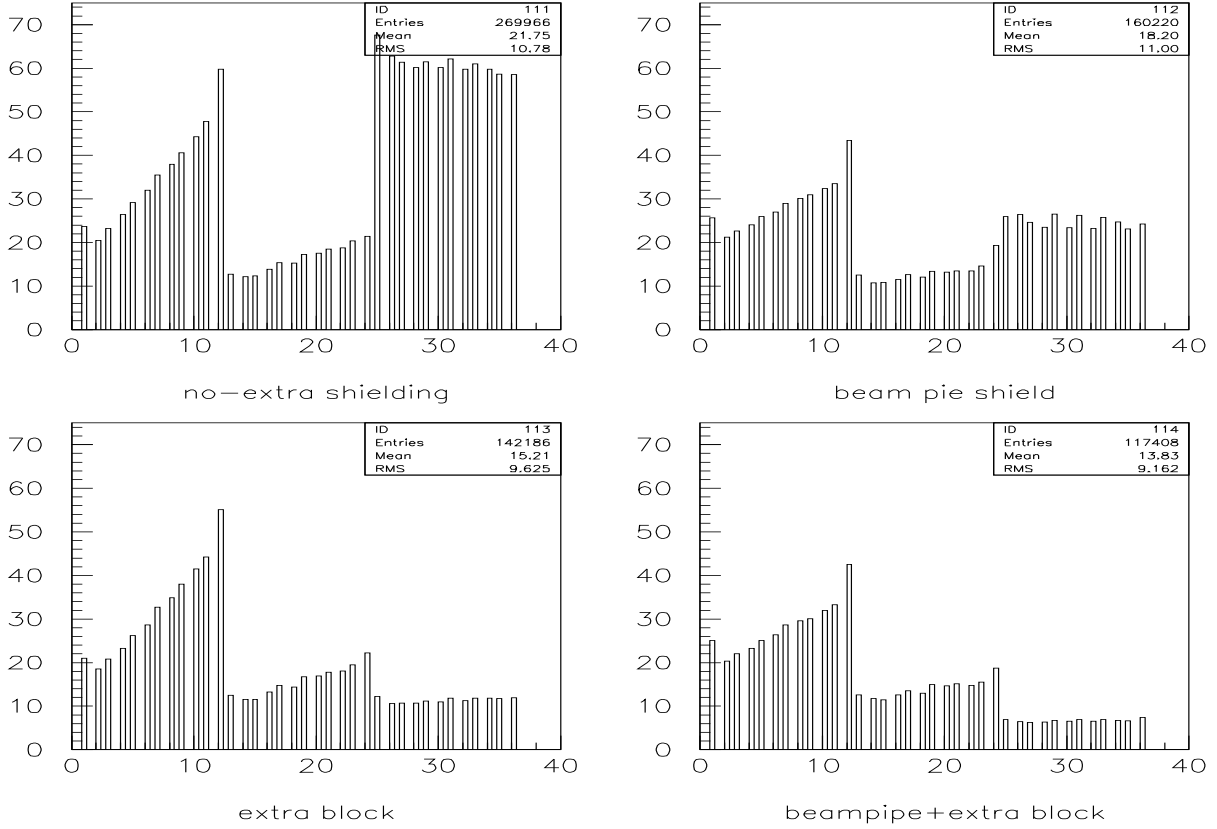
hypothesis that the muon system hits form a track which emanates from the nominal beam origin with production angles x'_o, y'_o, and momentum p. It is important to emphasize that this is a simulation of a "stand-alone" trigger. There is no use of any tracking information from the inner tracker; all information comes from the muon system.

For expediency we make several simplifications. We use a significantly simplified magnetic description, and a single bend approximation for the field traces. All equations are linearized in the 3 fit parameters x'_o, y'_o, and q/P which means that the fit is a classic, non-iterative linear fit. These simplifications keep the number of CPU cycles low and reduce the amount of computing hardware required to execute the trigger.

It is important to note that although the fitting process has been simplified, the GEANT modeling of the muon system has not. A complete magnetic trace is used throughout. Appropriate multiple scattering and dE/dx losses are incorporated. A realistic luminous region is used and non-prompt muons are generated from detached vertices.

Figure 4.39 quantifies the rejection power and relative efficiency of this tracking dimuon

trigger. The J/ψ efficiency is plotted versus the minimum bias rejection ratio. The J/ψ efficiency is normalized to events where both muons from the J/ψ have momentum greater than 5 GeV/c and both muons also leave hits in all three stations of the muon system. All reconstructed muons are required to have $\chi^2 < 25.2$ and the two muons must have opposite reconstructed charge and appear in two different octants. The main branch of the "cut tree" is a requirement on the minimum radius of all the muon hits. Branching off is a set of increasingly tighter cuts on the maximum χ^2. The third branch is a set of cuts on the minimum reconstructed P_T.

We are able to achieve a rejection of 600 to 1 with an efficiency of nearly 50% with the principal cuts being a radius greater than 32 cm, a $\chi^2 < 14.4$, and a minimum $P_T > 0.4$ GeV/c, although several different cut selections give essentially identical results.
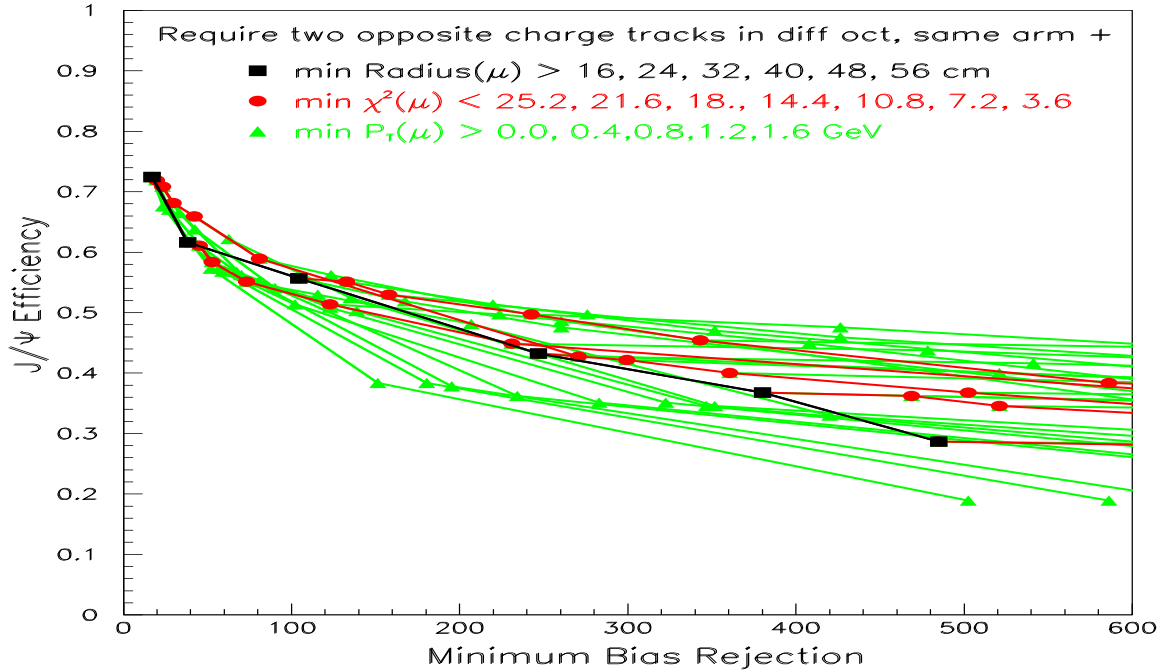
Figure 4.39: J/ψ efficiency versus minimum bias rejection rate for cuts on the minimum radius, maximum χ^2, and the minimum muon P_T. Two oppositely charged tracks in different octants in the same arm must pass the relevant cut. Black lines connect the squares which show the variation as the minimum radius is increased. From each black square a red line connecting the circles shows the change as the maximum χ^2 cut is decreased. From each red circle a green line connecting the triangles shows the variation as the minimum reconstructed muon P_T is increased. All information in this stand-alone trigger comes from hits in the muon system alone.

4.11.3   Muon Trigger Summary

Using a realistic GEANT simulation, which increases the muon detector occupancy by a factor of 100 with respect to a naive simulation, and the straightforward tracking algorithm

described in Section 4.11.2, we are able to obtain a 600:1 rejection ratio with efficiency of nearly 50%. This trigger will be implemented using a modification of the hardware being developed for the silicon pixel vertex trigger. With a rejection of 600:1, the dimuon trigger uses only a small fraction of the Level 1 bandwidth which is dominated by the vertex trigger, which has a rejection of 100:1. Therefore, this trigger is suitable for both calibrating the vertex trigger and taking physics data. Following the Level 1 trigger (at either Level 2 or Level 3), we can gain further rejection by requiring the tracks which are found by the muon system to correspond to tracks found by the silicon pixels and forward trackers. After requiring a link we can also cut on the more accurate forward-tracker momentum, require the track be detached from the primary vertex, and/or make an invariant mass cut.

4.12 The BTeV Trigger System

The trigger system is crucial for the success of BTeV. It finds B events by taking advantage of the main difference between these events and typical hadronic events—the presence of detached beauty or charm vertices. The trigger detects these vertices by utilizing the superior pattern recognition capabilities of the pixel detector to reconstruct tracks and vertices in the first stage of the trigger, Level 1. This is referred to as the Level 1 vertex trigger, which is the primary trigger for the experiment. In addition to the vertexing capabilities of Level 1, the trigger system includes an independent Level 1 muon trigger (described in the previous section) that receives data from the muon detector to select J/ψ and prompt muon events. Besides providing interesting physics on its own, the muon trigger is used to calibrate the vertex trigger.

Results from the Level 1 vertex trigger are combined with results from the Level 1 muon trigger in the Global L1 (GL1) trigger, which ultimately selects the beam crossings that pass the first level trigger. Data that survive the selection criteria are assigned to a Level 2/3 processor for Level 2 analysis. Data that survive Level 2 will be analyzed by Level 3 algorithms that decide whether or not the data should be recorded on archival media.

To perform the large number of calculations needed to process and select B events at a rate of 7.6 million beam crossings per second, we require a massively parallel system with several thousand computational elements. These elements include large Field Programmable Gate Arrays (FPGAs), Digital Signal Processors (DSPs), and general-purpose microprocessors. FPGAs are used at the earliest stage of the processing pipeline to perform large numbers of rudimentary calculations that are required for pattern recognition. DSPs offer more programming flexibility than FPGAs, and are used for the Level 1 trigger calculations that entail track and vertex reconstruction. Moreover, the I/O rate capabilities of DSPs are important at Level 1, since we require high bandwidth to get data to the processors. At Levels 2 and 3 the I/O rate requirements are less critical (data rates are lower than at Level 1), and we have decided to use general-purpose microprocessors for this part of the trigger. The microprocessors provide programming flexibility and significant processing power.

This section provides an overview of the BTeV trigger with references to ongoing trigger R&D described in greater detail in Chapter 5. Many, if not most, of the results for the trigger system presented in the May 2000 BTeV Proposal are still valid today and will not be presented here. One exception is a significant development that promises to drastically reduce the technical risk of the trigger system. Since submission of the May 2000 Proposal, an NSF funded project called RTES (Real Time Embedded Systems) [22] has begun to develop a semi-autonomous, self-monitoring, fault-tolerant and adaptive framework to address issues facing complex computing architectures such as the BTeV trigger. The RTES project is described in Chapter 5.

4.12.1 Trigger Overview

The trigger system consists of three levels [23]. Each level contributes to the reconstruction of events, and successive levels impose more and more refined selection criteria to select B events and reject light-quark background events. At Level 1 the trigger reduces the beam crossing rate of 7.6 MHz by a factor of 100 while maintaining high efficiency for B decays that can be successfully reconstructed in the spectrometer. The tracks and vertices found at Level 1 are passed to Level 2. At Level 2 we improve the reconstruction of tracks and vertices by reviewing the pixel data used at Level 1, and by including additional pixel hits in the tracks. At Level 3, all of the data for a beam crossing are available and are used to impose the selection criteria for the final trigger decision. The trigger rate is reduced by an additional factor of 20 by Levels 2 and 3.

As mentioned previously, BTeV will operate at a luminosity of 2×10^{32} cm^{-2} s^{-1}, corresponding to an average of two interactions per beam crossing at a crossing rate of 7.6 MHz. Average event sizes will be ∼100 KB after zero-suppression of data is performed by front-end detector electronics. Since every beam crossing will be processed, this imposes an extremely high data rate of ∼800 GB/sec on the experiment.
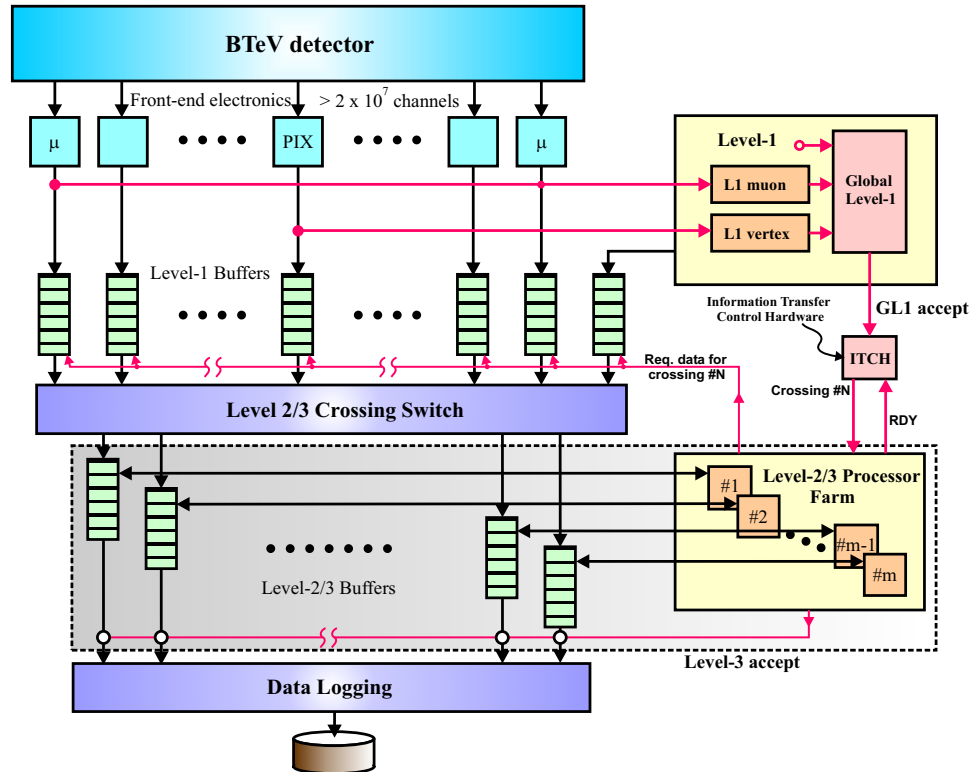

Figure 4.40: BTeV Three-Level Trigger Architecture

BTeV will employ the three-level hierarchical trigger architecture shown in Fig. 4.40, to

handle this high rate. Sparsified data from all detector components will be sent via optical links to Level 1 buffers. Data from the pixel and muon detectors will also be sent to Level 1 trigger processing elements. Trigger results from the Level 1 muon and vertex triggers will be passed on to the Global Level 1 (GL1) trigger manager, where decisions will be stored as a list of accepted beam-crossing numbers by the Information Transfer Control Hardware (ITCH). Level 1 will reject 97.5% of all incoming events, thereby reducing the data rate by a factor of $\sim$100 to $\sim$20 GB/sec.

Levels 2 and 3 (L2/3) will be implemented with a cluster of commodity CPU nodes. A request from an idle L2/3 node will be sent to the ITCH, which will respond by assigning a beam-crossing number to that node. This node will then request a subset of the data (mostly pixel data) for that beam crossing from Level 1 buffer managers. A switch will combine data for the same crossing and route them to the buffer of an L2/3 node allowing a more refined analysis that will further reduce the data rate by a factor of $\sim$10.

If the data satisfy the Level 2 selection criteria, the same processing node will then enter the Level 3 phase and request that data from the rest of the sub-detectors be transferred from Level 1 to Level 3 buffers (L2/3 buffers will simply be the RAM attached to the processing node). Using complete information from the detector, Level 3 will reduce the number of accepted crossings by at least an additional factor of $\sim$2. We believe that Level 3 will be able to further compress the data for accepted beam crossings by a factor of $\sim$4, which means that we expect the data rate out of Level 3 to be $\sim$200 MB/sec.

4.12.2   Level 1 Vertex Trigger Algorithm

The first phase of the Level 1 vertex trigger algorithm is the pattern recognition that uses pixel hits to find tracks. This is also referred to as track-segment finding [24]. This phase of the algorithm starts by finding the beginning and ending segments of tracks in two separate regions of the pixel planes, an inner region close to the beam axis and an outer region close to the edge of the pixel planes. The search for the beginning and ending segments of tracks is restricted to these inner and outer regions, respectively. Segments are found using hit clusters from three adjacent pixel stations in the defined regions. Inner segments are required to point back to the beam axis while outer segments are required to project outside pixel plane boundaries. Once these segments are found, they are then matched to form complete tracks in the segment matching stage.

After complete tracks are found, the track and vertex reconstruction phase of the trigger performs calculations to determine the momentum of each track and calculate its transverse distance from the beam axis. Primary vertices are found by looping through all tracks with transverse momenta $p_T \leq 1.2$ GeV/c that appear to originate close to the beam line. Remaining tracks are then tested for their detachment from the primary vertices that were found. The Level 1 vertex trigger selects events if there are at least n tracks in the same arm of the BTeV detector satisfying the following criteria: $p_T^2 \geq 0.25$ (GeV/c)^2, $b \geq m\sigma$, and $b \leq 2$ mm, where b is the impact parameter and n and m are tuned to achieve the desired rejection of minimum-bias events. For a single-arm spectrometer we may choose to take

advantage of these selection criteria to select events with B decays that are directed towards the instrumented arm of the spectrometer. This can be done to increase the efficiency for B events in the one-arm spectrometer compared to the two-arm spcectrometer.

Our studies indicate that the Level 1 vertex trigger is able to reject 97.5% of all minimum-bias events while accepting ~60-70% of the B events that would survive our offline analysis cuts.

4.12.3 Level 1 Vertex Trigger Hardware

A block diagram of the Level 1 vertex trigger is shown in Fig. 4.41. Data from all 30 stations of the pixel detector are sent to FPGA-based pixel processors that group individual pixel hits into clusters. Hit clusters from three neighboring pixel stations are routed to FPGA hardware that finds beginning and ending segments of tracks in the pattern recognition phase of the trigger. Track segments found at this stage are sorted by a switch according to their beam crossing number, and routed to a DSP in the track/vertex farm. This DSP performs segment matching, as well as track and vertex reconstruction. Based on initial studies done for the BTeV proposal, we estimated the average processing time per beam crossing for the combined segment matching plus track and vertex reconstruction to take ~350 μs on a single 150 MHz TI TMS320C6711 floating-point DSP. Since the time between beam crossings is 132 ns, this would require a total of ~2,500 DSPs in the track/vertex farm in order to examine every beam crossing. These estimates of our processing needs are compared to real timing results in the trigger R&D section of Chapter 5.

We are currently developing a prototype board for the segment matching, tracking, and vertexing portion of the Level 1 trigger. This prototype has four DSPs so that we can study parallel processing with DSPs. Simulated data will be sent from a host computer to an FPGA buffer manager that distributes the data to each DSP. Reconstructed tracks will be returned to the host computer, trigger results from each processor will be sent through an FPGA interface to an on-board μ-controller and forwarded to GL1, and a second on-board μ-controller will be used as a communications channel to a supervisor and monitor. This allows commands to be sent to the board, initialization of the DSPs, and provides hardware monitoring and fault detection. JTAG ports will be used for real-time debugging and initial start-up of the prototype. More details about the trigger prototype can be found in Chapter 5.

4.12.4 Levels 2/3

The Level 2 algorithm refines the tracks found at Level 1 by adding pixel clusters from the planes located between the "inner" and "outer" track segments. It then performs a Kalman-filter track fit, and improves the momentum resolution to about 5–10%. One of two requirements must be satisfied to select an event. A secondary vertex must be present, or the collection of detached tracks must satisfy a minimum p_T cut. The result is a joint light-quark rejection of 1000–1 per beam crossing for Levels 1 and 2 combined and ~50% overall efficiency
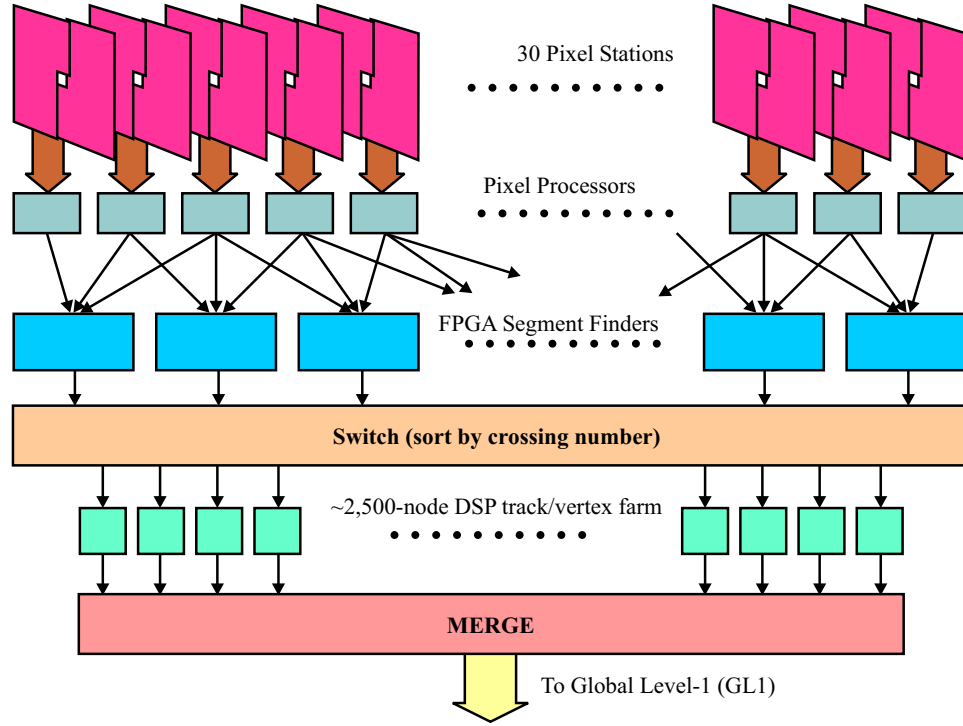
Figure 4.41: BTeV Level-1 vertex trigger.

for most B decays of interest. The execution time of the Level 2 algorithm extrapolates to about 15 milliseconds per beam crossing on the type of processor described below. This performance is sufficient for BTeV operating at the design luminosity. Additional details of improvements made to the algorithms are presented in the trigger R&D section in Chapter 5.

The Level 2/3 trigger is implemented as a farm of commercial processors. These could, for example, be INTEL, PowerPC, or AMD processors running the LINUX operating system. We expect that by the time BTeV runs, processor clock speeds will easily exceed 2.5 GHz. Given an average decision time of 15 ms per Level 2 node, we will need about 2000 of these CPUs.

4.13 Data Acquisition System

In BTeV, the Data Acquisition System, the DAQ, and the trigger are intimately connected. To accomodate the BTeV trigger algorithms, which operate asynchronously on beam crossings and do not have fixed latency, substantial event buffering is required at each trigger level and between the final trigger and the system which records the data on mass storage. The function of the DAQ is to transfer data from the detector to the trigger system, provide the buffering and data movement between levels of the trigger system, and from the trigger system to permanent storage.

4.13.1 Data Movement between Front End Electronics Boards and Buffer Memories

Preliminary testing indicates that interference problems are minimal when data compression and serialization logic is placed directly on the front-end modules. The baseline design will therefore assume fast serial I/O for all front-end systems.

Data from the front-end electronics is collected by "Data Combiner" boards. The Data Combiners group small data packets from multiple front-end sources into one larger packet, reducing processing overhead in the buffers and switching network. They also route each data packet to one of eight independent branches (or "highways"). The architecture of the trigger and data acquisition ssytem is shown in Figure 4.42. The highway implementation allows the switching network to be built from several smaller commercial switches, instead of one large (possibly in-house developed) switch, at a significant cost savings. Before the data is forwarded to the switching network, it is held in the "Level 1 Buffers" pending the first level trigger decision. More than 97.5% of the events fail the first level trigger and are discarded.

The Data Combiners are currently located near the detector and drive the optical links to the Level 1 Buffers. We are studying the possibility of implementing an asymmetric ring protocol in the front-end module interface so that the Data Combiner function can be moved to the other end of the fiber. This has some potential for cost reduction and improved load balancing. Connections to the front-end boards and from Data Combiners to the Level 1 Buffers will be based, as much as possible, on the emerging 3GIO specification. Connections from the Level 1 Buffers to the switching network will likely be Gigabit Ethernet.

4.13.2 Data Buffering for the Level 1 Trigger

The first level trigger is highly parallel, with a significant software component. As a result, the average Level 1 decision time, and the accompanying buffer requirement, are two orders of magnitude greater than in previous systems. The first level trigger also has the distinction of operating asynchronously, which means that the worst-case decision time may be increased by another two orders of magnitude. The BTeV system will digitize, sparsify, and transmit data at the beam crossing rate of 7.6 MHz into off-detector buffer memories. With this approach

applied to all subdetectors, the first level buffers can hold many beam crossings of data and can provide the average latency required for the Level 1 trigger to make its decision. Buffers of this size would be cost-prohibitive if implemented in either analog or digital memory in the front-end ASICs. Commodity DRAM is the only reasonable alternative, with all detector channels digitized at the full crossing rate.

Inputs to the Level 1 trigger are provided by the front end systems over dedicated links. Currently, the pixel detector and muon detector are used in the Level 1 trigger.

4.13.3 Data Buffering and Movement from the Level 1 to Level 2/3 Trigger

Three distinct logical trigger levels are described above. From an engineering perspective, there is little difference between Level 2 and Level 3; these levels are both executed in general purpose processors. The only distinction between these levels is that the start of the Level 3 processing presupposes that ALL data have been transferred to the processor, whereas the Level 2 processing operates only on a subset of the total data.

Following the first level trigger decision, which rejects all but 2.5% of the beam crossings, a much more modest volume of approximately 15-20 GBytes/sec must be buffered and eventually transferred to the level 2/3 trigger system. The Level 2/3 trigger is performed with a highly parallel system of commericial microprocessors, which also operates asynchronously with variable latency. The rate is now low enough so that this data movement can be easily accomplished with a commercial switching network. The Level 1 Buffers will include a standard interface and processor, and will appear to the Level 2/3 processors as networked servers. This allows the use of off-the-shelf communications software during the initial implementation. It also supports a variety of access modes, from staged to full transfer of data, under control of the individual L2/3 processors.

The specifications shown in Table 4.11 are used as the baseline for the BTeV data acquisition. These numbers represent both arms of the detector.

event size	100 kBytes
number of detector data links	5000
number of L1 data buffers	400
number of L2/3 data links	64
number of L2/3 processors	2500

Table 4.11: Estimates of Hardware for BTeV Trigger and Data Acquisition System

The total system buffer memory, assuming 400 L1/switch input buffers and 64 switch output buffers, is almost 100 Gigabytes. Buffers in the L1/2/3 processors will push total system memory requirement to approximately 400 Gigabytes. We will actually have more than a Terabyte of buffer memory, in case there are unexpected backgrounds or noise.
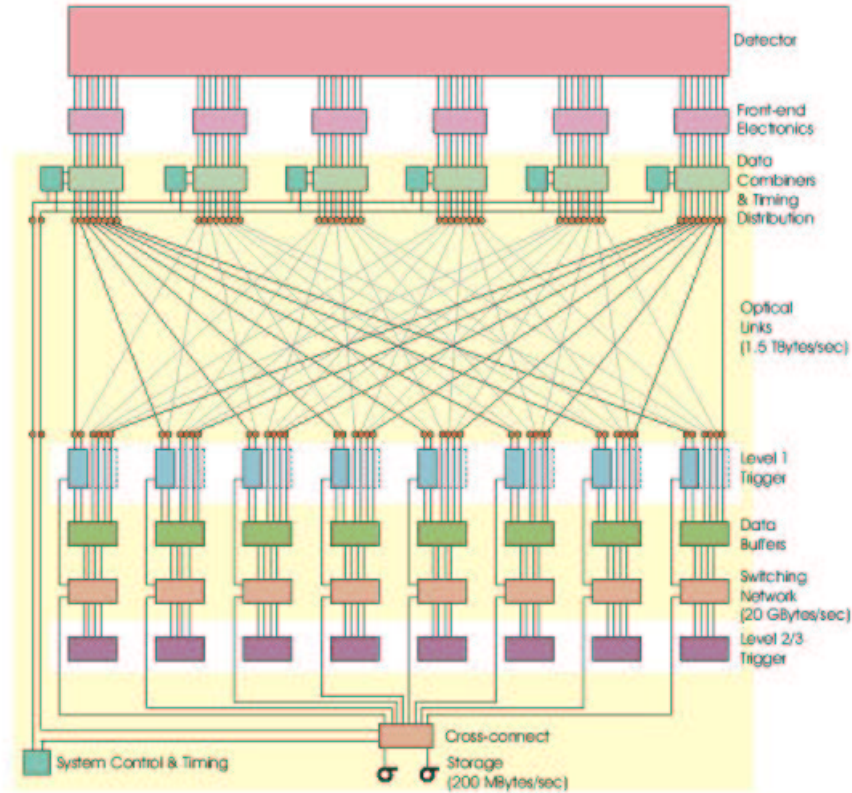
Figure 4.42: Simplified Data Acquisition System showing eight "highways".

4.13.4 Data Logging: Movement of Data from the Level 2/3 Processors to Mass Storage Systems

Each event is handled by only one Level 2/3 processor. (i.e., an event is not scattered across processors nor is it copied to more than one processor). All accepted events need to be moved out of the L2/3 processors and onto tape for long term data storage, and a fraction of the events need to be made available for online monitoring (by "consumer processes").

Events coming out of the Level 3 processors will not be raw data, but already processed data (except for a highly prescaled sample used for monitoring the data reduction algorithm itself). This should shrink the event size from 200 kBytes to 50 kBytes. Assuming an event size of 50 kBytes, and a 4 kHz event rate to the loggers, the data rate to tape is on the order of 200 MBytes/sec. The consumer processes will also add an additional 5-10% of throughput.

Since the data logging rate out of each Level 3 processor is small, it is less cost effective to attach logging media to these individual nodes than to provide a small number of separate logger nodes. The necessary bandwidth to the logger nodes is also small (2-3%) compared to the raw data coming up the Level 2/3 farms, so the same switch could be used to pass

158

the event to the logger nodes as well. Alternatively, a dedicated network could be provided between the Level 3 processors and the logging nodes. In the current plan, a single event is routed to the next free logging node but buffering several events in the Level 3 processors and sending them out together is possible if it turns out to be beneficial.

The number of logging nodes themselves is clearly a function of the data rate. It is assumed that data will first be buffered to disk before being written to tape. This serves a dual purpose; buffering enough data before a transfer to keep the tape drives streaming, and protecting against tape media errors and tape drive failures. With current market technology, a single processor node can handle 10 Mbytes/sec to tape including the initial disk write. We will therefore require a minimum of 20 data logging nodes. We are planning for twice this number to have a safety factor and to be able to handle failures.

4.13.5   Slow Control and Monitoring, Hardware Management, and Parameter Control

The data acquisition system also supplies several other key services to the experiment. It includes a slow control and monitoring system, which can initialize, control, and monitor the front end hardware and the components of the trigger and DAQ systems. It can also monitor and, in some cases, control various environmental conditions, such as temperature, humidity, etc. It provides facilities for run control, logging of monitoring and diagnostic information, alarms generation, and the operator interface. These functions are supported by an extensive and sophisticated system of databases, which will provide uniform access to key parameters and permit long term trending and analysis.

Bibliography

[1] "ATLAS Pixel Detector Technical Design Report", CERN/LHCC 98-13, available at http://atlasinfo.cern.ch/Atlas/GROUPS/INNER_DETECTOR/PIXELS/tdr.html

[2] Y. Arai, *et al.*, "A modular straw drift tube tracking system for the Solenoidal Detector Collaboration experiment, Part I: Design"; Nucl. Instrum. Meth. A 381 (1996) 355.

[3] ATLAS Inner Detector Technical Design Report, CERN/LHCC/97-16,17.

[4] F.M. Newcomer, R. Van Berg, J. Van der Spiegel and H.H. Williams, Nucl. Instrum. Meth. A 283 (1989) 806.

[5] G. Tonelli, *et al.*, "The R&D program for silicon detectors in CMS"; Nucl. Instrum. Meth. A 435 (1999) 109.

[6] M.A. Frautschi, "Radiation Damage Issues for the SVX II Detector"; CDF/DOC/SEC_VTX/PUBLIC/2368.

[7] W. Adam *et al.*, Nucl. Inst. & Meth. **A343**, 60 (1994).

[8] J.L. Rosen, Proceedings of The Fifth International Workshop on $B-$Physics at Hadron Machines, Los Angeles, USA, Oct. 13-17, 1997, published in Nucl. Inst. and Meth. A408 (1998) 191; S. Kopar, Proceedings of the The 3rd International Workshop on Ring Imaging Cherenkov Detectors Weizmann Institute of Science Ein-Gedi, Dead-Sea, Israel, Nov. 15-20, 1998.

[9] P. Carter, Proceedings of the The 3rd International Workshop on Ring Imaging Cherenkov Detectors Weizmann Institute of Science Ein-Gedi, Dead-Sea, Israel, Nov. 15-20, 1998. "Proposal for Dual Radiator RICH for HERMES", E. Cisbani *et al.*, Hermes Internal Note 97-005.

[10] LHC-B, Technical Proposal, CERN LHCC 98-4, LHCC/P4, 1998.

[11] R. Forty, CERN-PPE/96-176, Sept. 1996 published in Proc. of the 4th Int. Workshop on $B-$physics at Hadron Machines, Rome, Italy, June 1996, F. Ferroni, P. Schlein (Eds.), North-Holland, 1996.

[12] E. Albrecht *et al.*, "Performance of Hybrid Photon Detector Prototypes With 80% Active Area For The RICH Counters of LHCb", submitted to Nucl. Inst. & Meth. **A**, See also GLAS-PPE-1999-22 (hep-ex/0001053) and Nucl. Inst. & Meth. Phys. Res. **A433**, 159 (1999).

[13] E. Blucher, B. Gittelman, B. K. Heltsley, J. Kandaswamy, R. Kowalewski, Y. Kubota, N. Mistry, A. Bean, and S. Stone, "Tests of Cesium Iodide Crystals for an Electromagnetic Calorimeter," Nuclear Instruments & Methods **A249**, 201 (1986).

[14] We note that a past favorite, CsI (undoped), was attractive from many points of view. However, it is not radiation hard enough. Furthermore, it is not quite fast enough to completely produce all its charge in under one crossing. Lead glass has been rejected because it is not likely to survive the yearly radiation dose.

[15] CMS, "The Electromagnetic Calorimeter Project Technical Design Report," CERN/LHCC 97-33, CMS TDR 4 (1997).

[16] R. J. Yarema *et al..*, A Fast Wide Range Charge Integrator and Encoder ASIC For Photomultiplier Tubes," FEMILAB-PUB-92-311 (1992). This chip was developed for KTEV.

[17] A.N. Annenkov *et al.*, "Systematic Study of the Short-Term Instability of PbWO$_4$ Scintillator Parameters under Irradiation," CMS Note 1997-055.

[18] Private communication from Ed Blucher. The dominant cause of the constant term seems to be a differing crystal response depending on where on the face of the crystal the incident photon strikes. This effect was not observed in the CLEO CsI calorimeter (see ref. 1).

[19] Y. Kubota *et al..*, "The CLEO II Detector," Nuclear Instruments & Methods **A320**, 66 (1991).

[20] J.M. Butler *et al.*, "Study Of Fast Gases, Resolutions And Contaminants In The D0 Muon System," Nucl. Instrum. Meth. **A290**, 122 (1990).

[21] S. Bhadra, S. Errede, L. Fishback, H. Keutelian and P. Schlabach, "The Design And Construction of the CDF Central Drift Tube Array," Nucl. Instr. Meth. **A268**, 92 (1988).

[22] E.E. Gottschalk, The BTeV DAQ and trigger system–some throughput, usability and fault tolerance aspects, Proc. CHEP 2001, Beijing, Sept. 3-7 2001, p. 628.

[23] M.H.L.S. Wang for the BTeV Collaboration, BTeV Level 1 Vertex Trigger, FERMILAB-Conf-01/336-E.

[24] E.E. Gottschalk, BTeV detached vertex trigger, Nucl. Instrum. Meth. A 473 (2001) 167.

Chapter 5

BTeV R&D Program

Introduction

In this chapter, we describe the status of the BTeV R&D program, including its recent accomplishments and its plans for the next year, or, in some cases, two years.

R&D is critical to the ultimate success of BTeV. We use established technologies where possible. However, in order to meet the requirements described in Chapter 3, several new technologies have to be developed. In some cases, even where we have chosen "existing technologies," they are still relatively new technologies which have been developed by others, but have not yet been tested in large scale operation. In some cases where we have chosen existing technologies, we will use them in different ways or expose them to different environments than the ones they were developed for. This means that we must do some research and development, or at least some development, on every subsystem.

In the following, we describe the R&D effort associated with each major detector component, the trigger, and the data acquisition system. The various activities include development of analog and digital ASICs, studies of radiation hardness, ageing studies, simulations, finite element analyses, materials testing, mechanical mockups, bench tests, beam tests, reliability studies, and production yield studies, to name a few. A prototype will be constructed for every detector subsystem and for the trigger and data acquisition system. All detector prototypes will be operated in test beams over the next two years. All materials will be tested for radiation hardness at the required level and for ageing and environmental robustness. Critical calibration systems will also be tested thoroughly. It is through these efforts that we intend to guarantee that our designs will meet our requirements and that we can build the BTeV detector on time and on budget.

The R&D program has been supported by DOE through Fermilab and the DOE University program, NSF, INFN, and IHEP. We have also received significant support from the universities whose physicists are participating in the experiments.

5.1 Pixel Detector R&D

5.1.1 Introduction

One of the defining characteristics of BTeV is the plan to use a vertex trigger as the primary trigger for the experiment. The pixel detector is required to provide high resolution space points (better than 9μm for tracks of all angles) which will be used by this trigger. This imposes both fast readout and large bandwidth requirements on the front end electronics. To minimize the extrapolation error, the detector will be placed as close as possible to the interaction point and hence will be exposed to a significant level of irradiation. At our maximum projected luminosity, it is expected that the innermost pixel detector will receive a fluence of 1×10^{14} minimum ionizing particles/cm^2/year. This significant radiation environment means that all components of the pixel system have to be radiation hardened.

Since the submission of the BTeV Proposal two years ago, we have made great progress in the development of the individual components required to build the BTeV pixel detector. Our R&D has also started to address the system engineering aspects. This section describes the main accomplishments achieved during this period.

The major components of the pixel detector system are the sensor, readout chip, sensor-readout-chip connection (bump bonding), high-density interconnection between the pixel readout chips and the system control elements, and the mechanical support and cooling system. We have been designing and purchasing these components, assembling units and testing them in beams and exposing them to intense radiation. We have also performed detailed simulation studies to understand the various design issues for the components as well as system aspects. Through these efforts, not only are we learning what is needed for BTeV, but we are gaining the necessary experience and know-how to build the actual pixel detector for the BTeV experiment. One of the highlights of this effort is the successful demonstration in a test beam during the 1999 Fermilab fixed target run of the resolution that can be achieved with a pixel detector. Fig. 5.1 shows the resolution as a function of the incident beam angle for a pixel detector [1]. Two curves and data points are included in the figure: the solid line and circles show prediction and measurements done with an eight-bit ADC external to the pixel readout chip to take charge sharing between pixels into account; the dashed curve and triangular data points illustrate the simulation and measurements obtained if we were to use only binary (on-off) readout. The clear advantage of using charge sharing, made possible by analog readout, is evident and for all incident angles, a resolution of better than 9μm has been obtained.

5.1.2 Sensor development

The main challenge is to have a radiation hardened detector which will survive and remain operational after significant radiation damage to both the surface and the bulk of the silicon sensors.

The bulk damage is mainly due to the non-ionizing energy loss (NIEL) which, through the displacement of atoms in the crystal lattice, creates new energy levels, effectively acting
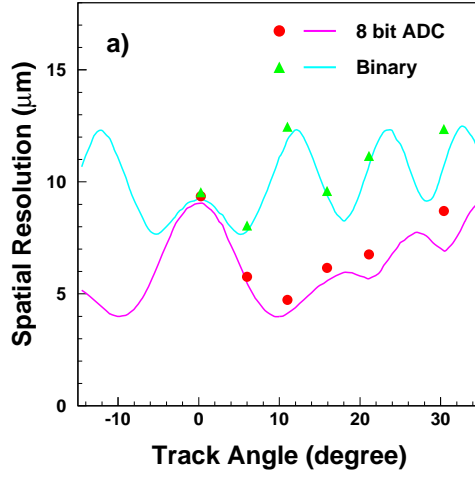
Figure 5.1: Resolution as a function of the angle of the incident beam. Data was taken with prototype pixel detectors during the 1999 Fermilab fixed target run. The detectors were instrumented with the earliest versions of the pixel readout chip FPIX0 at Fermilab. The curves represent the predicted resolution: the oscillating curve is the simulated digital resolution and the lower one assumes 8-bit charge digitization. The circles and triangles are extracted from the data.

as acceptors. Therefore the effective doping concentration will change with irradiation. For very-high-dosage irradiation, this will eventually lead to inversion of the conduction type of the bulk material (type-inversion), increases in leakage current and depletion voltage, changes in capacitance and resistivity, and charge collection losses. These are problems that need to be addressed by all the next generation hadron collider experiments. As a result, there is a worldwide effort to address these technical challenges. Solutions include the design of multiple guard ring structures to avoid avalanche breakdown along the sensor edges, low resistivity silicon substrates to delay type inversion, thin detectors to reduce the depletion voltage required, and oxygenated silicon wafers to reduce the effects of radiation-induced defects in the silicon lattice [2].

In order to increase the useful operation time of the silicon sensors, operation with partial depletion has to be considered. This is more suitable for n-type pixel readout, because after type inversion the depleted region will grow from the n+ side of the junction. For this reason, the BTeV pixel sensors have $n^+/n/p^+$ configuration. In these detectors, the charge collecting pixels are defined by the n-implants that are isolated from their neighbors. Without isolation, the accumulation layer induced by the oxide charge would short the individual n^+ pixels together. We have explored two isolation techniques:

- The p-stop isolation where a high dose p-implant surrounds the n-region.

- The p-spray isolation developed by the ATLAS collaboration, where a medium dose shallow p-implant is applied to the whole n-side. To increase the radiation hardness and also the breakdown voltage before irradiation, a "grading" of the p-spray implantation (moderated p-spray) is required [3]

We have tested prototype p-stop sensors produced by SINTEF. The base material is low resistivity (1.0-1.5 KΩ cm) silicon, in a ¡100¿ lattice, 270 μm thick. Some of the wafers have been oxygenated. A few of these sensors have been exposed to a 200 MeV proton beam at the Indiana Cyclotron Facility (IUCF). To characterize these sensors before and after irradiation, we measured bulk parameters of the sensors including the bias voltage dependence of the leakage current, the full depletion voltage, breakdown voltage, and the temperature dependence of the leakage current [4].

Figure 5.2 shows the leakage current measurements before and after irradiation up to a fluence of 2×10^{14} 200 MeV protons cm^{-2} for a SINTEF p-stop sensor. The measurement after irradiation was performed at various temperatures (23^oC, 10^oC, 0^oC, and -10^oC) and as expected, we observed that the leakage current decreases exponentially with temperature.
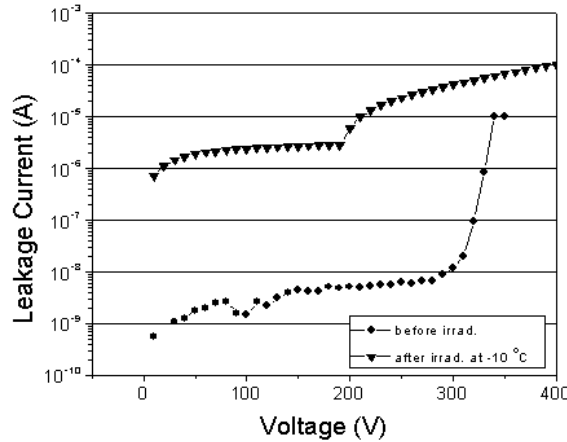

Figure 5.2: Leakage current measurements before (at room temperature) and after (at -10^0C) irradiation to 4×10^{14} p/cm^2 for a SINTEF p-stop sensor.

The other bulk damage is the change in effective doping density which is reflected in a change in the full depletion voltage. Fig. 5.3 shows the dependence of the full depletion voltage on the proton irradiation fluence for a few p-stop sensors made from standard and oxygenated wafers. At a fluence of 4×10^{14} p cm^{-2}, the full depletion voltage is still rather low, even lower than the value before irradiation. This characteristic is due to the low resistivity of the starting silicon material. This result, together with the fact that the breakdown voltage is still high compared to the full depletion voltage after irradiation, means that the BTeV pixel detector can be fully depleted without excessively high bias voltage even after a few years of operation.
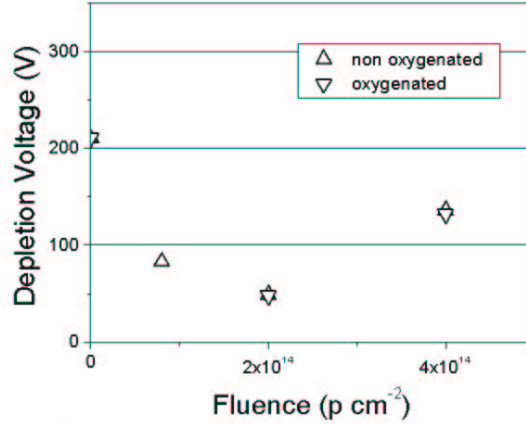
Figure 5.3: Full depletion voltage as a function of the fluences of the proton irradiation for normal and oxygenated sensors.

We have recently also started to characterize moderated p-spray sensors obtained from three vendors via the ATLAS collaboration. Typically, the initial leakage current of these detectors was found to be about 10 nA/cm^2, similar to the p-stop sensors. Furthermore, the breakdown voltage before irradiation, for these sensors, is rather high as expected. During the next few months, we will perform irradiation studies on these sensors.

We also plan to study both the p-stop and the moderated p-spray detectors in a test beam to study the charge collection properties before and after irradiation and compare the results with the predictions from simulation.

5.1.3 Pixel readout chip

The use of the pixel detector data in the first level trigger means that the BTeV pixel readout chip must be capable of reading out all hit information from every $p\overline{p}$ interaction. Furthermore, the pixel readout chip should be optimized for the 132 ns time between crossings planned for the Tevatron collider. It must be radiation hard so that it can be used close to the beamline. This requires a pixel readout chip with a low noise front-end, an unusually high output bandwidth, and implemented in a radiation-hard technology. During the last few years, a pixel readout chip has been developed at Fermilab to meet these requirements. This has been done through several stages of chip development, each of increasing complexity [5].

Recently, the pixel readout chips have been implemented in two different commercial 0.25 μm CMOS processes following radiation tolerant design rules (enclosed geometry transistors and guard rings) [6]. The preFPIX2I chip, containing 16 columns with 32 rows of pixel cells, and complete core readout architecture, was manufactured by a vendor through CERN [7]. The preFPIX2Tb chip, contains, in addition to the preFPIX2I chip features, a new programming interface and 14 digital-analog-converters (DAC) to control the operating

166

and threshold settings of the whole chip. It was manufactured by Taiwan Semiconductor Manufacturing Company (TSMC).

To study total dose and Single Event Effects (SEE), samples of these prototype chips have been exposed to 200 MeV protons at IUCF. The comparison of the chip performance before and after exposure shows the high radiation tolerance of the design [8]. Chips have been exposed to as much as 7.4×10^{14} protons-cm^{-2} (about 43 Mrad) and no evidence of catastrophic failure or deterioration of the functionality of the readout chip has been observed. In particular, no radiation induced SEE, such as Latch-Up or Gate-Rupture has been observed. Fig.5.4 shows the effect of radiation on amplifier noise.
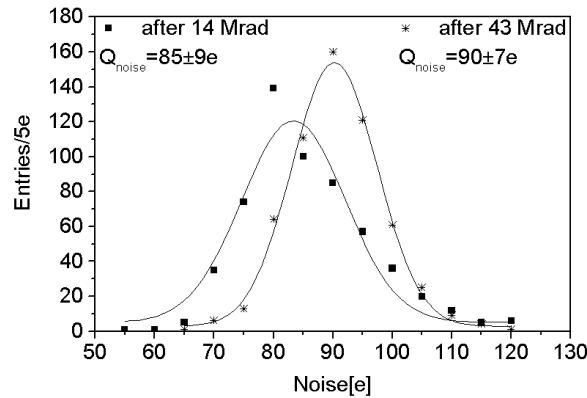

Figure 5.4: Measured noise in the 576 pixel cells of preFPIX2Tb chip after 14 and 43 Mrad of proton irradiation.

An important feature of the preFPIX2Tb chip is the implementation of on-chip DAC's in order to minimize the number of external I/O lines. The change of the DAC behavior due to the proton irradiation has been measured and is shown in Fig.5.5. The three curves shown correspond to the deviation from the linear fit to the unirradiated data for total dose of 0, 14, and 43 Mrad. It can be seen that the linearity and accuracy of the DAC output remains acceptable after 43 Mrad total dose.

We have also measured the Single Event Upset (SEU) cross-section of static registers implemented on the preFPIX2Tb chips, in order to establish the sensitivity of our design to radiation induced digital soft errors. The measurements consisted of detecting bit error rates in the static registers controlling the readout chip front-end operating conditions and the pixel cell response. The single bit upset cross-section measured for the DAC's located on the chip periphery was $(5.5 \pm 0.6 \pm 0.5) \times 10^{-16}$ cm^2 while for the mask and charge-injection registers located inside each pixel cell was $(1.9 \pm 0.2 \pm 0.2) \times 10^{-16}$ cm^2 (where the first error is statistical and the second systematic due to uncertainty in the beam fluence) [9]. We tested and did not observe any dependence of the upset rate on the beam incidence angle or clock frequency up to 16 MHz.

Our measurements of the SEU rate implies that the SEU bit error rate in the BTeV pixel detector is small enough that it will not be necessary to design explicitly SEU tolerant
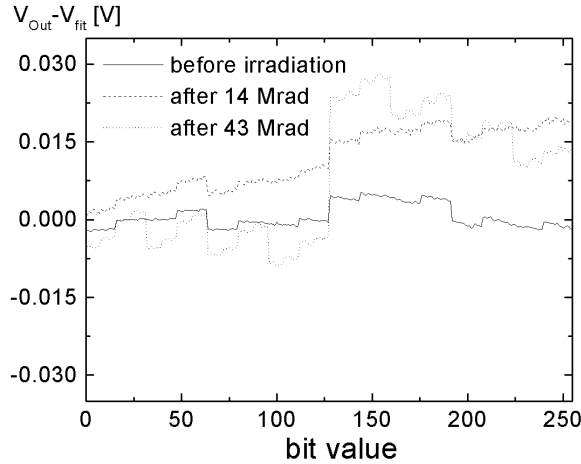
Figure 5.5: DAC analog response before and after 14 and 43 Mrad total dose exposure to 200 MeV protons. The full scale (255 counts) corresponds to about 1.7V

registers. Rather, the SEU rate can be comfortably handled by a periodic readback of the chip configurations during data-taking and a download of the chip configuration whenever an upset is detected.

Based on the experience gained, we intend to submit a full-size BTeV pixel readout chip soon. That chip will have 22 columns by 128 rows. The new section to be included in the chip is a high speed data output interface which accepts data from the core, serializes the data, and transmits the data off chip.

5.1.4 Bump bonding development

The BTeV pixel detector, like all other pixel systems used in or planned for HEP experiments, is based on a hybrid design. With this approach, the readout chip and the sensor array are developed separately and the detector is constructed by flip-chip mating the two together. This method offers maximum flexibility in the development process, choice of fabrication technologies, and sensor materials. However, it requires the availability of a highly reliable, reasonably low cost fine-pitch flip-chip attachment technology. We have focused our study on two options: indium bumps, and Pb-Sn solder bumps.

A series of yield and stability tests were performed on bump-bonded test structures. These tests were done with indium, fluxed-solder, and fluxless-solder bumps from a number of commercial vendors. Our tests have validated the use of indium and fluxless-solder as viable technologies. The failure rate obtained from this large scale test is about 2×10^{-4} which is adequate for our needs [10].

In order to check the long term reliability of the bump-bonding technology, we monitored the quality of the connectivity over a period of one year. In addition, we performed thermal cycling: exposure to -10^0C for 144 hours and $+90^0$C for 48 hours in vacuum. Furthermore,

we irradiated some of these test structures with a ^{137}Cs source up to a dose of 13 Mrad. The typical failure rate of both types of bumps under these stringent tests was found to be a few $\times 10^{-4}$. These results show that both techniques are highly reliable [11].

One of the remaining concerns is that thermal stress on the bumps due to the Coefficient of Thermal Expansion (CTE) mismatch of the bump material, silicon, and the substrate material on which the detector is placed. We have recently embarked on a study of this problem and results are expected in the next few months.

5.1.5 Multichip Module

Each pixel readout chip includes a high density of control and data output lines at the periphery. These lines need to be connected to the back-end electronics. A full set of pads is available on the readout chip for these interconnection purposes. This is achieved through a high density, low mass flex circuit wire bonded to a number of readout chips to form a multichip module.

Each pixel half-plane will be made up of a number of these multichip modules. The module is the basic building block of the pixel detector system.

The pixel module is composed of three layers. The lowest layer is formed by the readout integrated circuits (ICs). The back of the ICs is in thermal contact with the supporting structure, while the top is flip-chip bump-bonded to the pixel sensor. A low mass flex-circuit interconnect is glued on the top of this assembly, and the readout IC pads are wire-bonded to the flex-circuit (see Fig.5.6).
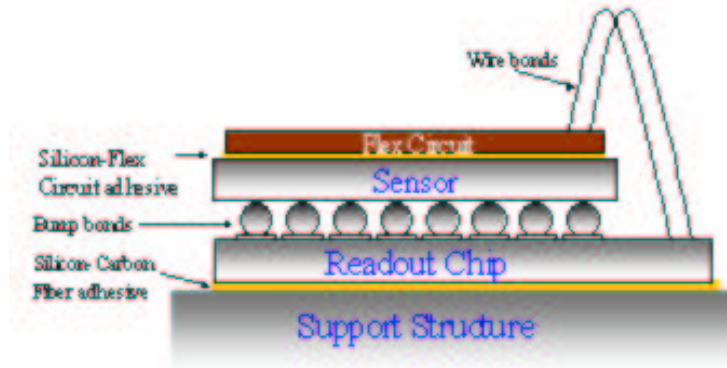
Figure 5.6: Sketch of the pixel multichip module stack

We are presently developing prototypes of the pixel module based on the earlier version of the pixel readout chip FPIX1 to assess the electrical and mechanical performance of such assembly, as well as to acquire early insights on the construction process and yield. A previous module was already manufactured with great success [12].

The FPIX1 interface with the data acquisition system was not optimized to reduce the number of interconnections. The large number of signals in this prototype imposes space

constraints and requires aggressive circuit design rules, such as 35μm trace width and trace-to-trace clearance of 35μm and four metal layers. A circuit with such characteristics is very difficult to obtain and very few places have such manufacturing expertise. The Engineering Support and Technical Division at CERN manufactured the FPIX1 interconnect flex circuit. Fig. 5.7 shows a picture of the flex circuit. Several design strategies to minimize electrical noise and guarantee signal integrity were incorporated in the layout and are being evaluated.

The interface adhesive between the flex-circuit and the pixel sensor has to compensate for mechanical stress due to the CTE mismatch between the flex circuit and the silicon pixel sensor. Two alternatives are being pursued.

Two partial assemblies of this pixel module have already been characterized. One is a single FPIX1 readout chip flip-chip mated to a SINTEF sensor using indium bump bonds. The flex circuit is pasted on top of the sensor. The second pixel module has three readout chips wire-bonded but does not have a pixel sensor.
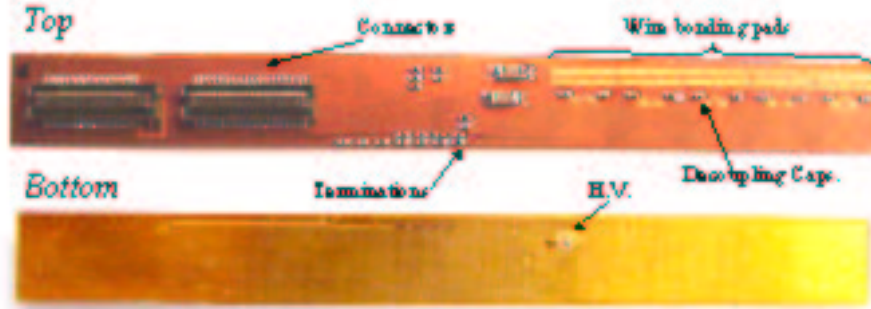

Figure 5.7: Picture of the flex-circuit made by CERN.

These modules were characterized for noise and threshold dispersion. These characteristics were measured by injecting test charge in the analog front end of the readout chip with a pulse generator. The results for various thresholds are summarized in Table 5.1 and 5.2 [13]. These results are comparable with previous characterization results of single readout IC mounted on a printed circuit board. No crosstalk problem has been observed between the digital and analog sections of the readout chip and the flex circuit.

5.1.6 Mechanical support

At the time of the BTeV proposal, the baseline pixel detector design called for the pixel sensors to be mounted in a single large vacuum box. The sensors were to be electrically separated from the circulating beams by a thin aluminum shield, but not located in a separate vacuum enclosure. Subsequent outgassing tests and analysis have led us to conclude that the pixel detector must be located in a separate vacuum enclosure from the beams. Our current design calls for the two detector halves each to be mounted in a sealed vacuum enclosure, separated from the beamline by a thin aluminum membrane, and connected to a

Single bare chip				Single chip with sensor			
μ_{Th}	σ_{Th}	μ_{Noise}	σ_{Noise}	μ_{Th}	σ_{Th}	μ_{Noise}	σ_{Noise}
7400	360	75	7	7800	410	94	7.5
6400	330	78	12	6500	390	110	11
5400	390	79	11	5500	380	110	13
4400	380	78	11	4400	380	110	15
3500	380	79	12	3350	390	120	20
2500	370	77	13	2300	390	120	21

Table 5.1: Performance of the one-chip FPIX1 module without and with sensor. μ represents mean values of distributions and σ's are their RMS. All numbers are given in equivalent electrons. There is no significant increase in noise and threshold dispersion with the sensor attached.

Setting	Chip 1				Chip 2				Chip 3			
$V_{Th}(V)$	μ_{Th}	σ_{Th}	μ_{Noise}	σ_{Noise}	μ_{Th}	σ_{Th}	μ_{Noise}	σ_{Noise}	μ_{Th}	σ_{Th}	μ_{Noise}	σ_{Noise}
1.95	5210	451	93	11	5100	501	105	12	5900	432	85	10.5
2.05	3305	412	80	10	3340	390	92	12	4200	410	87	11
2.15	1540	440	77	11	1850	420	79	11				

Table 5.2: Performance of the three-chip FPIX1 module. μ represents mean values of distributions and σ's are their RMS. All numbers are given in equivalent electrons.

large aluminum box by bellows. Only with this separation of vacuum volumes can a vacuum of 10^{-7} torr be achieved on the beamline.

Significant progress has been made on the engineering design of the overall mechanical support, the vacuum vessel, motor drive assembly, and the individual substrates on which the pixel modules will be mounted. In some cases, early prototypes have been made and evaluated.

Each pixel station is assembled on two substrates, with the surfaces machined to a shingle profile so that there is complete coverage of the active area by the pixel modules. The current baseline design for the substrate is based on a concept developed by Energy Sciences Laboratory, Inc. (ESLI, San Diego, CA). The substrate will be a carbon-carbon composite structure, with flattened glassy carbon tubes to carry coolant, and "fuzzy carbon" fibers extending radially out from the tubes. The shingled surface will be created by machining these fibers after the structure is "carbonized" at very high temperature. A prototype (see Figure 5.8) is on order and will be available for testing in the fall.

The "fuzzy carbon" substrates are expected to be extremely light weight, to provide efficient cooling of the pixel readout chips, and to match the CTE of silicon well enough to allow for construction at room temperature and operation at approximately $-10^{o}C$. How-
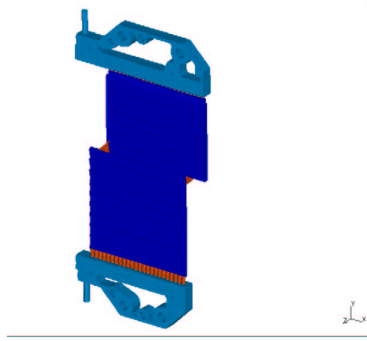
Figure 5.8: Conceptual design of the fuzzy-carbon substrate.

ever, since these substrates can only be manufactured by ESLI, and have not yet been proven to be robust enough, we are also pursuing other substrate designs using beryllium and pocofoam.

Figure 5.9 shows the design of the vacuum vessel and support structure for the pixel detector. Each pixel station will be attached by brackets to a C-shaped support frame. Both the bracket and the frame will be made out of carbon fiber material. Signal feedthrough the vacuum vessel is done by a number of multilayer printed circuit boards with high density multipin connectors. Actuator assemblies located outside the vacuum vessel will be used to control the movement of the pixel stations in and out of the beam during data-taking and beam refill.

The major assembly steps have been worked out for the current design. The mechanical strength of all the important elements such as RF-shield, substrate mounting brackets, C-fiber support cylinder, and vacuum vessel were checked with finite-element-analysis (FEA) calculations to make sure that any deflections and stresses under load are acceptable. To verify the calculations, the manufacturing process, and assembly procedure, a prototype support cylinder and support brackets were made out of carbon fibers. Dummy aluminum substrates were then mounted (see Fig. 5.10) to the cylinder using the brackets on a co-ordinate measuring machine table. Known loads were then applied to the substrate and the deflection of the brackets were measured. Good agreement with the FEA results were obtained.

Work has also started on the vacuum system design. One of the first things that needs to be done is to understand the gas load. We are currently building a 10% mock-up pixel system using material which is as close as possible to that of the real detector. A vacuum vessel and system is almost ready for pumping down. The plan is to measure the outgassing rate as a function of operating temperature. Prototype printed circuit boards which carry the signals from inside to outside the vacuum vessel have also been tested and the results validate our conceptual design. Progress has also been made in better understanding of how to manufacture and de-gas the RF shield and bellows that will result in an accelerator

172

vacuum pressure of 10^{-7} torr.

To check the robustness of the high density flex circuits after multiple flexes due to the movement of the pixel detector in and out the beam, cable flexing tests have been started. Initial results look promising.
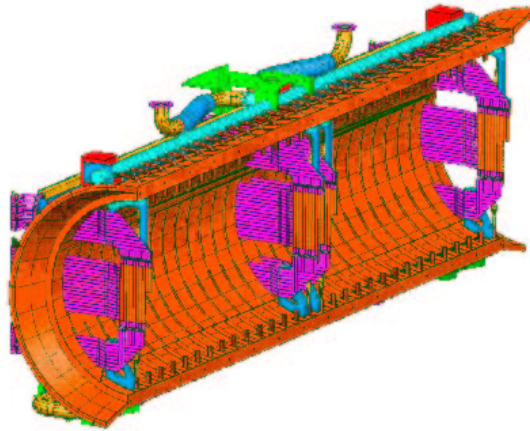
Figure 5.9: Side view of the vacuum vessel and support structure for the pixel detector.

Figure 5.10: Picture shows aluminum dummy substrates supported by brackets made out of carbon fiber on to a carbon support frame.

5.1.7   Future R&D Plan

In the 1999 beam test, we demonstrated the construction and operation of single-chip pixel detectors. The results also showed that the resolution achieved with such a detector is better

than 9 μm at all angles of incidence within the acceptance of the BTeV spectrometer. We plan to carry out another series of beam tests over the next two years starting this summer.

The primary goals of the beam test are to measure the efficiency, charge sharing, and resolution as a function of the irradiation previously accumulated on pixel detectors, under various conditions of incident angle of the track, threshold setting, and bias voltage of the sensors and with readout chips from various vendors.

We plan to build, install, and operate a pixel detector telescope based on 6 to 8 single-chip pixel detector planes. This will provide us with useful operational experience of a small scale pixel detector system. We also plan to test a 5-chip pixel module in the test beam.

Prototype mechanical and cooling support structures made out of fuzzy-carbon and Be have been ordered and their mechanical and thermal properties will be evaluated.

Our next step is to address system issues. From our test beam experience, as well as operational experience from other large experiments, systems issues such as power supply, grounding, cabling, and connectors are potentially the most problematic areas. To understand and address these system issues, we plan to assemble a 10% system. With such a system, we can also carry out a thorough investigation of a complete electrical, mechanical and cooling system.

This will also enable us to operate a small system in the real C0 environment in a prototype Roman pot structure. Issues such as rf pickup, shielding, and fast readout coupled to a prototype trigger processor can be studied in detail there. At the same time, it will allow us to understand a lot better the yield at the various steps of production, as well as how to assemble reliably the full scale pixel system.

Bibliography

[1] J.A. Appel et al., Performance of prototype BTeV silicon pixel detectors in a high energy pion beam, FERMILAB-Pub-01/229E, to be published in *Nucl. Instrum. Meth. A*.

[2] F. Lemeilleur et al., 3rd RD48 Status Report, CERN/LHC 2000-009 (31 December 1999).

[3] ATLAS Pixel Detector Technical Design Report, CERN/LHCC 98-13.

[4] M.R. Coluccia et al., Characterization of prototype BTeV silicon pixel sensors before and after irradiation, FERMILAB-Conf-01/344E.

[5] D.C. Christian et al., Development of a pixel readout chip for BTeV, *Nucl. Instru. Meth.* A435 (1999), 144.

[6] P. Jarron et al., 3rd RD49 Status Report Study of the Radiation Tolerance of ICs for LHC, CERN/LHCC 2000-03 (13 January 2000), D.C. Christian et al., FPIX2: A Radiation-hard Pixel Readout chip for BTeV, FERMILAB-Conf-00/316E.

[7] J. Hoff et al., PreFPIX2: Core Architecture and Results, FERMILAB-Conf-00/260E.

[8] G. Chiodini et al., Radiation tolerance studies of BTeV pixel readout chip prototypes, FERMILAB-Conf-01/214E.

[9] G. Chiodini et al., Single event effects in the pixel readout chip for BTeV, FERMILAB-Conf-01/369E.

[10] S. Cihangir et al., Characterization of indium and solder bump bonding for pixel detectors, *Nucl. Instru. Meth.* A476 (2002), 670.

[11] S. Kwan et al., A Study of Thermal Cycling and Radiation Effects on Indium and Solder Bump Bonds, FERMILAB-Conf-01/377E.

[12] S. Zimmermann et al., Development of high data readout rate pixel module and detector hybridization at Fermilab, *Nucl. Instru. Meth.* A465 (2001), 224.

[13] S. Zimmermann et al., Development of a High Density Pixel Multichip Module at Fermilab, FERMILAB-Conf-01/247E.

5.2 Silicon Forward Tracker R&D

The R&D program for the Silicon forward tracker is organized along four main directions:

- development/choice of the Silicon microstrip sensors;

- development of the front-end read-out electronics;

- development of the detector support mechanics and the embedded cooling system;

- development of the Data Acquisition System (DAQ) for use in bench tests, beam tests, and quality assurance.

We report here on progress achieved thus far in each of these R&D directions.

5.2.1 Silicon microstrip sensors

Two groups are working in this area, namely INFN-Milano and the University of Tennessee. The first goal of this R&D effort is to find out if one of the microstrip sensors currently available on the market, is suitable for BTeV applications. We are presently considering the sensors developed by Hamamatsu and ST Microelectronics (France) for the CMS experiment. They are very promising and simple since they are of the p/n type and feature a very a high breakdown voltage, typically around 800 V, which can ensure a full depletion even after radiation-induced type inversion. They should meet the requirements for BTeV.

We are characterizing samples in Milano (see Fig 5.11)and in Tennessee (see Fig 5.12) using two identical test stations developed by the IDE-AS company (Oslo, Norway) for this kind of application

The stations, which include a fast-preamplifier and a read-out section, have several features, which allow the user to change the preamplifier electrical parameters to permit a full characterization of the sensors. We have successfully installed the two stations and are now testing the sensors with a β-source and an infrared laser. The two sensors we are working on in Milano produced by ST, are 9×9 cm^2 wide and are assembled in a daisy-chain configuration (see Fig 5.13 and Fig 5.14), identical to that foreseen for BTeV. This allows us to study the performance of long strips. The sensors under investigation in Tennessee are single sided versions of Hamamatsu S6934. These devices have 640 strips with a 50 μm pitch on 3.2 cm square wafer. The read-out strips are AC coupled. In Tennessee, we are preparing to test the wider sensors produced by Hamamatsu for CMS.

The infrared laser source we assembled in Milano can be focused into a few micron wide spot by means of a lenses and can be moved by actuators along X and Y-directions (see Fig 5.15). This system will be crucial in speeding up all the quality checks on the sensors during the final production phase.
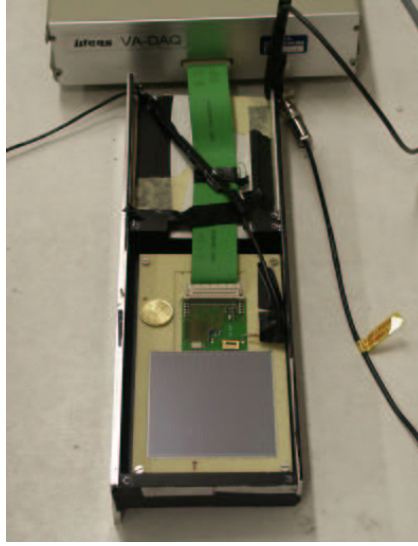
Figure 5.11: A prototype microstrip detector attached to the IDE-AS system box in Milano

5.2.2 Front-end read-out electronics

The aim of the project is to develop a new read-out chip which has to be very fast, low noise and data driven. The chip has to sustain rather high radiation doses and to read out long strips having a typical capacitances of the order of 20 pF. For this chip we plan to use a digital section based on an architecture similar to what we developed for the pixel read-out chip.

Two steps have been already accomplished in this effort: the choice of the technology and the definition of the basis circuitry for the analog channel. The chosen technology for integration is a deep sub-micron process, which can be made highly radiation resistant with some proper layout prescriptions. In particular we are considering the TSMC (Taiwan) process with 0.25 μm minimum feature size, which has been successfully used by other groups.

The basic scheme of the analog channel, together with some particularly significant test structures, has been completely simulated and is shown in Fig 5.16. The channel includes a charge-sensitive preamplifier, a second-order semi-Gaussian shaper and a comparator to provide 1-bit information, generating a logical 1 at the output if a signal exceeding the comparator threshold is detected. Fig 5.17 shows the waveforms (from Eldo simulations) at the output of the three circuit blocks as a response to an input current signals of short duration, corresponding to a 4 fC charge delivered by the detector. The corresponding files are now available and ready for the preparation of the layout. We have evaluated the costs for a preliminary submission and have already received offers for the CAD work for the layout.

We are now ready for the submission of the analog channel prototype and the related

Figure 5.12: A panoramic view of the sensor test station at the Tennessee University

test structures.

The Milano and Pavia groups are working on this project with P. F. Manfredi as general coordinator.

5.2.3 Detector support mechanics and cooling

This R&D project is logically divided in three parts: the development of the micro-strip inner support, which provides a local support for the microstrip planes and all their components; the development of the micro-strip outer support, which holds the inner support; and the development of the cooling system for the front-end read-out chips. The first part is carried on by the Milano group, the second one by the Frascati and Milano groups, and the third one by the Bergamo group.

The main goal of this effort is to design a very light structure in order to minimize the amount of material inside the tracking volume.

We have already developed a prototype design for the inner support in collaboration with PLYFORM, a Milano based company with long experience in this sector having built parts of the support structures for the CDF and ATLAS vertex detectors. The support structure (see Fig 5.18 and Fig 5.19)is realized with carbon fibers and allows for a very precise relative positioning of all the components belonging to a same station. PLYFORM will produce a mock-up structure for tests of functionality shortly. By the end of the year we will have the complete prototype support structure in carbon fiber for a whole station.

At this time we consider as a base-line solution for cooling a water/glycol mixture circulating in a duct embedded into the support structure, but we are also investigating other
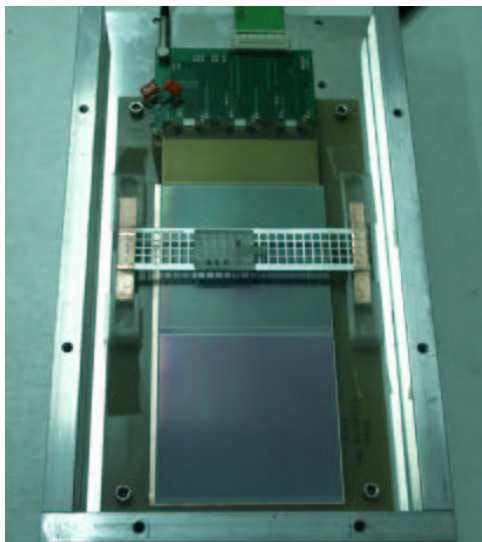
Figure 5.13: The two ST sensors assembled in a daisy-chain configuration. The sensor pitch is 183 μm and the total number of strips is 512. At the bottom of the figure the read-out chips and the fan-out circuit are visible.

interesting possibilities. The Bergamo group has started the simulation work for several different cooling systems. They are investigating the performance of each system as well as the deformations induced in the mechanical structure. It is our intention, once the simulation work is finished, to assemble prototype systems to validate the simulations and to test their cooling performance.

The R&D activity on the outer support has just started. Several ideas have already been discussed and one in particular seems very promising. Instead of using a separate support for strips, we are considering the possibility to integrate it directly into the nearby straw structure. The idea is to reinforce, by means of carbon fibers, the straw structure in the region covered by the strip inner support in such a way that it can be made rigid enough to hold an entire strip station. The straw tubes could also benefit from this additional rigidity, since their own support structure could, in principle, be simplified and made lighter in the central region. Even the strip signal and power cables could be integrated in the same structure by simply depositing on it the required amount of copper stripes. We are working on this and plan to prepare a complete design in the near future.

5.2.4 DAQ system

The R&D activity for the design of a DAQ system, which can be used for tests of the Silicon Strip Detectors both in bench tests in the lab and in beam tests, has already reached significant milestones. We are sure that this experience can be profitably used to design the future DAQ for BTeV.

The DAQ design is based on the PCI bus protocol, a widely used standard in the com-
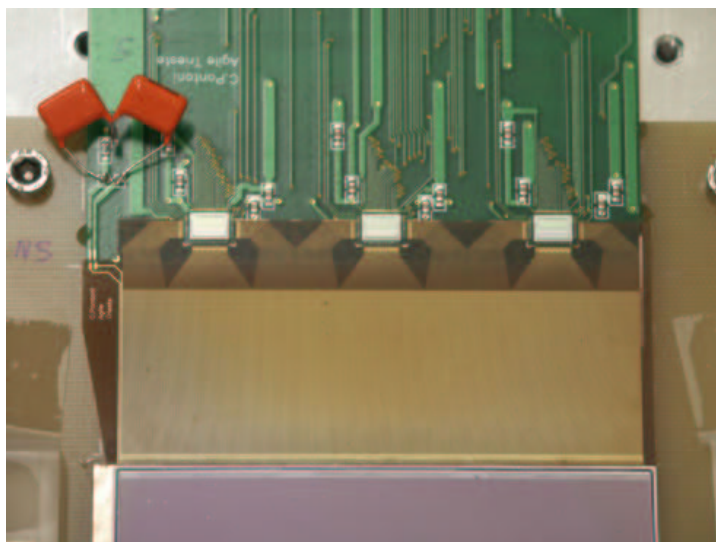
Figure 5.14: A magnification of the previous figure to show details of the read-out chips and the fan-out circuit.

puting industry, which offers several benefits, one being relatively low cost. The digital part of the Silicon Strip Detector front-end is designed to be practically the same as that of the Pixel Detector, thereby allowing for a common read-out scheme for these two detectors. In our design each detector is connected to a PCI board containing an FPGA (for logic control) and two 1 Mb memories; several PCI boards are lodged together on a PCI bus extender and finally connected to a host DAQ PC. Each time a strip (or a pixel) has data above threshold, the address along with pulse height and time-stamp information are sent to the PCI board to be stored on one of the two local memories. The FPGA's are programmed to handle the swapping between these two local memories and synchronization with the external read-out process (running on the host DAQ PC) in such a way to smoothly handle a sustained data rate, adequate to the beam test requirements. The central idea in this design, is keeping the event-builder algorithm as simple as possible, since an event, defined by all hits marked by equal time-stamp, is spread out over several PCI boards which can in principle receive data at different rates. In absence of a specifically defined strategy to synchronize the flushing of these memories, this sparse read-out scheme generates events spread-out over large chunks of memory, making the event builder extremely cumbersome. We have therefore designed an elegant mechanism to restrict the components of an event to be contained in a limited amount of memory, taking advantage of our ability to program the FPGA to generate interrupt signals. The principle of operation of this read-out scheme is the following:

- data are received from a detector by the corresponding PCI board in one of its two internal memories

- as soon as any memory in the system is full, all boards are synchronously commanded
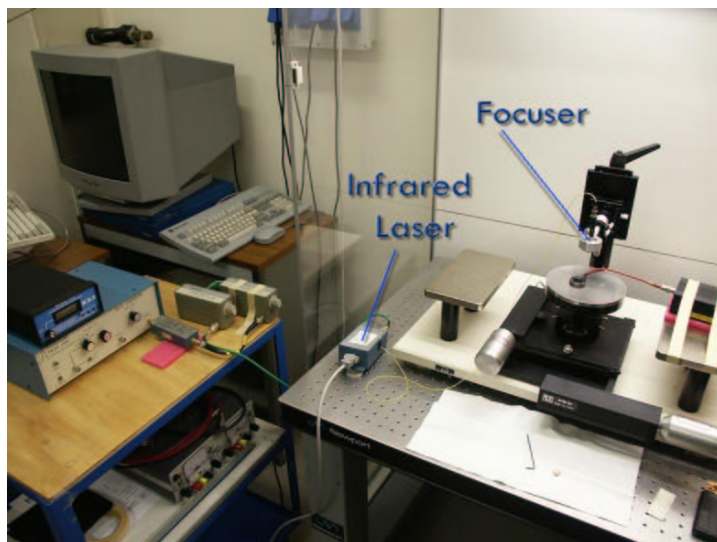
180

Figure 5.15: The infrared laser station with the X/Y moving chuck.

to swap their memories. The ones used so far are frozen and immediately read-out to the host computer, while the others are used to continue reading events from the detectors without any data loss.

- events are fed to the host computer on a statically allocated shared memory, acting as a compensating buffer to allow for unexpected data rate fluctuations.

- data are then continuosly flushed from this memory to disk by a consumer process, building events on the fly.

This is an event-driven scheme: data are collected as soon as they are produced by a detector, and no burden is placed on the DAQ software to generate signals to start a read-out chain. This is important, since it allows testing the full functionality of the detector in an environment similar to the one envisaged for the final data taking, where no trigger is used to read-out events.

Several components of this read-out have already been implemented, on a Linux platform:

- the PCI board and the microprogramming of the FPGA to send and generate control signals and interrupts.

- an abstract interface to the underlying driver (currently we are using a licensed driver, produced by Jungo). This will allow us to switch to other drivers should competitive ones emerge in the future.

- the interrupt-handler processes, in charge of starting the read-out of a PCI memory, synchronizing the read-out of all other boards and transfering data to an external shared memory

Analog channel
for the BTeV Forward Silicon Tracker
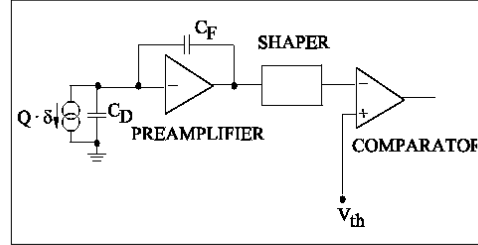
Figure 5.16: Basic scheme of the analog channel for BTeV microstrip front-end
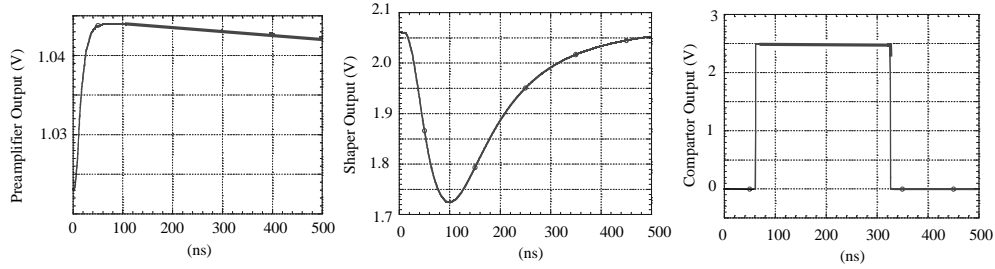
Figure 5.17: Waveforms at the output of the three circuit blocks of Fig 5.16 for 1 Minimum Ionizing Particle as simulated by ELDO.

- the read-out process, owner of the shared memory and responsible for synchronizing with the consumer process to flush events on a storage media

- the event-builder (a prototype)

- a package for message transmission among cooperating process (based on the native Linux IPC protocol)

We have already in place a code management system, based on CVS, that allows us to keep track of successive releases of the code, making it possibile to allow concurrent development at all participating institutions.

Future developments of this project encompass several key aspects:

- a sophisticated error detection system, taking into account both faults generated by the hardware (such as broken components or loss of synchronization) as well as those

182
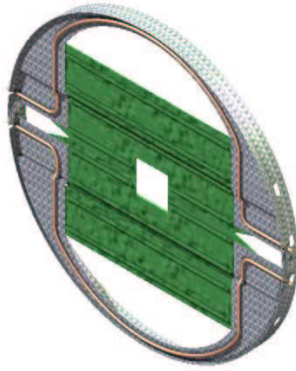
Figure 5.18: 3D sketch of the inner support for a single silicon plane. The back side of the plane is shown together with the cooling ducts. In grey is the carbon fiber structure, in green the ladders of silicon sensors and in red the cooling ducts.

generated by beam conditions (e.g., memories swamped by surge in beam intensity); and

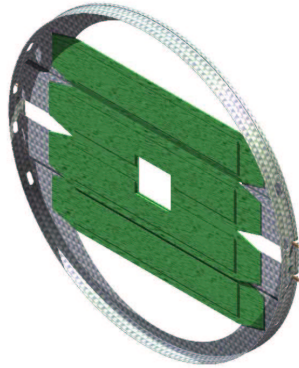- a set of GUIs to allow users to drive the DAQ system.

Figure 5.19: 3D sketch of the inner support for a single silicon plane. The front side of the plane is shown.

Figure 5.20: The support structure is such that the three views can be stacked to form a station. Reference pins guarantee a very precise relative alignment when assembling the components of the structure.

5.3   Straw Tube Tracker R&D

The Straw Tube Tracker is part of the forward tracking system. The major functions of the forward tracking system are to provide high precision momentum measurements for tracks found in the pixel system, to reconstruct tracks that do not pass through the vertex detector and to project tracks into the RICH and EM Calorimeter. The baseline system consists of 7 stations (1 arm). Most of the solid angle is instrumented using straw tubes. The high occupancy region near the beam is instrumented with silicon microstrip detectors. Each Straw Tube station consists of 3 views and each view has 3 close-packed layers. The following is a summary of our recent R& D work; details can be found on our website [1].

5.3.1   Single Straw Prototype

In order to become familiar with the operation of a straw tube detector, we obtained an old straw chamber from the Focus experiment and set up the hardware and software necessary to read out cosmic ray data. This included a flammable gas system so we could test various gas mixtures, high voltage supplies, low voltage supplies, CAMAC based TDCs, scintillation counters for triggering and a LabView based DAQ.

We have about 1000 straws that were designed at the University of Indiana for BTeV, based on the design of the Atlas straws. These are made of two layers of kapton. The inner conductive layer is carbon loaded kapton with a thin film of aluminum deposited on it. The outer layer is plain kapton.

We constructed several single straw prototypes using these straws. This required designing end plugs to attach the straws to an end plate. The anode wires are then attached to an insulated anode board, inside a gas volume.(see Fig 5.21)
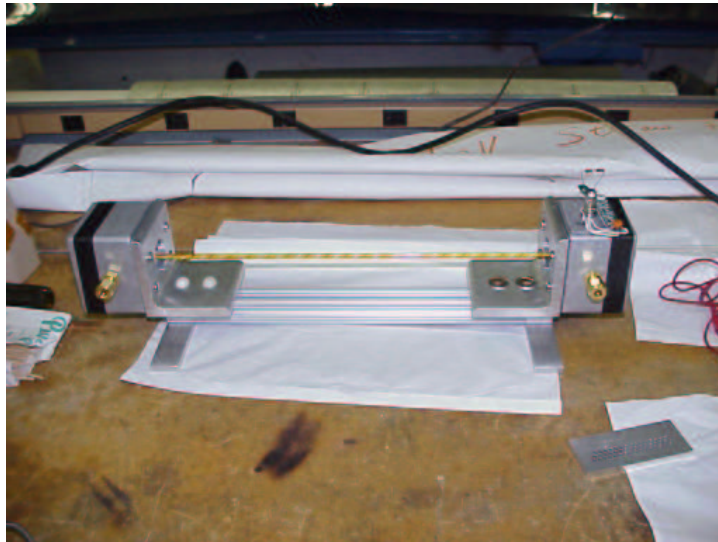

Figure 5.21: Single Straw Prototype

The anode wire is kept centered in the straw with helical structures called "twisters". For short straws one twister at each end is sufficient but straws longer than 80 cm need additional twisters. We obtained twisters from 3 different manufacturers. It is important that the twisters have smooth surfaces in order to not snag the wires. The twisters obtained from A.F. Leis in Columbus, Ohio were of good quality. Those from the other manufacturers needed extra smoothing. We used the electronics from the FOCUS chamber to read out these prototypes.

Gas gain measurements were done with an ^{55}Fe source and a 50:50 Ar/Ethane gas mixture. The University of Houston group has started doing ageing tests using a 100 mCi ^{90}Sr source. These studies will influence the final choice of gas and also test for problems that might occur with outgassing from materials such as the glue that we use to keep the twisters fixed in the straws.

5.3.2 Wire Stringing and Tension Measurement

The 25 μm diameter, gold-plated tungsten anode wires are inserted into the straws by blowing a lead wire through, tying the anode wire to the lead wire and pulling the lead wire back. A weight is hung from the wire to apply the correct tension. We have successfully strung wires through straws up to 4m long without any problems. The setup is shown in Fig 5.22.
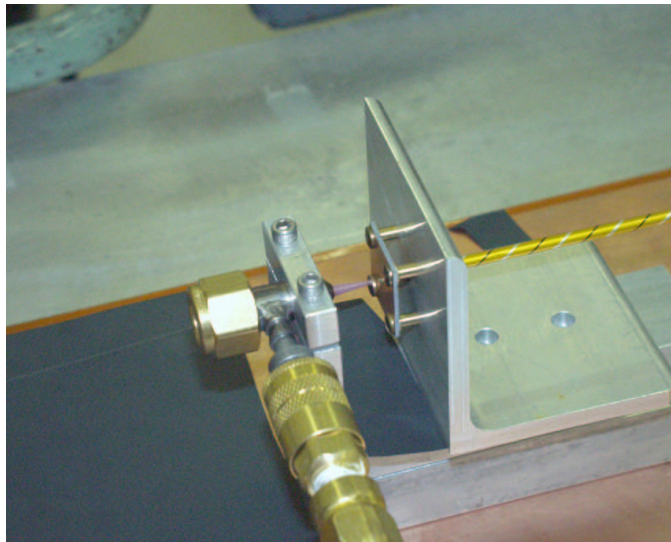
Figure 5.22: Nozzle for wire stringing

The tension on the anode wire needs to be approximately 50g. During production it will be necessary to have an efficient method to check the tension of each wire as it is strung. With the aid of an undergraduate student from UC Davis (Long Pham) we have set up an acoustic excitation method for measuring tension – a loudspeaker is used to induce a mechanical resonance in the wire. A potential of 50V is put on the wire so the capacitance variation induces a signal. The current setup uses a LabView data acquisition system that

generates a variable frequency to drive the loudspeaker and plots the response of the signal as a function of frequency. The resonance is easily observed. We are working on developing a faster system.

In order to reduce the occupancy, the straws are read out at both ends, the anode wires being separated in the middle by a fused glass capillary tube. The group at the University of Virginia is planning to build a wire fusing machine based on the design of the one used for ATLAS.

5.3.3   Straw Stretch/Tension Tests

In the summer of 2001 we had a high school teacher, Jan Dudzik, set up a system to test the response of the straws to changes in temperature and humidity. Three straws approximately 1m in length were hung vertically with a weight attached and placed in a box where we could control the temperature and humidity. The change in length of the straws was measured with inductive proximity sensors. The results are shown in Fig 5.23. The straw responded very slowly to changes in humidity, probably because the straw was sealed which will not be the case when running the experiment. We decided that it would be more realistic to fix the length of the straws and measure the change in tension as a function of environmental conditions.

This has been done using a load cell to measure the tension. The results are shown in Fig 5.24. A straw was set up in a frame and stretched until it had a tension of about 190g. The tension rapidly decreased to about 160g. The relative humidity was then decreased from 37% to 0.5% and the tension increased to 260g. When the humidity was increased again to 37% the tension dropped to 120g. We cycled the humidity several times between 37% and 0% and the tension varied from 120g to 260g as expected, showing that the initial reduction in humidity stretched the straw irreversibly but was stable after that. From these tests we have learned that it will be necessary to run the straws under well controlled environmental conditions. We plan to flow dry nitrogen in a volume surrounding the straws to keep the humidity close to 0%. It is necessary to apply a tension of about 200g to each straw in order to keep it straight. We have the straw now held under zero humidity and are looking at long term changes in tension.

5.3.4   Two-Module Prototype Construction

The final BTeV Straw system will be built in "half-views". Each half-view will have several modules where a module consists of 3 layers of 16 straws. We have constructed a 2-module prototype to be used in a beam test later this year. The construction of a module proceeds as follows: the straws are cut to the correct length and twisters are glued in; the 3 layers of straws are set up on a corrugated base to form a close-packed array; the end-plugs are inserted into the end-plates and silver epoxy is injected into the region around the plugs; the end-plates are attached to the straws; finally the outside of the endplates is potted with structural epoxy. (see Fig 5.25)
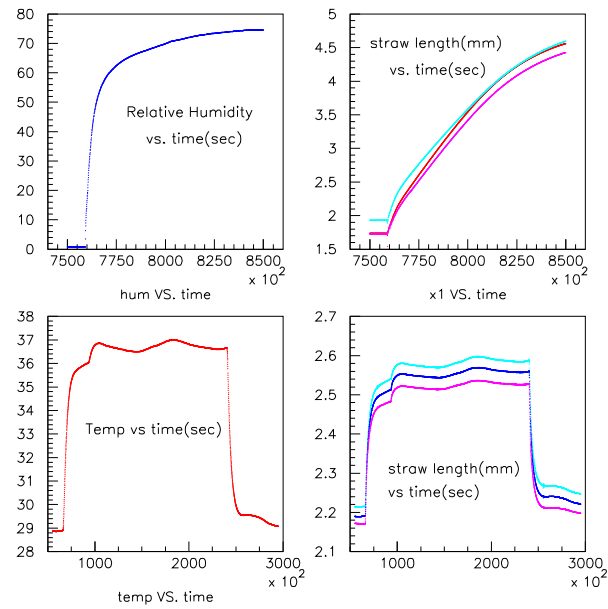
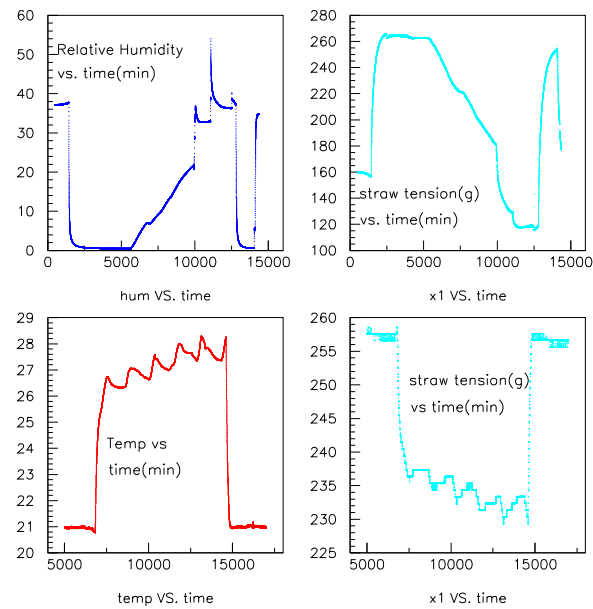Figure 5.23: Straw Length dependence on humidity and temperature

Figure 5.24: Straw Tension dependence on humidity and temperature

188
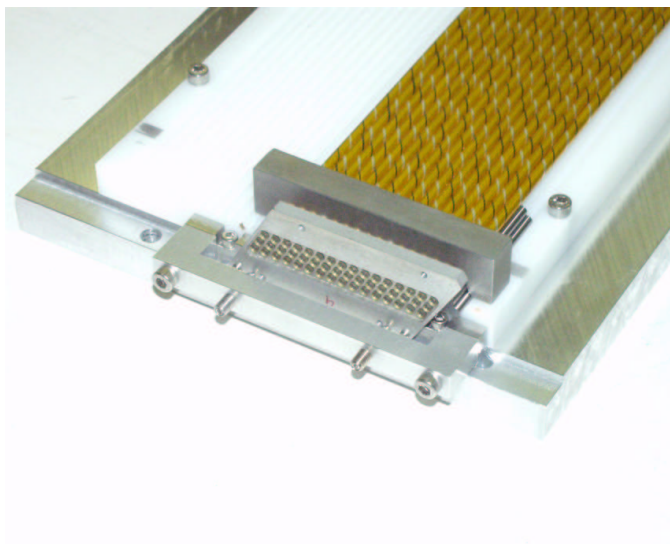
Figure 5.25: Straw module assembly

Anode boards were designed with connectors to COT cards(from the CDF Central Open-cell Tracker). Each COT card has three 8-channel ASDQ chips ([2]). The output of the COT cards is converted from LVDS to ECL via a translator board so we can use existing LeCroy TDCs. We have discovered several problems while constructing these modules: (1) The straws are not perfectly round which makes it difficult to have them close-packed without bowing outwards. (2) About 20% of the straws have leaks. This was unexpected as we had tested a few straws early on and had not found any leaks. The leaks are associated with places where there appears to be a lack of glue between the two layers of kapton. (3) Silver epoxy was used to attach the anode boards to the module end-plates and shorted out a couple of traces on the anode plate.

We believe the problems of out-of-roundness and lack of sufficient glue are solvable as we have done measurements of the straws to be used for the CKM experiment and found that they do not have these problems. We plan to order more straws with stricter quality control on the construction.

5.3.5   Other R&D

If an anode wire breaks it will draw a lot of current and probably trip the HV power supply. As each HV channel will supply many straws we are investigating the possibility of using a fuse for smaller sets of straws. The group at Southern Methodist University (SMU) has identified a commercially available fuse that is possibly suitable for this application. They have obtained some samples and are conducting tests. We have had discussions with Oak Ridge National Laboratory about the design of the front-end boards and they have some seed money to do preliminary design work.

We have made a detailed design of the flammable gas system to supply the BTeV straws

STATION 3 HALF-VIEW FRAME ASSEMBLY
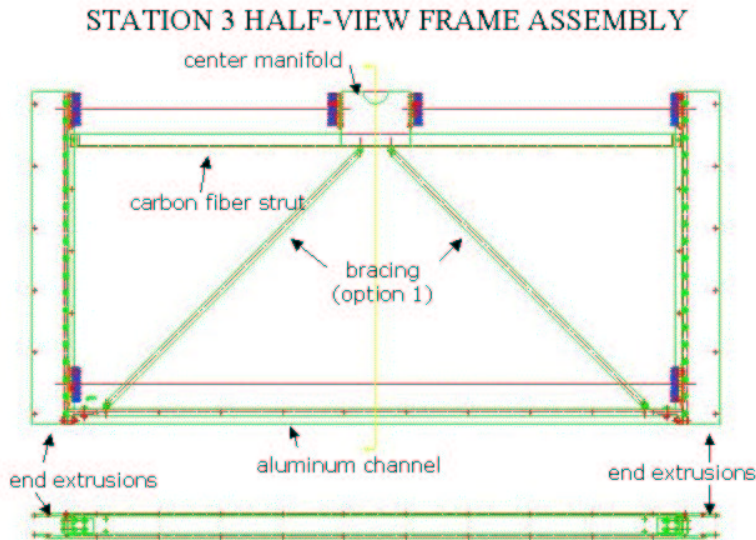
Figure 5.26: Half-View Frame

[3]. The group at SMU is designing a gas gain monitoring system.

We are planning to do radiation damage tests on all materials that will be used in the straw tracker.

We have a preliminary design of the half-view frame that will be used to support the straw modules, shown in Fig 5.26. A finite element analysis has been done to examine the flexing of the frame due to the tension on the straws. A mechanical model of the frame for a station 3 chamber is under construction. This will be put under the tension in order to test that the calculations are realistic.

The group at Frascati is developing a method of accurately tracking the alignment of the straws with respect to the silicon microstrips.

5.3.6 Simulations

We have continued simulations of occupancy and radiation levels with the updated BTeV spectrometer. Drift time and gas gain calculations have been done using Garfield. We are refining tracking code to reconstruct tracks in the forward tracking system in order to check the effect of any design modifications.

Bibliography

[1] "BTeV Straws Web page",http://www-btev.fnal.gov/atwork/detector/straw

[2] "The ASDQ ASIC for the Front End Electronics of the COT", W. Bokhari et al., http://penn01.fnal.gov/ cot/doc/ASDQ-new.ps

[3] "BTeV Straw Gas System", Terry Tope, http://www-btev.fnal.gov/cgi-bin/DocDB/ShowDocument?docid=259

5.4 Ring Imaging Cherenkov Detector R&D

The RICH detector consists of a gas radiator (C_4F_{10}) followed by a spherical mirror focusing Cherenkov light onto arrays of Hybrid Photo-Diodes (HPDs). In the initial design, we planned to have an aerogel radiator in front of the gas radiator to improve low momentum particle identification. Cherenkov photons from both radiators were detected on the same array of HPD sensors. Based on detailed simulation studies that showed the small number ($\sim$10) of aerogel photons would be obscured by the overlapping rings of photons from the gas radiator, we have decided to replace the aerogel radiator with a liquid radiator (C_5F_{12}) that has its own Cherenkov light detection system consisting of traditional photomultiplier tubes (PMTs).

5.4.1 HPD Development

In an HPD, a photo-electron emitted by the photo-cathode is accelerated onto a segmented silicon diode by a very high voltage (~ 20 kV). The BTeV HPD is based on the cross-focusing tube developed by DEP in the Netherlands (Delft Electronic Products B.V.) working with the late Tom Ypsilantis and Jacques Seguinot as part of the LHCb group. Initially these tubes were developed with 61 silicon pixels inside. Much finer segmentation is needed in the LHCb RICH detectors, thus they plan to have 2048 pixels in each HPD tube. This makes it impossible to use the original DEP design in which pixel signals are individually transferred outside of the tube by means of pins. Therefore, the LHC-b group is developing their own silicon chip in which the diode is integrated with the front-end readout and both reside inside the tube. The diode segmentation needed in BTeV is 163 pixels per tube which represents a small modification of the original DEP scheme. This approach decouples development of read-out electronics from the HPD manufacture.

We developed the 163-channel HPD together with the DEP. The redesigned diode-package is shown in Fig. 5.27. Two tubes of this type have been manufactured by DEP and successfully tested at Syracuse. The pulse height spectrum for one of the HPD channels, obtained with low intensity LED light and VA-RICH readout electronics (adopted from the CLEO-III RICH) is shown in Fig. 5.28. Peaks due to one, two, and three photo-electrons reaching the same pixel within the integration time are observed. We have ordered 13 more HPDs, to be delivered by early Fall 2002. They will be used in a beam test of a prototype of the RICH later this year.

5.4.2 HPD Front End Readout

The HPDs will be equipped with binary readout. Each channel will have a discriminator with its threshold individually adjusted with an internal DAC. A Cherenkov photon detected by the HPD produces on average 5000 electrons. To achieve a signal to noise ratio of about 7:1, we are aiming at front-end electronics with equivalent noise charge of 700 electrons. We are working with IDE AS from Norway to develop such electronics. The Syracuse group

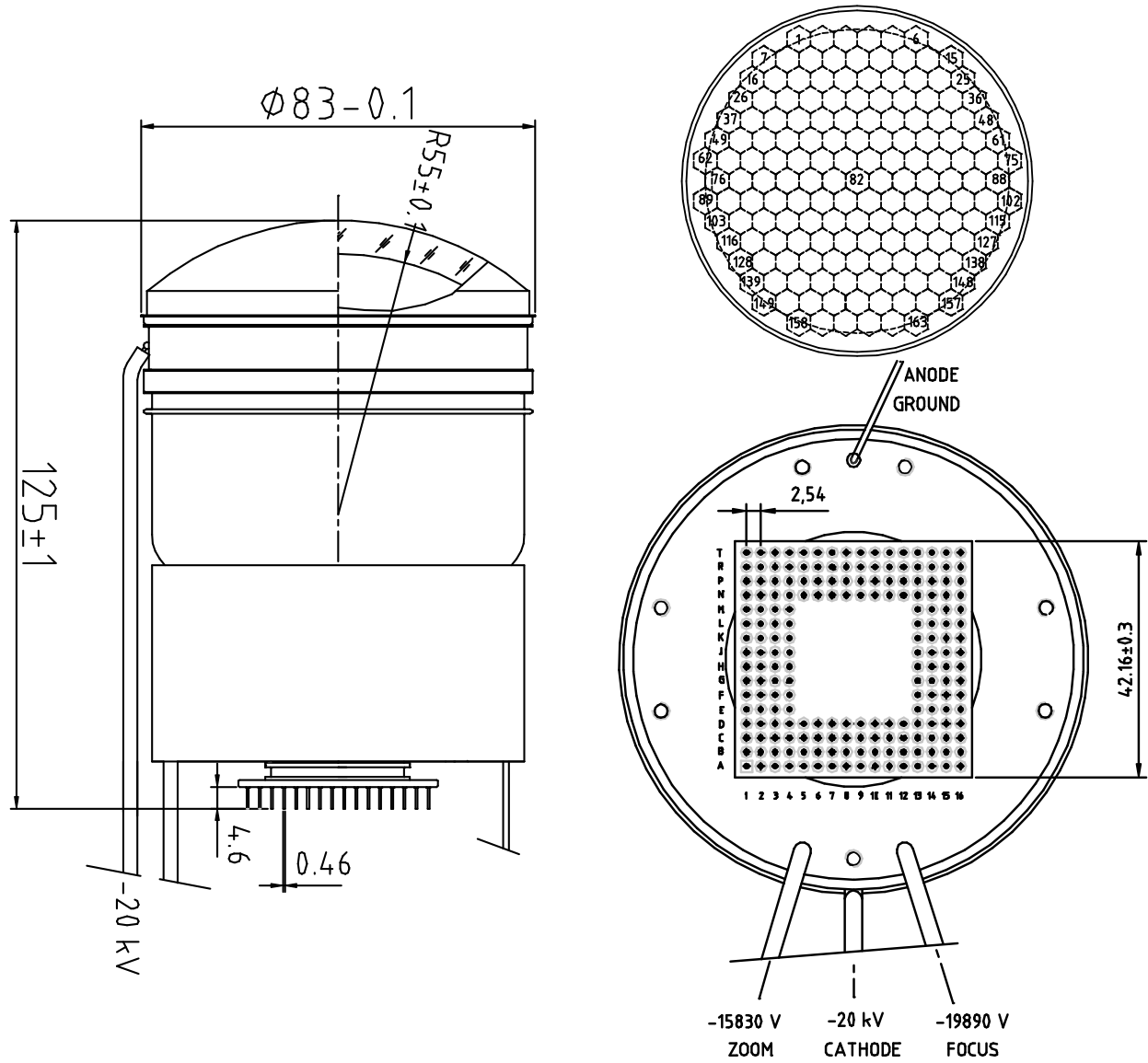Figure 5.27: BTeV HPD (DEP PP0380AT). The dimensions are given in mm. The 163 silicon pixels on the cathode are shown in the upper right drawing. The layout of pins penetrating the tube is illustrated in the lower right picture.
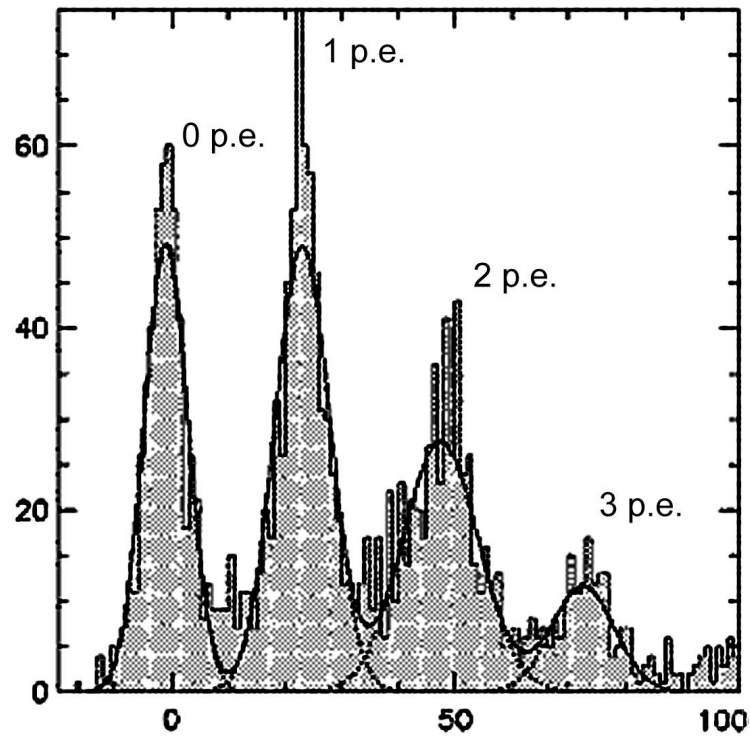
Figure 5.28: Pulse height spectrum obtained for BTeV HPD with VA-RICH readout. The pedestal peak is positioned at zero. The subsequent peaks corresponds to one, two and three detected photo-electrons.

previously worked with this company on development of a custom-made ASIC called VA-RICH and of associated front-end hybrid boards that were used in reading out the CLEO-III RICH detector. A different adaptation of the VA chip family has been produced for the BTeV HPD. We refer to this new ASIC as VA-BTEV. The VA-BTEV chip amplifies, shapes and discriminates the signal. It has a fast peaking time (72 ns) matched to Tevatron bunch crossing time (132 ns). The fall time (200 ns) extends the processed signal to the next bunch crossing, with negligible loss of Cherenkov light thanks to the small channel occupancy. Since each chip has 64 channels, a front-end board will house three of them. They will be connected to the HPD output pins via a small interface board. This analog part of the front-end hybrid will be well isolated from the digital part for the best signal to noise performance. Binary signals for each channels are fed in parallel into the digital part hosting an FPGA, which serializes the output, encodes channel address and attaches a time stamp.

The layout of the prototype VA-BTEV front-end boards is shown in Fig. 5.29. The first prototypes are now being tested on a bench using the DAQ system that later will be used in the RICH beam test. The next iteration of the design will have a flex circuit between the analog part (mounted directly to the HPD) and the digital part. This geometry is necessary to allow for close packing of HPDs. The next generation of the prototypes will be used in the beam test.

Figure 5.29: Layout of the first prototypes of BTeV RICH front-end hybrid board.

5.4.3 HPD High Voltage

The HPD requires application of three separate HV levels. The tube is sensitive to the stability of this applied power. We are using a relatively high noise power supply (Acopian) with 1 V of ripple, but RC filtering near the HPD renders this noise relatively harmless. We also have supplies with only 3 mv of rip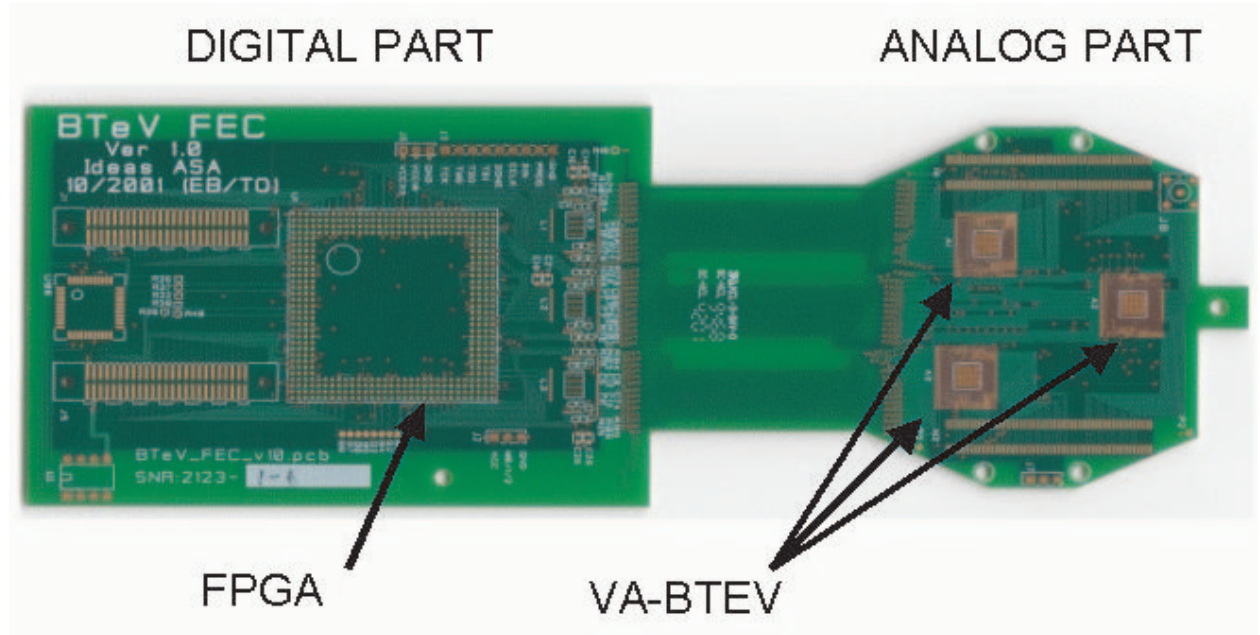ple (Matsuada) that could, in principle, work without filtering, though we are concerned about line pickup. We have determined that ripple greater than 10 mV at the HPD does degrade the signal-to-noise performance. In a full-scale distribution system, we may need to employ a low ripple supply as well as local filtering. Additional tests are in progress.

5.4.4 Mirrors

Spherical mirrors at the end of gas radiator focus Cherenkov photons onto the HPD arrays. The mirror curvature must have a radius of about 700 cm to match the RICH dimensions. Individual mirror tiles will have a hexagonal shape with a diameter of 60-80 cm. Mirror quality must be good enough to focus 95% of a parallel beam of light within a spot of 3 mm diameter, in order to preserve the Cherenkov angular resolution. One relatively cheap and well established technology to produce such mirrors is to use a glass substrate. The glass mirrors would add about 5% of radiation length in front of the EM calorimeter and require a much heavier support structure. We are investigating ways to reduce amount of material in the mirrors by using some composite materials like carbon fiber or foams to partially or completely replace the glass. Mirrors as thin as 1% of a radiation length can be built. We are determining if they have acceptable quality at an affordable price.

The Torino group has ordered two mirror prototypes from Turnov CZ (COMPAS R&D Consortium); one made out of glass, and the other with a thinner glass substrate reinforced by carbon fiber. Their quality will be soon investigated on a test bench at CERN. Since these mirrors have the right size and the right radius of curvature, we plan to use them in the gas RICH test beam set-up. CMA in Tucson AZ produced a mirror prototype for us using a carbon fiber substrate replicated on a glass master. The first CMA prototype has much shorter radius of curvature (190 cm), therefore it will be tested on a bench only. This technique was used to produce good quality mirrors for the HERMES RICH. The Torino group is collaborating with a local Italian company on developing a similar technique to reduce costs.

5.4.5 Liquid Radiator

The main limitation of the gaseous RICH is its inability to separate kaons from protons below the kaon radiation threshold (9 GeV/c) which dilutes same-side and away-side kaon tagging. The overall measure of flavor tagging, $\epsilon \mathcal{D}^2$, suffers by as much as 25% in the case of the B_s due to this effect. To fix this problem we previously proposed adding an aerogel radiator in front of the gas radiator, with aerogel Cherenkov photons detected in the same HPD array as used for gas photons. Such a dual radiator RICH has been in

operation for last few years in the HERMES experiment. Initial simulations of the aerogel radiator in BTeV RICH showed that it did separate kaons and protons below 9 GeV/c at some level. These initial studies neglected backgrounds from minimum bias events and from photon conversions in the BTeV detector components (beam pipe, tracking system, RICH radiators). More realistic simulations proved that no useful K/p separation could be achieved with aerogel detector, even after the Aluminum beam-pipe was replaced with Beryllium, and reconstruction algorithms were improved to suppress photo-conversion backgrounds. The aerogel fails because it produces large and faint Cherenkov rings that overlap many intense gas radiator rings as well as other aerogel rings. Pattern recognition of these faint images is just not possible in busy $p\bar{p}$ events. It should be noted, that track multiplicity in HERMES experiment is 1 or 2, compared to about 80 (on average) particles in the BTeV RICH. Thus, positive experience with aerogel radiator in HERMES does not carry over into the BTeV event environment.

We are now proposing to replace the aerogel radiator with a liquid radiator. The selected liquid radiator, C_5F_{12}, has much larger refraction index than aerogel ($n = 1.24$ vs. $n = 1.03$) producing more intense Cherenkov rings even from a thin layer of liquid. The C_5F_{12} radiator was successfully used in the other experiments (e.g. DELPHI, and SLD). Unlike an aerogel radiator, in which the Cherenkov photon yield is limited to a constant value by light scattering in the aerogel itself, the Cherenkov yield in liquid scales with radiator thickness. The large refractive index makes the Cherenkov rings even larger, which is actually beneficial, since optical paths of liquid photons now decouple from optical paths of gas photons. About two thirds of liquid photons hit the side-walls of the RICH where they can be directly detected without any focusing elements (so-called "proximity focus"). The fraction of gas photons striking the side-walls is essentially negligible as they are all incident at the mirror positioned at the end of the gas radiator. Thus, the two main limitations of aerogel radiator, faintness of the image and contamination from gaseous rings, are eliminated. At the same time, the refractive index of C_5F_{12} is low enough for kaon and proton Cherenkov rings to have sufficiently different radii up to 9 GeV/c to be distinguished with relatively large diameter PMTs instrumenting the side-walls. It should be also noted that although some liquid photons do reach the mirror (about one third), they do not contaminate gas images, since they are imaged outside the instrumented part of the HPD planes.

Simulations of the liquid radiator performance for a sample of low momentum ($<$ 9 GeV/c) kaons and protons are compared to the simulations of the aerogel radiator in Fig. 5.30. For aerogel (top picture) the distribution of protons in $\chi^2(K) - \chi^2(p)$ is essentially indistinguishable from the distribution obtained for kaons. (Here, each χ^2 is defined as $-2\log(Likelihood)$ as described in chapter 4.) For the same sample of events and tracks, the liquid radiator (bottom picture) produces good separation of these two particle species.

We expect the chromatic error for C_5F_{12} radiator with photons detected in the visible range (wavelengths above 300 nm) to be 3.7 mrad per photon. This error should be combined in quadrature with a photon position error reflecting the size of the PMT face. Two-inch PMTs would result in a photon position error of 3.5 mrad and an overall single photon resolution of 4.9 mrad. The number of PMTs and therefore the phototube cost can be cut
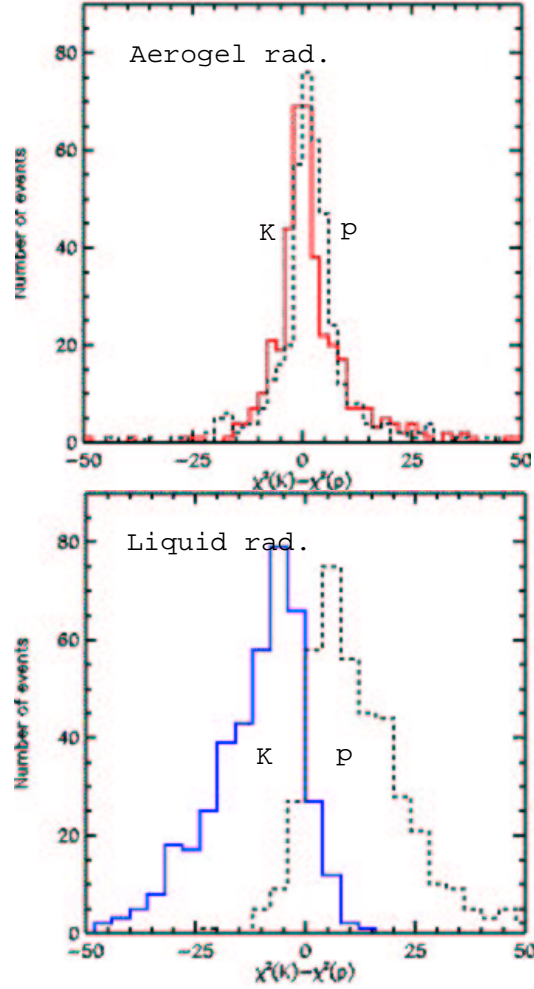
Figure 5.30: Performance of the RICH detector with aerogel (top) and liquid radiator (bottom) on a sample of low momentum (4-9 GeV/c) tracks. The underlying environment is a beam crossing which contained a $b\bar{b}$ event and on average two minimum bias events. Solid histograms show the kaon distribution, dashed histograms show the proton distributions.

in half by using 3" PMTs, with only 20% deterioration in Cherenkov angle resolution (5.3 mrad photon position error, 6.2 mrad overall). To cover the most illuminated parts of the RICH walls we will need roughly 5,000 3" PMTs per arm. With this coverage and with the liquid radiator 1 cm thick we expect to detect about 12.4 photons per track, resulting in a per track resolution of 1.88 mrad. Since at 9 GeV/c, kaon and proton Cherenkov angles differ by 5.34 mrad, separation would be 2.8 standard deviations for well-isolated Cherenkov images. Separation improves substantially for lower particle momenta.

Because of the large number of PMTs needed, minimizing cost per PMT is essential. The cheapest PMTs with single photo-electron capability are conventional head-on tubes, with 8-stage box dynode structure. With HV around 1 kV, their gain is of the order of a few times 10^5 and collection efficiency well above 90%. A standard bialkali photo-cathode with a borosilicate glass window provides a peak quantum efficiency around 30%. Dark count rate is orders of magnitude below the level that would impact RICH performance. At present, we are in contact with four different manufactureres making such photo-tubes in 3" size: Burle, Electron Tubes, Photonis and Hamamatsu. We are testing their PMTs in order to establish single photoelectron detection capability and efficiency loss in a magnetic field. We have already tested sample tubes from Hamamatsu and we are now testing Burle PMTs. We will soon test PMTs from Electron Tubes and Photonis. A single-photon response measured for R6233 PMT from Hamamatsu is shown in Fig. 5.31.
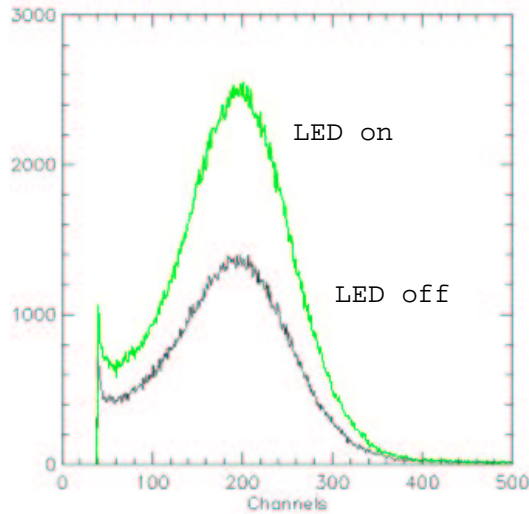
Figure 5.31: Pulse height spectrum obtained with R6233 PMT from Hamamatsu connected to MCA exposed to attenuated LED light (upper histogram). Dark counts (lower histogram) accumulated for the same readout live time. The single photo-electron peak is clearly visible with a good peak-to-valley ratio. Dark counts also show the single photo-electron peak because of thermionic emission of electrons from the photo-cathode.

It is possible that it will be cost effective to order PMTs with integrated voltage divider boards, that could also serve for their mechanical support. Further R&D will be needed to

identify a manufacture with the best price per performance ratio.

We have had initial discussions with IDE AS about front-end electronics which would have similar architecture as our HPD front-end boards but a simpler design. One front-end board would serve 64 PMTs, with signal cables soldered on both ends. Further work on PMT read-out scheme is needed.

We will also need to prototype the liquid radiator. The mechanical containment for the liquid will have a carbon fiber upstream window and a transparent downstream window made of quartz for radiation resistance.

Eventually a small scale prototype will be built that will contain a liquid radiator and small PMT array, to verify our estimates of Cherenkov photon yield and Cherenkov angle resolution. The beam test of such prototype is planned a year after we test the gas radiator with the HPDs.

5.4.6 Magnetic Shielding of Photodetectors

Both HPDs and PMTs will be exposed to some fringe magnetic field from the return flux of the dipole magnet. Magnetic field calculations predict that the largest magnetic field in the HPD area will be around 100 Gauss; PMTs will see up to 15 Gauss (for the unshielded situation).

We performed calculations of distortions of electron trajectories inside the HPD tube and concluded that we can tolerate up to 5 Gauss field along the axis of the tube, and 0.25 Gauss in transverse direction, after shielding. We plan to verify these calculations by operating the HPD in a magnetic field on our test bench. To shield the magnetic field, the HPDs will be mounted inside a 1mm thick cylindrical mu-metal tubes extending 5 cm beyond the photocathode. We measured a shielding effect of these tubes on a bench and concluded that we can tolerate magnetic fields of up to 30 Gauss in the HPD area. The whole HPD array will be placed in a shielding box (mu-metal and iron sandwich) to reduce the 100 Gauss field down by a factor of 4.

PMTs will also be placed inside mu-metal tubes. These tubes can extend only up to 2 cm beyond the photocathode, otherwise significant shadowing effects occur. We operated shielded 3" PMT from Hamamatsu in the magnetic field and found good resistance to even strong transverse fields. The longitudinal field smoothly deteriorated single photoelectron detection efficiency. For the small fraction of PMTs exposed to the highest magnetic fields we may lose up to 15% of light yield, if all the field is longitudinal.

5.4.7 Radiation Damage Studies

The photon detectors and their readout electronics are situated beyond the aperture of the detector, and therefore are shielded from the interaction point by the dipole magnet elements. Our simulations indicate that the flux of slower particles bent by the magnet onto the PMT array will produce a delivered dose of up to 1 krad/year in the hottest spot. Radiation levels in the HPD area will be lower by a factor of 20. Measurements done by the other groups

show that PMTs with borosilicate glass windows would start deteriorating at an absorbed dose of 100 krad. We plan to conduct our own radiation damage studies for PMT windows and materials that we are considering for gas vessel window (e.g. acrylic).

5.4.8 Mechanical Design

The first iteration of the mechanical design has been completed for all RICH components. Fig. 5.32 illustrates a support scheme for HPDs. A mechanical mock-up of this structure was fabricated. It is being used to refine the design. The RICH beam test will serve as a test of the HPD array with all its elements.
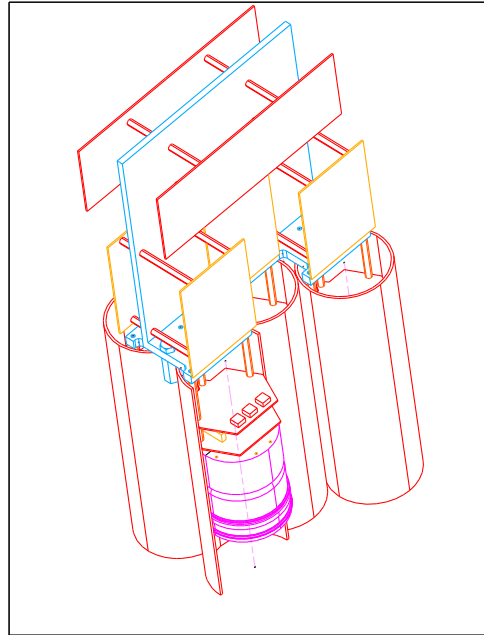
Figure 5.32: Mechanical support of HPDs. They are placed inside of mu-metal magnetic shields. One mechanical unit holds six HPDs (a "hexad"). The "T-spine" supports both the HPDs and the readout electronics.

Mirrors will be supported on three point system mounts that allow for fine adjustments. The prototype support structure was made and it will be used to support a mirror tile in the test beam.

5.4.9 Beam Test

A beam test of the gas radiator, together with a mirror tile and small HPD array is planed for the end of 2002. The test beam has threefold goal: to focus our R&D on HPDs and their readout, to prove that HPDs can be operated in closely packed array under realistic beam conditions and finally to verify our calculations for the expected light yield and Cherenkov angle resolution.

Progress towards the test beam of HPDs has been already described in the previous sections. Machining of the gas tank for the test beam will start soon at Syracuse.

A separated test beam of liquid radiator with an array of PMTs will be conducted a year later. Since this is not a new technology there is less urgency to perform this test.

5.5 Electromagnetic Calorimeter R&D

5.5.1 Introduction

We discuss here R&D on the three main aspects of the EM calorimeter. The key elements are the PbWO$_4$ crystals, the mechanical suppport and the readout electronics. In the final design the crystals will be wrapped with a white reflective paper, be glued to six stage photomulitplier tubes and read out with a modified version of the QIE chip. There will also be a light fiber attached to the crystal so we can input light from an LED.

Thus far we have had two test beam runs at the Institute of High Energy Physics, Protvino, Russia where the crystals have been exposed to both electrons and hadrons. In this case the crystals were wrapped with teflon and coupled to 10 stage Hamamatsu R5800 tubes, read out with a convential ADC.

We will also discuss the mechanical design for the crystal holder and the electronics.

5.5.2 PbWO$_4$ Crystals

The absolute light output of PbWO$_4$ crystals, often referred to as PWO, directly influences the energy and position resolutions. The uniformity of the light output also effects the resolution, especially at high energies. Since the crystals will be exposed to large particle fluxes, they have to be radiation resistant and any light output changes must be monitored. Thus, we need to understand the quality of currently produced crystals, in terms of their total light output, light output uniformity, and radiation hardness.

A test beam facility was constructed at IHEP, Protvino, Russia. It consists of an energy tagged and tunable electron beam and both moderate and ultra-high intensity hadron beams. We studied crystals produced in Shanghai, China, Bogoroditsk, Russia and Beijing, China.

Last year (2001) we have performed beam test studies of the energy and position resolution, effect of longitudinal uniformity on the energy resolution, and radiation damage of the PWO crystals. The crystals were arranged in a 5x5 matrix. The electron beam was directed in the center of the matrix. The beam momentum and position were measured using four sets of drift chambers and an analyzing magnet. To disentangle various contributions to the energy and position resolution, several electron beam energies - 1, 2, 5, 10, 27, and 45 GeV - were used.

The energy resolution is described well using the function $\frac{\sigma_E}{E} = \sqrt{a^2 + \frac{b^2}{E} + \frac{c^2}{E^2}}$ (E in GeV), where a represents a constant term arising from calibration errors, leakage - mostly from the back of the crystals, and non-uniformity in the light collection efficiency along the length of the crystals. The stochastic term, $b = (1.8 \pm 0.1)\%$, arises from photon statistics and leakage of shower, mainly in the transverse directions outside the 5x5 crystal array. The last term $c = (2.4 \pm 0.2)\%$, usually arises from noise of the photon detection electronics, which in our case is negligible. In our studies, the momentum measurement error due to multiple scattering of electrons in the beam line contributes 2.2% to this term and accounts for what we observe. The beam test results for the energy resolution are shown in Figure 5.33.
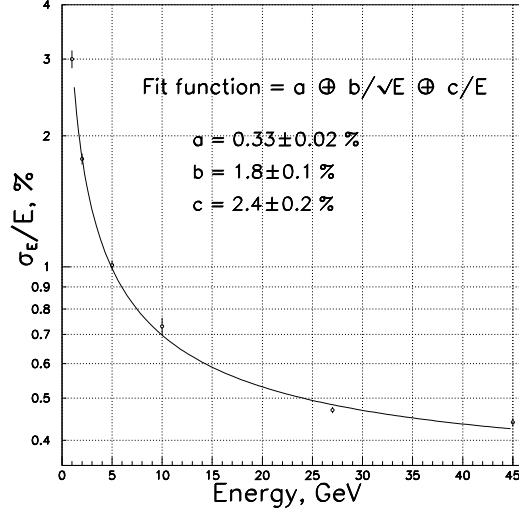
Figure 5.33: Measured energy resolution of the 5x5 crystal matrix.

The constant term is measured to be $a = (0.33 \pm 0.02)\%$. Our Monte Carlo studies show that the shower fluctuations and non-uniformity in light output contribute 0.23% and 0.27%, respectively. The measured longitudinal non-uniformity was used as an input in this Monte Carlo study. The total contribution to the constant term from taking these two terms in quadrature (denoted later as $\oplus$) is estimated to be 0.35%.

The same Monte Carlo studies show that shower fluctuation results in 0.72% contribution to b. To estimate the other major contribution in the b term we need to know the photo-electron yield. The vendors of the crystals BTCP, Russia and SCI, China measured this number to be about 10 pe/MeV using Cs^{137} and Co^{60} gamma sources and 2" PMT's with bialkalai photo cathode, covering the entire crystal end. Since the PMT's used in the beam test have sensitive areas of (22 ± 1) mm diameter attached to the crystal ends measuring 27 mm square, the covered area is only $(52 \pm 5)\%$. This implies that photo-electron yield in our beam test studies is 5 pe/MeV, and its contribution in the b term is $(1.45 \pm 0.07)\%$. Combining these two contributions as well as an additional contribution from non-uniformity to the b term, we expect b to be $(1.68 \pm 0.07)\%$, which is consistent with the measured value of $(1.8 \pm 0.1)\%$.

One of the major obstacles in our reaching these final resolution results turned out to be Photomutiplier (PMT) gain variations, which result from intensity variations of the electron beam. To monitor short term gain variations light pulses from a LED light source was injected into the crystals through optical fibers. We then read out the LED signal variation as a function of time. The time constant of the variation in PMT output was found to be typically about 10 minutes as shown in Figure 5.34 on the right, where the average pulse heights from LED pulser signals over 90 seconds are shown as a function of time. The left plot in Figure 5.34 shows correlation between the average LED signal and electron beam
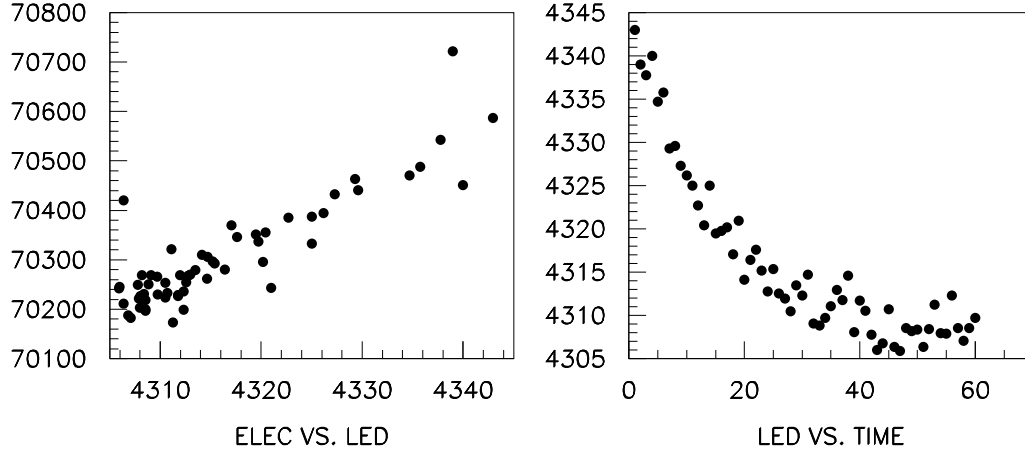
Figure 5.34: Correlation between the LED signal and 5x5 sum for electrons (left). Time dependence of the LED signal (right). Each point is an average over 90 seconds. Note the highly suppressed zero on the scales. (Data are at 27 GeV.)

pulse height. The correlation is good and the slope is close to 1. When the LED signal is used to correct the beam pulse heights, we were able to obtain the expected resolution.

The position resolution of the 5x5 matrix was also obtained using the test beam data. The resolution, averaged over electrons spread across the entire central crystal was calculated for each beam energy. From a two-term fit to the position resolution data we obtain $\sigma_x = (0.28 \pm 0.008) \oplus (3.32 \pm 0.02)/\sqrt{E}$ mm (E in units of GeV). It agrees well with the resolution expected from Monte Carlo simulation, which is $\sigma_x = 0.2 \oplus 3.5/\sqrt{E}$ mm.

The crystal longitudinal light output uniformity was measured using both radioactive sources at Minnesota, Syracuse and Protvino, and using a transverse muon beam at Protvino. The data were binned into 1 cm bins along the crystal length. For each bin the pulse-height distribution was fitted to a modified Landau distribution to obtain the peak position. The peak positions were fitted as a function of the coordinate along the crystal. For a group of the 25 crystals we obtain an average slope of 0.55%/cm with an rms variation of 0.15% in the region of the shower maximum $3 - 10$ radiation lengths from the front of the crystal. We do not observe any significant differences between the 5 Bogoroditsk and 20 Shanghai crystals. These measurements were consistent with the source measurements, but much more precise due to the high light yields.

To study the radiation hardness of the crystals, we irradiated them with intensive pion and electron beams using dose rates of up to 60 and 30 rad/hour, respectively. A few crystals were exposed to much higher radiation of 100 krad/hour in a dedicated facility for up to 2 Mrad of accumulated radiation (only crystals were exposed in this case, not the PMTs). Most crystals which received a dose rate of 30 to 60 rad/hour lost about 20% of their light

205
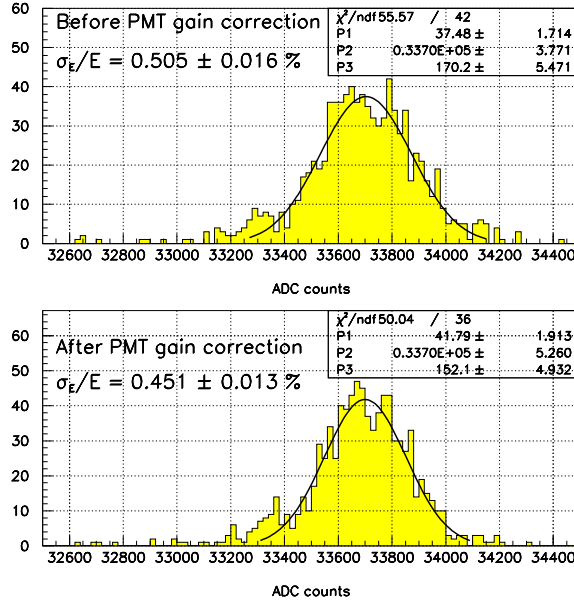
Figure 5.35: Energy resolution before and after the PMT gain correction using the LED pulser information. Data are collected using a 27-GeV electron beam.

outputs. The remaining crystals received up to 10 rad/hour and lost between a few per cent and 20%. With the electron beam, the light loss was about 15 to 20%. The small difference between the damage due to electron and pion radiation appears to be mostly accounted for by their difference in the radiation profile along the length of the crystal. With the electron beam, the radiation level reaches the highest level 5-7 cm into the crystal and falls sharply by two orders of magnitude at the PMT end, whereas with the pion beam, the radiation level stays more or less constant (within a factor of 2) after the maximum. A small effect due to the difference between the physical processes by which electrons and pions interact with matter cannot be ruled out.

At the extremely high radiation rates, which is 100 times larger than the highest radiation dose rate that any crystals in the BTeV environment will suffer, the two crystals, one from Bogoroditsk and the other from Shanghai, lost 2/3 of their light. These crystals received close to the maximum integrated dose for the worst case in BTeV in a few days, and there was no time for the natural recovery process in the crystals to work. (Typically, the crystals recover from radiation faster than the radiation rate in BTeV.) It is really reassuring that these crystals survived even this extreme environment.

Various tests of the PMT's proved that the light loss measured above was not due to radiation damage of the PMT's we used, which had regular borosilicate glass windows. The total dose they received was less than a few krad. These tests include subjecting the same PMT's to over 10 krad of radiation using a Cs^{133} source at Minsk, and a similar test done

at Minnesota using only window glasses obtained from the PMT manufacturer. However, during the fall 2001 beam test run, we found that the gain of PMT's easily changes by a few per cent and sometimes up to 5% depending on the history of signal intensities. These studies were initiated when we observed a small pulse-height change in the LED signal when the accelerator went down for a few hours. On a test bench, we analysed pulse heights when different DC light was superposed to pulsed light. We observed that the pulse height changes a few per cent even when the DC light produced less than 1 μA of anode current, and when the average anode current is increased to 10 μA, the change did not increase very much but it became more permanent. The change had a time constant of order 10 minutes.

From these observation, we had to conclude that non-trivial part of the light loss, which we attributed to radiation damage of crytals above, might be due to PMT gain changes caused by signal rate changes since the radiation dose level was controled by the signal particle intensity. Therefore, the numbers quoted above must be understood as upper limits.

We are working on the data analysis, where we are trying to separate the two effects: the PMT gain change and crystal radiation damage, using their differences in the time constants of the changes. Since the changes appear to depend on the history and not easily characterizable, if we want to know the radiation damage effect at a per cent level, we may have to change our strategy. We plan to use red LED light pulser (in addition to the current blue one) to monitor the PMT gain change alone in the future beam tests. Transmission of red light in the crystals is not effected by radiation damage.

We plan to continue beam tests with more crystals purchased from Shangai, Bogoroditsk, Beijing and possibly another facility at Apertiti, Russia. We need to evaluate the characteristics of PWO crystals, which will allow us to decide on crystal specifications which balance the physics performance and the cost of the calorimeter.

5.5.3   Mechanical Support Structure

The crystal support structure was assumed to be similar to the CMS endcap calorimeter for the 2000 proposal cost estimate, but we considered the $2.2M cost as rather expensive. In the last year, we have explored a more conventional design based on a grid structure using interlocking sets of vertical and horizontal aluminum strips instead of carbon-fiber cell-structure-based "CMS" design in an effort to bring down this cost, while maintaining the excellent calorimeter resolution.

The new design is depicted in Fig. 5.36, where, columns of crystals will be supported from 0.3 mm thick aluminum strips (or similar thickness carbon fiber) shown as closely spaced vertical lines in the Figure, that are strung vertically from top to bottom on a large frame structure. There will be a vertical strip between each column of crystals. Crystals will rest on 0.3 mm thick horizontal strips (closely spaced horizontal lines drawn only in the upper right quadrant) which run though slots machined in the vertical strips. There will be two horizontal strips (front and back) for each row of crystals. The horizontal strips will be anchored to the sides of the frame structure. The load of each crystal (1.4 kg) is transferred from the two horizontal strips to the adjacent vertical strips. The gap between the edge

of the crystal and vertical strip is small enough that the horizontal strips do not deflect significantly. The transfer of crystal load to the vertical strips is highly distributed as each pair of horizontal strips transfers the load of one crystal. The vertical strips transfer the load of a column of crystals to a mounting block over a large shear area. The mounting blocks attach to the frame structure with bolts.
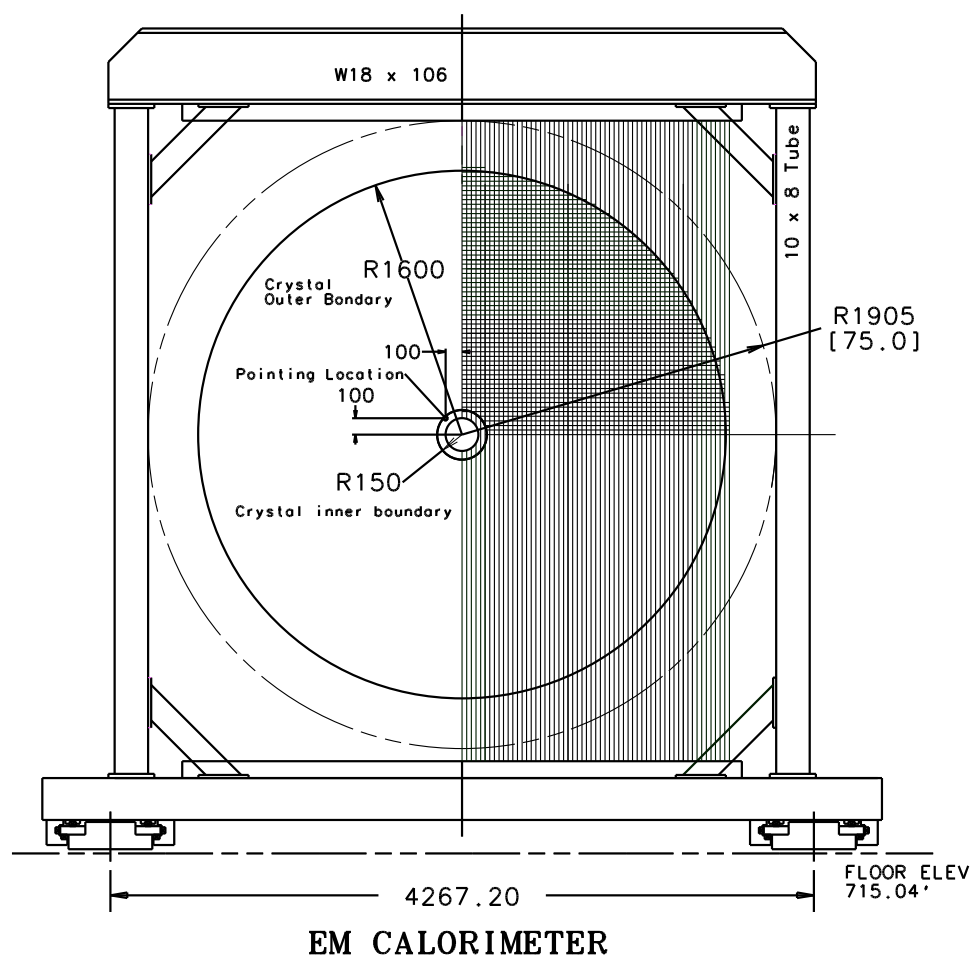
Figure 5.36: Front view of the EM calorimeter support structure. Dimensions are in mm except as indicated.

The frame is a simple square shaped structure. The top is a stiff beam that transfers the load of 100+ vertical strips to the two side columns. The base of the frame structure is attached to bearings and rails that allow the entire structure to move smoothly along the beam direction. The load paths of the structure are statically determinate and allow for design with relatively simple analysis. The stress in the most highly loaded vertical strips will be about 40% of the yield strength of sheet aluminum at the 2g loading condition. The vertical strips are oriented at the proper angle by pins located in the frame structure. Machining the slots in the vertical strips at the proper angle orients the horizontal strips. The

208

spacing of the vertical strips will be maintained along the entire length by small interlocking tabs and slots in the vertical and horizontal strips.

The cost effectiveness of the structural design depends on the ability to economically machine the thousands of slots in the vertical and horizontal strips. Laser cutting, which is a common commercial process, will be used to machine the slots. To evaluate the design concept and to obtain a preliminary cost estimates of cost-driving elements a prototype with 4 vertical and 12 horizontal columns is being constructed. The vertical strips for the prototype are 1/2 the length of the final design. Pictures can be viewed at http://home.fnal.gov/~howell/ecal_prototype_photos/ECAL_prototype_details.html.

5.5.4   Electronics

The PMT bases are being developed. A schematic diagram has been created and layout work is beginning. We plan to use a version of QIE for the front-end electronics, and have talked to the designer, as well as a few electronics engineers who have designed supporting electronics for previous versions of QIE. This chip was used in the KTeV calorimeter and we have confirmed that QIE is a good match to our needs.

When PPD engineers become available we will start these activities:

- A BTeV version of the QIE chip will be developed along with test boards that will serve in the process of evaluating the performance of the chip.

- A multi-channel ADC circuit board that will include the QIE chips will be developed.

- A PMT Cable Transition Card will be used to fan-in the signals from the PMT bases to the ADC cards.

- A Controller/DCB card will be used to interface between the ADC cards in a crate and the DAQ system.

- A commercial computer processor card will be selected to interface between the control system and the crate. A custom card will be developed to convert between the form factor of the commercial processor card and the form factor of the crate.

- A custom J3 backplane will be developed to facilitate I/O operations between the Controller/DCB card and the ADC cards.

5.6 BTeV Muon System R&D

5.6.1 Introduction

The BTeV muon group consists of three institutions, Vanderbilt University (lead institution) (VU), University of Illinois at Urbana-Champaign (UIUC) and University of Puerto Rico at Mayaguez (UPR). Research and development work on the muon system started in earnest when the group decided on the detector design and technology in 1998/99. Since then, the group has made significant progress on determining how the detector will be constructed and supported as well as a better understanding of the electronics layout.

5.6.2 Summary of the BTeV muon system

5.6.2.1 Baseline geometry

As shown in Fig. 5.37, two toroids, each 1 m long with 1.5 T fields provide the bending power for determining the muon momentum. The muon detectors will be set up in three stations, one between the toroids and two behind the toroids. The momentum can be measured using the two, well shielded, downstream stations and the nominal beam constraint. The station between the two toroids provides a powerful confirming hit to eliminate fake tracks.

5.6.2.2 Baseline detector

The basic building block in the construction of a detector station is a "plank" of thin walled (0.01") 3/8" diameter stainless steel proportional tubes as shown in Fig. 5.37. Thirty-two tubes, arranged in a double layer with an offset of half a tube are soldered at each end to a brass manifold and supported in the middle by a brass rib piece. This provides a sturdy, self-supporting building block which also acts as a Faraday cage to reduce external RF noise. Proportional tubes were selected because they are robust and have the necessary rate capability.
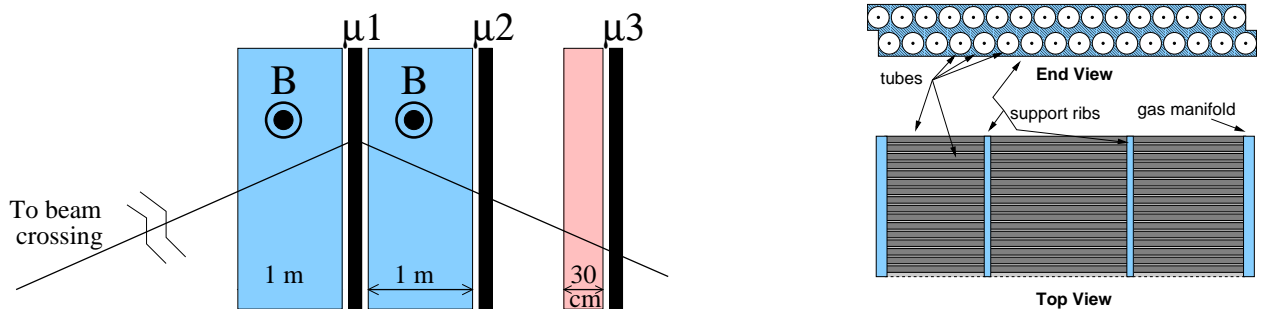

Figure 5.37: (left) Muon system geometry. (right) Views of one plank of proportional tubes.

The 0.5 cm wire spacing of this design has an effective spatial resolution of 5 mm/$\sqrt{12}$ = 1.4 mm with no dead regions between tubes. This meets our requirements for momentum resolution, drift time and occupancy.

To minimize occupancy at small radii and improve pattern recognition, each detector station consists of eight overlapping pie shaped "octants," shown in Fig. 5.38. There are four views (r, u, v, and r) in each octant as shown in Fig. 5.38. The r (radial) view is repeated to provide redundancy for the most important view and help reject fake tracks in the trigger. The u and v views are rotated $\pm 22.5^{\text{o}}$ to measure ϕ and resolve hit ambiguities, reducing the misidentification rate. The views stack on top of each other and are built from 12 planks/view. Pairs of octants, combined into quads, will be the structure moved into the spectrometer.
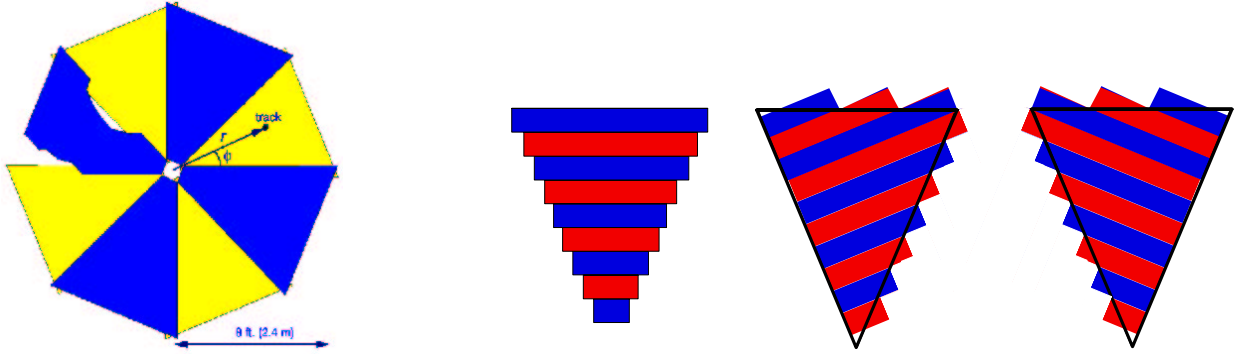
Figure 5.38: (left) Beams-eye view of one muon station (eight overlapping octants arranged in two layers). (right) Arrangement of planks to form each of the four views in an octant (r view is repeated). There will be 12 planks per octant (more than shown).

5.6.2.3 Front-end electronics

The front-end electronics will be similar to that used for the CDF central outer tracker (COT): one circuit board to deliver high voltage and a another circuit board with electronics to amplify and digitize the tube signal. Both boards will be located directly at the end of a group of 16–32 proportional tubes.

We plan to use the ASDQ integrated circuit developed at the University of Pennsylvania to amplify and digitize the signals coming from the proportional tubes. This chip is used in the Run-II CDF COT for a similar purpose. The ASDQ, amplifies the first ∼8–10 ns of the the signal and outputs an LVDS signal. This chip, when mounted on a circuit board, has a low effective threshold of about ∼2 fC (confirmed by tests at VU). The chip also features a double pulse resolution of ∼20 ns. The ASDQ digital signals will be sparsified, serialized, and read out using a standard Fermilab readout protocol. Fiber optic cables will transfer the data from a combination of 12 planks to a buffer memory.

5.6.3 Past research and development work

5.6.3.1 Detector design

The initial job of the muon group was to determine the detector design and technology to be used. The goals of the muon system were twofold:

1. Operate a dimuon trigger, independent of all other detectors, to provide calibration for the more ambitious vertex trigger and enhance the physics reach of dimuon events

2. Provide muon identification

Initial calculations and Monte Carlo studies were performed by the University of Illinois to obtain a rough idea of the detector requirements which would satisfy the muon system goals. These studies were used to set the initial toroid requirements, detector resolution, and station separations. The choice of a proportional tube system was influenced by many considerations including cost, neutron background, and the University of Illinois experience in building muon proportional tube systems.

5.6.3.2 Plank design/construction

The first round of plank prototypes (10 planks of 32 tubes each) were constructed in the first half of 1999. These planks were constructed in the following way:[1]

1. Tubes were cut to length in the machine shop from purchased stock.

2. Each tube was cleaned in an Alconox solution, rinsed, and dried with compressed air.

3. As shown in Fig. 5.39, a gold-plated tungsten wire was strung through a Delrin endpiece on one end of the tube, through the tube, and through another Delrin endpiece. The Delrin endpiece consists of a circular piece of Delrin with a lip at one end to hold it at the edge of a tube. A hole drilled through the center of the Delrin contains a small brass tube (crimp pin) extending out. The brass crimp pin also contained a double funnel inside to center the wire. Each Delrin endpiece also had three small holes for gas flow.

4. After stringing, one end of the tube was "crimped." The Delrin piece was inserted into the tube. Then a resistor lead was inserted in the brass crimp pin (along with the wire) and a commercial crimp tool was used to crimp everything together.

5. After crimping one end, the other end was attached to a calibrated weight to achieve the proper tension and the other end was crimped.

6. Continuity and high voltage tests on each tube ensured the crimp held and the wire did not break.

---

[1] pictures at http://www.hep.vanderbilt.edu/~sheldon/tubes/tube_fab.html

7. A plank was constructed from 32 strung tubes. The endcaps were machined from Noryl (plastic) and contained one hole for gas and 32 small holes for the end of the crimp pins (which connect to the electronics). The endcaps were glued to the end of planks.
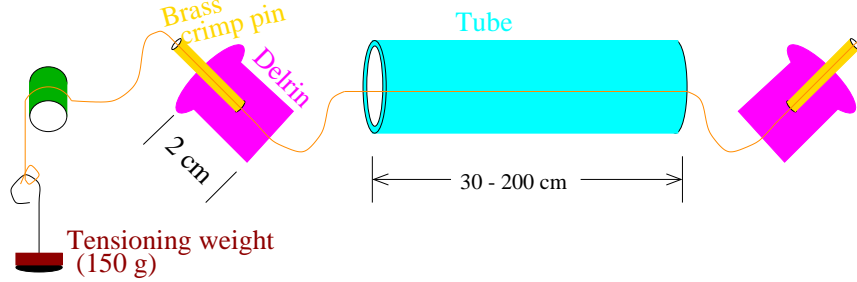
Figure 5.39: Diagram of the stringing process.

The construction of 10 planks in the spring of 1999 at VU provided us with valuable information. We found that $30\,\mu$m and $50\,\mu$m wire both work well while the $20\,\mu$m wire was harder to string and was not needed for the muon system. We found that one crimp often did not hold the wire in place while two crimps were almost always sufficient. The crimp was also not airtight requiring a glue or solder on the end of the crimp pins to ensure a good seal.

The 10 planks (six 1-footers, two 3-footers, and two 6-footers) were transported to Fermilab in June, 1999 for a test beam run. A stand on which the planks could be mounted was also designed and built at Vanderbilt which allowed the planks to be rotated and offset.

The front-end electronics were sample ASD8B cards from the University of Pennsylvania. Testing these boards revealed a high susceptibility to ambient RF noise. To reduce this noise, boxes to enclose the electronics were constructed out of circuit board and wrapped in copper tape. Interface cards to provide high voltage to the tubes and low voltage to the electronics were also designed and assembled. An interface card to convert the LVDS signal to ECL was also designed and built. High voltage, low voltage, and signal cables were also assembled. This work was done by VU and UPR.

The muon data acquisition system was written by VU using a CAMAC interface. TDC data from the planks and latches from the trigger scintillators were recorded. UIUC wrote much of the reconstruction software and an online event display. Participants from all three institutions took shifts for approximately 16 out of 24 hours for most of August and September. Pictures of the test beam run can be found at http://www.hep.vanderbilt.edu/ sheldon/tubes/test_beam.html.

Plateau curves on the planks showed that the planks are >95% efficient at $1.8\,$kV for a $30\,\mu$m wire with Ar/CO_2 gas which met our expectations. However, cross talk between channels was very high which resulted in many tubes in a plank firing with only one incident particle. This severely hindered attempts to measure individual tube efficiency or position resolution.

The susceptibility to external noise and extensive cross talk led to several design changes. One of the successors to the ASD8B chip (used in the test beam) was the ASDQ (proposed for the real muon system). Tests at VU proved that this chip was more resistant to external RF noise. We also redesigned the high voltage distribution card. To further protect the electronics from RF noise, plank design was changed to use a brass endpiece (instead of plastic) which was soldered to the stainless steel tubes. These two modifications solved the cross talk and external noise problems. The changes to the design also required changes in plank construction. Since the Delrin piece might melt or slip during the soldering process, the tubes needed to be strung after soldering the endpiece. A new new homemade crimp tool was created at VU which works in the restricted space available. The other change made was an aluminum box which contains the electronics and bolts to the endpiece, providing the last part of the Faraday cage. The Delrin piece and brass crimp pin design were also redesigned and supplied by UIUC. Pictures of the new design can be found at http://www.hep.vanderbilt.edu/∼wjohns/res/btev/proto2/.

5.6.3.3   Front-end design

At VU and Fermilab, work continues on developing the board which will be partnered to the ASDQ. The board will take 16 or 32 channels from a plank and send the data out. Initially, an analog-only board was proposed by VU; similar to the CDF (Run II) central outer tracker board. The proposed board would send LVDS signal through ribbon cable to an interceptor board which would digitize and timestamp the pulse and feed the data through a serializer and into the DAQ system. Fermilab proposed an alternative solution which combines these two functions into one board. Development work is continuing on this combined board. A prototype has been built at Fermilab and appears to satisfy the muon system requirements. Further testing of this board will take place in the summer, 2002 beam test. Initial testing results can be found at http://www.hep.vanderbilt.edu/∼wjohns/res/btev/proto2a/.

5.6.3.4   Detector construction/support

UIUC is developing detailed mechanical designs for mounting and assembly of the BTeV muon planks into quadrants. This involves considerable drafting work as well as the construction of a detailed 1/5-scale model of a complete quadrant. The scale model will help us formulate a plan for installation of the muon system as well as a plan for replacement and repair of broken planks during the run.

UIUC has also designed an adjustable jig with controllable heating elements in order to maintain precision tube lengths and properly orient the end caps with respect to the tubes and mounting plates during the assembly process. Such a jig is required to efficiently assemble the large number of tubes of many different lengths with adequate precision to allow us to mount the array in the confined space available.

5.6.3.5 Simulation work

All three muon group institutions have been involved in creating an accurate muon simulation in the BTeVGeant framework, including the complicated magnetic field resulting from having a dipole magnet inside a toroidal magnet (see chapter 4 for a discussion).

5.6.3.6 Construction database

At each step in the construction process the actions taken for each element of the detector are recorded in a database through the use of a barcode tracking system. We anticipate that these data will later be useful in inventory control and studying correlations of detector performance parameters.

5.6.3.7 Wire tension measurement

To assure that each tube is strung with a wire of the correct tension, the tension of each wire is measured by placing the plank in a magnetic field, driving the wire with a sinusoidal current, and measuring the induced EMF to find the resonant frequency. From this value the tension is computed.

Vanderbilt has developed a test stand which automatically measures the tensions in a plank full of tubes and stores the resulting information in the construction tracking database.

5.6.4 Future research and development work

During the past year we have constructed three planks at VU using our latest design, worked on by all three institutions. These planks are performing well in a cosmic ray test stand as shown in http://www.hep.vanderbilt.edu/~wjohns/res/btev/proto3/. We plan to construct 3–5 more planks to test during the summer of 2002. This test run will allow us to make many of the studies which we were unable to perform in 1999 due to noise problems. These studies include measuring speeds and responses of various gasses, measuring high rate effects, and measuring individual tube efficiency and resolution. The results of these tests should verify our design will be effective in the BTeV spectrometer.

Refinements of the plank construction will also be investigated in hopes of finding a method which reduces the construction time while maintaining the needed features. In particular, it has been proposed that tubes may be strung before joining the tubes to the endpiece. The problem of heating the Delrin piece beyond its melting point may be resolved by spot welding the tube and endpiece at a single point and filling the rest with glue rather than soldering the entire structure.

Work on the front-end electronics continues at VU and Fermilab. We plan to test the new combined analog/digital board during the summer, 2002 test beam.

UIUC will continue work designing tools to assemble and support the muon system.

All three institutions will also continue working on simulations and start writing reconstruction code.

5.7   Trigger R&D

One of the key features of BTeV is the vertex trigger, which is the primary trigger for the experiment. Most of the trigger R&D work prior to the submission of the BTeV proposal has been devoted to the vertex trigger, especially the implementation at Level 1. Since the submission of the proposal we have made substantial progress in the development of the Level 1 vertex trigger. We have also included the Level 1 muon trigger in our hardware design, made substantial improvements to the muon trigger algorithm, and we have performed a large number of studies as we continue the development of Level 2 and Level 3 trigger algorithms. Progress on all of these R&D developments will be presented in this section.

5.7.1   Level 1 Vertex Trigger

The Level 1 vertex trigger continues to be an important aspect of our trigger R&D effort. Since the submission of the BTeV proposal, this R&D work has focused on the following areas:

- Implementation of the pattern recognition (segment finding) algorithm in FPGA's (Field Programmable Gate Arrays)

- DSP (digital signal processor) timing studies for the segment matching, tracking, and vertexing portion of the Level 1 vertex trigger

- Timing studies on processors other than DSP's

- Data flow analysis and simulations

- Design and fabrication of a 4-DSP prototype board

We have new results on DSP timings that were obtained by optimizing the Level 1 vertex code for a DSP, and then running the code on a DSP. This approach gives us a more reliable assessment of the number of DSPs needed for the vertex trigger, as opposed to the approach we used for the BTeV proposal, for which we estimated CPU cycle counts based on a partial assembly language implementation of the code. With the optimizations and timing results achieved to date, the DSP code is close to the timing estimates presented in the proposal but a factor of 4 slower. This is reduced to a factor of 3 for a new DSP that will be available beginning in the second quarter of 2002. Even without further optimizations, we are confident that newer generations of DSP's will get us to the estimates stated in the proposal. However, in an effort to explore other processor alternatives for the Level 1 trigger we have started to investigate general purpose processors from Intel and Motorola. Preliminary results suggest that these processors exceed the proposal estimates by at least a factor of 2 or 3 in performance. Additional R&D will be needed to investigate the feasibility of implementing the Level 1 trigger hardware with these processors.

5.7.1.1 DSP Timing Studies

This section will focus on timing studies done on the segment matching, tracking, and vertex finding portion of the Level 1 vertex trigger. Since this is the portion of the Level 1 vertex trigger algorithm that will run on the DSPs, it will be referred to as the DSP algorithm. We stress the importance of timing results since execution speed directly determines the total number of DSPs required in the Level 1 farm and therefore its cost and complexity. We will also describe work done to address two concerns raised by the PAC's Technical Review Committee in 2000, specifically (1) the fact that the custom assembly language code described in the proposal had not been run on a DSP or DSP simulator to demonstrate that it works, and (2) the potential problems involved in maintaining custom assembly code throughout the lifetime of the experiment.

The starting point of our studies was a variant of original C language version of the code on which the optimized assembly language version used in the proposal was based. (The code whose performance we describe here was optimized for triggering efficiency. The code used in the proposal made small sacrifices in triggering efficiency to achieve significant enhancements in computing speed. This will be discussed more below.) All DSP timing studies were done on a Texas Instruments (TI) C6711 DSP Starter Kit (DSK) board with a 150MHz TI TMS320C6711 DSP.

The initial step taken was to get the original, unoptimized C code running on the DSK board to address issue (1) above. Once the code was running on the DSK, optimizations were introduced in two major phases to reduce the execution times. In the first phase, costly calls to external library functions were replaced with C intrinsics that map directly to DSP instructions, and all double-precision floating point operations were replaced with single-precision operations. In the second phase, the segment matching portion of the algorithm which accounted for over half of the total execution time was completely rewritten in order to avoid the need to try all possible combinations of inner and outer segments in searching for complete tracks. Data structures of the code were also reduced in size to allow assignment of data memory sections in the DSP's internal Level 2 Cache/SRAM. This reduces CPU pipeline stalls due to cache misses requiring fetches from external SDRAM. In order to address issue (2) above, we also made it a point to do all optimizations in C, resorting to assembly language programming only when necessary.

Execution times after each phase of optimizations were measured using the built-in profiler of TI's Code Composer Studio to count CPU cycles accumulated in the DSP's on-chip performance monitors. Due to the reasons cited above, execution times are improved by having code and data memory sections reside in internal RAM. Since the DSP code[2] exceeded the 64KByte size of the internal memory, groups of functions were profiled in separate sessions wherein only those functions being profiled were assigned in internal RAM. This was done with the view that upcoming processors in TI's roadmap will have enough internal memory to hold the complete DSP code.[3] The measured execution times for both optimiza-

---

[2]roughly 2,500 lines of C source code representing on the order of ~ 100KBytes in .data and .text memory sections.

[3]A new member of C671x family-TMS320C6713 will be sampling in 2Q02 with 256KBytes of on-chip L2

217

Section of	Proposal	DSP timing in CPU cycles per beam crossing			
DSP algorithm	estimates in	Before opt.	After Phase 1 opt.	After Phase 2 opt.	
	CPU cycles	10 BCO's	10 BCO's	10 BCO's	100 BCO's
Segment matching	24,200	1,296,778	503,012	164,836	168,113
Track processing	14,400	397,518	38,632	38,632	34,528
Vertetxing	14,673	264,429	34,720	34,720	32,938
Total	53,273	1,958,725	576,364	238,188	235,579

Table 5.3: Level 1 Vertex Trigger Timing Results

tion phases are presented in Table 5.3 where they are compared with estimates in the BTeV proposal. These results were obtained with 10 simulated (Pythia/Geant3) minimum-bias beam crossings with an average 2 interactions per crossing. For verification, the timing results for the second phase of optimizations was repeated with 10 times more statistics (Table 5.3, column 2). As these results show, execution times were reduced by nearly an order of magnitude ($1,958,725 \ cycles \rightarrow 235,579 \ cycles$) without resorting to custom assembly programming.

5.7.1.2 Optimizations with Custom Assembly Code

To see what performance gains could be achieved with custom assembly programming, code coverage of the segment matching routine was tested to identify sections on which optimizations would have the greatest impact. Using the intermediate assembler source code (totalling 1,329 lines) produced by the compiler for this routine as a starting point, custom assembly programming was done on the identified sections to make more efficient use of the DSP's 8 parallel execution units. 222 new lines of custom assembly code were written replacing roughly 20% of the compiler generated assembly code. Applying the procedure described above for measuring execution times on this optimized assembly version of the segment matching routine indicated a reduction of $\sim 2\times$ for this particular routine ($117,242 \ cycles \rightarrow 63,618 \ cycles$) and an overall reduction of over 20% for the complete DSP algorithm ($235,579 \ cycles \rightarrow 181,955 \ cycles$).

5.7.1.3 Efficiency-Speed Tradeoffs

As mentioned above, the code used at the time of the proposal made some small sacrifices of ultimate triggering efficiency to achieve speed ups which explain in part the differences reported above. The version of the algorithm used here is aimed at maximizing the triggering efficiency. We are now going back and reviewing those tradeoffs. However, given the likely availability of faster DSPs, we do not see this as an urgent priority. Moreover, as will be seen below, alternatives to DSPs are now available which may already have provided us with a

SRAM (enough to hold the complete DSP algorithm) and higher core speeds of 225MHz (33% reduction in execution times).

new approach which resolves nearly all remaining issues with respect to the Level 1 trigger speed.

5.7.1.4 Timing Studies on Other Processors

Investigations have also been done to measure execution times of the optimized C version of the DSP code on the following two general purpose processors: (a) 1.13 GHz Intel Pentium III-M, and (b) 500 MHz Motorola MPC7400 PowerPC G4. Additional optimizations done in C to utilize both processor's built-in vector execution units were introduced in the segment matching routine. Preliminary results are very encouraging indicating execution times roughly an order of magnitude better (Pentium III: $133,053\,cycles \times 0.88\,ns = 118\,\mu s$, PPC G4: $98,365\,cycles \times 2.0\,ns = 197\,\mu s$) than those for the optimized C code running on a 150 MHz TI TMS320C6711 DSP ($235,579\,cycles \times 6.67\,ns = 1,571\,\mu s$). Price/performance ratios of a PowerPC G4 based system seem quite promising compared to that based on a DSP. More work needs to be done, however, to investigate whether the I/O capabilities of these processors meet the requirements of the trigger.

5.7.2 Level 1 Muon Trigger

5.7.2.1 Code Development Infrastructure

We have developed an event driven analysis infrastructure that reads a user-specified list of muon Monte-Carlo input files, translates the event by event raw hit information into a more easily useable set of data structures, and provides the hooks necessary for the user to easily link their own analysis code. Developed in Visual C++, this system runs on any PC and is the basis of all algorithm development done so far.

5.7.2.2 Muon Trigger Algorithm Development and Testing

Work done prior to the submission of the BTeV Proposal in May, 2000 had demonstrated that when all available information is used (i.e. a fitting algorithm is applied to all possible hit combinations and the resulting χ^2 examined), good efficiency for muon tracks and adequate rejection of background could be obtained. The goal since this very important proof of principle has been to see if a simpler (hence potentially much faster) algorithm could achieve similar results.

By using a large set of Monte-Carlo generated "good muons" and studying both the correlations between hits in different views within a station, and the correlations between hits in similar views in different stations, we discovered that some simple relationships exist between hit muon tubes that belong to a single track. Not surprisingly, there is a very tight correlation between the hits in the various views of a given station, and this correlation can be used to distinguish sets of tubes that belong to the same track (which define a space-point in that station) from the otherwise enormous set of random combinations.

Slightly less intuitive is the fact that there is a very simple relationship between the radial coordinates of the three space-points (one per station) belonging to the same track. If we simply let these radial coordinates define points in the 3D vector space r1,r2,r3, we find that good muon tracks result in points that populate a simple plane in this space, and the random background combinations results in points that tend to not lie in this plane. This allows us to use simple geometric transformations on points in this space to, in effect, construct look-up tables to identify good tracks. Using such an approach, we have designed an algorithm whose performance seems comparable to the full-blown χ^2 fitting method, yet is simple enough that it should be able to run quickly on a DSP.

5.7.2.3   Muon Trigger Algorithm Timing Studies

We have implemented a tube-based lookup oriented trigger algorithm, as outlined above, in C code that runs on a TI TMS320C6711 DSP starter kit. We use this hardware, together with the TI's Code Composer Studio, to study the speed of the algorithm as various modifications are made. The code has not yet been optimized, and currently its speed is about an order of magnitude away from the performance assumed in the proposal. Part of the needed speed improvement will come from simply buying faster devices; part will come from further code optimization, and part will come from moving the space-point finding portion of the algorithm from DSP based code to upstream FPGAs. This is a work in progress, and we hope to have more reliable results in a few months.

5.7.3   Level 1 Hardware

5.7.3.1   Simulations and Data Flow analysis

The lack of queuing models and data-flow analyses of the BTeV trigger were ranked with high technical risk by the PAC's Technical Review Committee in 2000. A data flow analysis is now underway using two different approaches: modeling and simulation. This analysis was carried out through 2001, and will continue in 2002. We follow an iterative proceedure: a trigger architecture is proposed, mathematical models are used to analyze the data flow and buffering needs of the system, then simulations are used to validate the model assumptions, and the results are used to refine the proposed architecture. The data flow analysis was extended beyond the Level 1 trigger boundary into the pixel detector readout. The purpose of this is to understand how the readout function scrambles the data with respect to time and to explore the issues involved with time-demultiplexing the pixel data into parallel streams called "highways." Multiple highways reduce the bandwidth per data stream, and the number of highways will be chosen to match the most appropriate technology.

With respect to the Level 1 pixel trigger, the pixel preprocessors and segment finders have been fully modeled and simulated. The data flow analysis shows a very good degree of consistency between the modeling and the simulation results. Queue sizes and communication channel bandwidths are within reasonable margins. Once we begin the design stage and a full VHDL code has been generated, we can refine some of the parameters shown in the

modeling and simulation to optimize the design. In particular, the segment-finder FPGA algorithm is composed of similar module functions that work sequentially. The data flow analysis has helped to optimize the data pipelining and to detect underutilized modules. Some modules can be reused for more than one function. This is particularly important to minimize the silicon logic needed in the implementation.

In 2002 we plan to complete the data flow simulations. This requires modeling and simulating a farmlet of processors, which is the smallest grouping of processors on a single board. In our current design, a farmlet consists of four DSPs. The data flow simulations will be used to study and optimize the data flow from input buffers to the processors. Subsequent simulations will be used to study the dynamics of control and monitoring for the farmlet.

5.7.3.2 Segment Finding Algorithm Implementation and Simulation Status

The segment finding algorithm is being implemented in Very High Speed Integrated Circuit Hardware Description Language (VHDL). We are using this high level language in an attempt to keep the code somewhat portable between the various software tools that are currently available for field programmable gate arrays (FPGAs) and complex programmable logic devices (CPLDs). However, to make the most efficient use of device specific resources such as internal RAM or other custom features, the manufacturer's device specific library components are also incorporated into the design. The segment finding algorithm is currently being executed and simulated using the Quartus II design software from Altera. The simulations have validated the segment finding algorithm and produced two different implementations of the algorithm and may help us to optimize the trade-offs between cost and speed. There have been preliminary compilation, place-and-route, and simulation tests run so that silicon usage and timing estimates can be accumulated from these experiments for future comparisons. These estimates were used as inputs to WBS costs. The next goal is to move the existing VHDL code to other design software platforms. Our intent is to target devices from other programmable logic manufacturers. This will allow us to make direct price versus performance comparisons between device offerings from competing manufacturers.

5.7.3.3 Hardware investigations

There have been ongoing refinements of the Level 1 vertex trigger architecture. A trigger DSP prototype has been designed based on the current architecture. It is implemented as a motherboard containing I/O controllers and four daughter-card positions for processing elements. The daughter-card positions have a generic set of signal assignments to allow various processors to be accommodated. The current target processors are DSPs, and two daughter card designs for specific DSP chips are included in the prototype project.

The motherboard implements the following functions:

1. Input data buffering and management of data flow to the processing elements.

2. Output data buffering and management of data flow from the processing elements to the external data network.

3. Processing of control messages from the external control network.

4. Control and management of result messages generated by each processor.

The daughter board implements the following functions:

1. Contains flash and RAM memory, power supply and support chips for each processor.

2. Provides external power input connectors and serial port connections so that it can be operated stand-alone without the motherboard.

The project goals include:

1. Provide a platform to characterize processor-to-network interactions with several types of processors. This includes testing several data flow and buffer management techniques for the current architecture, which is based on a single data stream feeding multiple processors.

2. Characterize the impact of message traffic on processing bandwidth.

3. Provide a platform to develop and test the tracking algorithm code, and test with different processors.

4. Provide a platform to develop and test the trigger supervisor and monitor protocol. This includes initialization of the DSPs, fault detection, control and error messaging, and some hardware event histogramming.

The first two motherboards are assembled, have passed initial tests, and are providing the hardware platform for software development. The first DSP daughter card has been assembled, and initial tests have begun. This effort will continue through 2002.

5.7.4   Level 2

This section and the subsequent section present a progress report on the Level 2 and Level 3 triggers. Many of the details are ignored, since they have been presented in the BTeV proposal.

Since the BTeV proposal, the Level 2 and Level 3 code has been upgraded to handle the new pixel-detector geometry, which features z-staggered half-stations and a non-uniform checker-board of pixel chips. This was a relatively easy task because the Level 2 algorithm deals with three dimensional space points with coordinates that are expressed in a global coordinate system. Thus, only minor re-addressing schemes of the hit banks had to be done.

Unlike the Level 1 trigger R&D, we concentrate our effort for Level 2 on algorithm studies rather than CPU performance. Previous timing studies clearly indicate that our CPU and memory performance goals are achievable. Prior to describing the recent improvements, we now briefly describe the Level 2 trigger algorithm presented in our proposal. The input data

consists of (i) all Level 1 tracks and vertices (ii) the raw pixel hits (iii) optionally, hits from the first few forward tracking stations. Level 2 pixel tracks were seeded by Level 1 tracks. Missing hits were found, and these tracks were Kalman-fitted for the first time. In addition, new tracks of typically lower momentum were also reconstructed. Optionally, tracks were propagated forward and matching hits in the first few tracking stations were searched for, in order to improve the momentum resolution and provide "confirmation" for the tracks. Crude vertex fits were then performed. Detached tracks consistent with heavy quark decays surrounding the primary vertices were tallied. The final Level 2 trigger algorithm used detached vertices/tracks and the total detached p_t.

Based on further studies, we are now reaching the following conclusions:

- For forward tracking at Level 2, the advantages of using the first or second forward tracking stations is far from obvious. Although the first station does improve the momentum determination (from $\sigma_p/p \approx 5$ to 10% down $\approx 2\%$), such an improvement has only an indirect effect on the vertex. It simply allows us to measure the slope in the bend plane (y-z plane) a bit better. However, the y position resolution at the vertex does not improve significantly. Note that we currently have no direct momentum nor mass cuts in the vertex algorithm, to be able to trigger on various final states without bias. Although it has been proposed to confirm a pixel track with forward hits, the level of pattern recognition confusion in the first few tracking stations is much higher than in the pixel detector simply because the average detector occupancy jumps from $\approx 10^{-4}$ in the pixel to about 0.1 (first straw station).

  Thus, we focus on improving the pattern recognition in the pixel detector rather than attempting to sort out partially reconstructed forward tracks. This could also simplify the data aquisition system and thereby improve the throughput, as we would not have to wait for the silicon strip or straw data. However, the data aquisition system is still designed to be able to deliver this data prior to a Level 2 accept, in case specific future Level 2 triggers are based on momentum or mass cuts rather than pure vertexing.

- Secondary vertex reconstruction at Level 2 improves substantially the signal to noise discrimination at Level 2. That is, after performing genuine vertex fits, we now require the presence of at least one fitted secondary vertex prior to computing the total detached p_t, which has to be greater than 2.5 GeV/c. In order to recover single charged track b vertices (for instance, $B^+ \rightarrow \pi^+\pi^0$), we alternatively require a single detached ($> 4\sigma$) track with $p_t > 2.0$ GeV/c.

With these cuts, the Level 1 times Level 2 rejection rate on background crossings is about 1 in 1,000 and the Level 2 efficiencies for $B \rightarrow J/\psi K_s^0$ and $B^+ \rightarrow \pi^+\pi^0$ are about 90% and 94%, respectively. Histograms of the the total detached p_t are shown in Figure 5.40. The improvement relative to the results presented in the BTeV proposal comes mostly from the improved vertex fitting, while the pixel tracking performance remained virtually unchanged, despite significant changes in the design of the mechanical support and the geometry of the detector. Note that the single track efficiency for the Kalman fits could be improved upon,

as the description of the scattering surfaces in the fits could be more complete and precise. Also, a more sophisticated set of cuts will be possible in the future. Such cuts will be difficult to select without a more accurate description of the background, which is now dominated by beam crossings where multiple primary vertices occur within a a few cm of each other.

Pt Sum probability distributions .

Both curves are normalized to the Analysis & L1 accept rate for signal, and L1 accept rate for background.
For Pt > 2. ,
J/Ψ K0s efficiency ~ 80 %
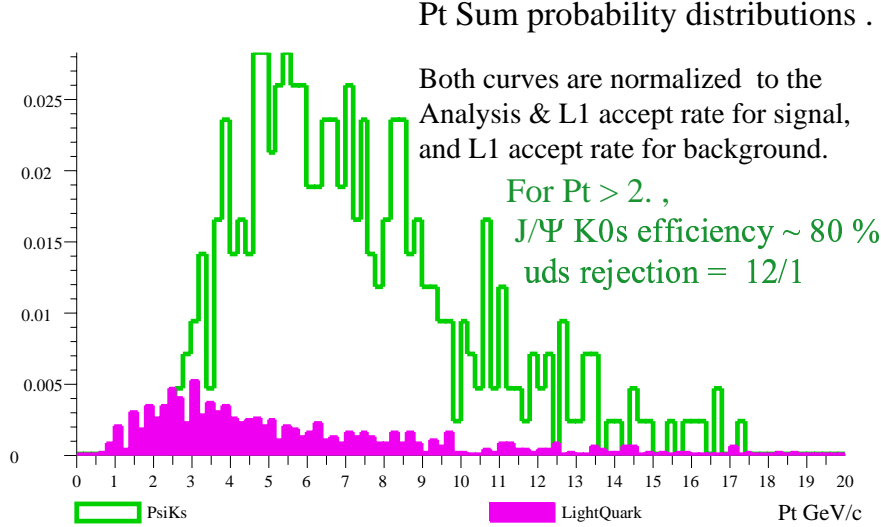uds rejection = 12/1

PsiKs   LightQuark   Pt GeV/c

Figure 5.40: Distribution of the total detached transverse momentum for signal and background, for crossings with a secondary vertex. Note that an additional 10% efficiency comes from the second acceptance criteria (one single detached track with $p_t > 2.5$)

5.7.5   Level 3

Work on a prototype of the forward tracking reconstruction package has started. The goals are (i) to study and benchmark this critical component of all Level 3 triggers and (ii) optimize the design of these tracking elements. We are currently able to reconstruct tracks throughout the spectrometer, up to the EM calorimeter front face, without any prompting from the Monte-Carlo truth tables. Based on the same set of raw data structures and elementary algorithms, we are progressing on two distinct fronts: pixel-seeded tracks and K_s^0's

5.7.5.1   Pixel to Forward Tracks

The reconstruction of the forward tracks coming from the interaction region is seeded by the pixel tracks (Level 2 tracks). Level 2 tracks are projected forward, to the z location of the straw and/or silicon strip stations. Note that we reconstruct tracks in both systems (straws

and silicon strip) in conjunction, as a typical track starts as silicon strip track but crosses into the straw system somewhere upstream of the RICH. For each track-station intercept, a track road (or foot-print) is computed based on the available fit. Hits are selected within these roads and a new Kalman fit is performed. For the straws, we fit a set of 2 or 3 hits within one stereo view to a given track rather than individual hits to avoid unnecessary combinatorics of many possible Kalman fits. Thus, left-right ambiguities are usually lifted prior to fitting. Arbitration among different possible Kalman fits for a unique Level 2 track seed is also performed at every tracking station. Such track-station Kalman-fitted intercepts are allowed to have one missing view. In addition, a single hopelessly confused tracking station can be skipped altogether.

The preliminary tracking efficiency versus momentum, for tracks reaching the RICH, is shown in figure 5.41. About half of the inefficiency is due to inaccuracies in the multiple-scattering accounting in the Kalman fits and the other half is due to pattern recognition confusion or double occupancy in the straws. The momentum resolution obtained via this full pattern recognition is in very good agreement with the fits performed in the context of BTevGeant, where all hits are always assigned to their respective tracks. Once station 6 (located in front of the RICH) is reached, the probability of accepting "ghost" tracks is quite small, about 0.5%.

We anticipate improvement in the efficiency with a better version of the Kalman fitter. The pattern recognition in the first straw station is rather difficult, due to the high occupancy. We are considering increasing the size of the silicon strip station, and, possibly, entirely eliminating the straw planes at that location (95 cm downstream of the magnet center). Conversely, the silicon stations located just in front of the RICH or the EM calorimeter have negligible acceptance for pixel-seeded tracks.

5.7.5.2 Preliminary K_s^0 Tracking Studies

We now briefly describe the reconstruction of the K_s^0 for which we have no (or not enough) pixel hits. From a detailed study on the track topology of these $\pi^+\pi^-$ pairs, we conclude that the largest reconstructable sample consists of tracks reaching straw station 6, for which we have 3 consecutive straw stations in the nearly field-free region beginning at $z \approx 2.75$ meters from the magnet center. Stations 4, 5 and 6 are located at $z \approx 2.9$, 3.3 and 3.8 meters from the magnet center, respectively. The following algorithm has been partly coded and is currently under study:

- Selection of "un-used" straw hits. We mark all the hits used in the above pixel-seeded Level3 tracks, as "used", thereby getting rid of about 1/3 to 1/2 of the available hits.

- Reconstruction of straw hit triplets (or doublets) within a straw stack (or "view"). Despite the lack of good constraints from unknown track slopes, the multiplicity of such small, 2D tracks within a station and a stack is not overwhelmingly large.

- Reconstruction of 2D track between stations 4, 5 and 6, for each stereo view
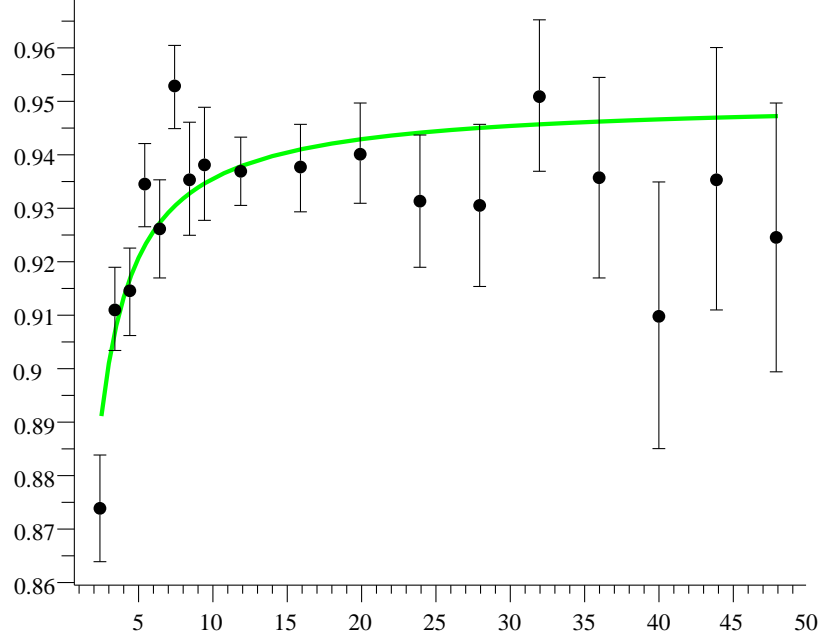
Efficiency vs longitudinal momentum

Figure 5.41: The preliminary efficiency versus the longitudinal momentum Pz (GeV/c) for the Level-2-seeded (pixel-seeded) Level 3 tracks. The fit is simply there to guide the eyes, the function if $E_\infty * (1 - k/Pz)$. The parameter k is obviously statistically significant, indicating problems at low momentum. Fortunately, this is where our geometrical acceptance drops sharply. Note that the loss of "efficiency" includes particles lost through interaction in the material of the detector and due to (recoverable) problems with the current detailed description of multiple scattering sources in the analysis program.

- 3D tracks between stations 4, 5, and 6.

- First reconstruction of a 3D K_s^0 vertex using the non-bend plane 2D vertex as a seed. The K_s^0 trajectory is constrained: it must come from the selected Level 2 primary vertex for which we have good detached p_t. This allows us to obtain a preliminary determination of the $\pi^+\pi^-$ and K_s^0 momenta as well as the K_s^0 mass.

- Search for confirming hits in upstream stations, followed by track and vertex refits.

Preliminary studies indicate that we can reconstruct K_s^0's that decay upstream of station 3 with about 60% efficiency. The loss of signal is mostly due to the high occupancy in the straws.

5.8 Data Acquisition R&D

5.8.1 Overview

The conceptual design of the BTeV readout and controls system has been outlined in the proposal. Since the proposal was submitted last year we have defined a baseline implementation, improved the overall throughput by 50% without increasing the costs and we began to evaluate the possible software architectures. This report begins with a brief system overview followed by more detailed discussion of the readout hardware and software as well as our plans for the detector control system.

By the time BTeV is operational the Tevatron will run with a bunch spacing of 132 ns corresponding to a crossing frequency of 7.6 MHz. For each crossing the BTeV detector will generate about 100 - 150 KBytes of data or roughly 1T Byte/second. The pixel detector dominates the data size with the second largest contribution coming from the electromagnetic calorimeter. Allowing for a 50% margin we designed the BTeV data acquisition system to handle a throughput of 1.5 T Bytes/s. Approximately 1% of the crossings will be accepted by the Level 1 trigger so that we have to route up to 15 GBytes/s to the Level 2/Level 3 trigger farm. Here the trigger rate will be reduced by a factor of 20 to approximately 4000 Hz. The expected reduction in data bandwidth is even larger as we plan to compress the data before it is sent to a mass storage system. In our baseline design we assume an output rate of 200 MBytes/s. A distributed software system will be developed to control and to configure the readout hardware.

Independent of the readout system, the BTeV detector control system will monitor the operation and performance of the many BTeV components. This system will be fully integrated with the Fermilab and Tevatron safety and security systems.

5.9 Data Acquisition Hardware

A schematic view of the readout system is shown in in the previous chapter. For each beam crossing the detector response is digitized and sent from the front-end electronics modules via serial links to so called Data Combiner Boards or DCBs. These custom designed modules combine data from several detector channels to an output stream which is sent over an optical fiber to the counting room. Here the data are buffered until a Level 1 trigger decision has been reached. Accepted events are passed on to the Level 2/Level 3 trigger farm and eventually transferred to a mass storage device. The design adopted for BTeV provides sufficient data throughput and minimizes the number of hardware modules that have to be developed by the collaboration. A single DCB design can easily be customized for different needs by different detector components. The data links and the Level 1 buffer modules are common to all of BTeV. Since the proposal was submitted we have refined the hardware architecture and decided to implement the system using multiple parallel data-paths called highways. Each highway (at least until a data fragment reaches the L2/L3 processing farm) will process every nth crossing, where n is the total number of highways. The exact number

of highways has yet to be determined, but is on the order of 8.

This approach greatly simplifies the data handling aspects of the system without compromising other requirements. For example, instead of a large number of small records a Level 1 buffer module now receives only 1/nth of the original number of messages. While the overall throughput remains the same - the average record is now larger - this is much better mapped to the performance characteristics of commercial network switches and hence easier to implement. A significant reduction in the number of control messages exchanged between the farm nodes, the Level 1 buffer system and the Global Level 1 processor(s) is another advantage of the highway architecture. During normal data taking operation the nodes of the Level 2/3 farm will be assigned to one of the highways. This will provide the highest throughput. All highways, however, will be cross connected via another network switch allowing each Level 2/3 computer access to the data in any of the Level 1 buffer modules. While the proposal kept open the option of custom designed switches we have now decided to use commercial Gigabit Ethernet switches.

In collaboration with the muon detector group we successfully tested a front-end board with ASDQ chips and an onboard serial data proving that with proper design digital noise does not affect the performance of nearby analog circuits.

Over the next year we intend to continue our tests and evaluations of components critical to the success of the BTeV data acquisition system. The activities planned include

- Development of a serial link board to test protocols, optical components and serializer/de-serializer chipsets.

- Evaluate FPGA chips. Implement a multi-channel TDC in an FPGA recently developed by Altera.

- Begin work on the Level 1 buffer design to provide a module for the trigger group allowing them to continue their development work.

- Development of the front-end part of the front-end - DCB link and integration on the next version of the muon readout board.

- Complete requirement documents and specifications.

5.9.1 Data Acquisition Software

A vast amount of software is needed to operate an experiment of BTeV's complexity. Broadly speaking this can be divided into the following categories

- Run Control including configuration of the readout hardware

- Detector and environmental control

- Error and alarm handling and recovery

- User interface and remote access including security

- Persistency and archive

Since the submission of the proposal we have continued to develop the software architecture of the BTeV data acquisition system and defined the requirements and functionality of the software components listed above. This process will continue with the expectation to have a detailed model of the readout and control software by the end of the year. In parallel to this effort we have chosen two critical components for a careful evaluation of commercial and free solutions. The first is the message passing system, which provides the communication path between all software components. The proper selection of this tool is of critical importance. The other component we will evaluate over the next year are commercial detector/process control systems. We will try to learn which system is best suited for the control and monitoring of the BTeV detector and its environment. We will also investigate a recent trend in the HEP computing community to use similar tools for detector and run control and to establish an overall experiment control system. As with the readout hardware we will base our system on commercial components and take advantage of successful software packages developed by the HEP community. We are establishing contacts with other laboratories and in particular with those groups involved in data acquisition software development for LHC experiments.

5.9.2   Summary and Future Plans

The conceptual design of the BTeV readout system is well advanced. For our baseline implementation we have relied on commercial products and industrial standards wherever possible. Interface modules and data links to the front-end modules as well as the intermediate event buffers have to be custom designed but no new technologies have to be developed for these purposes. Over the next year we will begin to evaluate commercial network components and the design of critical components for the data combiner and the Level 1 buffer modules will start as well. On the software side we plan to evaluate commercial and freeware message passing systems that will form the core layer of our distributed run control system. On top of that we will complete the design of the system architecture and define the interfaces between different components so that development work can proceed at several locations. As part of this we will further develop the interface to the RTES effort. We intend to base the detector control system on commercial software packages. Initial contacts with vendors have been established. Within the next year the evaluation phase should be completed.

5.10 BTeV Real-Time Embedded Systems R&D

5.10.1 Introduction

A major challenge facing BTeV is the software infrastructure required to keep the trigger system operating, to assure that it is working correctly, and to detect and adapt to fault conditions both within the trigger itself and within the experiment and accelerator environment. BTeV physicists have formed an alliance with computer scientists and engineers at four universities (Illinois, Pittsburgh, Syracuse, and Vanderbilt) in part to address these issues. This collaboration is researching the design and implementation of high-performance, heterogenous, fault-tolerant and fault-adaptive real-time embedded systems, of which the BTeV trigger is an excellent example. This research is being funded by a $5 million, 5-year award from the National Science Foundation's Information Technology Research program. While this research will be applicable to a wide variety of problems in science, medicine, and industry, one important deliverable of the research is an operating system for the BTeV trigger.

5.10.2 Project Overview

The BTeV trigger system is an example of a very large-scale real-time embedded computer system that:

- achieves ultra high computational performance through use of parallel hardware architectures;

- achieves and maintains functional integrity via distributed, hierarchical monitoring and control;

- is required to be highly available; and

- is dynamically reconfigurable, maintainable, and evolvable.

BTeV will produce very large streams of data which must be processed in real-time using data dependent computation strategies. Such systems are inextricably tied to the environment in which they must operate, and must perform complex computations within the timing constraints mandated by their environments. These systems require ultra high performance (on the order of 10^{12} operations per second). This level of performance requires parallel hardware architectures, which in the case of BTeV is composed of a mix of thousands of commodity processors, special purpose processors such as Digital Signal Processors (DSPs), and specialized hardware such as Field Programmable Gate Arrays (FPGAs), all connected by very high-speed networks. The systems must be dynamically reconfigurable, to allow a maximum amount of performance to be delivered from the available and potentially changing resources. The systems must be highly available, since the environments produce the data

streams continuously over a long period of time, and interesting phenomena important to the analysis being done are rare and could occur in the data at any time. To achieve the high availability, the systems must be fault tolerant, self-aware, and fault adaptive, since any malfunction of processing elements, the interconnection switches, or the front-end sensors (which provide the input stream) can result in unrecoverable loss of data. Faults must be corrected in the shortest possible time, and corrected semi-autonomously (i.e. with as little human intervention as possible). Hence distributed and hierarchical monitoring and control are vital.

The design and implementation of such systems cannot be achieved by the ad hoc approach of developing simple small-scale components and scaling them up into large-scale systems. Creating usable software for this type of real-time embedded system will require research into solutions of general problems in the fields of computer science and engineering. We plan to approach these problems in a way that is general, and to produce methodologies and tools that can be applied to many scientific and commercial problems. Issues such as fault tolerance and performance must be explicitly addressed at multiple levels in the system design. We propose advances in system design methodology, tools and runtime infrastructure to facilitate these and more issues involved in developing such systems. We further propose to develop the software to accomplish the design and implementation of the system and to study its performance, utility, and scalability on the actual BTeV hardware as it grows over the construction phase of the experiment. The result of this research will be software, design methodologies, and the documented experience of the project.

Several capabilities are required:

1. **System Modeling and Analysis** - Full-system performance estimations are needed during development, given the coupling that exists between different aspects of a system design (e.g. low-level architectural decisions can have a large impact on system-level performance and fault behavior). Designers need mechanisms for representing and evaluating the impact of these decisions. The design tool will serve as a framework for modeling and analyzing system designs via behavioral simulation, performance simulation, design verification, etc. The design tool will continue to be useful during operations to understand how to handle unanticipated situations, which often arise in HEP research;

2. **System Configuration Management** - Configuration of a large-scale networked processing system is a complex problem, more so when the system is susceptible to faults. A robust configuration management infrastructure is required, with the ability to specify reconfiguration strategies at different levels. The fault mitigation infrastructure is intricately coupled to the configuration management infrastructure - means to capture the specifics of the coupling are necessary;

3. **Runtime Environment and Hierarchical Fault Detection/Management** - The deployment, execution and reconfiguration of the components must be carefully managed, especially when the cost of downtime is high, as is the case for BTeV. Runtime

environment control is essential. A system-wide infrastructure is required for rapidly detecting, isolating, filtering, and reporting faults. In very large-scale heterogeneous systems a single centralized fault management solution is clearly not feasible. Hierarchical distributed fault mitigation is necessary, with the ability to specify fault mitigation policies at different levels of abstraction (system, network, node, etc.).

The researchers on this project have extensive experience in developing all of the above capabilities. For example, a high-level design tool is required to support the overall design, deployment, and evolution of BTeV-type systems. The Model Integrated Computing (MIC) approach, developed at the Institute of Software Integrated Systems (ISIS), Vanderbilt University, assists the creation of domain-specific modeling, analysis, and program synthesis environments for building complex, large-scale computer-based systems. Integrated models created in this environment represent all relevant factors of a physical system. Models can be subjected to many types of rigorous analysis, for verifying the behavior and performance of the system prior to implementation. Central to this approach is the concept of a "configuration," which is a particular organization of computing resources, such as processors, network components, memory buffers, and storage elements, and a particular allocation of software components and datasets on them, including task schedules and message routes. Systems can be synthesized (or generated) from the models when the designer is satisfied with the analysis results. The Design and Analysis Environment will consist of: a) graphical modeling language/environment for system specification; b) synthesis tools for interfacing the models with commercially available and custom analysis tools; and c) synthesis tools for generating configurations from specifications, for configuring fault managers, and for configuring operation managers. The synthesized configurations are deployed and executed in the Runtime Environment. The primary interaction between the Design and Runtime environments is through the synthesis process. However, feedback from the Runtime to the Design environment is possible in advanced fault scenarios that require re-synthesis and re-deployment. While MIC provides the basic infrastructure, research is required to define: (1) modeling language and composition methodologies suitable to BTeV's application; (2) mapping techniques for models to/from analysis tools; (3) large-scale synthesis techniques.

The Illinois, Pittsburgh, and Syracuse groups have extensive experience in fault detection and mitigation, as well as real-time operating systems. Very Light Agents (VLAs), developed by the groups at Pittsburgh and Syracuse, will be applied at the lowest level of the runtime hierarchy. Applied to DSPs, these are simple software entities, which can be implemented in a few dozen lines of assembly language, that take advantage of the exception-signaling and interrupt-handling mechanisms present in most DSP kernels to expose errors in the kernel behavior. When the VLA detects (e.g., by monitoring DSP exception signals) an error condition, it will report to an ARMOR (described next), which will take appropriate action such as disabling the execution thread or discarding the current data item. A similar mechanism will be explored for the monitoring and reporting of deadlines, traffic, processor loads, etc. Moreover, the interrupt mechanism will also be used to trigger reconfiguration of the software or hardware at this lowest level of the hierarchy. Note that since the software VLAs are small and interrupt-driven, the latency introduced by VLAs will be negligible.

Hardware VLAs can also be developed for FPGAs, consuming only small number of gates, and taking advantage of otherwise present communication resources. VLAs (software and hardware) in this context is new research area.

The fault tolerance and performance-oriented services offered to the system will be encapsulated in intelligent active entities (agents) developed at the University of Illinois called ARMORs (Adaptive, Reconfigurable, and Mobile Objects for Reliability). ARMORs are, by design, highly flexible processes, which can be customized to meet the runtime needs of the system. Variants of ARMORs will run on DSPs, L2/L3 processors, and other supporting processors throughout the system. ARMORs communicate through message passing and all functions of an ARMOR process and its runtime behavior are encapsulated in "elements." Elements constitute basic building blocks, which usually encapsulate elementary detection and recovery services available to the application. New functionality can be introduced into the system without disturbing existing functionality, as long as, from a resource or timing perspective, it does not affect the current system. In other words, the resource manager must implement some type of resource protection. Services provided by the elements are invoked by the ARMOR interface, which serves as a communication gateway with the outside world. The ARMOR interface has two primary responsibilities: (1) controlling the addition, removal, and replacement of constituent elements within the ARMOR, and (2) providing communication among ARMORs. An application can take advantage of ARMOR provided services (such as error detection and recovery) through the concept of an embedded ARMOR in which the core element structure of the ARMOR is linked to the user application process. The application code is lightly instrumented with the embedded ARMOR API to invoke the services provided by the underlying elements. In this configuration, the embedded ARMOR process appears as a full-fledged ARMOR to other ARMORs in the system and as a native application process to non-ARMOR processes. This permits BTeV physics applications to use the same apparatus for error handling as will be used to handle errors within the computing platform itself.

5.10.3   Strong Connection to BTeV

We believe that there are very significant advantages to connecting this research to the BTeV experiment. Not only will the software and methods produced by this research have significant impact on one of the most important areas of investigation in HEP, but the generalizable computer engineering research will also be directly applicable to a large class of similar real-time embedded computer systems. The BTeV trigger system hardware, which will be provided by Fermilab as part of the experiment, will supply an extremely important ingredient in this project: a large test-bed that represents millions of dollars of equipment and comes with a highly motivated set of users who will test the methodologies and tools developed in an extremely harsh environment over an extended period of time. The test-bed will be built gradually as the proposed research progresses, from a 5% system in 2002 to a full system in 2006-2007. It will therefore be possible for the software developers, aided and supported by the experimenters, to test and refine the software and strategies continuously

and incrementally throughout the lifetime of this project. The close interdisciplinary contact between the experimenters and computer scientists will also help introduce important computer science research into the HEP community, which has not always been aware of work that has been done in this area and has not taken full advantage of it.

5.10.4 Group Members

The team that has been assembled to carry out this research consists of the leaders of the BTeV trigger and data acquisition system development efforts and Computer Scientists/Engineers who are experts in the field of embedded systems, real-time systems, and fault tolerant computing. The Computer Scientists/Engineers come from the University of Illinois, the University of Pittsburgh, Syracuse University, Vanderbilt University, and Fermilab. The team is committed to carrying out the proposed R&D and implementing a series of systems of increasing size and complexity, using the experience gained at each stage to refine and improve the system until it is demonstrated to scale to the full BTeV system. More information on the research groups involved in this project is available at the project's website (http://www.hep.vanderbilt.edu/btev_rtes/).

5.10.5 Current and Proposed Activities

The group has been meeting regularly for 6 months, although the funding did not become available until the end of 2001. The computer science/engineering groups are just beginning to hire students and post-docs and are ramping up their operations. The group has written a work plan for their first year activities, and produced milestones for all five years of the project. These milestones are listed in Table 1.

Table 5.4: Project Milestones

Funding Year	Design Environment Milestone	Runtime System Milestone
FY1: Q1–2	Modeling language and environment (preliminary). Specify Interface to runtime environment.	Design of overall runtime system hierarchy (ARMOR + VLAs).
FY1: Q3–4	Synthesis of operations and Fault managers. DSP and LINUX Synthesis.	Design and implementation of VLA & ARMOR prototypes
FY2: Q1–2	Modeling language and environment. Design space (preliminary).	Communication structure between VLAs and the levels above.
FY2: Q3–4	Synthesis of performance simulator. Synthesis of all operations managers (final). Hardware synthesis.	Detection and recovery in Layer 1 of ARMOR. Study Dynamic load-balancing (DL).
FY3: Q1–2	Modeling language and environment (final). Design space.	Detection and recovery in Layer 2 of ARMOR; Study DL.
FY3: Q3–4	Synthesis to Diagnosability tool. Synthesis to performance simulator (final).	Detection and recovery in Layer 3 of ARMOR; Study DL.
FY4: Q1–2	Design space (final).	Full scale Runtime Environment test.
FY4: Q3–4	Synthesis to Reliability tool. Synthesis to Diagnosability tool (final).	Large scale evaluation on BTeV hardware and revision.
FY5: Q1–2	Synthesis to Reliability tool (final).	Final evaluation on BTeV hardware.